Title	Measurement of Polarization and Time-Dependent CP Asymmetry Parameters in B0→D*+D*-Decays
Author(s)	三宅, 秀樹
Citation	大阪大学, 2005, 博士論文
Version Type	VoR
URL	https://hdl.handle.net/11094/2659
rights	
Note	

Measurement of Polarization and Time-Dependent CP Asymmetry Parameters in $B^0 \to D^{*+}D^{*-}$ Decays

DISSERTATION
Presented in Partial Fulfillment of the Requirements
for the Degree of Doctor of Science
in the Graduate School of Osaka University

Hideki Miyake
Osaka University
February 2005

Acknowledgment

First of all I would like to express my great acknowledgement to my supervisor, Prof. Taku Yamanaka, for giving me a chance to explore this marvellous and interesting world, and a lot of supports and advices. I greatly appreciate Prof. Yorikiyo Nagashima for introducing me into the world of the high energy physics. I am deeply thankful to Dr. T. Hara, Dr. M. Yamaga and Dr. K. Sumisawa for teaching me the basis of high energy in Yamanaka and Nagashima lab.

I also appreciate the all Belle and KEKB members, especially members of the double charm group, *CP* fit group and SVD group for many suggestions and discussions with them. I am grateful to Prof. Y. Sakai, Prof. T. E. Browder, Prof. J. Haba, Prof. M. Tanaka, Prof. Y. Yamada, Dr. T. Tsuboyama, Dr. T. Kawasaki, Dr. T. Aushev, Dr. E. Heenan, Dr. J. Zhang, Dr. T. Higuchi, Dr. M. Yokoyama, Dr. T. Tomura and Dr. T. Nakadaira. I am deeply grateful to Dr. K. Trabelsi for helping my analysis with precious advises. I would like to thank "KEK dinner members"; Dr. N. Abe, Dr. A. Ishikawa, Dr. H. Kakuno and Dr. S. Nishida for keeping my health in Tsukuba life.

My thanks go to the all members of the Yamanaka and Nagashima Groups at Osaka University. I owe special thanks to my colleagues Dr. K. Nitta, Dr. K. Hara, Mr. K. Manabe and Mr. K. Kotera for their kindness and friendship. I am very much thankful to my colleagues Mr. T. Hojo, Mr. K. Sakashita, Mr. T. Ikei, Mr. T. Oba, Mr. B. Takeshita, Mr. Y. Tamai, Ms. Y. Ikemoto, Mr. Y. Shibata, Mr. E. Tanaka, Mr. S. Komatsu, Mr. N. Nishi, Mr. N. Hayama, Mr. S. Aizawa, Mr. A. Kakehashi, Ms. Y. Hattori, Mr. D. Heffernan, Mr. S. Kajiwara, Ms. R. Murayama and Mr. Y. Kuroki. I enjoyed conversations with them, in which I was sometimes given interesting suggestions and ideas. I would like to thank secretaries of Yamanaka and Nagashima Groups: Ms. S. Tsuzuki, Ms. N. Sugimoto and Ms. M. Kawaguchi for their help. I am also indebted to my parents for their help in the long period.

Last but not least, I would like to reveal my cordial thanks to Prof. M. Hazumi. Without his precious advices and suggestions from extensive knowledge and innumerable discussions with him, this thesis work wouldn't have finished.

Abstract

We present measurements of the polarization parameters and CP-violating asymmetries in $B^0 \to D^{*+}D^{*-}$ decays using a 140 fb^{-1} data sample collected at the $\Upsilon(4S)$ resonance with the Belle detector at the KEKB energy-asymmetric e^+e^- collider. The $B^0 \to D^{*+}D^{*-}$ decay is governed by the $b \to c\bar{c}d$ transition and provides a unique way to test the Standard Model. We collect 130 fully reconstructed neutral B meson signals via the $B^0 \to D^{*+}D^{*-}$ decay mode. The $B^0 \to D^{*+}D^{*-}$ decay is a mixture of CP-even and CP-odd components as the $D^{*+}D^{*-}$ system is a superposition of S-, P-, and D-waves. We measure the fraction of each decay amplitude to extract CP asymmetry parameters correctly. We obtain the following polarization parameters:

$$\begin{aligned} R_\perp &= 0.19 \pm 0.08(\text{stat}) \pm 0.01(\text{syst}), \\ R_0 &= 0.57 \pm 0.08(\text{stat}) \pm 0.01(\text{syst}). \end{aligned}$$

The results suggest that the fraction of CP-odd component ($R_\perp$) is small. Using these fractions of polarization components, CP asymmetry parameters are extracted from the proper time difference distribution of B meson decays, which is obtained from the distance between decay vertices of pair-produced B mesons. The flavor of the accompanying B meson is determined from inclusive properties of its decay products. We obtain:

$$\begin{aligned} \mathcal{S}_{D^{*+}D^{*-}} &= -0.75 \pm 0.56(\text{stat}) \pm 0.12(\text{syst}), \\ \mathcal{A}_{D^{*+}D^{*-}} &= -0.26 \pm 0.26(\text{stat}) \pm 0.06(\text{syst}). \end{aligned}$$

These are the first measurement at Belle, and are consistent with the Standard Model expectations. Thus this thesis establishes the analysis method of CP asymmetry measurements in the case we need elaborate angular analyses. More precise measurements of this process with larger statistics in the future will enable us to test whether a new physics effect is seen in the $b \to c\bar{c}d$ transition.

Contents

List of Figures

List of Tables

Chapter 1

Introduction

1.1 Motivation

A concept of symmetry has been playing a central role to understand the nature in terms of modern physics. For example, conservation of energy is led from a time-translation symmetry by the Noether's theorem. We sometimes realize, however, that such symmetry is broken. An example is parity violation in weak interactions, which is an asymmetry between left and right. It does not mean an imperfection of the nature but an imperfection of understanding of the nature we had before the discovery of parity violation. The observation of parity violation helped us to find out the mechanism of the weak interaction. Studies of asymmetries are important to deepen our understanding of the nature.

The CP asymmetry, which arises from the essential difference between matter and anti-matter, is particularly important among such asymmetries, since it is closely related to the fundamental structure of both microscopic and macroscopic world. CP violation was experimentally discovered in 1964 in the neutral Kaon system [1]. There was no physicist who expected such a result until the moment. This completely unexpected result opened a new era of flavor physics.

In 1973, Kobayashi and Maskawa made a proposal which is known as the Kobayashi-Maskawa (KM) mechanism [2]. It explained the origin of CP violation with six quarks in the Glashow-Weinberg-Salam (GWS) framework [3]. In this model, CP violation arises from an irreducible complex phase in the Cabibbo-Kobayashi-Maskawa (CKM) quark-mixing matrix. Today we call a group of theories based on GWS, CKM and Quantum Chromo Dynamics (QCD) the Standard Model (SM). Though the SM has been supported by many experiments [4, 5, 6] over 30 years, CP violation had been observed only in the neutral Kaon system. In 1980, Bigi, Carter and Sanda [7] pointed out that the neutral B-meson system can have a large time-dependent CP asymmetry induced by the B^0-$\overline{B}^0$ mixing. Two B factories, experiments to observe CP violation in the B-meson system with a high luminosity, were proposed and constructed in Japan and U.S.A.. In 2001, Belle [8] and BaBar [9] collaborations observed CP violation in the $b \to c\bar{c}s$ transition as expected by the SM.

Although this result strongly supports that the source of CP violation is dominated by the SM framework, many tests remain before one can conclude that the KM phase is the only source of CP violation. It is unlikely that the SM is the ultimate model to describe the nature, because there are many open questions in the SM. Examples include the origin of three generations, similar but different characteristics of leptons and quarks, and many free parameters. Many models beyond the SM, such as models based on Supersymmetry (SUSY) and Grand Unified Theories (GUT), have been proposed to solve these issues. These models in general expect more than one source of CP violation, whereas the SM has the only one KM phase. CP violation is expected to be a good probe for confirming the SM or detecting new physics beyond the SM.

Another reason that we should investigate CP violation is in the Cosmology. In 1967, Sakharov pointed out [10] that CP violation is essential for our universe to evolve from the Big-Bang to the present figure. However, the magnitude of CP violation in the SM is too small to generate this matter-dominant universe [11]. A new source of CP violation can be a breakthrough to resolve this issue.

Because most of new physics models are not sensitive to the $b \to c\bar{c}s$ transition, measurements of CP asymmetries with different decay processes, such as $b \to c\bar{c}d$, $b \to sq\bar{q}$ and $b \to s\gamma$, are important. $B^0 \to D^{*+}D^{*-}$ is a suitable mode for this purpose. It is dominated by the $b \to c\bar{c}d$ transition, having a large branching fraction ($\sim 0.1\%$) and a possibility of a sizable contribution from the loop diagrams (called the penguin diagrams [12]). In the SM framework, the CP asymmetry of this mode should not be far from that of the $b \to c\bar{c}s$ transition. Thus a large discrepancy from the SM prediction suggests existence of new physics beyond the SM.

The goal of this thesis is to present a measurement of time-dependent CP asymmetries in the $B^0 \to D^{*+}D^{*-}$ decay. The outline of this thesis follows: In chapter 2, we show the principle of the measurement for time-dependent CP asymmetries. The experimental apparatus is described in chapter 3. In chapter 4, we explain the $D^{*+}D^{*-}$ selection method. Polarization should be measured before the CP analysis to disentangle states with different CP parities. Its measurement is shown in chapter 5. In chapter 6, we explain in detail the method of the time-dependent CP asymmetry measurements and show the results. Chapter 7 is devoted to discussions on our results. Finally, conclusion is given in Chapter 8.

In this introduction, we describe phenomenology of time-dependent CP violation in B decays to a CP eigenstate. We also define CP asymmetry parameters $\mathcal{S}_{CP}$ and $\mathcal{A}_{CP}$. We then define the Unitarity Triangle in the SM framework and show present constraints on it. After that we explain characteristics of $b \to c\bar{c}d$ transitions and show advantages of the $B^0 \to D^{*+}D^{*-}$ mode in terms of the clean measurement of CP asymmetries. In section 1.5, we discuss expectations on $\mathcal{S}_{CP}$ and $\mathcal{A}_{CP}$ in and beyond the SM. In section 1.6, we describe a time-dependent differential decay rate that contains information on polarization.

1.2 Phenomenology of time-dependent CP violation in B decays

1.2.1 Time evolution of the neutral B mesons

A neutral B_d meson produced by the strong interaction is a pure flavor eigenstate, $(\overline{b}d)$ or $(b\overline{d})$. The former is denoted by B^0 and the latter is by $\overline{B}^0$ [13]. Generally, if mass eigenstates and flavor eigenstates are different, time-dependent oscillation occurs. Here, time evolution of the neutral B meson state at time t is given by an admixture of pure B^0 and $\overline{B}^0$:

$$|B(t)\rangle = a(t)|B^0\rangle + b(t)|\overline{B}^0\rangle. \tag{1.1}$$

The time-dependent Schrödinger equation is:

$$i\frac{d}{dt}\begin{pmatrix} a(t) \\ b(t) \end{pmatrix} = \mathcal{H}\begin{pmatrix} a(t) \\ b(t), \end{pmatrix}, \tag{1.2}$$

where Hamiltonian $\mathcal{H}$ is denoted as:

$$\mathcal{H} = \mathbf{M} - \frac{i}{2}\mathbf{\Gamma} = \begin{pmatrix} M_{11} - \frac{i}{2}\Gamma_{11} & M_{12} - \frac{i}{2}\Gamma_{12} \\ M_{21} - \frac{i}{2}\Gamma_{21} & M_{22} - \frac{i}{2}\Gamma_{22} \end{pmatrix}. \tag{1.3}$$

$\mathbf{M}$ and $\mathbf{\Gamma}$ are the mass matrix and the decay matrix, respectively. $M_{21} = M_{12}^*$ and $\Gamma_{21} = \Gamma_{12}^*$ are required from the definition of Hermitian matrices. CPT invariance assumption guarantees $M \equiv M_{11} = M_{22}$ and $\Gamma \equiv \Gamma_{11} = \Gamma_{22}$. Eigenvalues $\mu_\pm$ of this Hamiltonian are obtained as:

$$\mu_\pm = M - \frac{i}{2}\Gamma \pm \sqrt{(M_{12} - \frac{i}{2}\Gamma_{12})(M_{12}^* - \frac{i}{2}\Gamma_{12}^*)}. \tag{1.4}$$

Both mass eigenstates can be described by mixing parameters q and p:

$$\begin{aligned} |B_1\rangle &= p|B^0\rangle + q|\overline{B}^0\rangle \text{ for } \mu_+, \\ |B_2\rangle &= p|B^0\rangle - q|\overline{B}^0\rangle \text{ for } \mu_-, \end{aligned} \tag{1.5}$$

with

$$\frac{q}{p} = \sqrt{\frac{M_{12}^* - \frac{i}{2}\Gamma_{12}^*}{M_{12} - \frac{i}{2}\Gamma_{12}}}. \tag{1.6}$$

and $|p|^2 + |q|^2 = 1$. Mass eigenstates of B mesons are denoted by B_1 (m_1, Γ_1) and B_2 (m_2, Γ_2), where m_1 (m_2) and Γ_1 (Γ_2) are the mass and decay rate of B_1 (B_2). They are given by:

$$\begin{aligned} m_1 &= \Re\mu_+, \ \Gamma_1 = -2\Im\mu_+, \\ m_2 &= \Re\mu_-, \ \Gamma_2 = -2\Im\mu_-, \end{aligned} \tag{1.7}$$

For convenience, we define a mass difference Δm, a decay rate difference $\Delta\Gamma$, an averaged mass $\overline{m}$ and an averaged decay rate $\overline{\Gamma}$, respectively:

$$\begin{aligned}
\Delta m \equiv& m_2 - m_1, \\
\Delta\Gamma \equiv& \Gamma_1 - \Gamma_2, \\
\overline{m} \equiv& \frac{m_1 + m_2}{2}, \\
\overline{\Gamma} \equiv& \frac{\Gamma_1 + \Gamma_2}{2}.
\end{aligned} \tag{1.8}$$

Time evolution of B_1 and B_2 is written as:

$$\begin{aligned}
|B_1(t)\rangle &= e^{-i\mu_+ t}|B_1\rangle = e^{-im_1 t - \Gamma_1 t/2}|B_1\rangle, \\
|B_2(t)\rangle &= e^{-i\mu_- t}|B_2\rangle = e^{-im_2 t - \Gamma_2 t/2}|B_2\rangle.
\end{aligned} \tag{1.9}$$

From Eq. (1.5) to (1.9), time evolution of both B^0 and $\overline{B}^0$ is acquired:

$$\begin{aligned}
|B^0(t)\rangle &= g_+(t)|B^0\rangle + \frac{q}{p} g_-(t)|\overline{B}^0\rangle, \\
|\overline{B}^0(t)\rangle &= g_+(t)|\overline{B}^0\rangle + \frac{p}{q} g_-(t)|B^0\rangle,
\end{aligned} \tag{1.10}$$

where

$$\begin{aligned}
g_\pm(t) =& \frac{1}{2} e^{-im_1 t} \cdot e^{-\Gamma_1 t/2} \left[1 \pm e^{-i\Delta m t} \cdot e^{\Delta\Gamma t/2} \right] \\
=& \frac{1}{2} e^{-i\overline{m} t} \cdot e^{-\overline{\Gamma} t/2} \left[e^{i\Delta m t/2} \cdot e^{-\Delta\Gamma t/4} \pm e^{-i\Delta m t/2} \cdot e^{\Delta\Gamma t/4} \right].
\end{aligned} \tag{1.11}$$

Since $\Delta\Gamma/\Gamma \sim \mathcal{O}(10^{-3})$ in the neutral B_d system, we take $\Delta\Gamma = 0$ in the following, and redefine B decay rate $\Gamma \equiv \overline{\Gamma} = \Gamma_1 = \Gamma_2$. Equation (1.11) then becomes:

$$g_\pm(t) = e^{-i\overline{m} t} \cdot e^{-\Gamma t/2} \left[\frac{e^{i\Delta m t/2} \pm e^{-i\Delta m t/2}}{2} \right]. \tag{1.12}$$

Finally, time evolution of both B^0 and $\overline{B}^0$ is:

$$\begin{aligned}
|B^0(t)\rangle &= e^{-\Gamma t/2} \left[\cos\frac{\Delta m t}{2} |B^0\rangle + i\frac{q}{p} \sin\frac{\Delta m t}{2} |\overline{B}^0\rangle \right], \\
|\overline{B}^0(t)\rangle &= e^{-\Gamma t/2} \left[\cos\frac{\Delta m t}{2} |\overline{B}^0\rangle + i\frac{p}{q} \sin\frac{\Delta m t}{2} |B^0\rangle \right],
\end{aligned} \tag{1.13}$$

where factor $e^{-i\overline{m}t}$ is canceled by a phase convention.

1.2.2 Time-dependent CP violation

We consider the case that B^0 and $\overline{B}^0$ mesons decay into a same final state f_{CP} that is a CP eigenstate. Decay amplitudes are defined by

$$\begin{aligned} A_{CP} &\equiv \langle f_{CP}|H|B^0\rangle, \\ \overline{A}_{CP} &\equiv \langle f_{CP}|H|\overline{B}^0\rangle. \end{aligned} \tag{1.14}$$

Each time-dependent decay amplitude is written by using Eq. (1.13) as :

$$\begin{aligned} A_{CP}(t) =& A_{CP}e^{-\Gamma t/2}[\cos\frac{\Delta mt}{2} + i\lambda_{CP}\sin\frac{\Delta mt}{2}], \\ \overline{A}_{CP}(t) =& \overline{A}_{CP}e^{-\Gamma t/2}[\cos\frac{\Delta mt}{2} + i\lambda_{CP}^{-1}\sin\frac{\Delta mt}{2}], \end{aligned} \tag{1.15}$$

where we define

$$\lambda_{CP} \equiv \frac{q}{p}\cdot\frac{\overline{A}_{CP}}{A_{CP}}. \tag{1.16}$$

As explained later, $|q/p| \sim 1$ holds in the neutral B_d system within the SM framework. Therefore $|\lambda_{CP}|^2 = |\overline{A}_{CP}|^2/|A_{CP}|^2$ holds.

The time-dependent decay rates are then written as:

$$\begin{aligned} \Gamma(B^0(t)\to f_{CP}) \equiv& |\langle f_{CP}|H|B^0(t)\rangle|^2 \\ =& \frac{e^{-\Gamma t}}{2}|A_{CP}|^2\left[(|\lambda_{CP}|^2+1) - (|\lambda_{CP}|^2-1)\cos\Delta mt - 2\Im\lambda_{CP}\sin\Delta mt\right], \\ \Gamma(\overline{B}^0(t)\to f_{CP}) \equiv& |\langle f_{CP}|H|\overline{B}^0(t)\rangle|^2 \\ =& \frac{e^{-\Gamma t}}{2}|\overline{A}_{CP}|^2\left[(|\lambda_{CP}^{-1}|^2+1) - (|\lambda_{CP}^{-1}|^2-1)\cos\Delta mt - 2\Im\lambda_{CP}^{-1}\sin\Delta mt\right] \\ =& \frac{e^{-\Gamma t}}{2}|A_{CP}|^2\left[(|\lambda_{CP}|^2+1) + (|\lambda_{CP}|^2-1)\cos\Delta mt + 2\Im\lambda_{CP}\sin\Delta mt\right]. \end{aligned} \tag{1.17}$$

The time-dependent CP asymmetry is defined as:

$$\begin{aligned} a_{CP}(t) \equiv& \frac{\Gamma(\overline{B}^0(t)\to f_{CP}) - \Gamma(B^0(t)\to f_{CP})}{\Gamma(\overline{B}^0(t)\to f_{CP}) + \Gamma(B^0(t)\to f_{CP})} \\ =& \frac{(|\lambda_{CP}|^2-1)\cos\Delta mt + 2\Im\lambda_{CP}\sin\Delta mt}{|\lambda_{CP}|^2+1} \\ =& \mathcal{A}_{CP}\cos\Delta mt + \mathcal{S}_{CP}\sin\Delta mt, \end{aligned} \tag{1.18}$$

where we define CP asymmetry parameters

$$\begin{aligned} \mathcal{S}_{CP} \equiv& \frac{2\Im\lambda_{CP}}{|\lambda_{CP}|^2+1}, \\ \mathcal{A}_{CP} \equiv& \frac{|\lambda_{CP}|^2-1}{|\lambda_{CP}|^2+1}. \end{aligned} \tag{1.19}$$

1.2.3 Meaning of CP asymmetry parameters

$|q/p| \sim 1$ means that $q/p \sim e^{-i\phi_M}$, where ϕ_M is a CP-violating weak phase difference in the mixing. $\overline{A}_{CP}/A_{CP}$ can also have a weak phase difference ϕ_D and also an amplitude ratio $r \equiv |\overline{A}_{CP}/A_{CP}|$. Then Eq. (1.16) becomes:

$$\lambda_{CP} = (e^{-i\phi_M}) \cdot (r \cdot e^{-i\phi_D}) = r \cdot e^{-i(\phi_M + \phi_D)}. \tag{1.20}$$

Equation (1.20) means that we have two sources of CP violation. One source is existence of the decay amplitude difference ($r \neq 1$). It makes $|\lambda_{CP}| \neq 1$, then $\mathcal{A}_{CP} \neq 0$ in Eq. (1.19). This type of CP asymmetry is called "direct CP violation". Another source is existence of the phase interference ($\phi_M + \phi_D \neq 0$). It makes $\Im\lambda_{CP} \neq 0$, then $\mathcal{S}_{CP} \neq 0$ in Eq. (1.19). This type of CP asymmetry is called "mixing-induced CP violation".

In the rest of this thesis, we discuss CP violation with these CP asymmetry parameters, $\mathcal{S}_{CP}$ and $\mathcal{A}_{CP}$.

1.3 CKM Matrix and Unitarity Triangle

In the SM framework, left-handed quarks form three doublets under the weak SU(2) interaction:

$$\begin{pmatrix} u \\ d' \end{pmatrix}_L \begin{pmatrix} c \\ s' \end{pmatrix}_L \begin{pmatrix} t \\ b' \end{pmatrix}_L . \tag{1.21}$$

The weak eigenstates (d', s', b') are a linear combination of the mass eigenstates (d, s, b):

$$\begin{pmatrix} d' \\ s' \\ b' \end{pmatrix} = \mathbf{V}_{\text{CKM}} \begin{pmatrix} d \\ s \\ b \end{pmatrix} \equiv \begin{pmatrix} V_{ud} & V_{us} & V_{ub} \\ V_{cd} & V_{cs} & V_{cb} \\ V_{td} & V_{ts} & V_{tb} \end{pmatrix} \begin{pmatrix} d \\ s \\ b \end{pmatrix}, \tag{1.22}$$

where $\mathbf{V}_{\text{CKM}}$, a 3×3 unitarity matrix, is called the Cabibbo-Kobayashi-Maskawa (CKM) matrix [2]. The Wolfenstein parametrization [19] is convenient to grasp a character of this matrix:

$$\mathbf{V}_{\text{CKM}} = \begin{pmatrix} 1 - \lambda^2/2 & \lambda & A\lambda^3(\rho - i\eta) \\ -\lambda & 1 - \lambda^2/2 & A\lambda^2 \\ A\lambda^3(1 - \rho - i\eta) & -A\lambda^2 & 1 \end{pmatrix} + \mathcal{O}(\lambda^4). \tag{1.23}$$

Here A, ρ and η are real parameters and $\lambda = \sin\theta_C \sim 0.22$, where θ_C is called the Cabibbo angle [20]. V_{ub} and V_{td} are in particular interesting, because their complex phases make weak interaction violate CP symmetries. Another interesting character is unitarity of the matrix, $\sum_j V_{ij}V_{kj}^* = \sum_j V_{ji}^* V_{jk} = 0$ $(i \neq k)$. The most useful relation among six of them is:

$$V_{ud}V_{ub}^* + V_{cd}V_{cb}^* + V_{td}V_{tb}^* = 0. \tag{1.24}$$

Equation (1.24) can be expressed as a triangle in the complex plane, which is called the "Unitarity Triangle". It is convenient to normalize Eq. (1.24) by $|V_{cd}V_{cb}^*|$, since one side is aligned to the real axis and its length becomes one. Then the coordinates of the vertices of the triangle are: $(0,0)$, $(1,0)$ and $(\overline{\rho},\overline{\eta})$, where

$$\begin{aligned}\overline{\rho} &\equiv \left(1-\frac{\lambda^2}{2}\right)\rho,\\ \overline{\eta} &\equiv \left(1-\frac{\lambda^2}{2}\right)\eta.\end{aligned} \tag{1.25}$$

Figure 1.1 shows the rescaled Unitarity Triangle, where

$$\begin{aligned}\phi_1 &\equiv \pi - \arg\left(\frac{-V_{tb}^*V_{td}}{-V_{cb}^*V_{cd}}\right),\\ \phi_2 &\equiv \arg\left(\frac{V_{tb}^*V_{td}}{-V_{ub}^*V_{ud}}\right),\\ \phi_3 &\equiv \arg\left(\frac{V_{ub}^*V_{ud}}{-V_{cb}^*V_{cd}}\right)\end{aligned} \tag{1.26}$$

are three angles of the triangle. As described later in this chapter, non-zero values for ϕ_1, ϕ_2 and ϕ_3 are directly connected to observable CP asymmetries.

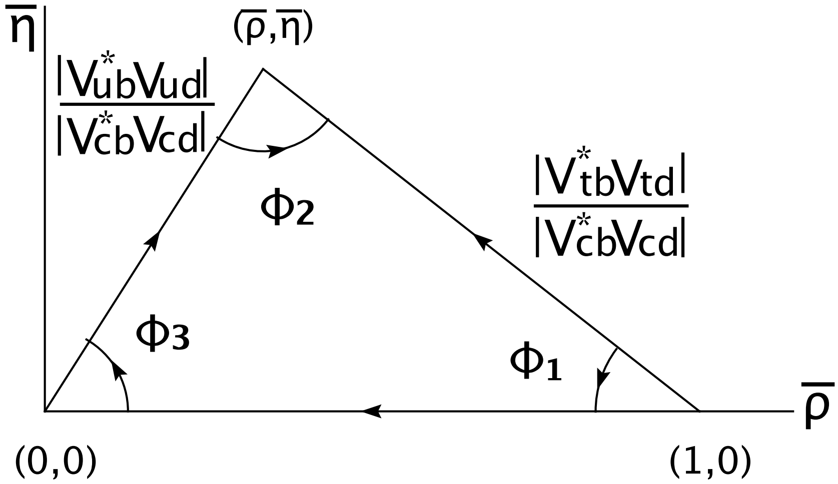

Figure 1.1: *Rescaled Unitarity triangle.*

1.3.1 B^0-$\overline{B}^0$ mixing in the Standard Model

In the SM, B^0 and $\overline{B}^0$ can mix through the second order weak interactions known as the "box-diagram" (Fig. 1.2). Now this B^0-$\overline{B}^0$ mixing is described in terms of CKM matrix elements. Theoretical computations indicate [21],

$$\begin{aligned}M_{12} &\propto (V_{tb}V_{td}^*)^2 m_t^2,\\ \Gamma_{12} &\propto (V_{ub}V_{ud}^* + V_{cb}V_{cd}^*)^2 m_b^2 = (-V_{tb}V_{td}^*)^2 m_b^2,\end{aligned} \tag{1.27}$$

where m_t (m_b) is the top (bottom) quark mass.

This is qualitatively explained as follows: Since the intermediate state of B^0-$\overline{B}^0$ mixing is dominated by the virtual top quark that is the heaviest quark, M_{12} is governed by m_t. On the contrary, B^0 ($\overline{B}^0$) should decay to particles lighter than the bottom quark. With an approximation that the masses of charm quark and other light quarks are well below m_b, Γ_{12} is determined by m_b. Thus we obtain

$$\left|\frac{\Gamma_{12}}{M_{12}}\right| \sim \mathcal{O}\left(\frac{m_b^2}{m_t^2}\right) \ll 1. \tag{1.28}$$

With this condition, Eq. (1.6) becomes:

$$\begin{aligned} \frac{q}{p} &= \sqrt{\frac{M_{12}^*}{M_{12}}} + \mathcal{O}\left(\frac{\Gamma_{12}}{M_{12}}\right) \\ &\simeq \frac{V_{tb}^* V_{td}}{V_{tb} V_{td}^*}. \end{aligned} \tag{1.29}$$

Then $|q/p| \sim 1$ holds.

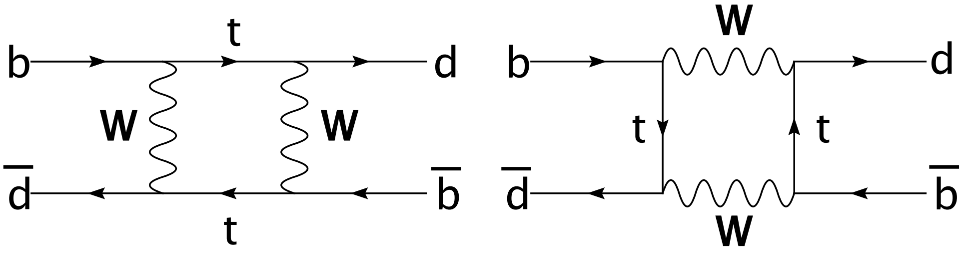

Figure 1.2: *box-diagrams for the B^0-$\overline{B}^0$ mixing.*

1.3.2 *CP* violation in $B^0 \to J/\psi K_S^0$ Decay

A CP asymmetry parameter, $\sin 2\phi_1$, has been measured with $b \to c\bar{c}s$ modes, in particular, $B^0 \to J/\psi K_S^0$ decays. A remarkable feature of $J/\psi K_S^0$ is its very small hadronic uncertainties in the SM framework.

In the CKM matrix [Eq. (1.23)], their amplitudes are approximated by the power of λ. A larger amplitude is called CKM-allowed and a smaller is called CKM-suppressed. Furthermore, internal spectator diagrams like Fig. 1.3 are suppressed since the internal vertex should cancel the color of the spectator. This is called a color-suppressed decay, and external spectator diagrams are called color-allowed decays.

The tree diagram of the $B^0 \to J/\psi K_S^0$ decay [Fig. 1.3 (left)] is color-suppressed and CKM-allowed. Though the loop diagrams with c and t virtual quarks have the same order of CKM matrix elements as the tree diagram, their weak phase is also the same as the tree diagram. Therefore measured CP asymmetry is not affected. Only a loop diagram including a virtual u quark has a different weak phase. But this diagram is CKM-suppressed by $\mathcal{O}(\lambda^2)$ compared to the tree diagram. Moreover, additional suppression arises from generating a heavy color singlet $c\bar{c}$ pair from gluons and to make J/ψ. Therefore the penguin pollution is negligible and only one weak phase contributes to CP violation. As a result, mixing induced CP asymmetry parameter $S_{J/\psi K_S^0}$ should be equal to $\sin 2\phi_1$ to a good approximation.

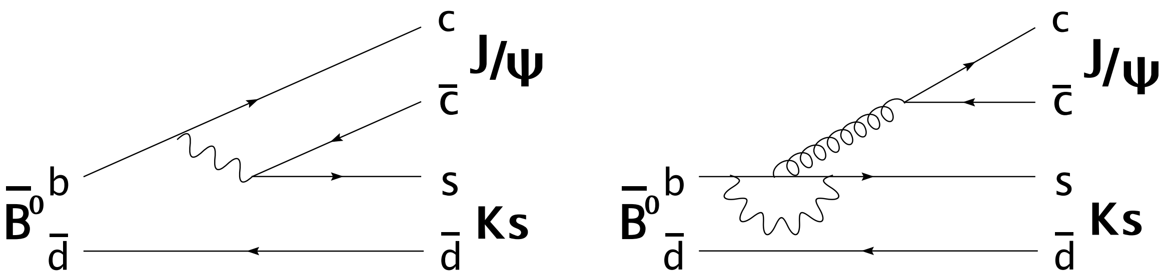

Figure 1.3: *Left (right):* $B^0 \to J/\psi K_S^0$ *tree (penguin) diagram. The tree diagram is color-suppressed due to the internal vertex.*

The present[1] world average of the CP asymmetry parameter is

$$\sin 2\phi_1 = 0.731 \pm 0.056 \text{ [13]}. \tag{1.30}$$

In the rest of this paper, we regard this value as the reference of $\sin 2\phi_1$. Figure 1.4 shows the current unitarity triangle constraints obtained from various experiments including $\sin 2\phi_1$ measurements.

1.4 $B^0 \to D^{*+}D^{*-}$ Decay Amplitude

As mentioned previously, a measurement of time-dependent CP asymmetries via the $b \to c\bar{c}d$ [14] transition is important to check the consistency of the SM framework and to search for new physics beyond the SM. In this section, we first show the detailed reason why $b \to c\bar{c}d$ is suitable for such tasks. Then we explain special features of the $B^0 \to D^{*+}D^{*-}$ mode.

One of common characteristics over all $b \to c\bar{c}d$ modes is that they are sensitive to the CP asymmetry parameter $\sin 2\phi_1$. Although $b \to c\bar{c}s$ is also sensitive to $\sin 2\phi_1$, comparison with different quark transitions is an important test to check the SM consistency. There are some new physics models [15] that expect sizable CP asymmetry corrections from the dominant phase ($= \phi_1$ for $b \to c\bar{c}d$) up to 0.6.

Promising final states of such $b \to c\bar{c}d$ modes include $B^0 \to D^+D^-$, $B^0 \to D^{*\pm}D^{\mp}$, $B^0 \to D^{*+}D^{*-}$ and $B^0 \to J/\psi\pi^0$ etc. Table 1.1 summarizes characteristics of these modes.

---

[1] In August 2004, Particle Data Group published the latest version of the review of particle properties. These numbers are almost the same as those in the previous review [13]. Therefore, in this paper, we use the numbers taken from [13].

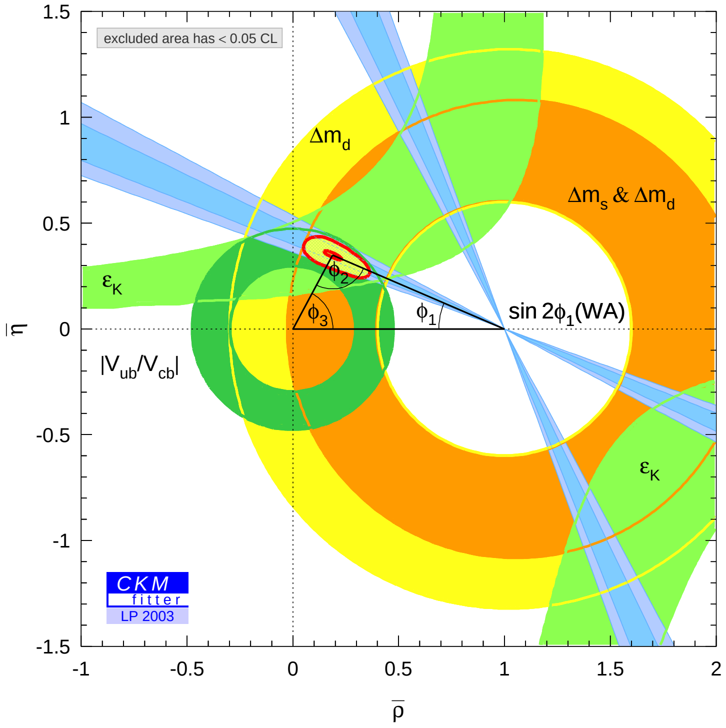

Figure 1.4: *Experimental constraints to the unitarity triangle. The unitarity triangle constraints obtained from various experiments in the* $\overline{\rho} - \overline{\eta}$ *plane are plotted. The mixing parameter* Δm_d (Δm_s) *in the* B_d (B_s) *system, CKM matrix element* $|V_{ub}/V_{cb}|$*, the* CP *violation parameter* ϵ_K *in the neutral* K *meson system, the* CP *violation parameter* $\sin 2\phi_1$ *in the neutral* B *meson system are plotted. The four bands crossing at (1, 0) represents* $\sin 2\phi_1$ *measurements including* $B^0 \to J/\psi K^0_S$.

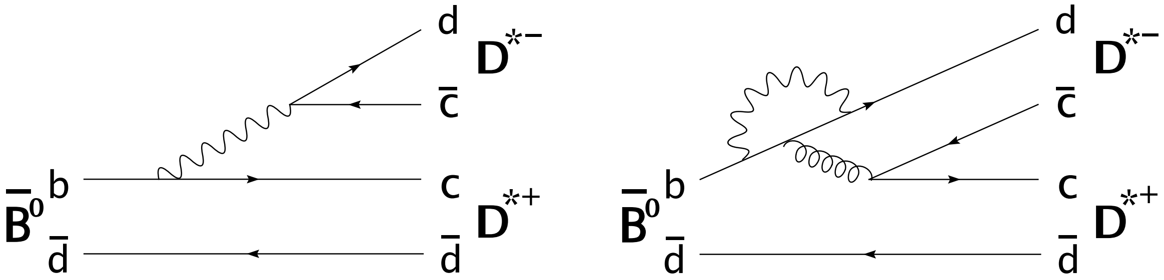

Figure 1.5: *Left (right):* $B^0 \to D^{*+}D^{*-}$ *tree (penguin) diagram. The tree diagram dominates the total decay amplitude. The strong penguin is dominant for the penguin diagram. The electroweak penguin and the exchange diagram are negligible since their contribution is at most a few % of the strong penguin.*

The color-allowed $D^{(*)}D^{(*)}$ decays have relatively large branching fractions of $\mathcal{B} \sim 0.1\%$. A color-suppressed decays like $J/\psi\pi^0$ can have the same order of sensitivity owing to higher reconstruction efficiencies.

Both tree and penguin amplitudes are CKM-suppressed with the same order of CKM factors [$\mathcal{O}(\lambda^3)$]. Since new physics effects can enter in both tree and penguin diagrams in the $b \to c\bar{c}d$ decay, a new physics model that is not CKM-suppressed may give a relatively large enhancement to measured CP asymmetries. Furthermore, the penguin diagram in the SM framework has a different weak phase from the tree diagram. As explained later, magnitude of a penguin diagram with a different weak phase may make a sizable pollution in the measured CP asymmetry and may cause large uncertainty in the SM expectation.

Among various $b \to c\bar{c}d$ decays, $B^0 \to D^{*+}D^{*-}$ decay has advantages. First, the penguin pollution is expected to be relatively small, at a few% level due to the vector-vector decay [16]. Second, it is experimentally clean, since there is few background from generic $B\bar{B}$ decays, due to the high purity of $D^{*\pm}$ mesons.

The vector-vector decay feature also makes the $D^{*+}D^{*-}$ final state a mixture of CP-even and CP-odd components. Although it gives some dilution to a measured CP asymmetry, we can extract correct CP-violation parameters by knowing the fraction of each component. This technique is called the angular analysis [17]. The CP-odd fraction is expected to be about 5.5% in the SM [18].

Decay mode	Color	CKM	Decay type	Branching fraction ($\times 10^{-4}$) [13]
D^+D^-	A	S	PP	$< 9.4(90\%\ CL)$
$D^{*+}D^- + D^+D^{*-}$	A	S	VP+PV	11.7 ± 3.5
$D^{*+}D^{*-}$	A	S	VV	8.7 ± 1.8
$J/\psi\pi^0$	S	S	VP	0.22 ± 0.04
$J/\psi K^0_S$	S	A	VP	$(8.5 \pm 0.5) \times 1/2$

Table 1.1: *Characteristics of $b \to c\bar{c}d$ transitions available for time-dependent CP asymmetry measurements. $J/\psi K^0_S$ is also shown for comparison.* A (S) *means an allowed (suppressed) decay and* P (V) *means a Pseudo-scalar (Vector) particle.*

1.5 CP violation in $B^0 \to D^{*+}D^{*-}$

1.5.1 The simplest case

We first discuss the simplest case where the dominant amplitude in the $D^{*+}D^{*-}$ decay is the tree diagram (Fig. 1.5). In this case, only one CKM phase appears in decay amplitudes:

$$\begin{aligned} A(D^{*+}D^{*-}{}_i) \equiv& \langle D^{*+}D^{*-}{}_i|\mathcal{H}_{\rm eff}|B^0\rangle \equiv V_{cd}V_{cb}^* \cdot \mathcal{M}_i, \\ \overline{A}(D^{*+}D^{*-}{}_i) \equiv& \langle D^{*+}D^{*-}{}_i|\mathcal{H}_{\rm eff}|\overline{B}^0\rangle \equiv V_{cd}^*V_{cb} \cdot \overline{\mathcal{M}}_i, \end{aligned} \tag{1.31}$$

where $D^{*+}D^{*-}{}_i$ is a final state of $D^{*+}D^{*-}$ which has a fixed angular momentum, i, and thus is a CP eigenstate, and $\mathcal{M}_i$ is a matrix element for each final state.

From Eq. (1.16) and (1.29), we obtain

$$\begin{aligned}\lambda_i &= \frac{q}{p} \cdot \frac{\overline{A}(D^{*+}D^{*-}{}_i)}{A(D^{*+}D^{*-}{}_i)} \\ &= \frac{V_{td}V_{tb}^*}{V_{td}^*V_{tb}} \cdot \frac{V_{cd}^*V_{cb}\overline{\mathcal{M}}_i}{V_{cd}V_{cb}^*\mathcal{M}_i} \\ &= \eta_i e^{-2i\phi_1}\end{aligned} \tag{1.32}$$

where η_i is the CP parity of each final state. CP asymmetry parameters [Eq. (1.19)] become:

$$\begin{aligned}\mathcal{S}_{D^{*+}D^{*-}{}_i} &= -\eta_i \sin 2\phi_1, \\ \mathcal{A}_{D^{*+}D^{*-}{}_i} &= 0.\end{aligned} \tag{1.33}$$

This result is exactly the same as the $J/\psi K_S^0$ case and there is no direct CP violation ($|\lambda_i| = 1$) in this decay, because only one weak phase is involved.

1.5.2 More than one phase in the Standard Model

In the case that penguin diagram cannot be ignored, we have 3 CKM factors in the decay amplitude to the $D^{*+}D^{*-}$ final state:

$$\begin{aligned}A(D^{*+}D^{*-}{}_i) =&\langle D^{*+}D^{*-}{}_i|\mathcal{H}_{\text{eff}}|B^0\rangle = V_{ud}V_{ub}^*\mathcal{M}_i^{(u)} + V_{cd}V_{cb}^*\mathcal{M}_i^{(c)} + V_{td}V_{tb}^*\mathcal{M}_i^{(t)}, \\ \overline{A}(D^{*+}D^{*-}{}_i) =&\langle D^{*+}D^{*-}{}_i|\mathcal{H}_{\text{eff}}|\overline{B}^0\rangle = V_{ud}^*V_{ub}\overline{\mathcal{M}_i}^{(u)} + V_{cd}^*V_{cb}\overline{\mathcal{M}_i}^{(c)} + V_{td}^*V_{tb}\overline{\mathcal{M}_i}^{(t)},\end{aligned} \tag{1.34}$$

where $\mathcal{M}_i^{(j)}$ ($j = u, c, t$) are the generic amplitudes apart from the explicitly shown CKM factors.

Using Eq. (1.24), Eq. (1.34) becomes:

$$\begin{aligned}A(D^{*+}D^{*-}{}_i) &= V_{cd}V_{cb}^*\mathcal{T} + V_{td}V_{tb}^*\mathcal{P} \\ &= V_{cd}V_{cb}^*\mathcal{T}(1 - |\mathcal{R}|e^{-i\phi_1}e^{i\delta}), \\ \overline{A}(D^{*+}D^{*-}{}_i) &= V_{cd}^*V_{cb}\overline{\mathcal{T}} + V_{td}^*V_{tb}\overline{\mathcal{P}} \\ &= V_{cd}^*V_{cb}\overline{\mathcal{T}}(1 - |\mathcal{R}|e^{i\phi_1}e^{i\delta}),\end{aligned} \tag{1.35}$$

where $\mathcal{T} \equiv \mathcal{M}_i^{(c)} - \mathcal{M}_i^{(u)}$ is a tree-dominant amplitude, $\mathcal{P} \equiv \mathcal{M}_i^{(t)} - \mathcal{M}_i^{(u)}$ is a pure penguin amplitude,

$$\begin{aligned}\mathcal{R} \equiv & \; -\left|\frac{V_{td}V_{tb}^*}{V_{cd}V_{cb}^*}\right| \cdot \frac{\mathcal{P}}{\mathcal{T}} \\ = & \; |\mathcal{R}|e^{-i\phi_1}e^{i\delta}\end{aligned} \tag{1.36}$$

and $\delta \equiv \delta_{\mathcal{P}} - \delta_{\mathcal{T}}$ is a strong phase difference between $\mathcal{P}$ and $\mathcal{T}$.

Using Eq. (1.29) and (1.35),

$$\begin{aligned}\lambda_i = & \ \frac{q}{p}\cdot\frac{\overline{A}(D^{*+}D^{*-}{}_i)}{A(D^{*+}D^{*-}{}_i)} \\ = & \ \frac{V_{td}V_{tb}^*}{V_{td}^*V_{tb}}\cdot\frac{V_{cd}^*V_{cb}\overline{\mathcal{T}}(1-|\mathcal{R}|e^{i\phi_1}e^{i\delta})}{V_{cd}V_{cb}^*\mathcal{T}(1-|\mathcal{R}|e^{-i\phi_1}e^{i\delta})} \\ = & \ \eta_i\cdot\frac{e^{-i\phi_1}-|\mathcal{R}|e^{i\delta}}{e^{i\phi_1}-|\mathcal{R}|e^{i\delta}}.\end{aligned} \tag{1.37}$$

In this case, CP asymmetry parameters [Eq. (1.19)] become:

$$\begin{aligned}\mathcal{S}_{D^{*+}D^{*-}i} &= \eta_i\frac{-\sin 2\phi_1+2|\mathcal{R}|\sin\phi_1\cos\delta}{1+|\mathcal{R}|^2-2|\mathcal{R}|\cos\phi_1\cos\delta}, \\ \mathcal{A}_{D^{*+}D^{*-}i} &= \frac{2|\mathcal{R}|\sin\phi_1\sin\delta}{1+|\mathcal{R}|^2-2|\mathcal{R}|\cos\phi_1\cos\delta}.\end{aligned} \tag{1.38}$$

Direct CP violation will occur when the penguin amplitude exists ($\mathcal{R}\neq 0$) and the strong phase difference exists ($\sin\delta\neq 0$).

1.5.3 With new physics beyond the Standard Model

When a new physics term contributes to the $D^{*+}D^{*-}$ decay, the total decay amplitude can be written as:

$$\begin{aligned}A(D^{*+}D^{*-}{}_i) =& |A_{SM}|e^{i\phi_{SM}}e^{i\delta_{SM}}+|A_{NP}|e^{i\phi_N}e^{i\delta_{NP}} \\ =& V_{cd}V_{cb}^*\mathcal{T}(1-|\mathcal{R}|e^{-i\phi_1}e^{i\delta}+|\mathcal{N}|e^{i\phi_N}e^{i\delta_N}), \\ \overline{A}(D^{*+}D^{*-}{}_i) =& \overline{|A_{SM}|}e^{-i\phi_{SM}}e^{i\delta_{SM}}+\overline{|A_{NP}|}e^{-i\phi_N}e^{i\delta_{NP}} \\ =& V_{cd}^*V_{cb}\overline{\mathcal{T}}(1-|\mathcal{R}|e^{i\phi_1}e^{i\delta}+\overline{|\mathcal{N}|}e^{-i\phi_N}e^{i\delta_N}),\end{aligned} \tag{1.39}$$

where A_{SM} (A_{NP}), ϕ_{SM} (ϕ_N), δ_{SM} (δ_{NP}) are the amplitude, CP violating phase and CP conserving phase of the SM (new physics). In the SM, ϕ_{SM} and δ_{SM} correspond to the weak phase and strong phase, respectively. It is defined for convenience as $|\mathcal{N}|\equiv\frac{|A_{NP}|}{|V_{cd}V_{cb}^*|}$ and $\delta_N\equiv\delta_{NP}-\delta_{\mathcal{T}}$.

Then the λ_i becomes:

$$\begin{aligned}\lambda_i &= \frac{q}{p}\cdot\frac{\overline{A}(D^{*+}D^{*-}{}_i)}{A(D^{*+}D^{*-}{}_i)} \\ &= \eta_i\cdot\frac{e^{-i\phi_1}-|\mathcal{R}|e^{i\delta}+|\mathcal{N}|e^{-i(\phi_1+\phi_N)}e^{i\delta_N}}{e^{i\phi_1}-|\mathcal{R}|e^{i\delta}+|\mathcal{N}|e^{i(\phi_1+\phi_N)}e^{i\delta_N}}.\end{aligned} \tag{1.40}$$

As a result, we obtain:

$$\begin{aligned}\mathcal{S}_{D^{*+}D^{*-}i} =& \ \eta_i[-\sin 2\phi_1+2|\mathcal{R}|\sin\phi_1\cos\delta-|\mathcal{N}|^2\sin(2\phi_1+2\phi_N) \\ &+2|\mathcal{N}|\{|\mathcal{R}|\sin(\phi_1+\phi_N)\cos(\delta-\delta_N)-\sin(2\phi_1+\phi_N)\cos\delta_N]/L, \\ \mathcal{A}_{D^{*+}D^{*-}i} =& \ [2|\mathcal{R}|\sin\phi_1\sin\delta+2N\{|\mathcal{R}|\sin(\phi_1+\phi_N)\sin(\delta-\delta_N)+\sin\phi_N\sin\delta_N\}]/L,\end{aligned} \tag{1.41}$$

where

$$\begin{aligned} L &= 1 + |\mathcal{R}|^2 - 2|\mathcal{R}|\cos\phi_1\cos\delta \\ &\quad + |\mathcal{N}|^2 - 2|\mathcal{N}|\{|\mathcal{R}|\cos(\phi_1+\phi_N)\cos(\delta-\delta_N) - \cos\phi_N\cos\delta_N\}. \end{aligned} \tag{1.42}$$

For small $|\mathcal{R}|$ and $|\mathcal{N}|$,

$$\begin{aligned} \mathcal{S}_{D^{*+}D^{*-}i} &\sim \eta_i \frac{-\sin 2\phi_1 + 2|\mathcal{R}|\sin\phi_1\cos\delta - 2|\mathcal{N}|\sin(2\phi_1+\phi_N)\cos\delta_N}{1 - 2|\mathcal{R}|\cos\phi_1\cos\delta + 2|\mathcal{N}|\cos\phi_N\cos\delta_N}, \\ \mathcal{A}_{D^{*+}D^{*-}i} &\sim \frac{2|\mathcal{R}|\sin\phi_1\sin\delta + 2|\mathcal{N}|\sin\phi_N\sin\delta_N}{1 - 2|\mathcal{R}|\cos\phi_1\cos\delta + 2|\mathcal{N}|\cos\phi_N\cos\delta_N}. \end{aligned} \tag{1.43}$$

From factorization with a heavy quark limit, $\delta \sim 12^\circ$ [22] and $|\mathcal{R}| \sim 0.02$ [16] are expected. Figure 1.6 shows $\mathcal{S}_{D^{*+}D^{*-}}$ and $\mathcal{A}_{D^{*+}D^{*-}}$ distribution based on the SM and beyond the SM assumptions. For an illustration, $\delta_N = \delta$ is assumed. Since the SM contribution is relatively small, a large discrepancy from Eq. (1.33) strongly suggests existence of a new physics term.

1.6 Polarization as a dilution factor to CP analysis

1.6.1 Representations of Polarization

In the previous sections, we assumed that the $B^0 \to D^{*+}D^{*-}$ decay amplitude is dominated by one angular momentum state. In general, however, there can be three possible eigenvalues, $L = 0$, 1 or 2, for the angular momentum between D^{*+} and D^{*-}.

The polarization of $D^{*\pm}$ and resulting angular distributions for daughter particles thus depend on how these three states are mixed. We consider three different bases to describe the polarization for the $B^0 \to D^{*+}D^{*-}$ decay; the partial wave basis, the helicity basis and the transversity basis. In the partial wave basis, we use the orbital angular momentum L to distinguish three orthogonal states. The helicity basis is indexed by the helicity, which is the spin projection of the daughter particle to its momentum vector. The transversity basis is indexed by the transversity, which is the spin projection of the one daughter particle to the normal of the other daughter's decay plane. All of them are mathematically equivalent, but they have different characteristics in the experimental points of view. Figure 1.7 (left) shows angular distributions of polarized states on bases mentioned above. In this section, we describe an overview of each basis and relation to CP parities. Detailed explanations are given in Appendix B.

1.6.2 Partial Wave Basis

When a B meson (spin-0) decays into two vector (spin-1) mesons, three orbital angular momentum eigenvalues $L = 0, 1, 2$ are allowed due to the angular momentum conservation.

A general decay amplitude is given as a superposition of partial wave states:

$$A_{\text{tot}} = s|0,0\rangle + p|1,0\rangle + d|2,0\rangle, \tag{1.44}$$

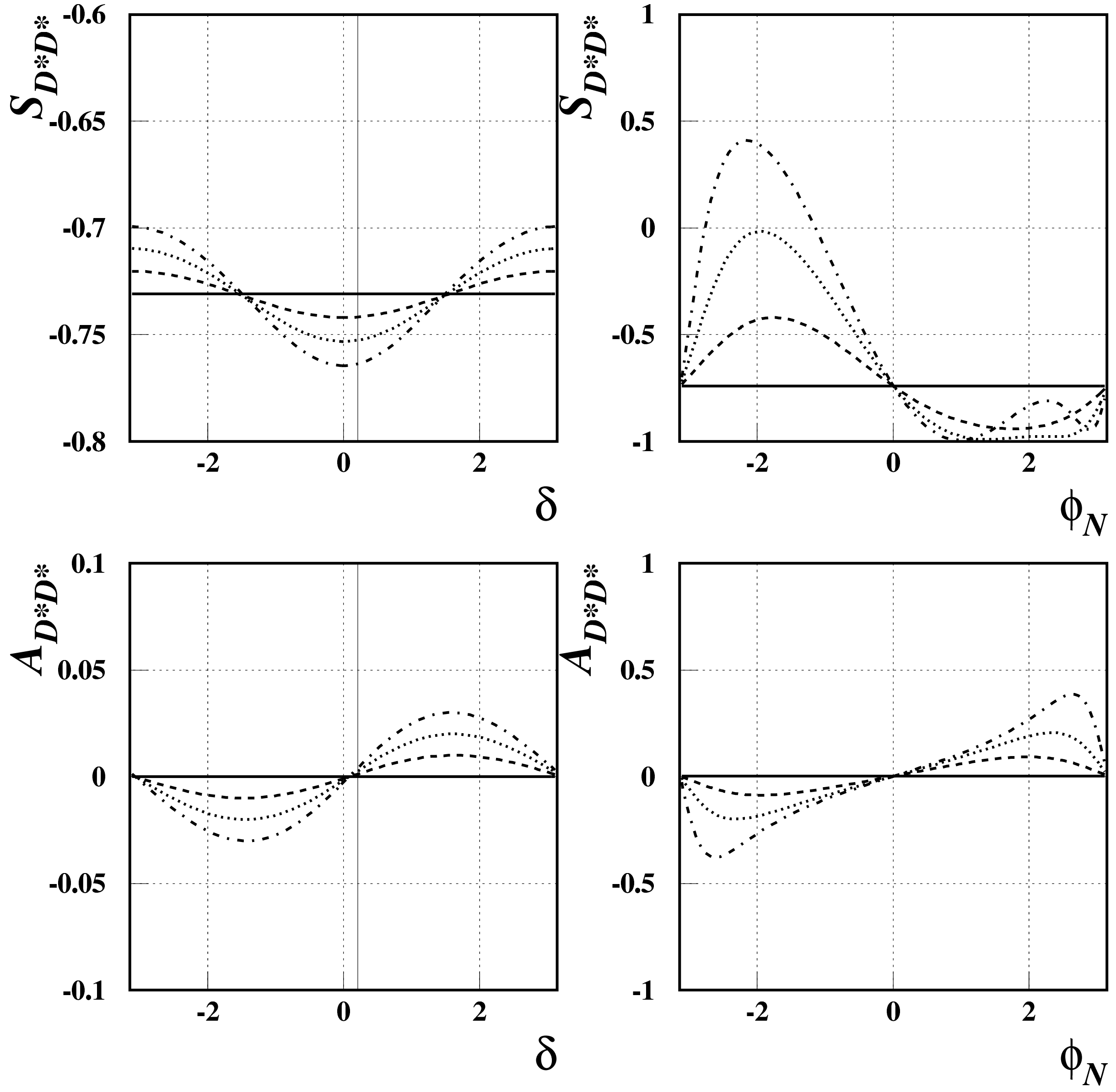

Figure 1.6: $\mathcal{S}_{D^{*+}D^{*-}}$ *and* $\mathcal{A}_{D^{*+}D^{*-}}$ *including contributions from the SM (beyond SM) loop diagrams as a function of* δ (ϕ_N)*. Figures on the left columns show the SM expectations with* $|\mathcal{R}|$ *= 0.0 (solid), 0.02 (dashed), 0.04 (dotted) and 0.06 (dashed-dotted). Vertical lines indicate a theoretical prediction for* δ (12°)*. Figures on the right column show the cases beyond the SM,* $|\mathcal{N}|$ *= 0.0 (solid), 0.2 (dashed), 0.4 (dotted), 0.6 (dashed-dotted), with* $|\mathcal{R}| = 0.02$ *and* $\delta = \delta_N = 12°$*. Note that the scale for the figures on the left column is* 1/10 *of those in the right column. Since the SM penguin contribution is always small, it can be neglected. With new physics effects,* $\mathcal{S}_{D^{*+}D^{*-}}$ *is enhanced around* $\phi_N = -2$ *and* $\mathcal{A}_{D^{*+}D^{*-}}$ *is enhanced around* $\phi_N = \pm 3$.

where $|L, M\rangle$ represents a partial wave labeled by the total orbital angular momentum L and its z component M. An amplitude of each partial wave is labeled by the spectroscopic notation, s, p or d.

Let us consider CP transformation for the $B \to V\overline{V}$ decay in the partial wave basis. Parity transformation in the $B \to V\overline{V}$ decay is lead from the following consideration: We define a $B \to V\overline{V}$ state as a two body system in the B rest frame

$$|\psi\rangle \equiv |L, M\rangle = \int d^3\hat{p} Y_M^L(\hat{p}) |\vec{p_1}\rangle |\vec{p_2}\rangle, \tag{1.45}$$

where $|\vec{p_i}\rangle$ denotes an i-th particle that has momentum $\vec{p_i}$ in the B rest frame, $\hat{p}$ is a normalized relativistic momentum vector. The Parity transformation is:

$$\begin{aligned} P|\psi\rangle =& \eta_1\eta_2 \int d^3\hat{p} Y_M^L(-\hat{p}) |\vec{p_2}\rangle |\vec{p_1}\rangle \\ =& \eta_1\eta_2(-1)^L \int d^3\hat{p} Y_M^L(\hat{p}) |\vec{p_2}\rangle |\vec{p_1}\rangle \\ \overset{P_{12}}{=}& \eta_1\eta_2(-1)^L |\psi\rangle \\ =& (-1)^L |\psi\rangle, \end{aligned} \tag{1.46}$$

where $\eta_i (i = 1, 2)$ is the intrinsic parity. We use $Y_M^L(-\hat{p}) = (-1)^L Y_M^L(\hat{p})$ and use the fact that permutation P_{12} is symmetric from Bose-Einstein statistics.

To do the C transformation, we note that it is equivalent to a product of the spatial (Parity) transformation P, spin transformation P_σ and permutation P_{12}. First we redefine $B \to V\overline{V}$ states as

$$|\psi\rangle \equiv \int d^3\hat{p} Y_M^L(\hat{p}) |q\vec{p_1}\sigma_1\rangle |\overline{q}\vec{p_2}\sigma_2\rangle, \tag{1.47}$$

where $q(\overline{q})$ denotes a particle (anti-particle) and σ_i denotes its spin. Charge transformation becomes:

$$C|\psi\rangle = \eta_C \int d^3\hat{p} Y_M^L(\hat{p}) |\overline{q}\vec{p_1}\sigma_1\rangle |q\vec{p_2}\sigma_2\rangle, \tag{1.48}$$

where η_C is charge parity. Also

$$\begin{aligned} \psi \xrightarrow{P}& \eta_1\eta_2(-1)^L \int d^3\hat{p} Y_M^L(\hat{p}) |q\vec{p_2}\sigma_1\rangle |\overline{q}\vec{p_1}\sigma_2\rangle \\ \xrightarrow{P_\sigma}& \eta_1\eta_2(-1)^L(-1)^S \int d^3\hat{p} Y_M^L(\hat{p}) |q\vec{p_2}\sigma_2\rangle |\overline{q}\vec{p_1}\sigma_1\rangle \\ \xrightarrow{P_{12}}& \eta_1\eta_2(-1)^{L+S} \int d^3\hat{p} Y_M^L(\hat{p}) |\overline{q}\vec{p_1}\sigma_1\rangle |q\vec{p_2}\sigma_2\rangle, \end{aligned} \tag{1.49}$$

where transformation of the spin part uses the fact that we consider two spin-1 particles.

Therefore C transformation is:

$$\eta_C = (-1)^{L+S}. \tag{1.50}$$

CP parity η_{CP} is a product of Eq. (1.46) and (1.50):

$$\eta_{CP} = (-1)^L, \tag{1.51}$$

where we used $J = L + S = 0$ for the B decay.

From Eq. (1.51), we find S- and D-waves are CP-even, while P-wave is CP-odd. It means that the magnitude of measured CP asymmetry is diluted by opposite CP components. In order to avoid this bias, we have to extract decay amplitude of both CP components with utilizing decay angles that are governed by the angular momentum. This is called an angular analysis. Unfortunately, we have difficulty to apply such an angular analysis in the partial wave basis, since it is not adequate for a relativistic system. Therefore, we have to adopt a more suitable basis.

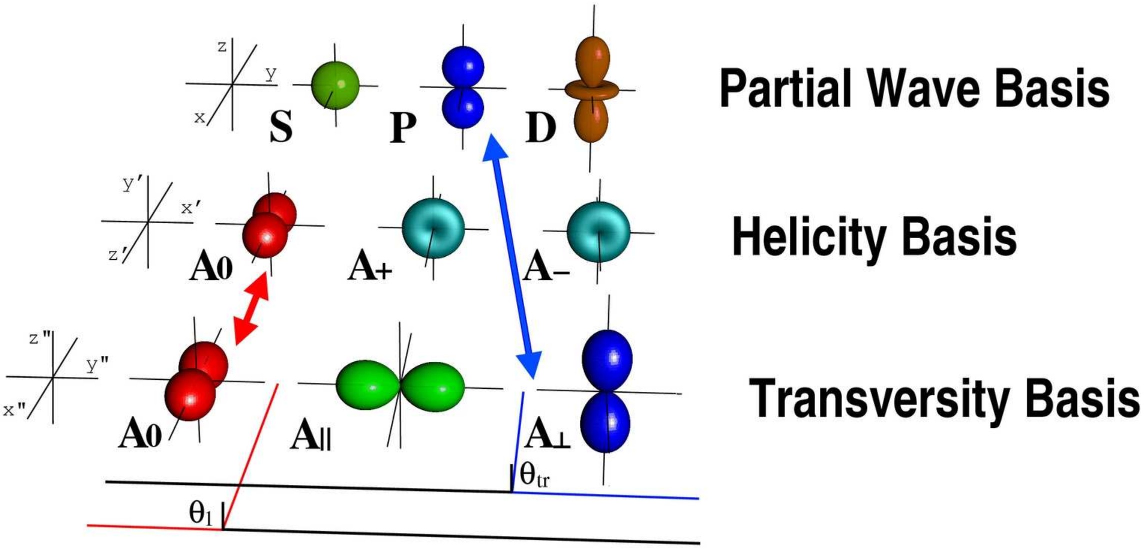

Figure 1.7: *Angular distributions of each polarized state of* $B^0 \to D^{*+}D^{*-}$ *on different bases. Top, middle, bottom rows correspond to the partial wave basis, the helicity basis and the transversity basis, respectively. For the partial wave basis,* D^{*+} *angular distribution are shown. For the helicity and transversity basis, the angular distribution of* π^+ *from* D^{*+} *are shown. Arrows indicate that two amplitudes are equivalent. Each state in the transversity basis can be distinguished by* θ_{tr} *and* θ_1*.*

1.6.3 Helicity Basis

The partial wave basis has been employed in non-relativistic systems as an effective analysis tool. However, in the relativistic system, we meet some difficulty owing to the Lorentz-boost. For example, an orbital angular momentum is defined in the rest frame of a parent particle, whereas a spin angular momentum is defined at the rest frame of its daughter. Therefore calculation becomes complicated.

If we choose the quantization axis along with the direction of the Lorentz-boost, i.e. the momentum vector, the definition becomes unique everywhere. Then the helicity λ, the spin projection to the axis, becomes:

$$\lambda \equiv \frac{\vec{J} \cdot \vec{P}}{|\vec{P}|}, \tag{1.52}$$

where $\vec{J}$ is a total angular momentum vector and $\vec{P}$ is a momentum vector. Since it is invariant under rotation and Lorentz-boost, treatment of angular momentum becomes easy.

In case of $B \to V_1 V_2$ decay, spin-1 daughters fly back-to-back along with the decay axis in the B rest frame. Therefore, allowed helicity states are

$$(\lambda_1, \lambda_2) = (+1, +1),\ (0, 0),\ (-1, -1). \tag{1.53}$$

We define corresponding helicity amplitudes $A_\lambda \equiv \langle f_\lambda | \mathcal{H}_{\text{eff}} | B \rangle$, where $\lambda = 1, 0, -1$ and $|f_\lambda\rangle$ denotes each helicity state. As seen in Fig. 1.7 (middle), A_0 is longitudinal to the helicity axis and $A_\pm$ is transverse.

P transformation of each helicity amplitude is defined in Appendix B:

$$PA_{+1} = A_{-1}, \quad PA_0 = A_0, \quad PA_{-1} = A_{+1}. \tag{1.54}$$

Note that $|f_{\pm 1}\rangle$ are not parity (and also CP) eigenstates.

Figures 1.8 (upper) show projected decay angular distributions in the helicity basis. We find that the decay angle $\cos\theta_1$ and $\cos\theta_2$ (angles between helicity axes and momenta of their daughters) are sensitive to longitudinal polarization (A_0), but not CP contents. Information about CP contents is buried in interference terms and is difficult to be treated with limited statistics. Therefore, we need to consider a better basis keeping the merit to use the helicity projection.

1.6.4 Transversity Basis

The transversity basis [17] is introduced by modifying the helicity basis in order to treat CP information:

$$\begin{aligned} &A_0 && (P : +1), \\ &A_\parallel \equiv \frac{A_{+1} + A_{-1}}{\sqrt{2}} && (P : +1), \\ &A_\perp \equiv \frac{A_{+1} - A_{-1}}{\sqrt{2}} && (P : -1). \end{aligned} \tag{1.55}$$

CP transformation is known from Eq. (1.50) and (1.55):

$$\begin{aligned} \overline{A}_0 \equiv \quad & CPA_0 = A_0 && (CP : +1), \\ \overline{A}_\parallel \equiv \quad & CPA_\parallel = A_\parallel && (CP : +1), \\ \overline{A}_\perp \equiv \quad & CPA_\perp = -A_\perp && (CP : -1). \end{aligned} \tag{1.56}$$

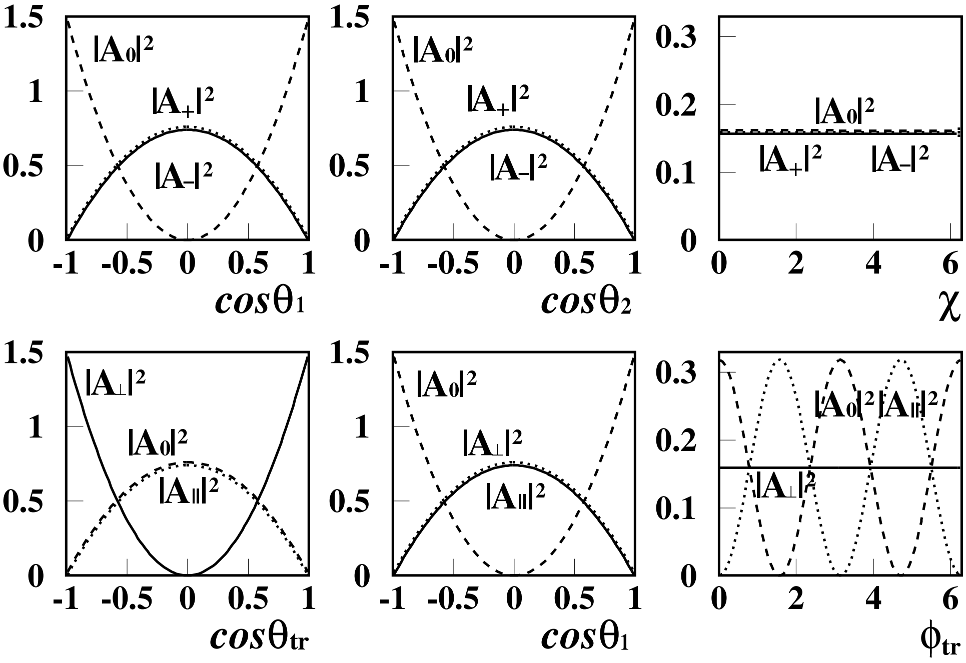

Figure 1.8: *Projected angular distributions onto individual decay angles. Figures in the upper (lower) row show the helicity (transversity) basis distributions. Definition of helicity angles is given in Appendix B. Dashed, dotted, solid curves correspond to* A_0*,* A_+ *(*$A_\perp$*),* A_- *(*$A_\parallel$*), respectively. Different* CP *components are separated in the* $\cos\theta_{tr}$ *projection.*

Full angular distribution is also obtained by applying the same procedure to the angular distribution of the helicity basis:

$$\begin{aligned}
\frac{1}{\Gamma}\frac{d^3\Gamma}{d\cos\theta_{tr} d\cos\theta_1 d\phi_{tr}} &= \frac{9}{32\pi}\frac{1}{|A_0|^2+|A_\parallel|^2+|A_\perp|^2} \\
&\Big\{ 4|A_0|^2\cos^2\theta_1\sin^2\theta_{tr}\cos^2\phi_{tr} \\
&+2|A_\parallel|^2\sin^2\theta_1\sin^2\theta_{tr}\sin^2\phi_{tr} \\
&+2|A_\perp|^2\sin^2\theta_1\cos^2\theta_{tr} \\
&+\sqrt{2}\Re(A_\parallel^* A_0)\sin 2\theta_1\sin^2\theta_{tr}\sin 2\phi_{tr} \\
&-\sqrt{2}\Im(A_0^* A_\perp)\sin 2\theta_1\sin 2\theta_{tr}\cos\phi_{tr} \\
&-2\Im(A_\parallel^* A_\perp)\sin^2\theta_1\sin 2\theta_{tr}\sin\phi_{tr} \Big\}, \qquad (1.57)
\end{aligned}$$

where we introduce three decay angles, θ_{tr}, θ_1 and ϕ_{tr}. Detailed calculation is explained in Appendix B.

An exact definition of transversity basis is the following: In the B rest frame, the x-axis is defined as the decay axis between D^{*+} and D^{*-}. We then move into the D^{*+} rest frame. The transversity plane (the x-y plane) is defined with this axis and daughter particles of D^{*-}. The z-axis, which is normal to this plane, is given by $\vec{x}\times\vec{y}$. We define 3 decay angles: θ_{tr} is the angle between the z-axis and a slow pion from D^{*+}, ϕ_{tr} is the angle between the $x-$axis and the momentum vector of the slow pion from D^{*+} projected onto the transversity plane, and θ_1 is the angle between the x-axis and a slow pion from D^{*-} in the D^{*-} rest frame. Similar definitions are also used for $D^{*\pm} \to D^{\pm}\pi^0$ decays. Figure 1.9 shows definitions of this frame. Angular distributions of the transversity basis are shown in Fig. 1.7 (bottom).

We characterize each amplitude in the transversity basis:

- A_0, longitudinal polarization to the decay axis,
- $A_\parallel$, transversely parallel polarization to the D^{*-} polarization (on the decay plane),
- $A_\perp$, transversely perpendicular polarization to the decay plane.

From Fig. 1.8 (lower), we find that different CP components can be distinguished by a single angular term, $\cos\theta_{tr}$. This is the most important advantage of the transversity basis. It is explained by the transversity τ, which is the spin projection to the normal of the decay plane.

We consider a reflection (not parity transformation but just an ordinal mirror) of a particle on the decay plane. The reflection, which consists of P transformation and 180 degree rotation, is explained as :

$$R_P \equiv Pe^{i\pi J_z} = \eta e^{i\pi\tau}, \qquad (1.58)$$

where J_z (τ) is a projection of total (spin) angular momentum to the normal of the plane and η is intrinsic parity of the particle.

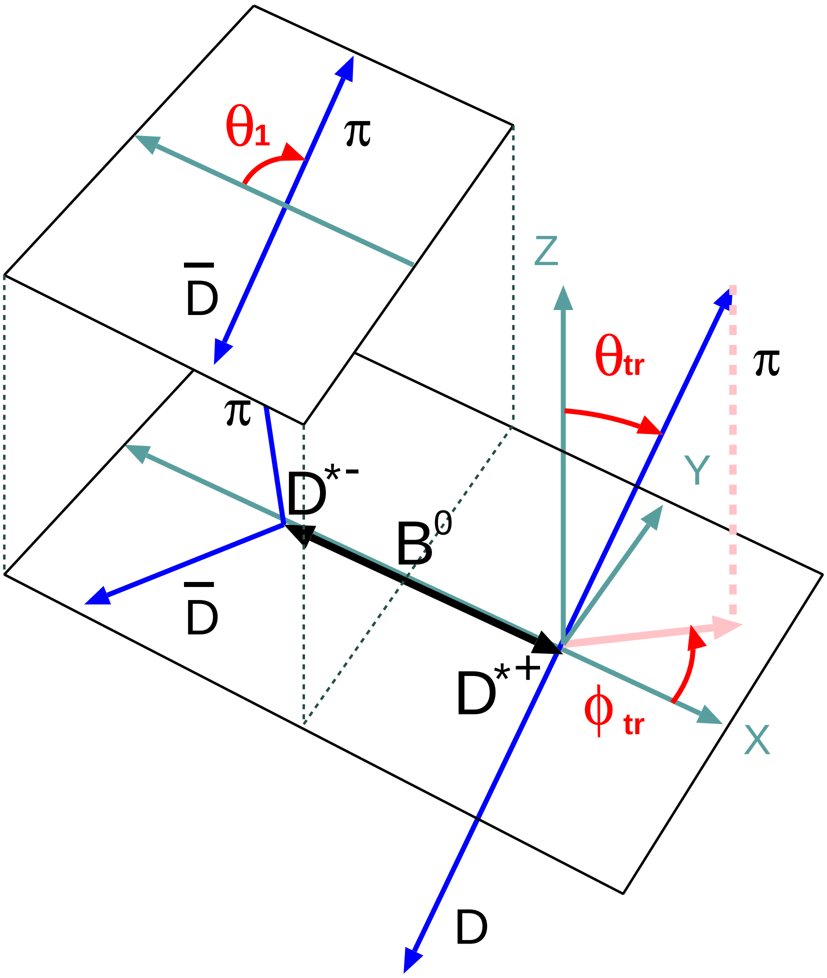

Figure 1.9: *The transversity frame for $B^0 \to D^{*+}D^{*-}$. D^{*+} polarization is anchored by D^{*-} decay plane at D^{*+} rest frame. Floated plane is D^{*-} rest frame to measure θ_1.*

Though a transversity is defined in the rest frame of each particle on the decay plane, they can be linearly added owing to Lorentz-invariance and the fact that all quantizing axes are parallel. In case of $B \to D^{*+}D^{*-}$, we have three particles to be considered, $D^{*+}, \overline{D}^0(D^-), \pi^-(\pi^0)$. Since their spins are 0 except for D^{*+}, total transversity corresponds to D^{*+}. Then

$$CP = \eta_{CP} e^{i\pi\tau}, \tag{1.59}$$

where η_{CP} is intrinsic CP parity. We used $J = 0$ for the B decay.

Furthermore, in case of $B \to V\overline{V}$ decays, interchange of helicities, which are scalar (spin-0) daughters of the vector meson making decay plane, flips the CP sign. Therefore $\eta_{CP} = -1$. Thus we obtain

$$CP_{D^{*+}D^{*-}} = (-1)^{1+\tau}, \tag{1.60}$$

where $\tau = 0$ ($\tau = \pm 1$) corresponds to CP-odd (CP-even).

This can be intuitively explained as following. Orbital angular momentum and spin angular momentum of $B^0 \to D^{*+}D^{*-}$ is determined uniquely, because B^0 is spin-0 particle. In case of $D^{*+}D^{*-}$, transversity basis satisfies that there is no orbital and spin angular momentum except for D^{*+}. Therefore, transversity τ, projection of D^{*+} spin angular momentum, remembers the orbital angular momentum of $D^{*+}D^{*-}$. In short, τ knows CP sign of the $D^{*+}D^{*-}$ partial wave. This is the reason why D^{*+} polarization anchored by D^{*-} decay plane is effective for CP analysis.

Now we turn to the time-dependent angular distribution. Full angular distribution of $B \to D^{*+}D^{*-}$ decay in the transversity basis is shown in Eq. (1.57). Interferences between differently polarized states are concealed with integration of ϕ_{tr}:

$$\frac{1}{\Gamma}\frac{d^2\Gamma(\overset{(-)}{B^0}\to D^{*+}D^{*-})}{d\cos\theta_{tr} d\cos\theta_1} = \frac{9}{16}\sum_{i=0,\|,\perp}|\overline{A}_i|^2 H_i(cos\theta_{tr}, cos\theta_1), \tag{1.61}$$

where angular terms are:

$$\begin{aligned} H_0(\cos\theta_{tr},\cos\theta_1) &= 2\sin^2\theta_{tr}\cos^2\theta_1, \\ H_{\|}(\cos\theta_{tr},\cos\theta_1) &= \ \ \sin^2\theta_{tr}\sin^2\theta_1, \\ H_{\perp}(\cos\theta_{tr},\cos\theta_1) &= 2\cos^2\theta_{tr}\sin^2\theta_1. \end{aligned}$$

and A_i's are redefined as the normalized decay amplitudes for $i = 0, \|, \perp$:

$$|A_0|^2 + |A_{\|}|^2 + |A_{\perp}|^2 = 1. \tag{1.62}$$

From Eq. (1.32) and (1.56), CP violating parameters for each amplitude are:

$$\lambda \equiv \lambda_0 = \lambda_{\|} = -\lambda_{\perp}. \tag{1.63}$$

This is always true when only the tree diagram contributes to the $D^{*+}D^{*-}$ decay. We note that Eq. (1.63) is held in case of an equivalent penguin contribution to each polarization. Therefore any set of λ's discussed in previous sections can be inserted.

Applying Eq. (1.15) and (1.63) to Eq. (1.61), time-dependent differential decay rates are also rewritten as follows:

$$\begin{aligned} \frac{1}{\Gamma}\frac{d^2\Gamma(\overset{(-)}{B^0}(t)\to D^{*+}D^{*-})}{d\cos\theta_{tr} d\cos\theta_1} &= \frac{e^{-\Gamma t}}{4}\sum_{i=0,\|,\perp} R_i\cdot\frac{9}{16}H_i(cos\theta_{tr}, cos\theta_1) \\ &\quad \left\{1 + q\left(\frac{|\lambda|^2-1}{|\lambda|^2+1}\cos\Delta mt + \eta_i\frac{2\Im\lambda}{|\lambda|^2+1}\sin\Delta mt\right)\right\} \\ &= \frac{e^{-\Gamma t}}{4}\sum_{i=0,\|,\perp} R_i\cdot\frac{9}{16}H_i(cos\theta_{tr}, cos\theta_1) \\ &\quad \left\{1 + q(\mathcal{A}_{D^{*+}D^{*-}}\cos\Delta mt + \eta_i\mathcal{S}_{D^{*+}D^{*-}}\sin\Delta mt)\right\}, \end{aligned} \tag{1.64}$$

where the b-flavor charge q is $+1(-1)$ when the B meson at the time of production ($t = 0$) is $\overline{B}^0(B^0)$.

CP-violating parameters $\mathcal{S}_{D^{*+}D^{*-}}$ and $\mathcal{A}_{D^{*+}D^{*-}}$ are re-defined:

$$\begin{aligned}\mathcal{S}_{D^{*+}D^{*-}} &\equiv \frac{2\Im\lambda}{|\lambda|^2+1},\\ \mathcal{A}_{D^{*+}D^{*-}} &\equiv \frac{|\lambda|^2-1}{|\lambda|^2+1}.\end{aligned} \tag{1.65}$$

A polarization ratio for each amplitude is defined as:

$$R_i \equiv |A_i|^2. \tag{1.66}$$

1.7 Previous Measurements

The CLEO Collaboration first observed $B^0 \to D^{*+}D^{*-}$ decays [23] and reported the branching fraction and the CP-even fraction [24] with $(8-0.42) \pm 0.04(\mathrm{stat}) \pm 0.13(\mathrm{syst})$ candidates obtained from a sample of $9.7 \times 10^6 B\bar{B}$ pairs:

$$\begin{aligned}\mathcal{B}(B^0 \to D^{*+}D^{*-}) =&[0.99^{+0.42}_{-0.33}(\mathrm{stat}) \pm 0.12(\mathrm{syst})] \times 10^{-3},\\ CP\text{-even fraction} >&0.11(90\%\ \mathrm{CL}),\end{aligned} \tag{1.67}$$

The Belle Collaboration reported the branching fraction [25] with 11.0±3.7 candidates obtained from a sample of $22.8 \times 10^6 B\bar{B}$ pairs:

$$\mathcal{B}(B^0 \to D^{*+}D^{*-}) = [1.21 \pm 0.41(\mathrm{stat}) \pm 0.27(\mathrm{syst})] \times 10^{-3}, \tag{1.68}$$

The BaBar Collaboration also reported the branching fraction [26] with $(38-6.24) \pm 0.33(\mathrm{stat}) \pm 0.36(\mathrm{syst})$ candidates obtained from a sample of $22.8 \times 10^6 B\bar{B}$ pairs:

$$\mathcal{B}(B^0 \to D^{*+}D^{*-}) =[0.83 \pm 0.16(\mathrm{stat}) \pm 0.12(\mathrm{syst})] \times 10^{-3}, \tag{1.69}$$

and polarization and CP asymmetries [27] with 156 ± 14 candidates obtained from a sample of $88 \times 10^6 B\bar{B}$ pairs:

$$\begin{aligned}R_\perp =&0.063 \pm 0.055(\mathrm{stat}) \pm 0.009(\mathrm{syst}),\\ \Im(\lambda_+) =&0.05 \pm 0.29(\mathrm{stat}) \pm 0.10(\mathrm{syst}),\\ |\lambda_+| =&0.75 \pm 0.19(\mathrm{stat}) \pm 0.02(\mathrm{syst}),\end{aligned} \tag{1.70}$$

where λ_+ is an averaged CP violating parameter, which takes into account of different penguin amplitudes between CP-even and CP-odd components. It is defined by:

$$\begin{aligned}\frac{2\Im(\lambda_+)}{1+|\lambda_+|^2} &\equiv \frac{\frac{2\Im(\lambda_\parallel)}{1+|\lambda_\parallel|^2}|A_\parallel|^2 + \frac{2\Im(\lambda_0)}{1+|\lambda_0|^2}|A_0|^2}{|A_\parallel|^2+|A_0|^2},\\ \frac{1-|\lambda_+|^2}{1+|\lambda_+|^2} &\equiv \frac{\frac{1-|\lambda_\parallel|^2}{1+|\lambda_\parallel|^2}|A_\parallel|^2 + \frac{1-|\lambda_0|^2}{1+|\lambda_0|^2}|A_0|^2}{|A_\parallel|^2+|A_0|^2}.\end{aligned} \tag{1.71}$$

BaBar claims that CP asymmetries of $D^{*+}D^{*-}$ have a 2.5 σ discrepancy from the SM expectation if the penguin contribution is neglected.

Chapter 2

Principle of the Measurement

2.1 Coherent $B^0\overline{B}^0$ mixing in a B-factory experiment

Since the B meson is heavy, there are many decay modes with small branching fractions. Therefore high luminosity is needed to perform a precision measurement. The KEKB e^+e^- collider meets this requirement. Furthermore, an e^+e^- collider is in general superior to a hadron collider in studying complicated hadronic B decays, because QCD backgrounds are much smaller. Although we need proper time of the B meson to measure the time-dependent CP asymmetries from Eq. (1.18), it cannot be directly measured due to the very short lifetime of the B meson, τ_B ($\sim$ 1.5ps). If beam energies of a collider are asymmetric, this problem can be solved thanks to the Lorentz boost.

From these conditions and requirements, a B factory, an experiment with an asymmetric e^+e^- collider which produces a large number of B mesons, was proposed. Total energy of the asymmetric e^+e^- collider is adjusted to the $\Upsilon(4S)$ resonance which is one of bottomniums ($b\bar{b}$). Since the mass of the $\Upsilon(4S)$ resonance is just above the $B\bar{B}$ pair production threshold, almost all $\Upsilon(4S)$ resonances decay into B^+B^- or $B^0\overline{B}^0$ pairs. Branching fractions for two decay modes are nearly the same.

2.1.1 Time-dependent probability of a final state

As explained in the previous chapter, time-dependent CP violation arises from an interference between two diagrams that are responsible for both B^0 and $\overline{B}^0$ decays into the same CP eigenstate. Such a type of decaying is called a flavor-nonspecific decay. On the other hand, a flavor-specific decay means a decay in which the final state tells whether the parent is B^0 or $\overline{B}^0$. We also need to reconstruct a flavor-specific decay mode for the accompanying B meson in order to measure CP asymmetries.

Since $\Upsilon(4S)$ is produced from a virtual photon, its quantum numbers are $J^{PC} = 1^{--}$. The $B\bar{B}$ system conserves the quantum numbers, because $\Upsilon(4S)$ decays via strong interaction. Since a B meson is a pseudo-scalar particle, the $B\bar{B}$ system should have an orbital angular momentum $L = 1$. The states B^0B^0 and $\overline{B}^0\overline{B}^0$ are forbidden from Bose-Einstein statistics.

Therefore, an allowed state at a time of pair production is

$$|B_1B_2;0,0\rangle = \frac{1}{\sqrt{2}}(|B_1^0\rangle|\overline{B}_2^0\rangle - |\overline{B}_1^0\rangle|B_2^0\rangle), \tag{2.1}$$

where $|B_1B_2;t_1,t_2\rangle$ denotes a state with two B mesons, t_i $(i=1,2)$ is the proper time of B_i, and $|B_i^0\rangle(|\overline{B}_i^0\rangle)$ means the B meson whose flavor is B^0 $(\overline{B}^0)$ at $t=0$.

From Eq. (1.10), time evolution of the system with two B mesons becomes:

$$\begin{aligned}|B_1B_2;t_1,t_2\rangle =&\frac{1}{\sqrt{2}}e^{-\Gamma(t_1+t_2)/2}\left\{\cos\frac{\Delta m\Delta t}{2}\cdot\left(|B_1^0\rangle|\overline{B}_2^0\rangle - |\overline{B}_1^0\rangle|B_2^0\rangle\right)\right.\\ &\left.+i\sin\frac{\Delta m\Delta t}{2}\cdot\left(\frac{q}{p}|B_1^0\rangle|B_2^0\rangle - \frac{p}{q}|\overline{B}_1^0\rangle|\overline{B}_2^0\rangle\right)\right\},\end{aligned} \tag{2.2}$$

where $\Delta t \equiv t_2 - t_1$. The coherence seen in Eq. (2.1) is kept until one B meson decays. We redefine t_1 and t_2 as the decay times of each B meson. If we know the B flavor from one B decay (to a flavor-specific state) and Δt, we know the time-evolution of the accompanying B meson. In particular, we consider the case that one B decays into a CP eigenstate f_{CP} and the other into $l^\pm X$, which is a flavor-specific mode; B^0 $(\overline{B}^0)$ mesons decay into l^+X (l^-X) and decays with the opposite flavor are forbidden. Replacing the notations B_1 (B_2) with B_{CP} $(B_{\rm tag})$, which means a CP eigenstate (flavor-specific state), decay rates of the B mesons pair system become:

$$\begin{aligned}\Gamma(f_{CP},l^-X) =&|\langle f_{CP}\ l^-X|B_{CP}B_{\rm tag};t_{CP},t_{tag}\rangle|^2\\ =&\frac{1}{4}e^{-\Gamma(t_{CP}+t_{\rm tag})}A_{CP}^2A_{\rm tag}^2\\ &\left\{(|\lambda_{CP}|^2+1)-(|\lambda_{CP}|^2-1)\cdot\cos\Delta m\Delta t - 2\Im\lambda_{CP}\cdot\sin\Delta m\Delta t\right\},\\ \Gamma(f_{CP},l^+X) =&|\langle f_{CP}\ l^+X|B_{CP}B_{\rm tag};t_{CP},t_{tag}\rangle|^2\\ =&\frac{1}{4}e^{-\Gamma(t_{CP}+t_{\rm tag})}A_{CP}^2A_{\rm tag}^2\left|\frac{p}{q}\right|^2\\ &\left\{(|\lambda_{CP}|^2+1)+(|\lambda_{CP}|^2-1)\cdot\cos\Delta m\Delta t + 2\Im\lambda_{CP}\cdot\sin\Delta m\Delta t\right\},\end{aligned} \tag{2.3}$$

where the decay amplitude $A_{tag} \equiv \langle l^+X|B^0\rangle| = \langle l^-X|\overline{B}^0\rangle$ and the proper time $t_{CP}(t_{tag})$ is for $B_{CP}(B_{\rm tag})$.

With using $|q/p| \sim 1$ and normalizing Eq. (2.3) in $-\infty < \Delta t < \infty$, we obtain the conditional probability that we find f_{CP} at the time Δt:

$$\mathcal{P}_{CP}(q,\Delta t) = \frac{e^{-|\Delta t|/\tau_{B^0}}}{4\tau_{B^0}}\{1+q(\mathcal{A}_{CP}\cos\Delta m\Delta t + \mathcal{S}_{CP}\sin\Delta m\Delta t)\}, \tag{2.4}$$

where $q=+1$ (-1) for $B_{\rm tag} = B^0$ $(\overline{B}^0)$.

We then consider the $B^0 \to D^{*+}D^{*-}$ decay. Since the time-dependent angular distribution is given in Eq. (1.61), the total probability that we find $D^{*+}D^{*-}$ at Δt is:

$$\begin{aligned}\mathcal{P}_{D^{*+}D^{*-}}(q, \Delta t, \cos\theta_{tr}, \cos\theta_1) = \frac{e^{-|\Delta t|/\tau_{B^0}}}{4\tau_{B^0}} \sum_{i=0,\|,\perp} R_i \cdot \frac{9}{16} H_i(\cos\theta_{tr}, \cos\theta_1) \\ \left\{1 + q(\mathcal{A}_{D^{*+}D^{*-}} \cos\Delta m\Delta t + \eta_i \mathcal{S}_{D^{*+}D^{*-}} \sin\Delta m\Delta t)\right\}.\end{aligned} \tag{2.5}$$

From Eq. (2.5), we find that we need to reconstruct four variables to obtain $\mathcal{P}_{D^{*+}D^{*-}}$: transversity angles $\cos\theta_{tr}$ and $\cos\theta_1$, b-flavor of the flavor-specific decay mode (called tag side) q and the proper time difference Δt.

2.2 Measurement at the Belle experiment

In this section, we explain how to perform the measurements mentioned above, in the Belle experiment. It is divided into three stages: event reconstruction, Δt measurement and flavor tagging. Figure 2.1 shows the schematic view of the Belle experiment.

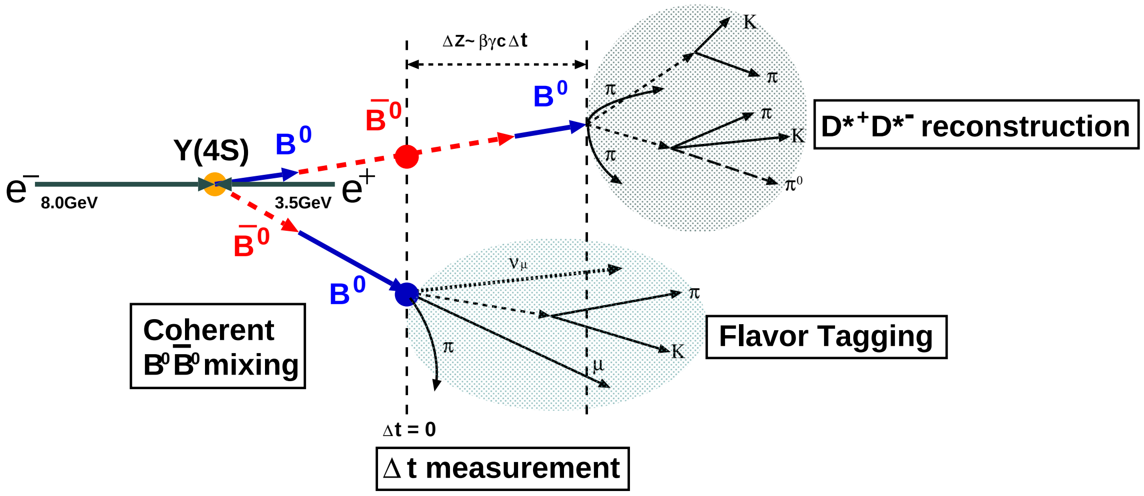

Figure 2.1: *Schematic view of the Belle Experiment.*

2.2.1 Event reconstruction

Event-by-event, transversity angles $\cos\theta_{tr}$ and $\cos\theta_1$ are obtained from the fully reconstructed $D^{*+}D^{*-}$ events. The full reconstruction is performed by evaluating the invariant mass that is obtained with combining the four-momenta of whole daughter particles. Each daughter particle is similarly combined or reconstructed with the Belle detector.

The decay chain is

$$\begin{aligned} B_{CP} \to & D^{*+}D^{*-} \to D\pi_s D\pi_s \to \{K^\pm, K^0_\mathrm{S}, \pi^\pm, \pi^0\}, \\ B_\mathrm{tag} \to & l^\pm X \to \{\mu^\pm, e^\pm, K^\pm, K^0_\mathrm{S}, \pi^\pm, \pi^0\} \\ \to & K^\pm X \to \{K^\pm, K^0_\mathrm{S}, \pi^\pm, \pi^0\}, \end{aligned} \tag{2.6}$$

where particles between braces mean a kind of daughter particles and π_s is a low-momentum pion (slow pion) from the D^* decay.

The transversity angles, $\cos\theta_{tr}$ and $\cos\theta_1$ can then be measured with reconstructed $B^0 \to D^{*+}D^{*-}$ candidate with following the definition that is described in Sec. 1.6.4. Polarization parameters, R_i are measured from time-independent angular distributions in Eq. (1.61).

In the case of $D^{*+}D^{*-}$, we need 4-10 charged tracks and 0-4 neutral particles in the CP side. It means that each track or particles carries a small momentum. Especially, we always have two slow pions whose momenta are below 300MeV/c. Therefore, having a high tracking efficiency in low momentum region is very important. An example of $B^0 \to D^{*+}D^{*-}$ candidate is shown in Fig. 2.2.

2.2.2 Δt measurement

In the Belle experiment, the momentum direction of the produced $\Upsilon(4S)$ resonance is nearly parallel to the z-axis (opposite to the e^+ direction). Since the B meson is almost at rest in the $\Upsilon(4S)$ center of mass system (cms), each B meson also flies along with this direction. The flight length becomes much longer than that in the $\Upsilon(4S)$ cms by the Lorentz boost. Proper time difference Δt can be obtained from Δz, which is a difference of the flight length projected to the z-axis:

$$\Delta t \sim \frac{\Delta z}{\beta\gamma c} \equiv \frac{Z_{CP} - Z_\mathrm{tag}}{\beta\gamma c}, \tag{2.7}$$

where Z_{CP} (Z_tag) is the z component of B vertex and $\beta\gamma = 0.425$ is a Lorentz factor. In this condition, the average flight length becomes $\beta\gamma c\tau_{B^0} \sim 200\ \mu$m. We need to determine each B vertex with a resolution better than the flight length. Therefore, precise vertex measurements are necessary.

2.2.3 Flavor Tagging

The flavor tagging is a technique to determine the flavor of B decaying into the flavor-specific decay mode. It is based on the idea that the charge of decay products reflects the charge of b quark. There are several ways to identify the flavor. The two most effective ways are to use a primary lepton from a semi-leptonic decay, $b \to W^-(\to l^-\overline{\nu})c$, and to use charged kaons from a cascade decay, $b \to c \to s$. Other methods and detail of tagging are described later. Figure 2.3 shows a schematic view of the flavor tagging method.

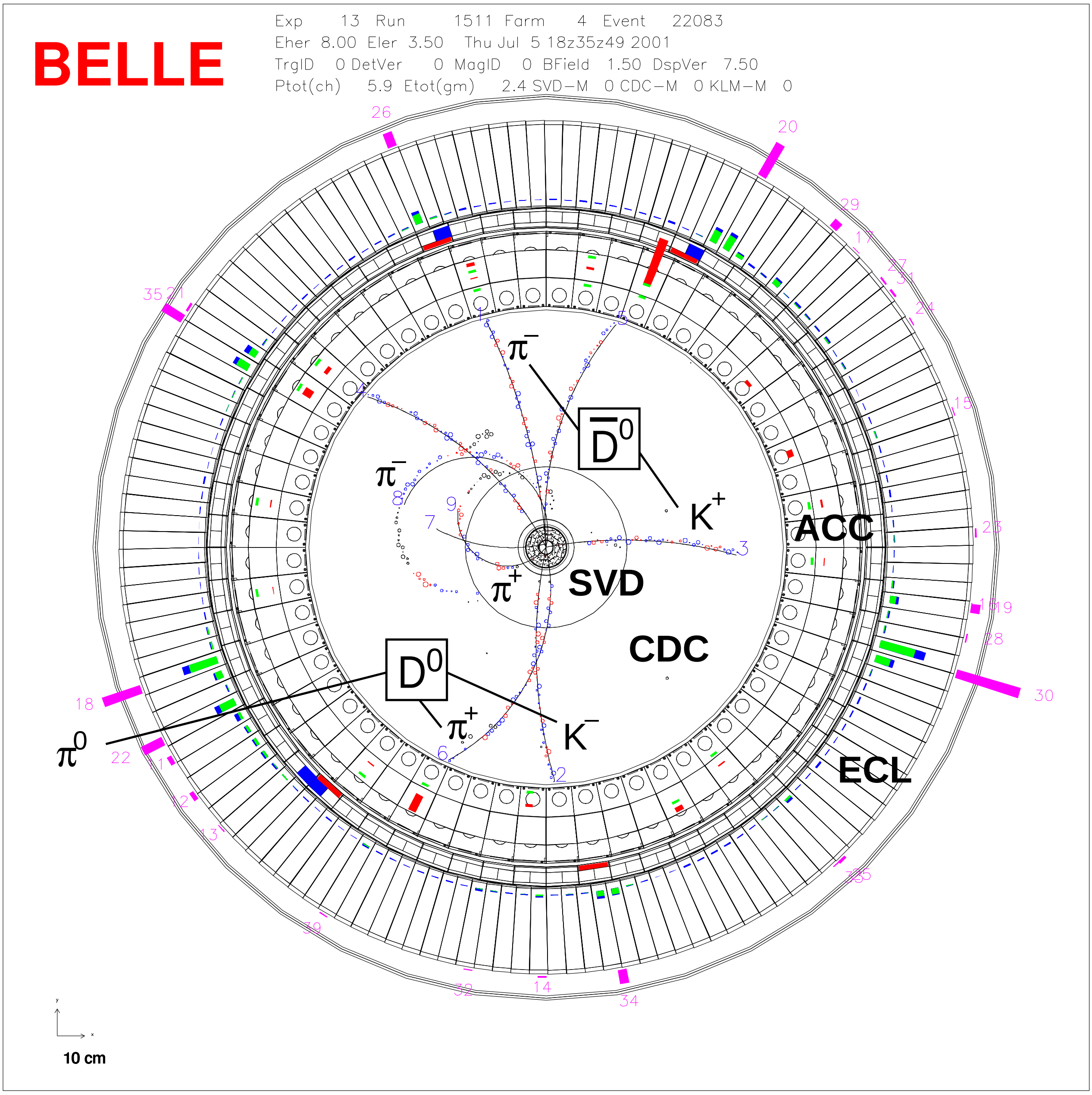

Figure 2.2: *An event display for a* $B^0 \to D^{*+}D^{*-}$ *candidate.* D^{*+} *decays to* D^0 $(\to K^-\pi^+\pi^0)$ π_s^+ *and* D^{*-} *decays to* $\overline{D}^0$ $(\to K^+\pi^-)$ π_s^-. *SVD and CDC are detectors for tracking charged particles, while ACC and ECL are detectors for particle identification. Description about each detector is explained in Chap. 3. Curves with number mean reconstructed charged tracks.*

Wrong Tag Fraction

Flavor tagging is not always perfect. For example, if the number of kaons in the system is wrong due to misidentifiaction or inefficiency, flavor tagging may fail or give opposite flavor information. There are also smaller physical processes that give opposite flavor to the dominant process, such as the charged kaon from the $\bar{c}$ decay in $b \to c\bar{c}s$ transition.

If the flavor tagging gives wrong flavor information, the probability density function Eq. (2.5) is diluted. We define the wrong tag fraction, w, which is the probability of incorrect flavor assignment. Then Eq. (2.5) becomes:

$$\begin{aligned}\mathcal{P}_{D^{*+}D^{*-}}(q, \Delta t, \cos\theta_{tr}, \cos\theta_1) &= \frac{e^{-|\Delta t|/\tau_{B^0}}}{4\tau_{B^0}} \sum_{i=0,\|,\perp} R_i \cdot \frac{9}{16} H_i(\cos\theta_{tr}, \cos\theta_1) \\ &\quad \left\{1 + q(1-w)(\mathcal{A}_{D^{*+}D^{*-}} \cos\Delta m\Delta t + \eta_i \mathcal{S}_{D^{*+}D^{*-}} \sin\Delta m\Delta t)\right\} \\ &+ \frac{e^{-|\Delta t|/\tau_{B^0}}}{4\tau_{B^0}} \sum_{i=0,\|,\perp} R_i \cdot \frac{9}{16} H_i(\cos\theta_{tr}, \cos\theta_1) \\ &\quad \left\{1 - qw(\mathcal{A}_{D^{*+}D^{*-}} \cos\Delta m\Delta t + \eta_i \mathcal{S}_{D^{*+}D^{*-}} \sin\Delta m\Delta t)\right\} \\ &= \frac{e^{-|\Delta t|/\tau_{B^0}}}{4\tau_{B^0}} \sum_{i=0,\|,\perp} R_i \cdot \frac{9}{16} H_i(\cos\theta_{tr}, \cos\theta_1) \\ &\quad \left\{1 + q(1-2w)(\mathcal{A}_{D^{*+}D^{*-}} \cos\Delta m\Delta t + \eta_i \mathcal{S}_{D^{*+}D^{*-}} \sin\Delta m\Delta t)\right\}.\end{aligned} \tag{2.8}$$

As a result, a measured CP asymmetry is diluted by the factor $(1-2w)$. Thus a precise estimation of w is needed to measure CP-violation parameters correctly. For this task, particle identification performs an important role.

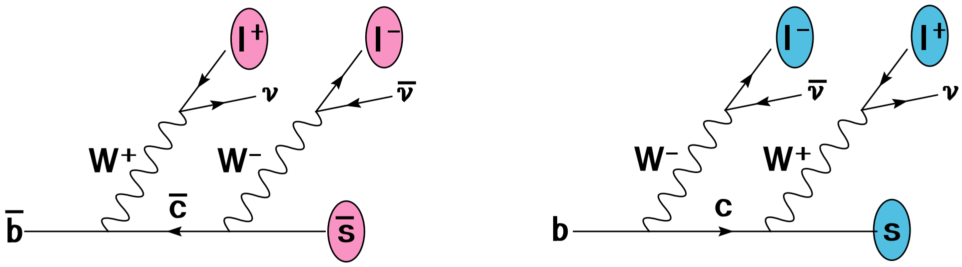

Figure 2.3: *A schematic view of flavor tagging. The primary and secondary leptons and an s quark from cascade decay remember the flavor of the parent b quark. Note that the secondary lepton has the opposite charge to the others. $B^0 \to D^{(*)}X$ decays are also available. Detail of flavor tagging is described later.*

Chapter 3

Experimental Apparatus

3.1 Overview

In this chapter, we describe the experimental apparatus of the Belle experiment. The Belle experiment is one of two B-Factories, which is performed at KEK (High Energy Accelerator Research Organization), Tsukuba, Japan. The KEK B-factory consists of the KEKB e^+e^- collider and the Belle detector. The KEKB collider has the highest luminosity in the world, and the high-sensitivity Belle detector has produced many physics results.

3.2 The KEKB Collider

The KEKB accelerator [30] is an asymmetric-energy e^+e^- collider, which aims at producing a large number of B and anti-B mesons like "factory". It consists of two storage rings, an 8 GeV electron ring (HER) and a 3.5 GeV positron ring (LER), and an injection linear accelerator (Linac). The circumference of both storage rings is about 3 km. The electrons (positrons) are accelerated to their full energies by the Linac and are injected into the HER (LER) ring. Figure 3.1 shows a schematic view of the KEKB collider.

The two storage rings are placed side-by-side in a tunnel 11 m below the ground level and only crossing at one point, which is called the interaction point (IP), in the Tsukuba experimental hall. The electrons and positrons collide with a finite crossing angle of ±11 mrad to avoid parasitic collisions.

The center of mass energy is 10.58 GeV, which corresponds to the mass of the $\Upsilon(4S)$ resonance that decays into a $B\bar{B}$ meson pair. The produced B meson is boosted due to the asymmetric energy with a Lorentz factor $\beta\gamma \simeq 0.425$ and fly about 200 μm on average nearly along the electron beam direction.

The design luminosity is $10 \times 10^{33}\mathrm{cm}^{-2}\mathrm{s}^{-1}$ which approximately corresponds to 10^8 $B\bar{B}$ pairs a year. The main parameters of the KEKB are summarized in Table 3.1. Figure 3.1 shows the luminosity history of the KEKB. As of July 2004, the KEKB has achieved a peak luminosity of $13.92 \times 10^{33}\mathrm{cm}^{-2}\mathrm{s}^{-1}$ and data recorded by the Belle detector corresponds to the integrated luminosity of 288 fb^{-1}. These are the world records at the

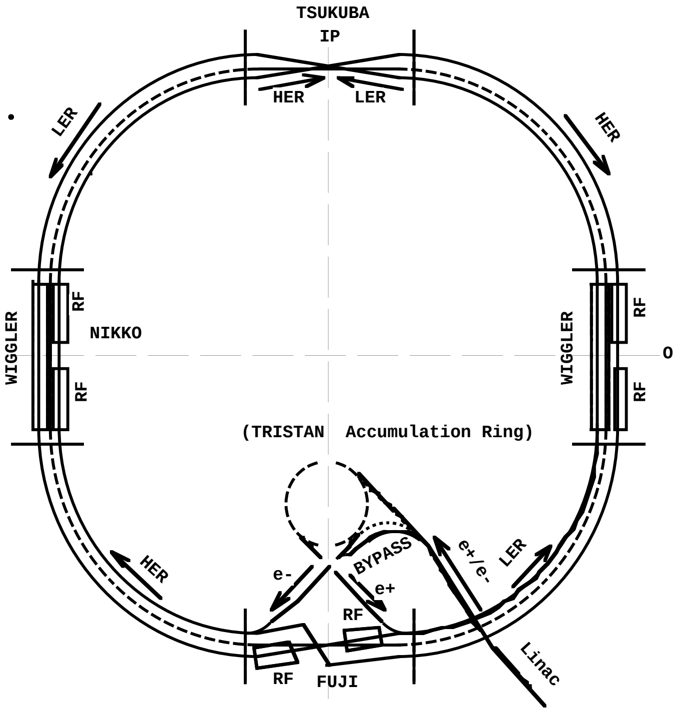

Figure 3.1: *Configuration of the KEKB collider.*

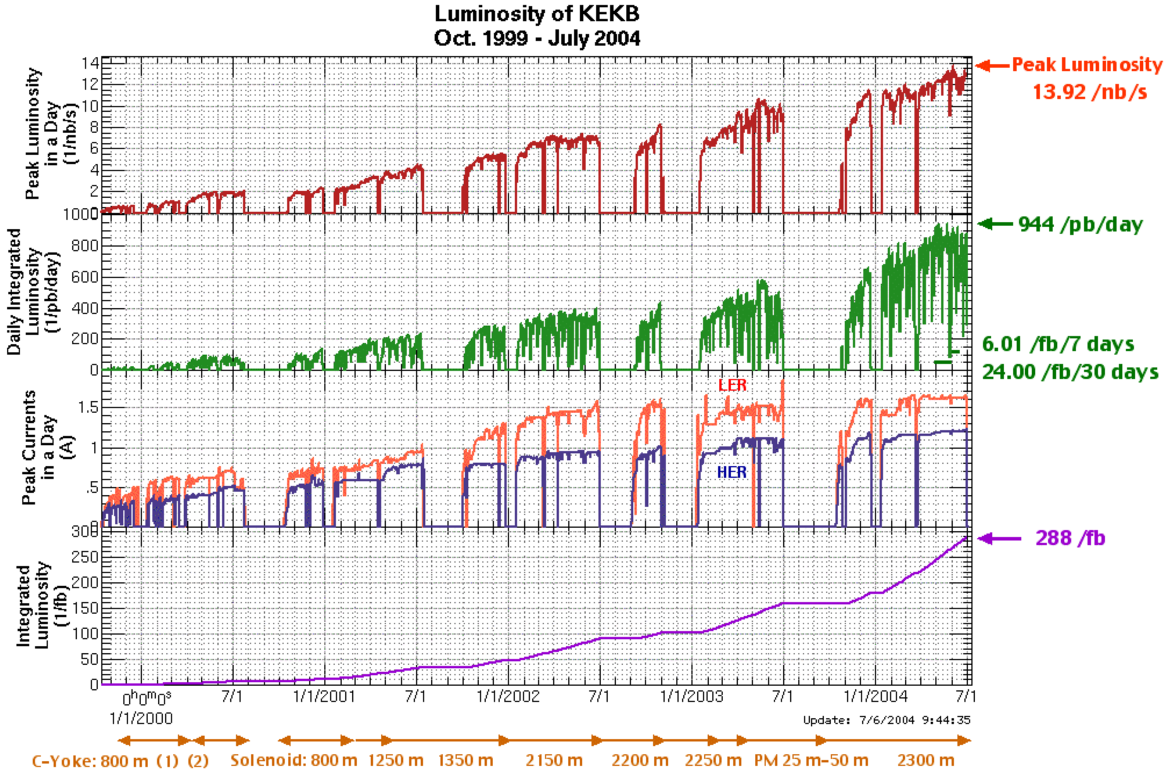

Figure 3.2: *Luminosity history of the KEKB collider.*

time.

3.3 The Belle Detector

3.3.1 Overview

The B meson decay produces many charged particles such as $K^{\pm}$, $\pi^{\pm}$ and neutral particles like γ, π^0 and $K^0_{\rm S}$. In order to measure time-dependent CP asymmetries in the $B^0 \to D^{*+}D^{*-}$ decay, we need to reconstruct and identify particles mentioned above with high efficiencies and measure vertex positions with good precision. The Belle detector was designed and constructed to satisfy these requirements.

The Belle detector is asymmetrically placed around the IP and consists of several sub-detectors to detect B decay products effectively. Figures 3.3 and 3.4 show the detector configurations. These sub-detectors are grouped into two: tracking devices and particle identification devices. As a tracking device, the silicon vertex detector (SVD), which is used for precise measurement of the B meson vertices, is located just outside of a cylindrical beampipe. Another tracking device, the central drift chamber (CDC) measures momentum of charged particles. The CDC is also utilized as a particle identification device for charged particles with measuring dE/dx. Aerogel Cherenkov counter (ACC) and time-of-flight counter (TOF) are placed radially outside of the CDC. Electromagnetic particles, photons and electrons, are detected and identified with an array of CsI(Tl) crystals (ECL) located inside the solenoid coil. The super-conducting solenoid provides a magnetic field of 1.5 T for momentum measurement of charged particles by the CDC. Penetrating particles, muons and $K^0_{\rm L}$ mesons, are identified by arrays of resistive plate counters interspersed in the iron yoke (KLM), which is located at the outermost part of the Belle detector. In addition to these sub-detectors, the Belle detector has the extreme forward calorimeter (EFC) to improve the experimental sensitivity to some physics processes such as $B \to \tau\nu$ and to provide luminosity information online. The detector performance is summarized in Table 3.2.

We define the Belle coordinate system, which is commonly used in this thesis: In the Cartesian coordinate system, $\vec{z}$ is defined as the opposite direction of the positron beam current; $\vec{y}$ is the vertically upward direction of the system; $\vec{x}$ satisfies the relation of the right-hand system, i.e. $\vec{x} = \vec{y} \times \vec{z}$. The cylindrical coordinate system is also defined: r is the radius in the x-y plane ($r = \sqrt{x^2 + y^2}$); θ is the polar angle from the z-axis; ϕ is the the azimuth angle around the z-axis. Figure 3.5 illustrates the definition. The detailed description of the Belle detector is found elsewhere [31]. We give a brief description of the major detector subsystems and analysis software relevant to the measurement of CP asymmetry parameters.

3.3.2 Beampipe

The beampipe around the IP is an important structure to measure the vertex position of B meson with the vertex detector, which is just outside of the beampipe. The thickness of the beampipe is designed to be minimized, since multiple Coulomb scattering and

Table 3.1: *Main parameters of KEKB.*

Ring		LER	HER	
Energy	E	3.5	8.0	GeV
Circumference	C	3016.26		m
Luminosity	$\mathcal{L}$	1×10^{34}		$\mathrm{cm}^{-2}\mathrm{s}^{-1}$
Crossing angle	θ_x	± 11		mrad
Tune shifts	ξ_x/ξ_y	0.039/0.052		
Beta function at IP	β_x^*/β_y^*	0.33/0.01		m
Beam current	I	2.6	1.1	A
Natural bunch length	σ_z	0.4		cm
Energy spread	σ_ε	7.1×10^{-4}	6.7×10^{-4}	
Bunch spacing	s_b	0.59		m
Particle/bunch	N	3.3×10^{10}	1.4×10^{10}	
Emittance	$\varepsilon_x/\varepsilon_y$	$1.8 \times 10^{-8}/3.6 \times 10^{-10}$		m
Synchrotron tune	ν_s	$0.01 \sim 0.02$		
Betatron tune	ν_x/ν_y	45.52/45.08	47.52/43.08	
Momentum compaction factor	α_p	$1 \times 10^{-4} \sim 2 \times 10^{-4}$		
Energy loss/turn	U_o	0.81†/1.5‡	3.5	MeV
RF voltage	V_c	$5 \sim 10$	$10 \sim 20$	MV
RF frequency	f_{RF}	508.887		MHz
Harmonic number	h	5120		
Longitudinal damping time	τ_ε	43†/23‡	23	ms
Total beam power	P_b	2.7†/4.5‡	4.0	MW
Radiation power	P_{SR}	2.1†/4.0‡	3.8	MW
HOM power	P_{HOM}	0.57	0.15	MW
Bending radius	ρ	16.3	104.5	m
Length of bending magnet	ℓ_B	0.915	5.86	m

†: without wigglers, ‡: with wigglers

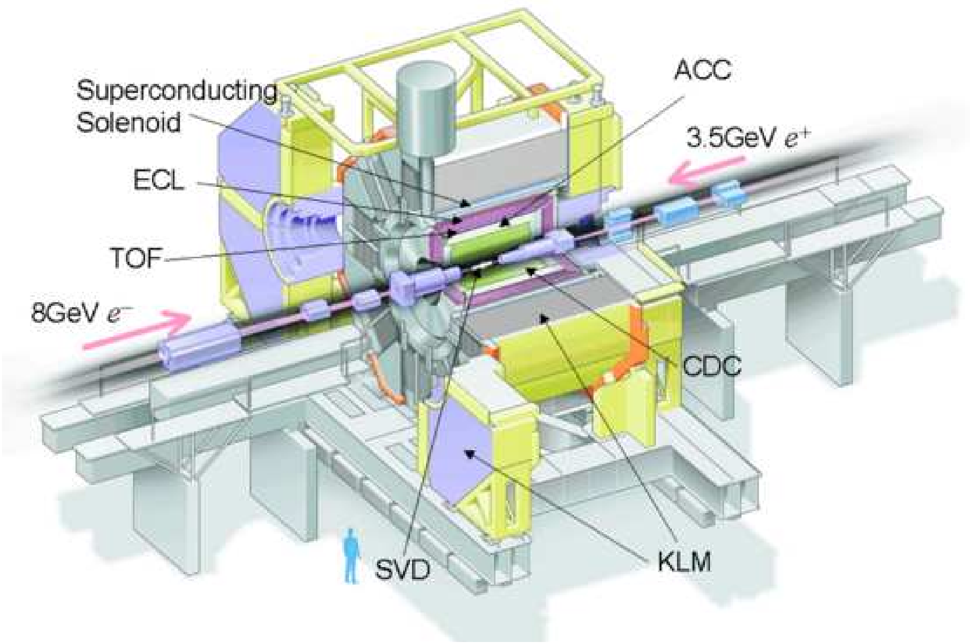

Figure 3.3: *Configuration of the Belle detector system.*

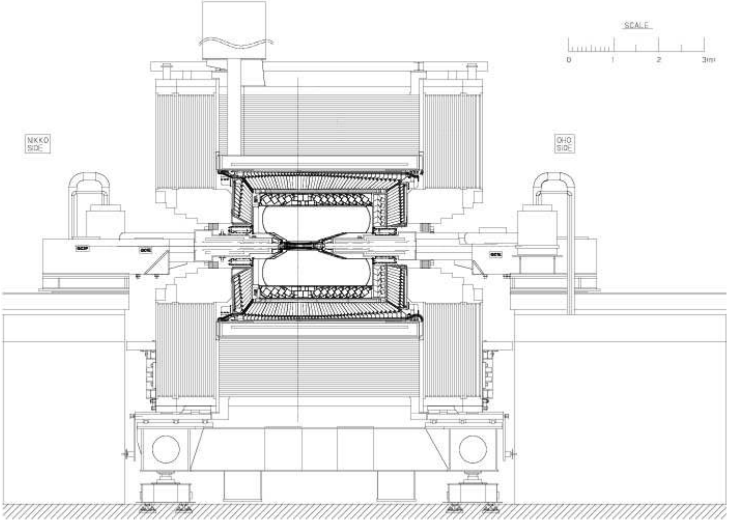

Figure 3.4: *Side view of the Belle detector.*

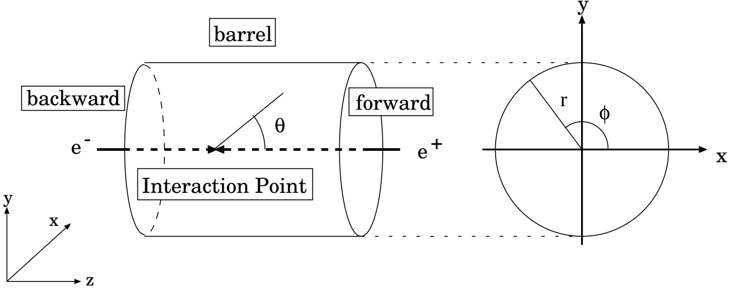

Figure 3.5: *Definition of the coordinate system.*

Detector	Type	Configuration	Readout	Performance
Beampipe	Beryllium double-wall	Cylindrical, r=2.0 cm 0.5/2.5/0.5(mm)=Be/He/Be		He gas cooled
SVD	Double sided Si strip	300 μm-thick, 3 layers r = 3.0 - 6.05 cm Length = 22 - 34 cm	ϕ: 40.96k z: 40.96k	$\sigma_{\Delta z}$ ~200 μm
CDC	Small cell drift chamber	Anode: 50 layers Cathode: 3 layers r = 8.3 - 86.3 cm $-77 \leq z \leq 160$ cm	A: 8.4 K C: 1.5 K	$\sigma_{r\phi} = 130\ \mu$m $\sigma_z \lesssim 200 \sim 1,400\mu$m $\sigma_{p_t}/p_t = (0.20p_t \oplus 0.29/\beta)\%$ $\sigma_{dE/dx} = 6\%$
ACC	$n : 1.01$ ~ 1.03 Silica aerogel	~12x12x12 cm^3 blocks 960 barrel / 228 endcap FM-PMT readout	1,788	$N_{p.e.} \geq 6$ K/π separation: 1.2<p<3.5GeV/c
TOF	Scintillator	128 ϕ segmentation r = 120 cm, 3 m-long	128×2	$\sigma_t = 100$ ps K/π separation: up to 1.2GeV/c
TSC		64 ϕ segmentation	64	
ECL	CsI (Towered-structure)	Barrel: r = 125 - 162 cm End-cap: z = -102 cm and +196 cm	6,624 1152 (F) 960 (B)	σ_E/E= 1.3 %/$\sqrt{E}$ σ_{pos} = 0.5 cm/$\sqrt{E}$
Magnet	Super conducting	inner radius = 170 cm		B = 1.5 T
KLM	Resistive plate counters	14 layers (5cm Fe+4cm gap) 2 RPCs in each gap	θ:16 K ϕ:16 K	$\Delta\phi$=$\Delta\theta$=30 mrad for K_{L}^0 $\sim$ 1 % hadron fake
EFC	BGO	2x1.5x12 cm^3	θ:5 ϕ:32	σ_E/E= $(0.3 \sim 1)\%/\sqrt{E}$

Table 3.2: *Performance parameters expected (or achieved) for the Belle detector (p_t in* GeV/c*, E in GeV).*

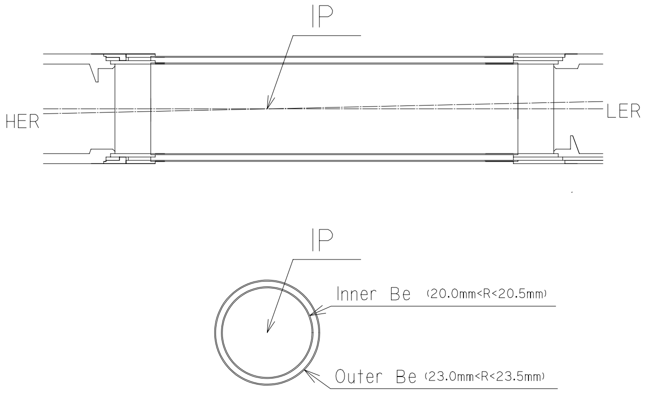

Figure 3.6: *The cross section of the beryllium beampipe at the interaction point.*

spatial distance between the IP and the vertex detector make the vertex resolution worse. Therefore, the beryllium beampipe was chosen. Figure 3.6 shows the cross section of the beryllium beampipe at the interaction region. The beampipe is a double-wall cylinder, whose radii are 20.0 mm and 23.0 mm, respectively. Each cylinder has 0.5 mm thickness. In order to manage beam-induced heating, a 2.5 mm gap between the cylinders works as a part of active cooling system, which provides a helium gas channel. The helium gas coolant is adopted to minimize the material in the beampipe. Outside the outer beryllium cylinder, a 20 μm thick gold sheet is attached in order to reduce the low energy X-ray background from the HER. The total thickness of the beampipe corresponds to 0.9% of a radiation length.

3.3.3 Silicon Vertex Detector (SVD)

The SVD plays a central role to measure time-dependent CP asymmetry parameters, since precise measurement of vertex positions for B meson pairs is indispensable. It also contributes to reconstruct charged particle tracks.

Figure 3.7 shows the geometrical configuration of the SVD. The SVD consists of three concentric cylindrical layers of silicon sensors and covers a polar angle $23^\circ < \theta < 139^\circ$. This corresponds to 86% of the full solid angle. The radii of the three layers are 30, 45.5 and 60.5 mm. The innermost, middle, and outermost layers consist of 8, 10 and 14 ladders, respectively. Each ladder is made up of two long or short half ladders that are mechanically jointed by a support structure but electrically independent of each other. Each long half ladder contains two double-sided silicon strip detectors (DSSD's) and a hybrid unit. Each short half ladder contains a DSSD and a hybrid unit. The innermost-layer ladder consists of two short half ladders. The middle-layer ladder consists of a short and a long half ladder. The outermost-layer ladder consists of two long half ladders. In total 102 DSSDs are used.

We use S6936 DSSDs fabricated by Hamamatsu Photonics, which were originally developed for the DELPHI experiment [32]. The overall DSSD size is 57.5×33.5 mm^2

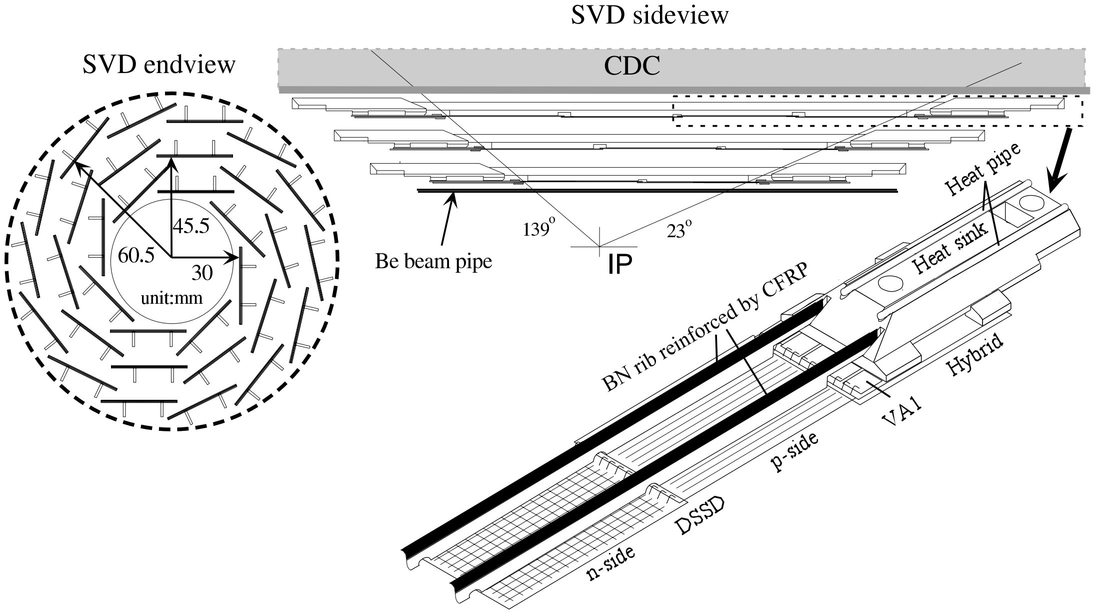

Figure 3.7: *Detector configuration of SVD.*

with a thickness of 300 μm. Each DSSD consists of 1280 sense strips and 640 readout pads on opposite sides. One side (called n-side) of a DSSD has n^+ sense strips oriented perpendicular to the beam direction to measure the z coordinate. The other side (called p-side) with longitudinal p^+ sense strips allows the ϕ coordinate measurement. The strip pitch is 25 μm for the p-side and 42 μm for the n-side. Each strip is biased via 25 MΩ polysilicon bias resistors. The bias voltage of 75V is supplied to the n-side, while the p-side is grounded. The schematic view of the DSSD is shown in Fig. 3.8. The n^+ strips are interleaved by p^+ implants (called p-stops) to separate the consecutive strips electrically. A charged particle passing through the depletion region of the n bulk silicon generates a pairs of an electron and a hole. The electrons and holes drift to each strip and make two dimensional hit signals. On the n-side, adjacent strips are read out by a single channel which gives an effective strip pitch of 84 μm. On the p-side, every other strip is connected to a readout channel. Charge collected by the floating strips in between is read from adjacent strips by means of capacitive charge division.

The signal of DSSDs is read out by the VA1 chip [33, 34]. The VA1 chip is a 128 channel CMOS integrated circuit fabricated by the Austrian Micro Systems (AMS) with a 1.2 μm CMOS process. It was specially designed for the readout of silicon vertex detectors and other small-signal devices. Five VA1 chips are on both sides of each hybrid unit. The total number of readout channels is 81920.

We estimate the performance of the SVD with the following two quantities: the SVD-CDC track matching efficiency and the impact parameter resolution of tracks with associated SVD hits. The SVD-CDC track matching efficiency is defined as the probability that a CDC track passing through the SVD acceptance has associated SVD hits in at least two layers, and in at least one layer with both the r-ϕ and r-z information. Tracks from K_S^0

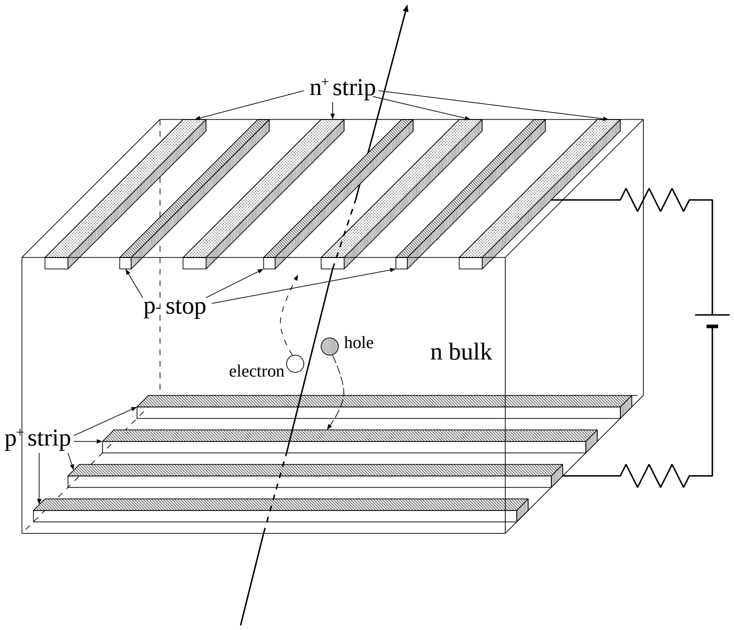

Figure 3.8: *Schematic drawing of the DSSD.*

decays are excluded since these tracks do not necessarily go through the SVD. Figure 3.9 shows the SVD-CDC track matching efficiency for hadronic events as a function of time. The average matching efficiency is better than 98.7%. The impact parameter resolution for reconstructed tracks is measured as a function of the tracks momentum p (measured in GeV/c) and the polar angle θ:

$$\sigma_{xy} = 19 \oplus 54/(p\beta \sin^{3/2}\theta)\ \mu\mathrm{m}, \tag{3.1}$$

$$\sigma_{z} = 42 \oplus 44/(p\beta \sin^{5/2}\theta)\ \mu\mathrm{m}, \tag{3.2}$$

where "$\oplus$" indicates a quadratic sum. Figures 3.10 show the momentum and angular dependence of the impact parameter resolution.

3.3.4 Central Drift Chamber (CDC)

The CDC is a the charged particle tracking system that provides their momenta from the curvature in the magnetic field given by the solenoid magnet. The CDC also measures dE/dx of charged tracks for particle identification. Since the $B^0 \to D^{*+}D^{*-}$ decay produces many low-momentum charged tracks, especially pions from the D^* decay (transverse momentum $p_t < 300\mathrm{MeV/c}$), The CDC was designed and constructed to detect them with high efficiency and good resolution.

The structure of the CDC is shown in Fig. 3.11. The longest wires are 2400 mm long. The outer radius is 874 mm and the inner one is extended down to 103.5 mm without any walls in order to obtain good tracking efficiency for low-p_t tracks by minimizing the material. The polar angle coverage is $17° \leq \theta \leq 150°$, which corresponds to 92% of the full solid angle.

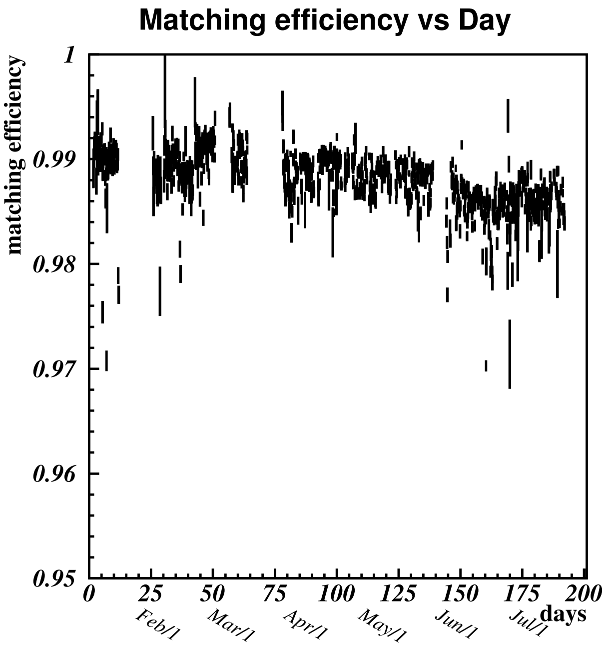

Figure 3.9: *Time-variation of the SVD-CDC track matching efficiency as a function of the date of data taking.*

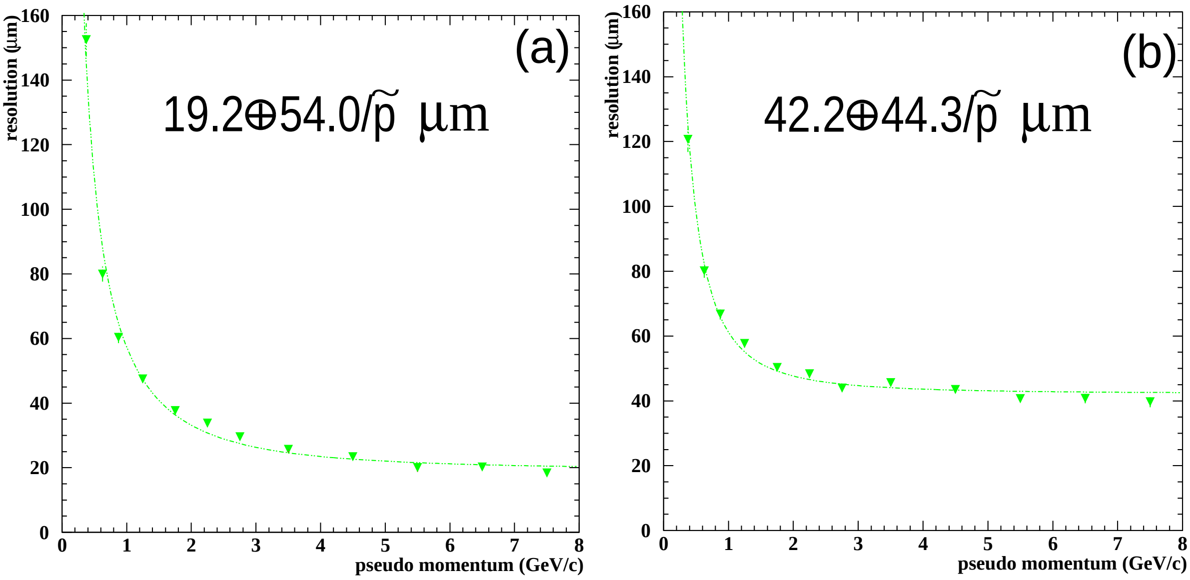

Figure 3.10: *Impact parameter resolution of charged tracks with associated SVD hits (a) for* σ_{xy}*; (b) for* σ_z*. Pseudo momentum* $\tilde{p} \equiv p\beta\sin(\theta)^{3/2}$ *for* σ_{xy} *and* $\tilde{p} \equiv p\beta\sin(\theta)^{5/2}$ *for* σ_z*.*

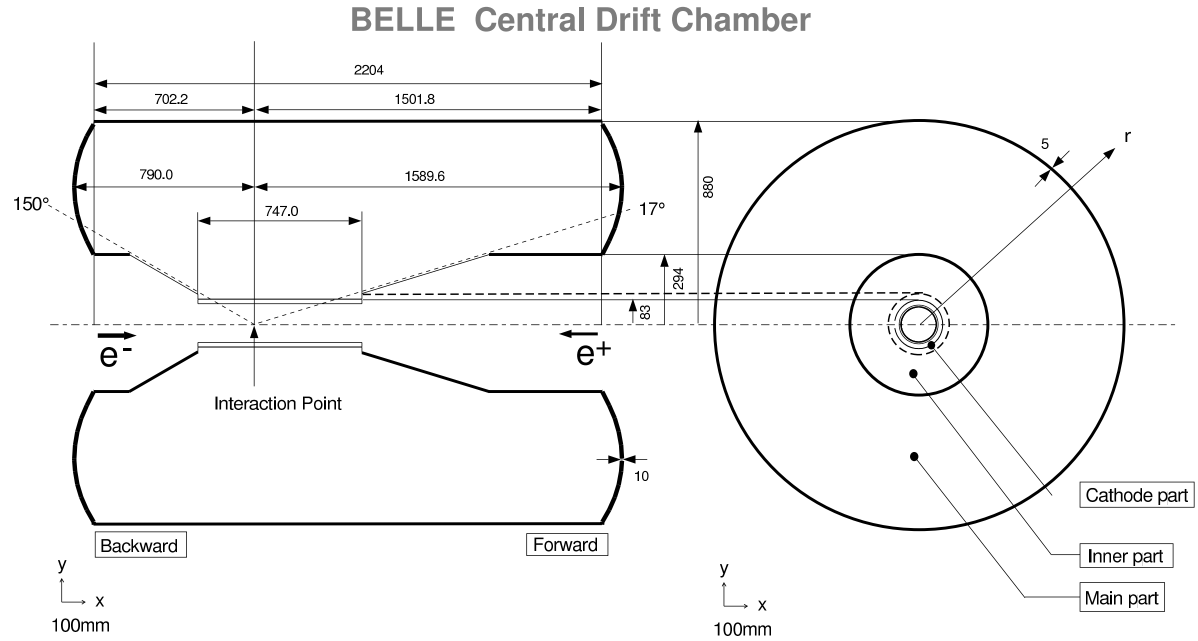

Figure 3.11: *Overview of the CDC structure. The lengths in the figure are in the units of* mm.

The CDC is a small-cell cylindrical drift chamber with 50 layers of anode wires, which consist of 32 axial- and 18 stereo-wire layers, and 3 cathode strip layers. The axial wires are configured to be parallel to the z axis, while the stereo wires are slanted by approximately ± 50 mrad, to provide z position information. Eight field wires providing drift electric field surround a sense wire, and the field wires and a sense wire form a drift cell. The cell structure is shown in Fig. 3.12. The CDC has a total of 8400 drift cells. A low-Z gas mixture, which consists of 50% He and 50% ethane (C_2H_6), is used to minimize multiple Coulomb scattering to ensure a good momentum resolution, especially for low momentum tracks. A charged particle passing through the CDC ionizes the gas. A charge avalanche is caused by the ionized gas and drifts to a sense wire with a specific drift velocity, then the measured signal height and drift time provide information of the energy deposit and distance from the sense wire. In the innermost part, the three cathode strip layers are installed to provide the z position measurements of tracks for the trigger system. The number of readout channel is 8400 for anode sense wires and 1792 for cathode strips. Figure 3.13 shows a scatter plot of measured dE/dx and particle momentum. Populations of pions, kaons, protons and electrons are clearly seen. Figure 3.14 shows the transverse momentum (p_t) resolution as a function of p_t. The p_t resolution is $(0.20 p_t \oplus 0.29/\beta)\%$, where p_t is in the unit of GeV/c.

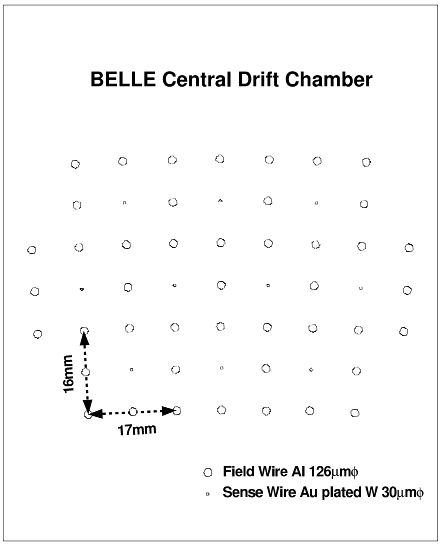

Figure 3.12: *Cell structure of CDC.*

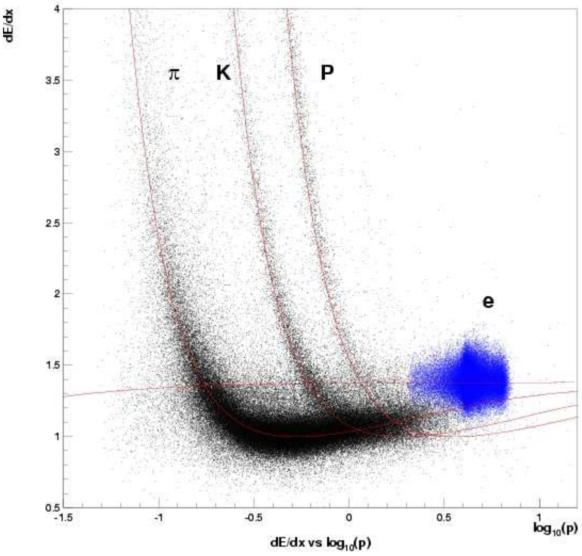

Figure 3.13: *The measured dE/dx versus momentum observed in collision data.*

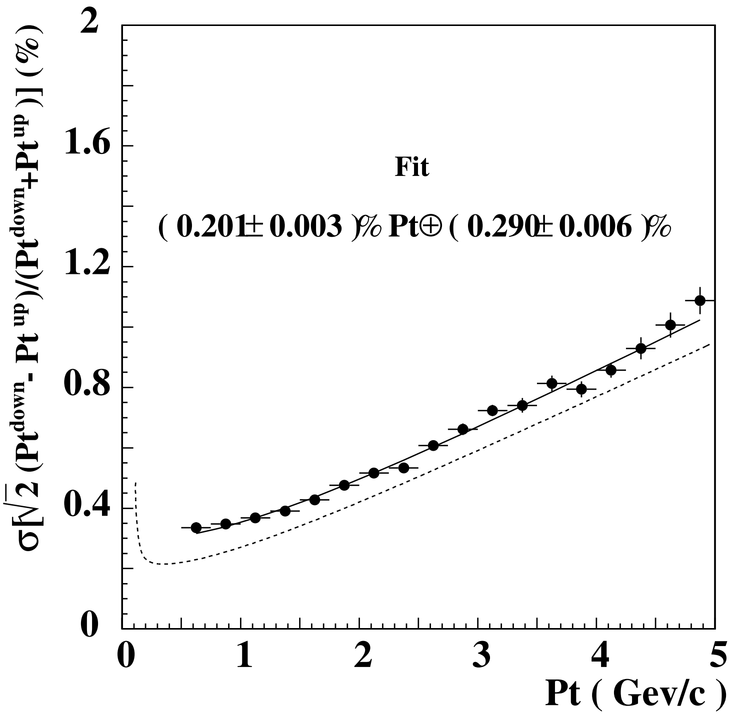

Figure 3.14: *The p_t dependence of p_t resolution for cosmic rays. The solid curve shows the fitted result ($0.201\% p_t \oplus 0.290\%/\beta$) and the dotted curve shows the ideal expectation for $\beta = 1$ particles.*

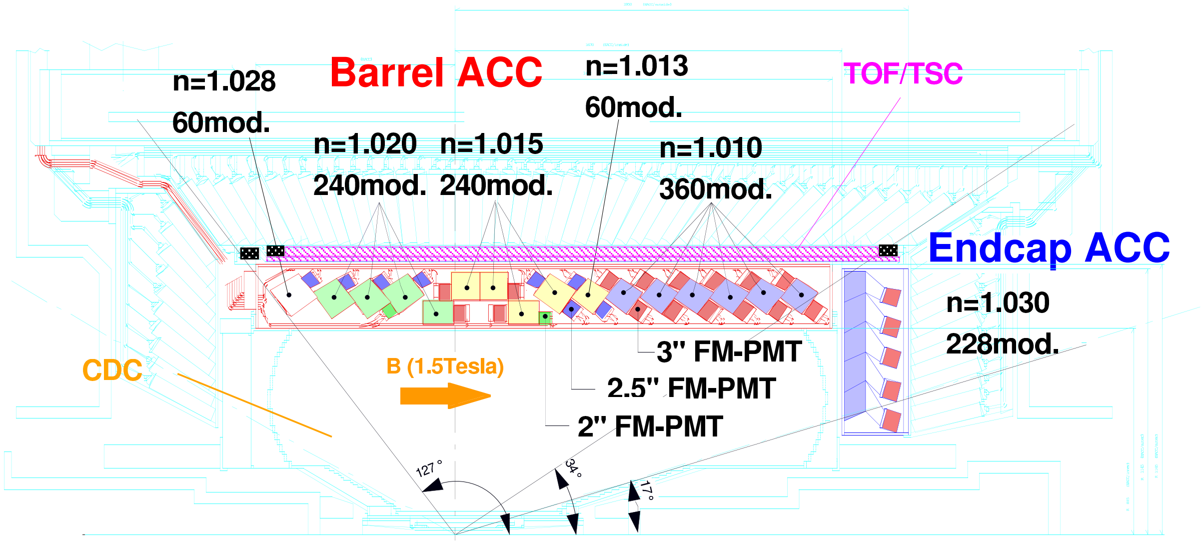

Figure 3.15: *The arrangement of ACC.*

3.3.5 Aerogel Cherenkov Counter (ACC)

The ACC provides particle identification information to distinguish charged kaons from charged pions whose momentum are from 1.2 GeV/c to 3.5 GeV/c, thanks to Cherenkov radiations of charged tracks. The momentum range covered by the ACC is beyond the reach of other particle identification system; i.e. the CDC (dE/dx) and the TOF (time-of-flight).

Cherenkov light is emitted when its velocity is larger than the light velocity in the matter:

$$n > \frac{1}{\beta} = \sqrt{1 + \left(\frac{m}{p}\right)^2}, \tag{3.3}$$

where m and p are the particle mass and the momentum of the particle, respectively, and n is the refractive index of the matter. Thus we can distinguish kaons from pions, with the selected matter of n which emits Cherenkov light for pions, but does not for heavier kaons.

The configuration of the ACC is shown in Fig. 3.15. The ACC consists of 960 counter modules segmented into 60 cells in the ϕ direction for the barrel part and 228 modules arranged in 5 concentric layers for the forward endcap part of the detector. All the counters are arranged in a semi-tower geometry, pointing to the IP. Each counter module consists of a block of silica aerogel in an aluminum box of 0.2 mm thickness and one or two fine mesh-type photomultiplier tubes (FM-PMTs) which can work in the 1.5 T magnetic field. The refractive indices of the silica aerogel blocks are selected to obtain the good pion/kaon separation for the whole kinematic range. For the barrel modules, the silica aerogel with five different refractive indices, $n = 1.010, 1.013, 1.015, 1.020$ and 1.028, are used depending on the polar angle. For the endcap module, the silica aerogel with $n = 1.030$ is used for low momentum particles, which is necessary for flavor tagging, to cover lack of the TOF in the endcap. The number of readout channels is 1560 for the barrel modules and 228 for the endcap modules.

Figure 3.16 shows the measured pulse height distributions for barrel ACC for $e^{\pm}$ tracks in Bhabha events and $K^{\pm}$ candidates in hadronic events, where $K^{\pm}$ candidates are selected by TOF and dE/dx measurements, together with the expectations from Monte Carlo (MC) simulation. Clear separation between $K^{\pm}$ and $e^{\pm}$ is seen.

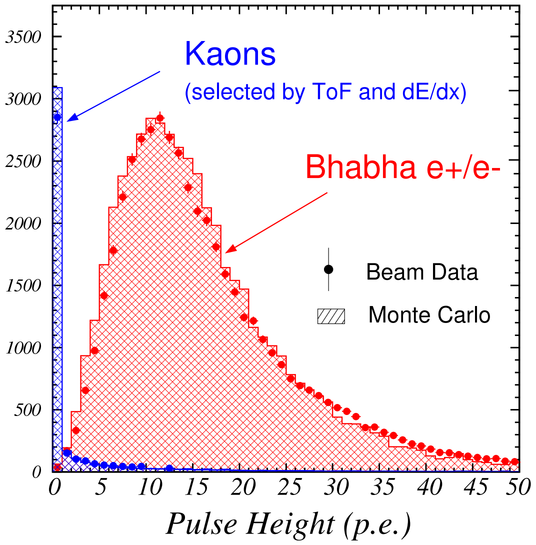

Figure 3.16: *Pulse-height spectra in units of photoelectrons observed by barrel ACC for electrons and kaons.*

3.3.6 Time of Flight Counter (TOF)

The TOF gives particle identification to distinguish charged kaons from charged pions, whose momenta are below 1.2 GeV/c. With using plastic scintillation counters, The TOF measures the elapsed time between a collision at the interaction point and the time when the particle hits the TOF layer. It is very powerful for particle identification in e^+e^- collider detectors. The TOF also provides fast timing signals for the trigger system. To sustain the fast trigger rate in any beam background condition, thin trigger scintillation counters (TSC) are appended just inside the TOF counter.

A relation between measured time T and the particle mass m is expressed as

$$T = \frac{L}{c\beta} = \frac{L}{c}\sqrt{1 + \left(\frac{m}{p}\right)^2}, \tag{3.4}$$

where p is the particle momentum and L is the flight path length. For $K^{\pm}$ and $\pi^{\pm}$ with a momentum of 1.2 GeV/c and a flight path length of 1.2 m, which is the distance between the interaction point and TOF, we obtain T of 4.3 ns and 4.0 ns, respectively. The

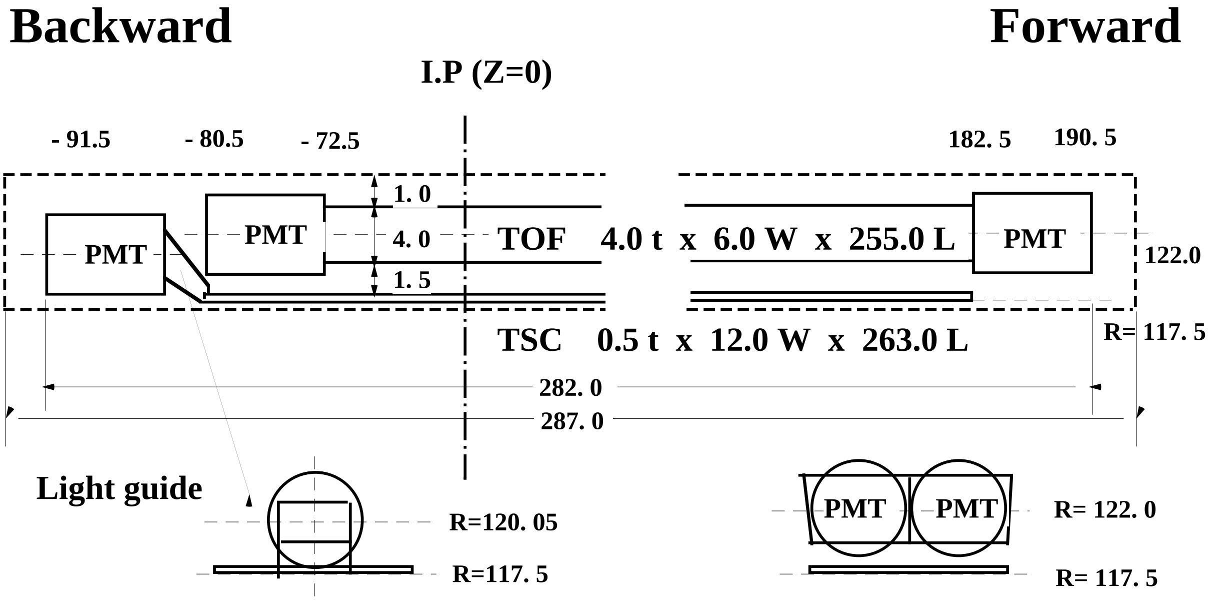

Figure 3.17: *Dimensions of a TOF/TSC module.*

TOF is designed to have 100 ps time resolution which separates these $K^{\pm}$ and $\pi^{\pm}$ at 3 σ significance.

The TOF system consists of 128 TOF counters and 64 TSC counters. Two trapezoidally shaped TOF counters and one TSC counter, with a 1.5 cm intervening radial gap, form one module. In total 64 TOF/TSC modules located at a radius of 1.2 m from the IP cover a polar angle range from 34° to 120°. The configuration of a TOF/TSC module is shown in Fig. (3.17). Each TOF counter is read out by a FM-PMT at each end. Each TSC counter is read out by only one FM-PMT from the backward end. The total number of readout channels is 256 for TOF and 64 for TSC.

Figure 3.18 shows TOF time resolution for forward and backward PMTs and for the weighted average as a function of z position in TOF module measured by $e^+e^- \to \mu^+\mu^-$ events. The resolution for the weighted average time is about 100 ps with a small z dependence.

The mass distribution that is obtained from TOF measurement is shown in Fig. 3.19. We have clearly separated distributions of kaons, pions and protons. The data points are consistent with the MC prediction that assumes time resolution of 100 ps.

3.3.7 $K^{\pm}/\pi^{\pm}$ Identification

Particle identification, especially $K^{\pm}/\pi^{\pm}$ separation, is crucial for this analysis, because it is used for reconstruction of the $B^0 \to D^{*+}D^{*-}$ decay and is also used for flavor tagging, The $K^{\pm}/\pi^{\pm}$ separation is based on three nearly independent observables: dE/dx measurement by CDC, TOF measurement, and measurement of the number of photoelectrons in the ACC. Since each of these detector covers different momentum and angular region,

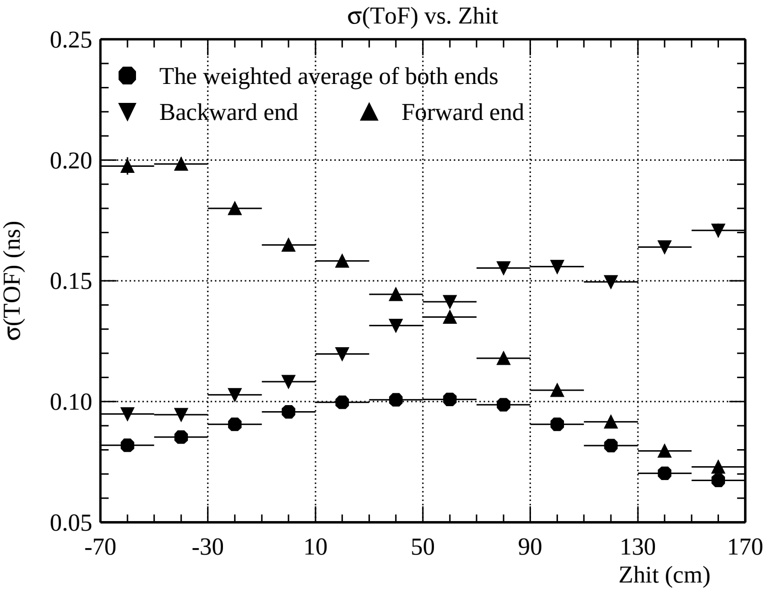

Figure 3.18: *Time resolution for* $e^+e^- \to \mu^+\mu^-$ *events.*

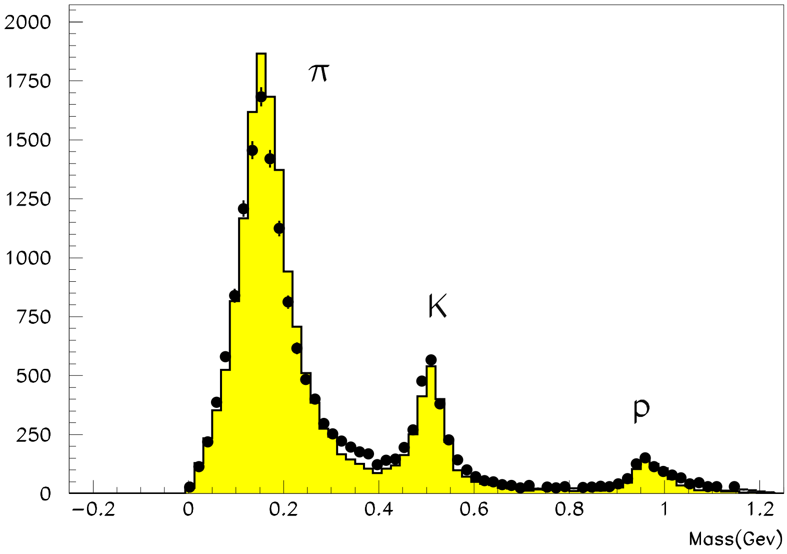

Figure 3.19: *Mass distribution from TOF measurement for particle momenta below 1.2 GeV/c. The histogram shows the expectation assuming time resolution of 100 ps. Points with error bars are obtained from hadronic events.*

their combination provides high performance of particle identification. For each charged track, we calculate probability with kaon and pion hypothesis for each sub-detector. We define the likelihood ratio $P_{K/\pi}$ to distinguish kaons from pions:

$$P_{K/\pi} \equiv \frac{\mathcal{L}(K)}{\mathcal{L}(K) + \mathcal{L}(\pi)}, \tag{3.5}$$

where $\mathcal{L}(K)$ and $\mathcal{L}(\pi)$ are products of sub-detectors' probabilities for $K^\pm$ and $\pi^\pm$, respectively. The validity of the $K^\pm/\pi^\pm$ separation is demonstrated with using $D^{*\pm} \to D^0(\to K^\mp\pi^\pm)\pi^\pm$ decays, which is shown in Fig. 3.20. For most of the momentum region, the measured $K^\pm$ identification efficiency exceeds 80%, while the π fake rate is kept below 10%.

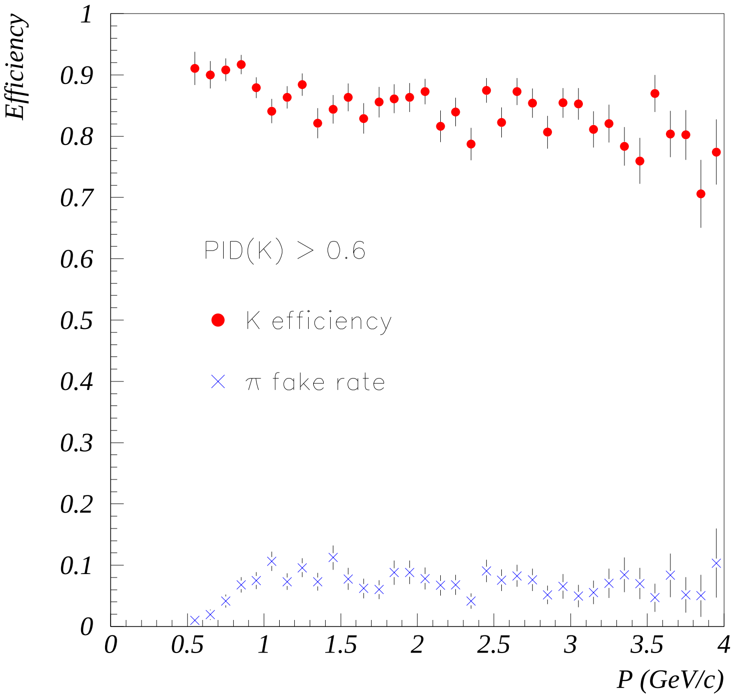

Figure 3.20: *K efficiency and π fake rate as a function of momentum.*

3.3.8 Electromagnetic Calorimeter (ECL)

The ECL contributes to identify electrons and photons, with measuring electromagnetic shower. Electrons are used for flavor tagging and photons are used for reconstruction of $\pi^0 \to \gamma\gamma$ decays and for reconstruction of $D^{*0} \to D^0\gamma$ decays in this analysis.

The overall configuration of the ECL is shown in Fig. 3.21. ECL consists of 8736 thallium-doped CsI crystal counters. Each CsI(Tl) crystal has tower shape of 30 cm long, which corresponds to 16.2 radiation lengths. Each crystal is arranged so that it points to the interaction point. The barrel part has 6624 crystals segmented into 46 in θ and 144

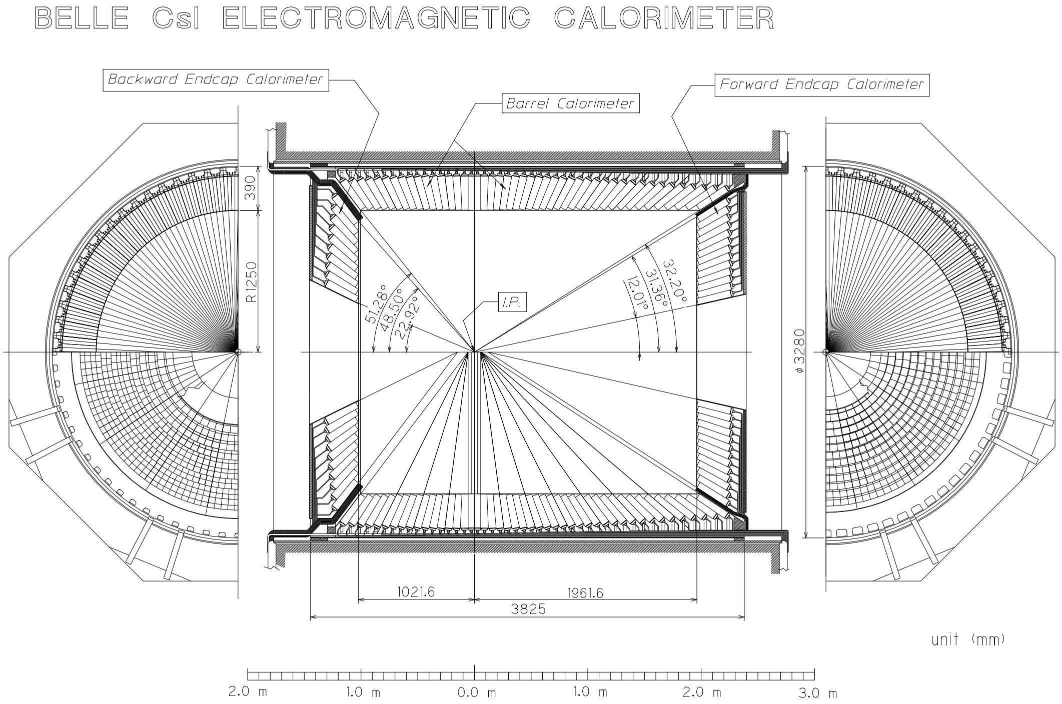

Figure 3.21: *Configuration of ECL.*

in ϕ. The forward (backward) endcap has 1152 (960) crystals segmented into 13 (10) in θ and 48-144 (64-144) in ϕ depending on θ. A signal from each crystal is read out by two 10 mm × 20 mm photodiodes. The total number of readout channels is 17472.

The energy resolution is measured as a function of incident photon energy for 3×3 matrices and for 5×5 of the ECL counters. The nominal resolution is measured to be

$$\frac{\sigma_E}{E} = (1.34 \oplus \frac{0.066}{E} \oplus \frac{0.81}{E^{1/4}})\% \tag{3.6}$$

with the study of 3×3 ECL matrices, where the unit of the photon energy E is in GeV. The position resolution is measured to be

$$\sigma_{\text{pos}} = (0.27 + \frac{3.4}{E^{1/2}} + \frac{1.8}{E^{1/4}})\text{mm}. \tag{3.7}$$

Figure 3.22 shows the energy resolution and the position resolution.

The electron identification primarily relies on a comparison between the charged particle momentum measured by the CDC and the energy deposit in the ECL. Electrons lose all their energy in ECL crystals by electromagnetic showers, while hadrons and muons do not make electromagnetic shower and deposit only a part of their energy in the ECL. The ratio of cluster energy measured by the ECL and charged track momentum measured by the CDC (E/p), therefore is close to unity for electrons and is lower for other particles. The lateral spread of ECL cluster is also used to distinguish electrons from hadrons. Because the radiation length of electrons is smaller than the interaction length of hadrons,

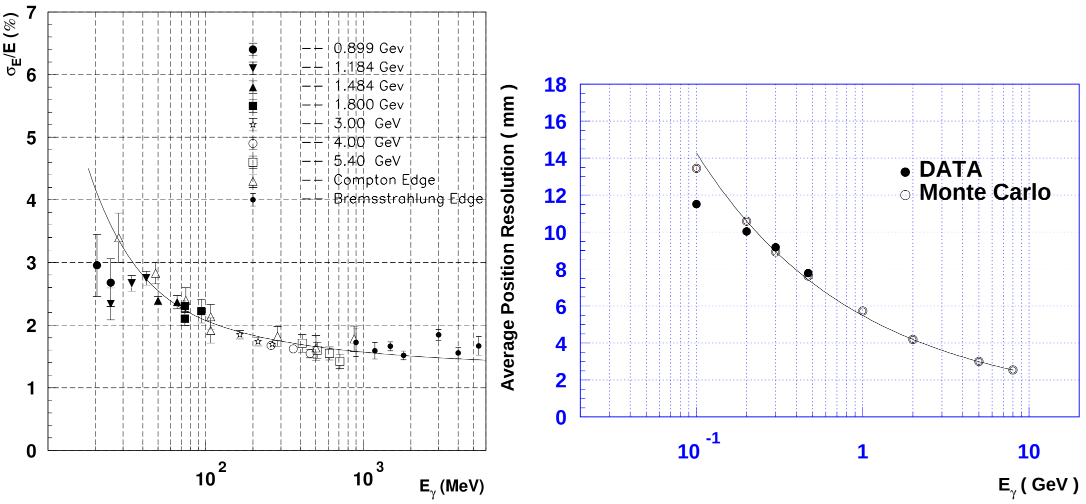

Figure 3.22: *The energy resolution (left) and the position resolution (right) of ECL as a function of incident photon energy.*

clusters made by hadrons tend to be wider than those of electrons. In addition to these ECL information, dE/dx measured by CDC and light yield of ACC are incorporated. Figure 3.23 shows the electron identification efficiency measured with $e^+e^- \rightarrow e^+e^-e^+e^-$ data and the fake rate for charged pions from $K^0_S \rightarrow \pi^+\pi^-$ decays as a function of momentum. The efficiency of electron identification is greater than 90 % and the hadron fake rate is about 0.3 % for $p > 1$ GeV/c. The details of electron identification are given elsewhere [36].

3.3.9 Solenoid Magnet

The super-conducting solenoid provides a magnetic field of 1.5 T, which is used for measurement of track momentum in the CDC. The super-conducting coil consists of a single layer of niobium-titanium-copper alloy embedded in a high purity aluminum stabilizer. It is wound around the inner surface of an aluminum support cylinder with 3.4 m in diameter and 4.4 m in length. Indirect cooling is provided by liquid helium circulating through a tube on the inner surface of the aluminum cylinder. Figure 3.24 shows the structure of the solenoid.

3.3.10 K_L and Muon Detector(KLM)

The KLM provides muon identification for charged particles with momenta greater than 0.6 GeV/c and also gives neutral kaon detection. Charged particles with momenta less than 0.6 GeV/c can not reach KLM.

The KLM consists of alternating layers of charged particle detectors and 4.7 cm thick iron plates. There are 15 resistive plate counter (RPC) superlayers and 14 iron layers in the octagonal barrel region and 14 RPC superlayers in each of the forward and backward

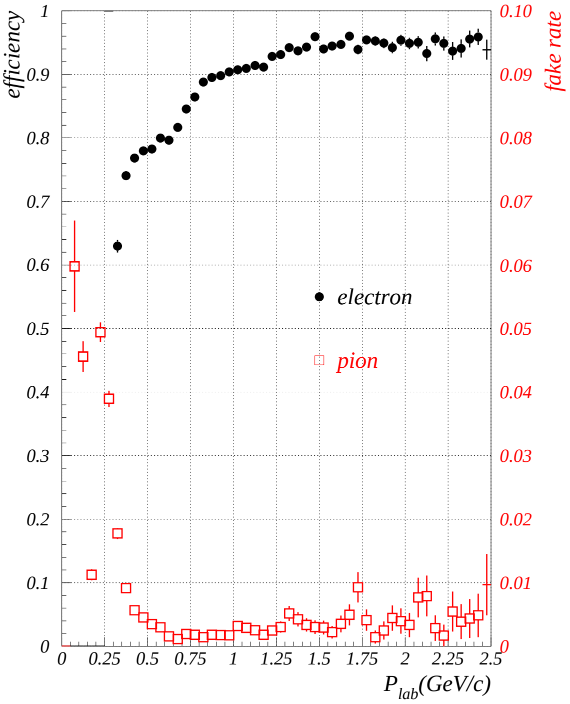

Figure 3.23: *Electron identification efficiency (circles) and fake rate for charged pions (squares). Note the different scales for the efficiency and fake rate.*

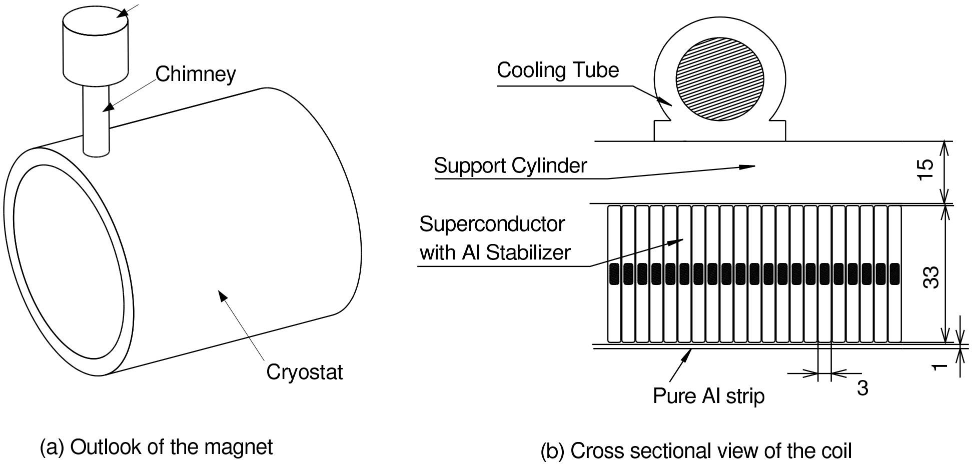

(a) Outlook of the magnet

(b) Cross sectional view of the coil

Figure 3.24: *An outlook of the solenoid and the cross-sectional view of the coil. The unit is mm.*

endcaps. The iron layers also serve as a return yoke of the magnetic flux provided by the super-conducting solenoid. Figure 3.25 shows the barrel part of the iron yoke. A cross section of a RPC superlayers is shown in Fig. 3.26. Each RPC superlayer consists of two RPC modules and provides θ-ϕ two dimensional information. The RPC is a kind of spark chamber, which has two electrodes with high resistivity ($\geq 10^{10}\Omega\cdot\mathrm{cm}$) separated by gass-filled gap that consists of 30% argon, 8% butane, and 62 % freon. A charged particle traversing the gas gap ionizes the gas and initiates a streamer in the gas. The streamer results in a local discharge of the glass plates. This discharge is limited by the high resistivity of the plates and induces a signal on external pickup strips. The iron plates provide a total of 3.9 hadronic interaction lengths for a particle traveling normal to the detector planes. K_L^0 interacting with the iron produces a shower of ionizing particles and is detected by RPC layers.

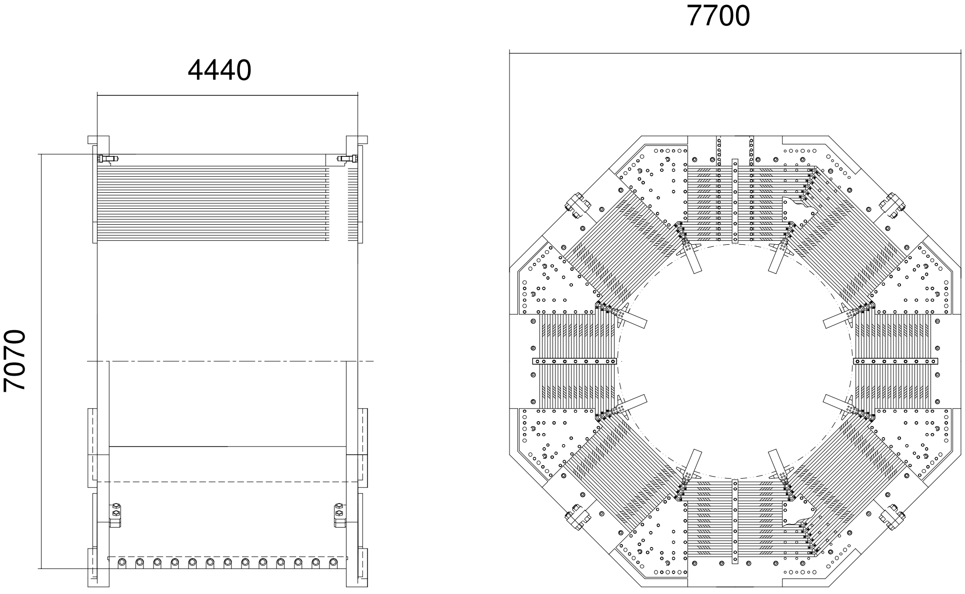

Figure 3.25: *Barrel part of the iron yoke. The unit is mm.*

The muon identification is based on the property difference in the matter between muon and other particles, especially pions that are dominating background. Muons pass through the KLM with small deflections and even penetrate if its momentum is grater than 1.5 GeV/c, while hadrons like pions are deflected by the strong interaction with iron and then stop within less iron layers than muons. These informations are parametrized by the number of penetrated iron plates and the reduced χ^2 calculated with the extrapolated charged track from the CDC and the position of KLM hits. The extrapolation is performed by the Kalman filtering method [37], which can pursuit randomly-scattered tracks even within non-uniform magnetic field. A likelihood ratio of the muon hypothesis and the pion hypothesis is made combining these two information and is used to separate muons from hadrons. Figure 3.27 shows the muon identification efficiency that is measured with cosmic muons as a function of momentum and the fake rate for $\pi^\pm$ measured with

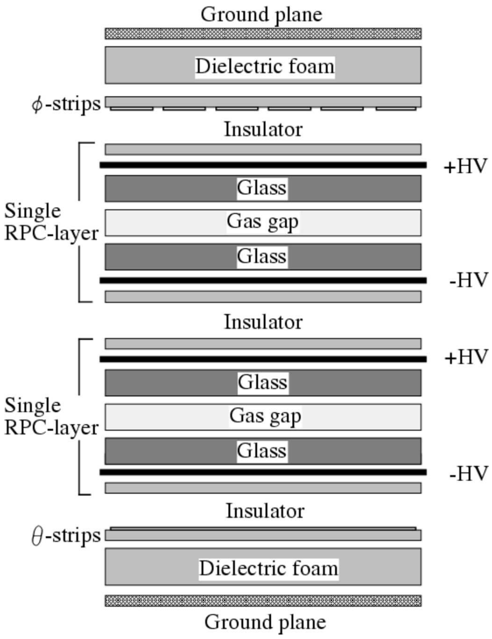

Figure 3.26: *Cross section of a KLM super-layer.*

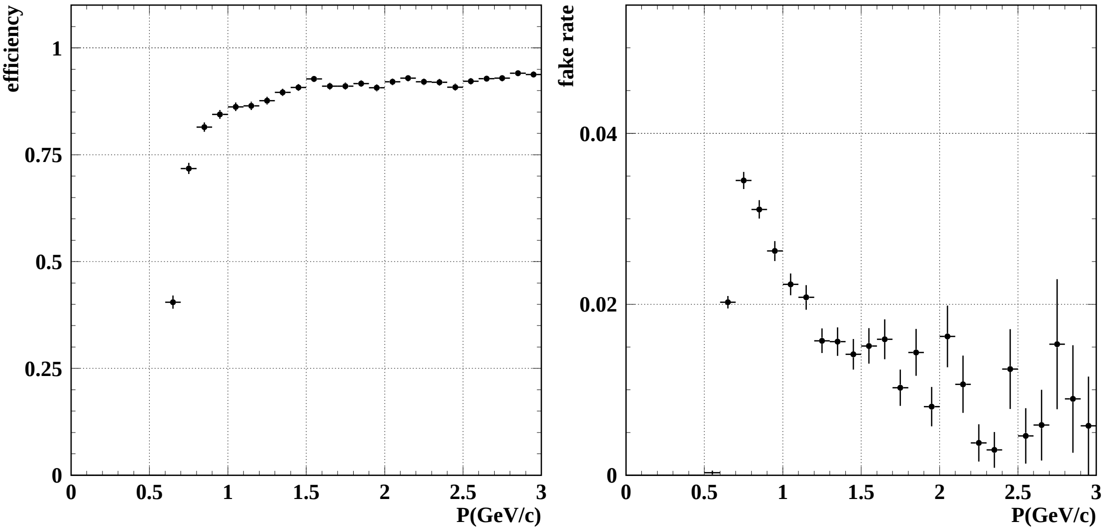

Figure 3.27: *Muon identification efficiency versus momentum in the KLM (left). Fake rate for charged pions versus momentum in the KLM (right).*

$K_S^0 \to \pi^+\pi^-$ decays. Typical efficiency for momentum greater than 1 GeV/c is better than 90%, while fake rate for $\pi^\pm$ is smaller than 2 %. The details of muon identification are given in [38].

3.3.11 Trigger and Data acquisition

The role of the trigger system is to distinguish interesting physics events from enormous uninteresting background events, and record the interesting events, using fast signals from sub-detectors. Because of the high beam current of KEKB, the trigger suffers from severe beam background. Since the rates of beam background are very sensitive to actual accelerator conditions, it is difficult to make a reliable estimate. Therefore, the trigger system is required to be flexible so that background rates are kept within the tolerance of the data acquisition system. It is also needed to have redundant triggers to keep the high trigger efficiency for physics events of interest.

The Belle trigger system consists of the Level-1 hardware trigger and the Level-3 software trigger. The latter is designed to be implemented in the online computer farm. Figure 3.28 shows a schematic view of the Belle Level-1 trigger system. It consists of the sub-detector trigger systems and the central trigger system called the Global Decision Logic (GDL). The sub-detector trigger systems are categorized into two parts: track triggers and energy triggers. The CDC and the TOF are used to yield trigger signals for charged particles. The CDC provides r-ϕ and r-z track trigger signals, while the ECL provides triggers based on the total energy deposit. The KLM provides additional trigger signals for muons. The ECL is used to trigger two-photon events and Bhabha events. The GDL combines the sub-detector trigger signals and makes a final decision to initiate a Belle-wide data acquisition within 2.2 μs from the beam crossing. The typical trigger rate is 200-250 Hz. With these redundant triggers, trigger efficiency for $B\bar{B}$ events is more than 99.5%.

A schematic view of the Belle DAQ system is shown in Fig. 3.29. The performance goal of the DAQ is to be operational at a maximum trigger rate of 500Hz, while keeping a dead time fraction of less than 10%. In order to achieve this requirement, the entire DAQ system is segmented into seven subsystems running in parallel. An eventbuilder combines the signals from sub-detectors into a single event record. The “detector-by-detector” parallel data streams are converted to an “event-by-event” data river and are sent to an online computer farm. The online computer converts an event data into an offline event format and performs a background reduction (the Level 3 trigger) after a fast event reconstruction. The data are then sent to a mass storage system located at the computer center 2 km away via optical fibers. A typical event data size is about 30 kB, which corresponds to the maximum data rate of 15 MB/s.

3.3.12 Offline Software and Computing

Collected data by the Belle detector are analyzed at the offline computer farm. It is necessary to deal with large data at a rate of 400 GB a day. Since the required computational power cannot be achieved by a single CPU, the parallel processing scheme by

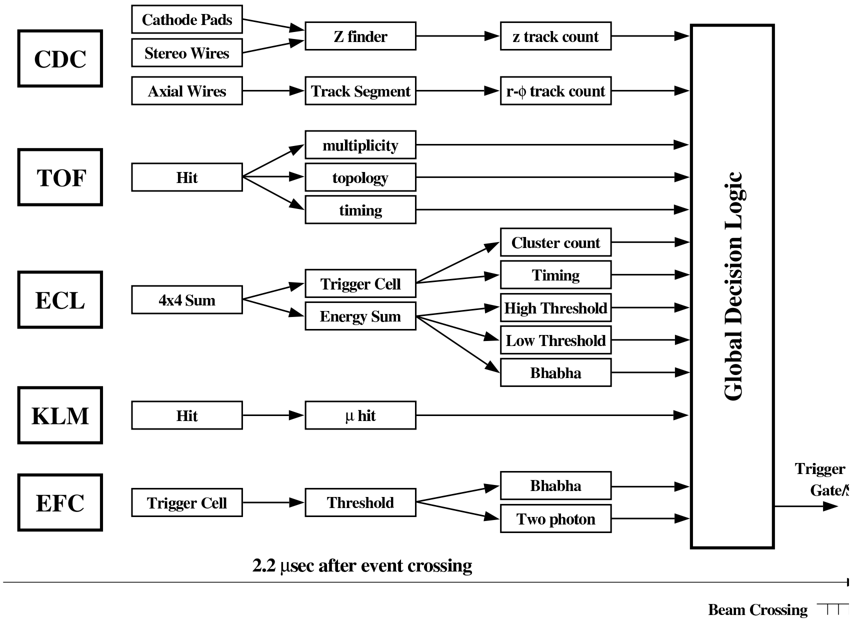

Figure 3.28: *The Level-1 trigger system for the Belle detector.*

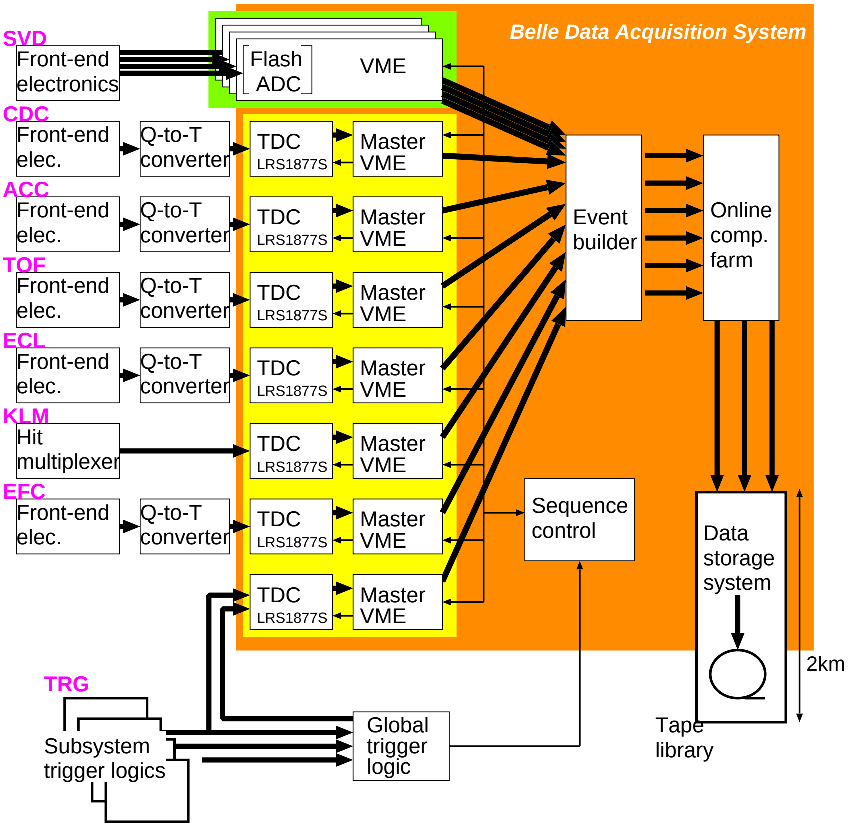

Figure 3.29: *Belle DAQ system overview.*

multi-CPU-servers is developed. Additional to 38 nodes of 4-CPU 500 MHz Ultra SPARC computing server, Belle has a PC farm which consists of about 500 nodes of 500-2.8 GHz 1-4 CPU Pentium III, Xeon and Athlon. In total, CPU power of 1.5 THz is equipped in the PC farm.

All software for the data acquisition and the data analysis except for a few HEP-specific and non-HEP-specific free software packages has been developed by the members of the Belle collaboration. Especially, the event processing framework, called BASF (Belle analysis framework), takes user's reconstruction and analysis codes as modules which are dynamically linked at the run time. The BASF takes care of input/output of event data, parallel processing and HBOOK [39] output.

The MC generation is also an important task of the computing. Using the MC sample, we study the detector response to the physics events and determine the analysis procedure. Especially for the $B^0 \to D^{*+}D^{*-}$ analysis, we need MC events at every stage, such as determination of polarization distributions, flavor tagging parameters and Δt resolution parameters.

The physical process of production and decay is simulated by event generator softwares. We use two event generator softwares: QQ [40] and EvtGen [41, 42]. QQ event generator was originally developed by CLEO and was modified for the use of the Belle analysis [43]. We use QQ to generate a large number of $\Upsilon(4S)$ decays to study background for $B^0 \to D^{*+}D^{*-}$ decays and polarization distributions. EvtGen is developed by CLEO and BaBar. It is designed so that the extension of the generator can be done easily by adding a new decay as a module. The B decay sample generated by EvtGen is used to study other processes including the flavor tagging algorithm, $B^0 \to D^{*+}D^{*-}$ reconstruction efficiencies and CP asymmetries. The detector response is simulated with the Belle full detector simulator called GSIM based on GEANT [44]. GEANT is a library developed at CERN to simulate reactions between particles and matters. The simulator takes the data from the event generator and traces the behavior of each particle in the detector, generating detector response which simulates the real detector output.

Chapter 4

Event Selection

4.1 Event Sample

This analysis is based on the data sample which is collected with the Belle detector from January 2000 to June 2003. In this period, the integrated luminosity of 140 fb^{-1} was accumulated on the $\Upsilon(4S)$ resonance. It corresponds to a sample of $152 \times 10^6 B\bar{B}$ pairs.

4.2 $B\bar{B}$ Event Selection

The collected data sample contains hadronic events including $B\bar{B}$ and other processes such as the Bhabha scattering, the radiative Bhabha, other lepton pair production, two-photon events and beam-gas interactions. Hadronic events consist of $B\bar{B}$ events and continuum events ($e^+e^- \to q\bar{q}$, where $q = u, d, s, c$). Dominant events in other processes are Bhabha and radiative Bhabha events. Although they have equivalent or larger cross sections than $B\bar{B}$ events, such backgrounds can be suppressed by the two selection procedures described in the following.

4.2.1 Non-Hadronic Event Suppression

In this stage, non-hadronic processes (the Bhabha, the radiative Bhabha, other lepton pair production, etc.) are suppressed. At first we define the "good" charged track and the "good" neutral cluster. The "good" track satisfies that its transverse momentum is larger than 0.1 GeV/c and its impact parameter $|dr|$ ($|dz|$) is smaller than 2.0 (4.0) cm, where the impact parameter is defined as the distance of the closest approach to the beam axis. The "good" cluster satisfies that its energy deposit is larger than 0.1 GeV, its polar angle θ is within $-0.7 < \cos\theta < 0.9$ and no charged track is associated to the cluster.

We then apply the following selection criteria:

- At least three "good" charged tracks must exist.
- More than one "good" cluster must be observed in the barrel region of the calorimeter.

- The absolute value of the momentum balance in the z-component calculated in the rest frame of the $\Upsilon(4S)$ resonance should be less than 50% of the energy.
- The event vertex, which is reconstructed from the "good" tracks, must be within 1.5 cm and 3.5 cm from the nominal interaction point (IP) in r and z, respectively.
- The total visible energy in the rest frame of $\Upsilon(4S)$, which is computed as a sum of the energy of "good" tracks assuming the pion mass and that of the "good" clusters, should exceed 18% of the center of mass energy.
- A sum of all cluster energies, after boosted back into the rest frame of the $\Upsilon(4S)$ resonance, should be between 10% and 80% of the cms energy.
- The invariant mass of particles found in hemispheres perpendicular to the event thrust axis is required to be greater than 1.8 GeV/c^2.

These selection criteria retain more than 99% of $B\bar{B}$ events, while keeping the contamination of non-hadronic processes smaller than 5%.

4.2.2 Continuum Event Suppression

In order to suppress hadronic background from the $e^+e^- \to q\overline{q}$ continuum, we define an event shape variable, R_2. The R_2 is the ratio of second to zeroth Fox-Wolfram moment [56] $R_2 \equiv H_2/H_0$. Here the i-th Fox-Wolfram moment, H_i, is defined as

$$H_i = \sum_{j,k} \frac{|\vec{p_j}||\vec{p_k}|}{E_{\text{vis}}^2} P_i(\cos\phi_{jk}), \tag{4.1}$$

where $\vec{p_j}$ ($\vec{p_k}$) is the momentum vector of j-th (k-th) particle, ϕ_{jk} is the angle between $\vec{p_j}$ and $\vec{p_k}$ in the cms, E_{vis} is the total visible energy in the event, and $P_i(x)$ is the Legendre polynomial of the i-th order.

R_2 is sensitive to the event shape: it becomes close to unity for jet-like events and close to 0 for spherical events. Since $B\bar{B}$ events are spherical while continuum events are jet-like, we can reject continuum events by cutting on R_2. We require $R_2 < 0.4$. Figure 4.1 shows R_2 distributions for the $B^0 \to D^{*+}D^{*-}$ signal MC and continuum events. Continuum events are obtained from the off-resonance data which are taken with the cms energy 50 MeV below the $\Upsilon(4S)$ resonance.

4.3 $B^0 \to D^{*+}D^{*-}$ Reconstruction

4.3.1 $D^{*+}D^{*-}$ Decay Chain

We reconstruct $B^0 \to D^{*+}D^{*-}$ decays with $D^{*+}D^{*-} \to (D^0\pi^+, \overline{D}^0\pi^-)$, $D^{*+}D^{*-} \to (D^0\pi^+, D^-\pi^0)$ or $D^{*+}D^{*-} \to (D^+\pi^0, \overline{D}^0\pi^-)$, where we use the following decay modes of D^0 and D^+:

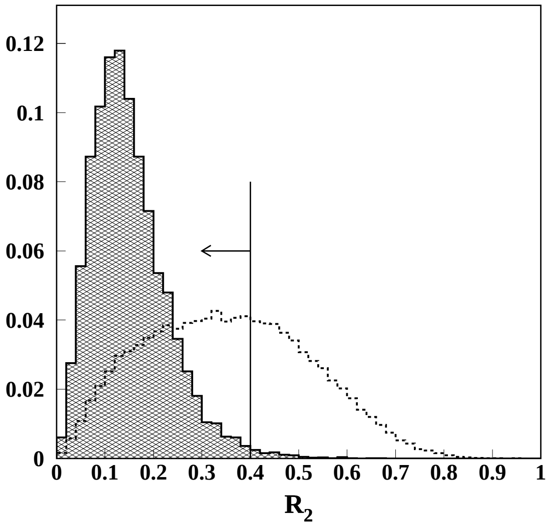

Figure 4.1: *R_2 distribution for $B^0 \to D^{*+}D^{*-}$ signal MC (solid hatched histogram) and for continuum events from off-resonance data (dashed open histogram). Vertical line shows the selection criteria.*

- $D^0 \to K^-\pi^+$, $K^-\pi^+\pi^0$, $K^-\pi^+\pi^-\pi^+$, K^+K^-, $K^0_S\pi^+\pi^-$, $K^0_S\pi^+\pi^-\pi^0$,
- $D^+ \to K^0_S\pi^+$, $K^0_S\pi^+\pi^0$, $K^0_SK^+$, $K^-\pi^+\pi^+$, $K^-K^+\pi^+$.

Here we exclude the case in which two K^0_S mesons are produced in the $B^0 \to D^{*+}D^{*-}$ decay.

First, we select light mesons such as $\pi^\pm$, $K^\pm$, π^0 and K^0_S. Then we reconstruct D and D^* mesons. After that, we reconstruct $B^0 \to D^{*+}D^{*-}$ events.

4.3.2 Reconstruction of Light Mesons

Charged Track Selection

To exclude poorly-reconstructed tracks, we require that the impact parameter $|dr|$ is less than 0.4 (6.0) cm and $|dz|$ is less than 4.0 (5.0) cm for a track without (with) associated SVD hits. Particle identification (PID) between charged kaons and pions is performed using the likelihood of each particle. We use the likelihood ratio, which is based on combined information of ACC, TOF and dE/dx in CDC.

$$\mathcal{P}(K/\pi) \equiv \frac{\mathcal{L}_K}{\mathcal{L}_K + \mathcal{L}_\pi}, \tag{4.2}$$

where $\mathcal{L}_i$ $(i = K, \pi)$ is a likelihood that the particle is i. We require $\mathcal{P}(K/\pi)$ is greater than 0.1 (0.2) to select a kaon track in a 2-body (3- or 4-body) D meson decays. For pion tracks, we require that $\mathcal{P}(K/\pi)$ is less than 0.9.

The selection criteria above are not applied to slow pions (π_s) that come from the $D^{*+} \to D^0\pi_s^+$ decays, and to charged pions that comes from the $K_S^0 \to \pi^+\pi^-$ decays.

Kinematic Fit

We reconstruct a decay vertex and an invariant mass with some kinematic variables of daughter particles, i.e. momentum and position. The vertex with better resolution is obtained by tuning daughter momenta and positions according to measurement errors so that all tracks pass a certain point. The point is regarded as the production vertex of daughter tracks. We call it the vertex-constrained fit. Similarly, we can improve the invariant mass resolution. We call it the mass-constrained fit.

Reconstruction of π^0

Neutral π meson candidates are reconstructed from pairs of two photons. The photon candidate is selected from ECL clusters which are not associated with any charged track and whose energy is more than 30 MeV. The invariant mass of the π^0 candidate, M_{π^0}, is a powerful index to select correctly reconstructed pions and to reject poorly reconstructed events and backgrounds:

$$M_{\pi^0}^2 = |\sum_i^2 E_{\gamma_i}|^2 - |\sum_i^2 \vec{P}_{\gamma_i}|^2, \tag{4.3}$$

where E_{γ_i} and $\vec{P}_{\gamma_i}$ are the energy and momentum of the i-th photon, respectively. A mass-constrained fit is performed to improve the π^0 momentum resolution. Reduced χ^2 of the fit is required to be less than 25. If the π^0 candidate is a daughter of a D meson, the candidate whose momentum is below 200 MeV/c is rejected, since signal to noise ratio is low. We require M_{π^0} to be within 119 and 146 MeV/c^2. The selected region corresponds to within the three standard deviations from the nominal π^0 mass. The region is asymmetric due to energy leakage in ECL. Figure 4.2 shows the invariant mass distribution of π^0 candidates.

Reconstruction of K_S^0

K_S^0 candidates are reconstructed from two oppositely-charged pions. A vertex-constrained fit helps improve the K_S^0 momentum resolution and reject combinatorial backgrounds. We define several variables to distinguish K_S^0 events from backgrounds: (i) $\Delta\phi$, which is the angle in the $r-\phi$ plane between the direction defined by the IP and the $\pi^+\pi^-$ vertex displacement, and the direction of $\pi^+\pi^-$ momentum; (ii) minimum impact parameter, dr_{min}, which is the closest distances of both pion tracks to the IP in the r-ϕ plane; (iii) d_z, which is the distance in z direction between two pion tracks at the cross point in the r-ϕ plane; and (iv) flight length of K_S^0 meson in the r-ϕ plane. Since average K_S^0 flight length is 5 cm in the detector, the flight length is correlated with the number of tracks associated with SVD hits. We find candidate K_S^0 mesons without CDC tracks associated with SVD hits, with small background contamination. If both pions have associated SVD hits, candidate K_S^0 mesons are also clean, since good momentum resolution of the pions results in a good invariant mass resolution. A K_S^0 candidate with only one track with SVD associated hits has worse resolution and larger combinatorial backgrounds.

Taking these into account, we select K_S^0 candidates with the following criteria:

1. If none of the two pions has associated SVD hits, $\Delta\phi$ is required to be less than 0.1 rad.
2. If one of the two pions has associated SVD hits, we require that $\Delta\phi$ is less than 0.4 rad, dr_{min} is more than 50 μm to suppress tracks from the IP, flight length is shorter than 9 cm and d_z is smaller than 40 cm.
3. In case both pions have associated SVD hits, we require that $\Delta\phi$ is less than 0.3 rad, dr_{min} is more than 30 μm and d_z is smaller than 1 cm.

Finally, the invariant mass is calculated for K_S^0 candidates, which pass the selection criteria described above, as

$$M^2_{K_S^0} = \left(\sqrt{M_\pi^2 + |\vec{P}_{\pi^+}|^2} + \sqrt{M_\pi^2 + |\vec{P}_{\pi^-}|^2}\right)^2 - |\vec{P}_{\pi^+} + \vec{P}_{\pi^-}|^2. \tag{4.4}$$

We require the invariant mass to be within 482 and 514 MeV/c^2, which corresponds to three standard deviations from the nominal K_S^0 mass. Figure 4.3 shows the invariant mass distribution of K_S^0 candidates.

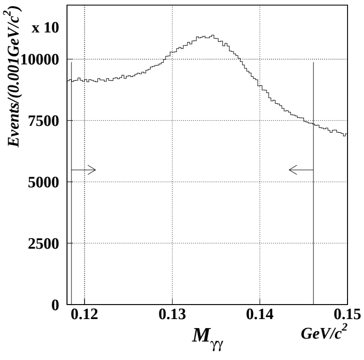

Figure 4.2: $\pi^0 \to \gamma\gamma$ *invariant mass distributions in data.*

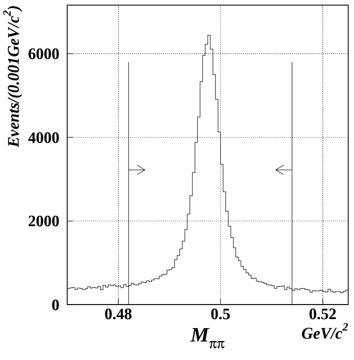

Figure 4.3: $K_S^0 \to \pi^+\pi^-$ *invariant mass distribution in data.*

4.3.3 Reconstruction of D

D meson candidates are reconstructed from candidate light mesons described above. The invariant mass of a D meson is calculated as

$$M^2_{D\to\sum_i^n X_i} = \left(\sum_i^n \sqrt{M_i^2 + |\vec{P}_i|^2}\right)^2 - |\sum_i^n \vec{P}_i|^2, \tag{4.5}$$

where D decays into an n-body state and X_i is an i-th decay product. We require that $M_{D\to\sum_i^n X_i}$ should be within 6 (3)σ from the nominal D mass for 2-body (3- or 4-body) modes where σ is each invariant mass resolution which is obtained from the signal MC. After the selection, a mass- and vertex-constrained fit is applied. Figure 4.4 shows the invariant mass distribution of each D^0 or D^+ decay mode.

4.3.4 Reconstruction of D^{*+}

D^{*+} meson candidates are reconstructed from $D^{*+}\to D^0\pi_s^+$ or $D^+\pi_s^0$, where π_s^+ (π_s^0) is a slow charged (neutral) pion whose momentum is below 300 MeV/c; the low momentum is due to a small mass difference between D^{*+} and D^0 (D^+) mesons. No PID is required for the charged π_s to keep a high reconstruction efficiency. Momentum resolution of π_s^+ is improved by refitting π_s^+ with a constraint with the IP while taking the finite B flight length into account. Since the mass difference resolution is better than the resolution of D^* mass, we select D^* mesons using this mass difference $\Delta M_{D^*,D}\equiv M_{D\pi_s}-M_D$. We require that $\Delta M_{D^*,D}$ is within 3.00 (2.25) MeV/c^2 for π_s^+ (π_s^0). After the B^0 candidate is reconstructed, momentum resolution of D^{*+} can be improved by refitting π_s^+ to the B^0 vertex, since the decay point of the D^* meson is almost the same as the decay point of B^0. Figure 4.5 shows mass distributions of D^{*+} decay candidates.

4.3.5 Reconstruction of B^0

A candidate of $B^0\to D^{*+}D^{*-}$ decay is a combination of two oppositely-charged $D^{*\pm}$ mesons. A vertex-constrained fit with IP constraint is performed to improve the momentum resolution. If multiple B candidates are reconstructed, we select only one B candidate based on the following variable:

$$\chi^2_{\text{mass}}\equiv\sum_i^2\left(\frac{\Delta M_{D_i^*,D_i}-\Delta M_{D^*,D}(PDG)}{\sigma_{\Delta M_{D^*,D}}}\right)^2+\sum_i^2\left(\frac{M_{D_i}-M_D(PDG)}{\sigma_{M_D}}\right)^2, \tag{4.6}$$

where $\Delta M_{D_i^*,D_i}$ (M_{D_i}) is the mass difference (mass) of i-th D^* (D) meson ($i=1,2$), $\Delta M_{D^*,D}(PDG)\equiv M_{D^*}(PDG)-M_D(PDG)$, where $M_{D^*}(PDG)$ and $M_D(PDG)$ are nominal masses of D^* and D [13], $\sigma_{\Delta M_{D^*,D}}(\sigma_{M_D})$ is the error of the mass difference (mass). The candidate with the smallest χ^2_{mass} is chosen. We then perform a vertex-constrained fit with the IP constraint. The vertex reconstruction is explained in detail in Sec. 6.1.

We introduce two kinematic variables, the energy difference, ΔE, and the beam-energy constrained mass, M_{bc},:

$$\begin{aligned}\Delta E &\equiv E_B^{\text{cms}}-E_{\text{beam}}^{\text{cms}},\\ M_{\text{bc}} &\equiv \sqrt{(E_{\text{beam}}^{\text{cms}})^2-(p_B^{\text{cms}})^2},\end{aligned} \tag{4.7}$$

where $E_{\text{beam}}^{\text{cms}}$ is the beam energy in the center of mass system (cms) and E_B^{cms} (p_B^{cms}) is the energy (momentum) of the B^0 candidate in the cms. Since resolution of the beam energy is much better than that of the B^0 candidate energy, M_{bc} is a good variable to

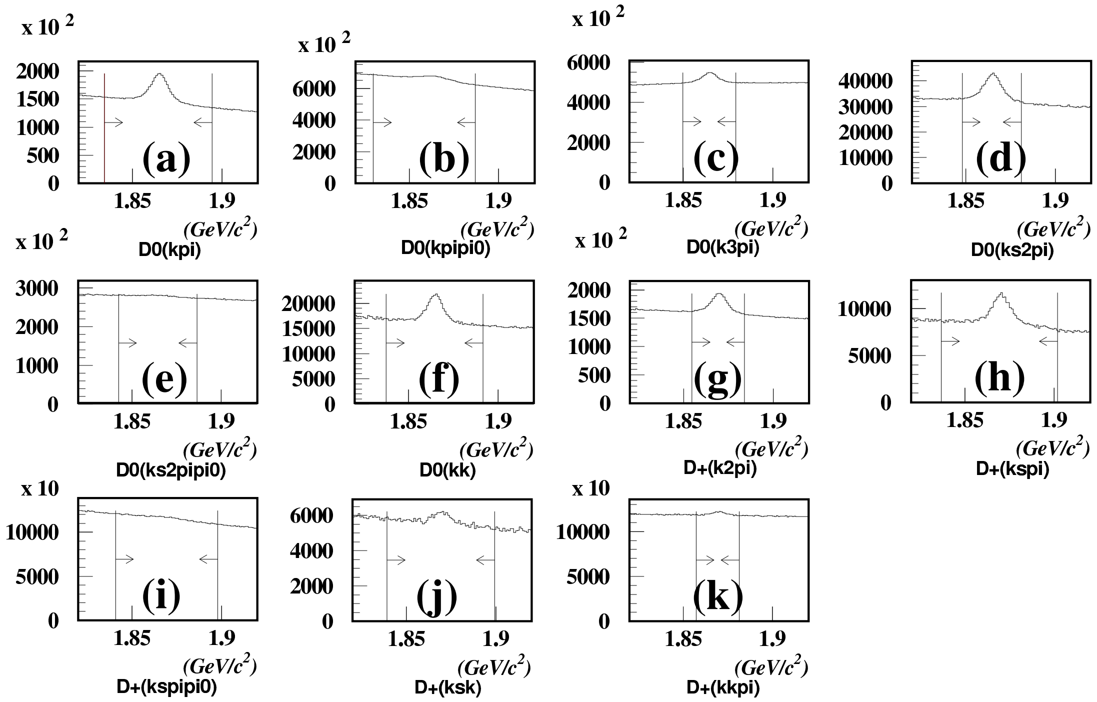

Figure 4.4: *D mass distributions in data. Each plot from (a) to (k) shows D decay-modes: $D^0 \to K^-\pi^+$, $D^0 \to K^-\pi^+\pi^0$, $D^0 \to K^-\pi^+\pi^-\pi^+$, $D^0 \to K^0_S\pi^+\pi^-$, $D^0 \to K^0_S\pi^+\pi^-\pi^0$, $\overline{D}^0 \to K^-K^+$, $D^+ \to K^-K^+\pi^+$, $D^+ \to K^0_S\pi^+$, $D^+ \to K^0_S\pi^+\pi^0$, $D^+ \to K^0_S K^+$ and $D^+ \to K^-K^+\pi^+$, respectively.*

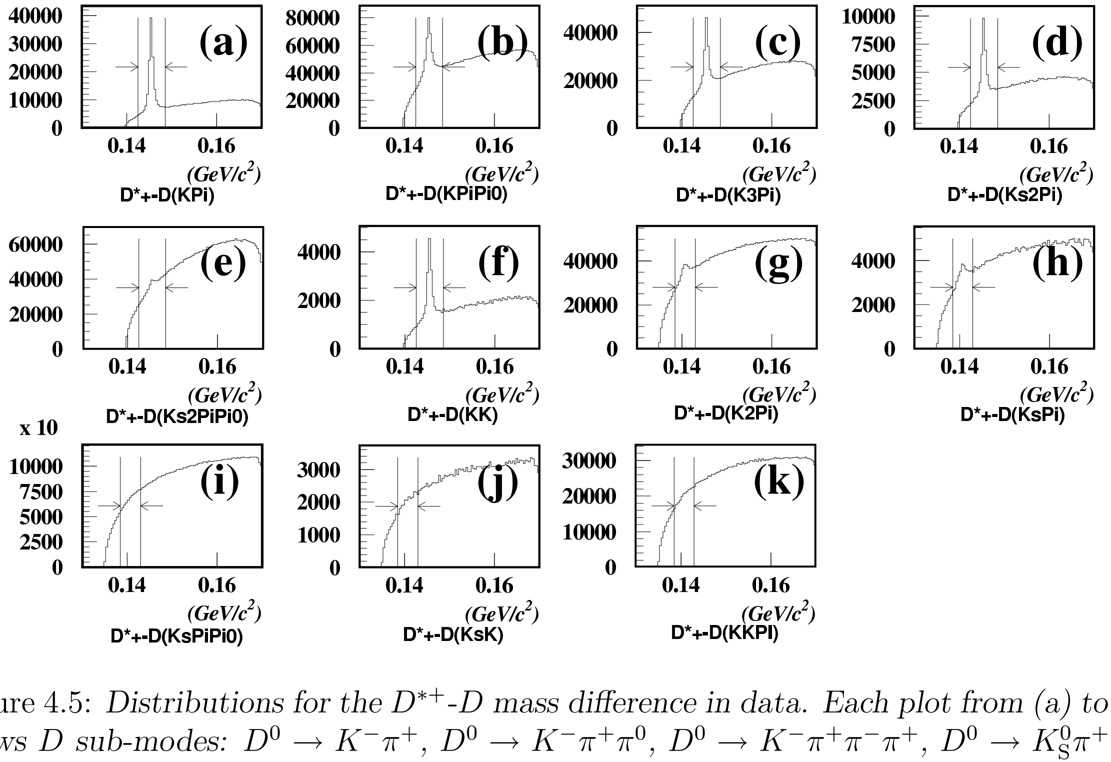

Figure 4.5: *Distributions for the D^{*+}-D mass difference in data. Each plot from (a) to (k) shows D sub-modes: $D^0 \to K^-\pi^+$, $D^0 \to K^-\pi^+\pi^0$, $D^0 \to K^-\pi^+\pi^-\pi^+$, $D^0 \to K^0_S\pi^+\pi^-$, $D^0 \to K^0_S\pi^+\pi^-\pi^0$, $\overline{D}^0 \to K^-K^+$, $D^+ \to K^-K^+\pi^+$, $D^+ \to K^0_S\pi^+$, $D^+ \to K^0_S\pi^+\pi^0$, $D^+ \to K^0_S K^+$ and $D^+ \to K^-K^+\pi^+$, respectively.*

separate B^0 signal from backgrounds. Because only a B meson pair is created by the beam collision, ΔE equals 0 for correctly reconstructed signal.

We define the "signal box", which is the rectangular region in the ΔE-$M_{\rm bc}$ plane; we require that $|M_{\rm bc} - M_B(PDG)|$ is within $3\sigma_{M_{\rm bc}}$ and $|\Delta E|$ is smaller than 40 MeV. The $M_{\rm bc}$ resolution, $\sigma_{M_{\rm bc}}$, is 3.5 (3.3) MeV/c^2 for the D^0-$\overline{D}^0$ (D^+-$\overline{D}^0$) sub-decay mode.

To suppress poorly-reconstructed events, we require that reduced χ^2 of the B vertex constrained fit, χ^2_{vtx}, is smaller than 40, and χ^2_{mass} is smaller than 5. Remaining candidates in the signal box are used for the polarization measurement and time-dependent CP asymmetry measurement. The $M_{\rm bc}$ (ΔE) distribution for the reconstructed $B^0 \to D^{*+}D^{*-}$ candidates within the ΔE ($M_{\rm bc}$) signal region is shown in Fig. 4.6. The two-dimensional distribution in the ΔE-$M_{\rm bc}$ plane is also shown in Fig. 4.6.

4.3.6 Background

Background studies are performed by using a large sample of MC events for generic MC ($B\bar{B}$ and $q\bar{q}$ continuum), which corresponds to an integrated luminosity of 340 fb^{-1}. Figures 4.7 show the background distributions in generic MC for $M_{\rm bc}$ and ΔE projections. We find no peaking background in the signal box. Though $B^0 \to D^*D$ decays cause a peak in the ΔE projection, it stays sufficiently apart from the signal box. Therefore it is not a serious problem in our analysis. The numbers of background components and their fractions are summarized in Table 4.1. The fractions of $B^0\overline{B}^0$, B^+B^- and $c\bar{c}$ components are almost equivalent.

Origin	ΔE-$M_{\rm bc}$	$R_2 < 0.4$	signal box(fraction %)
$B^0\overline{B}^0$	2653	2615	58 (33)
B^+B^-	2143	2130	50 (28)
$B\overline{B}$ all	4796	4745	108
$c\bar{c}$	4120	3730	67 (38)
$u\bar{u}$,$d\bar{d}$,$s\bar{s}$	305	252	3 (2)
$q\bar{q}$ all	4425	3982	70
BG all	9221	8727	178

Table 4.1: *Background in generic MC that corresponds to the integrated luminosity of* 340 fb^{-1}. *The number of background events after each cut is shown.*

4.3.7 Yield Extraction

Events in the signal box contain both signal events and backgrounds. Extraction of the signal yield is important, since it is needed to calculate the event-by-event signal fraction that is used to measure polarization and CP asymmetries.

The yield extraction is performed using the maximum likelihood method, which is explained in Appendix A. We perform a two-dimensional simultaneous fit on the ΔE-$M_{\rm bc}$ plane. The signal shape function $F_{\rm sig}$ is described by a single Gaussian for $M_{\rm bc}$

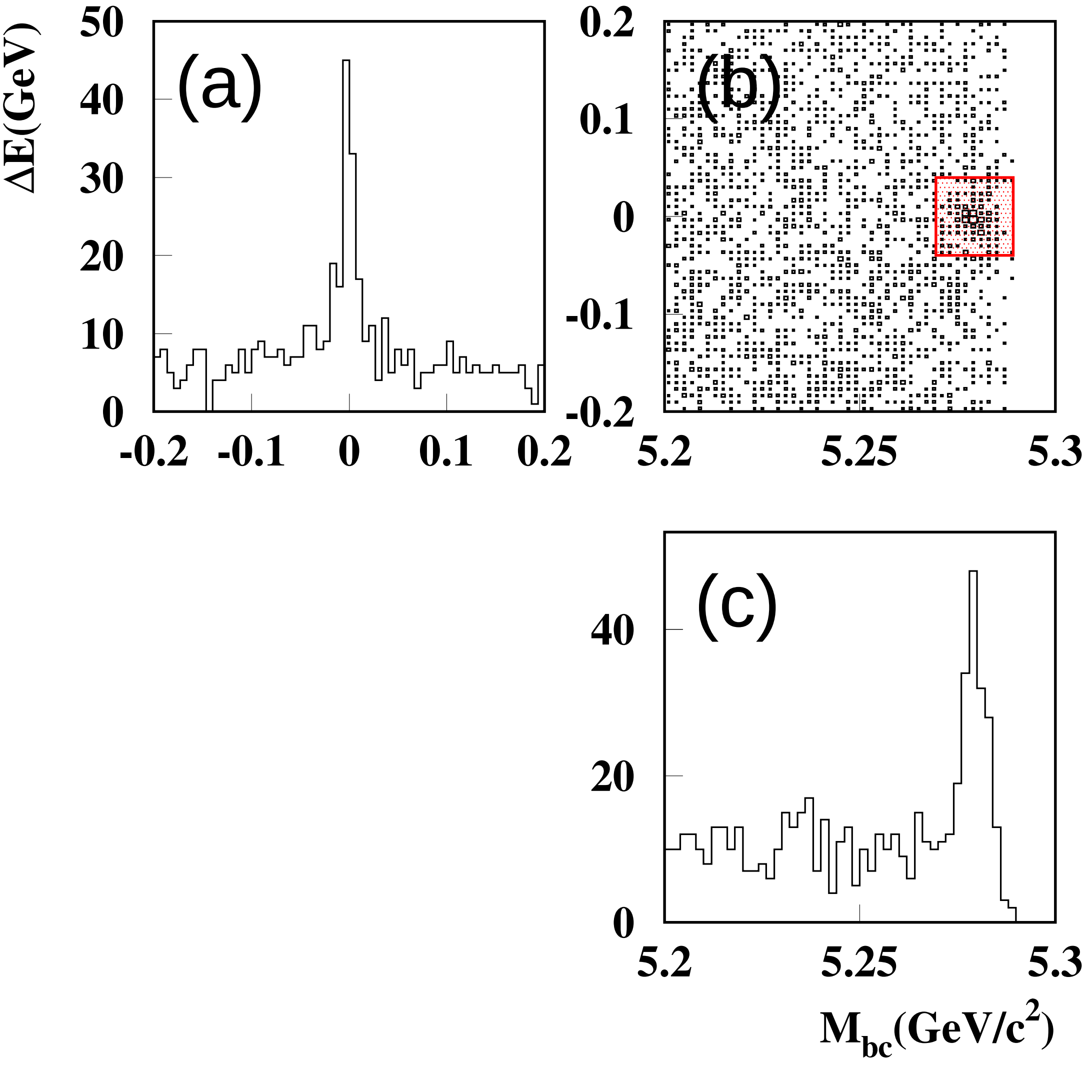

Figure 4.6: *(a) ΔE distribution for $B^0 \to D^{*+}D^{*-}$ candidates within the $M_{\rm bc}$ signal region; (b) Two-dimensional distribution in the ΔE-$M_{\rm bc}$ plane. The hatched area is the signal box; (c) $M_{\rm bc}$ distribution for $B^0 \to D^{*+}D^{*-}$ candidates within the ΔE signal region.*

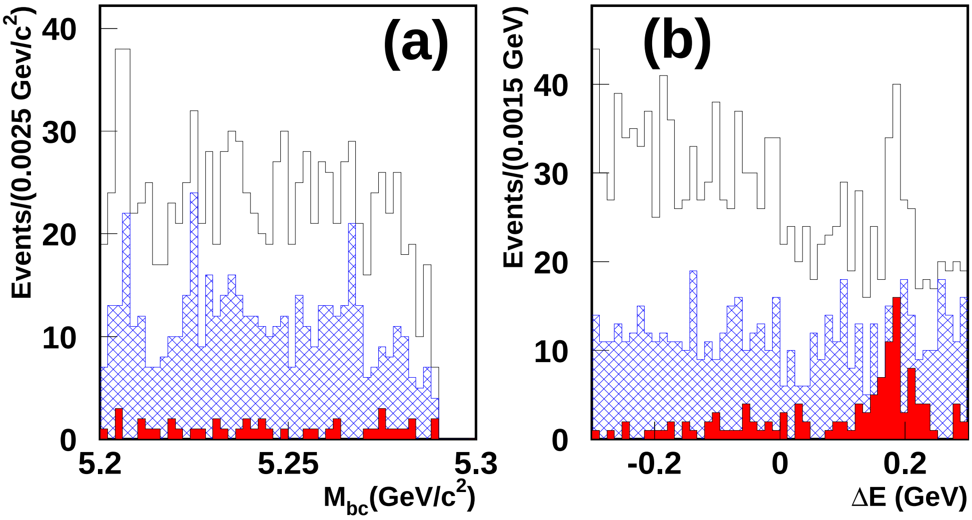

Figure 4.7: *Background distribution in generic MC ($B\bar{B}$ + $q\bar{q}$ continuum); (a) $M_{\rm bc}$ distribution within the ΔE signal region; (b) ΔE distribution within the $M_{\rm bc}$ signal region. Open histogram is total contribution from generic MC, the hatched histogram is continuum MC, and filled histogram is $B \to D^*D$ MC. Note that the assumed branching fraction for each $B \to D^*D$ is almost 3 times larger than the average branching fraction that was measured by $B^0 \to D^{*+}D^-$ and $B^0 \to D^{*-}D^+$ [13].*

and a sum of two Gaussian functions for ΔE, and the background shape function $F_{\rm bg}$ is described by the ARGUS background function [45] for $M_{\rm bc}$ and a linear function for ΔE:

$$\begin{aligned} F_{\rm sig}(\Delta E, M_{\rm bc}) &\equiv N_{\rm sig}[f_{\rm main}G(\Delta E;\mu_{\rm main},\sigma_{\rm main}) + (1-f_{\rm main})G(\Delta E;\mu_{\rm tail},\sigma_{\rm tail})], \\ &\times\ G(M_{\rm bc};\mu,\sigma), \qquad (4.8) \\ F_{\rm bg}(\Delta E, M_{\rm bc}) &\equiv N_{\rm bg}(1+c\Delta E), \\ &\times\ M_{\rm bc}\sqrt{1-\left(\frac{M_{\rm bc}}{E^{\rm cms}_{\rm beam}}\right)^2}\exp\left\{a\left[1-\left(\frac{M_{\rm bc}}{E^{\rm cms}_{\rm beam}}\right)^2\right]\right\}, \qquad (4.9) \end{aligned}$$

where $G(x;\mu,\sigma)$ is a Gaussian function

$$G(x;\mu,\sigma) \equiv \frac{1}{\sqrt{2\pi}\sigma}\exp\left[-\frac{(x-\mu)^2}{2\sigma^2}\right], \tag{4.10}$$

$\{N_{\rm sig}, N_{\rm bg}\}$ are normalization parameters, $\{\mu, \sigma, f_{\rm main}, \mu_{\rm main}, \sigma_{\rm main}, \mu_{\rm tail},\ \sigma_{\rm tail}\}$ are signal shape parameters, and $\{c, a\}$ are background shape parameters. Using these functions, the likelihood function is defined as

$$\mathcal{L}(\mathrm{f}^{\rm ave}_{\rm sig}) \equiv \prod f_{\rm sig}(\Delta E, M_{\rm bc}), \tag{4.11}$$

where signal fraction $f_{\rm sig}(\Delta E, M_{\rm bc})$ is described as a function of ΔE and $M_{\rm bc}$:

$$f_{\rm sig}(\Delta E, M_{\rm bc}) \equiv \frac{\mathrm{f}^{\rm ave}_{\rm sig}F_{\rm sig}(\Delta E, M_{\rm bc})}{\mathrm{f}^{\rm ave}_{\rm sig}F_{\rm sig}(\Delta E, M_{\rm bc}) + (1-\mathrm{f}^{\rm ave}_{\rm sig})F_{\rm bg}(\Delta E, M_{\rm bc})}, \tag{4.12}$$

where $f_{\rm sig}^{\rm ave}$ is the average signal fraction.

Signal shape parameters are determined with signal MC. Figure 4.8 shows signal MC distributions and fit results. These parameters are summarized in Table 4.2. Background shape parameters are obtained simultaneously in the fit. We divide the data sample to $D^{*+}D^{*-} \to (D^0\pi^+, \bar{D}^0\pi^-)$ and $D^{*+}D^{*-} \to (D^+\pi^0, \bar{D}^0\pi^-)$ sub-samples, to take different signal and background distributions into account. We call them "D^0-$\bar{D}^0$ combination" and "D^+-$\bar{D}^0$ combination", respectively. Each sub-sample has its own signal and background shape decided by its signal MC and data, respectively. Background parameters determined from data are summarized in Table 4.3.

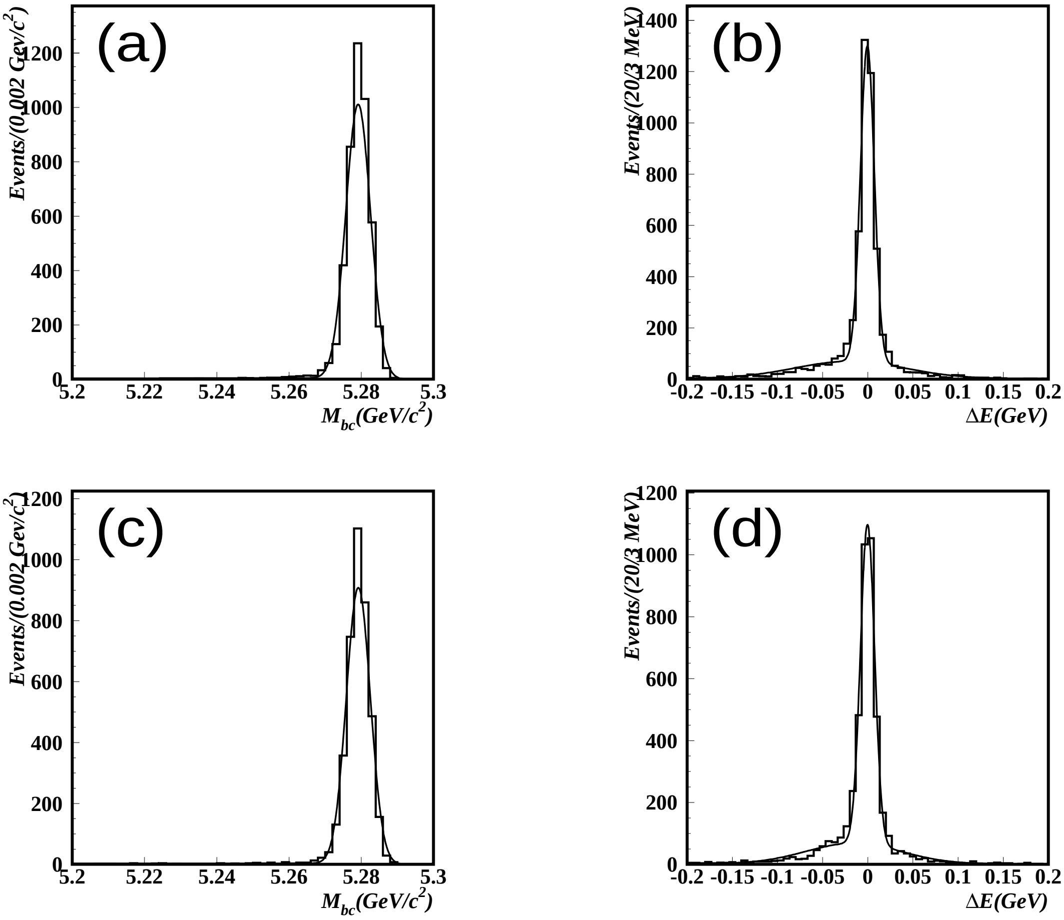

Figure 4.8: *Signal MC distributions are fit results for (a)* $M_{\rm bc}$ *projections for* D^0-$\overline{D}^0$ *combination; (b)* ΔE *projections for* D^0-$\overline{D}^0$ *combination; (c)* $M_{\rm bc}$ *projections for* D^+-$\overline{D}^0$ *combination; (d)* ΔE *projections for* D^+-$\overline{D}^0$ *combination.*

We find 2357 (1215, 1142) events in $5.2 < M_{\rm bc} < 5.3$ GeV/c^2 and $|\Delta E| < 200$ MeV region. Here the numbers in the parenthesis are for D^0-$\bar{D}^0$ and D^+-$\bar{D}^0$ combination, respectively. There are 194 (132, 62) events in the signal box. The fit mentioned above yields $129.5^{+12.9}_{-12.0}$ signal events. Estimated number of background events ($64.5^{+12.0}_{-12.9}$) is consistent with the expected number (~ 73) from generic MC study (Table 4.1).

Figures 4.9 show the fit results. Table 4.4 summarizes the signal yield for each decay mode.

Parameter		D^0-$\bar{D}^0$	D^+-$\bar{D}^0$
$M_{\rm bc}$	μ	5.27917 ± 0.00002	5.27919 ± 0.00002
	σ	0.00348 ± 0.00001	0.00332 ± 0.00001
ΔE	$\mu_{\rm main}$	-0.00041 ± 0.00005	-0.00031 ± 0.00005
	$\mu_{\rm tail}$	-0.0193 ± 0.0006	-0.0158 ± 0.0005
	$\sigma_{\rm main}$	0.00781 ± 0.00005	0.00785 ± 0.00006
	$\sigma_{\rm tail}$	0.0625 ± 0.0005	0.0525 ± 0.0006
	$f_{\rm main}$	0.690 ± 0.003	0.699 ± 0.003

Table 4.2: *Signal shape parameters*

Parameter	D^0-$\bar{D}^0$	D^+-$\bar{D}^0$
Argus a	-31.8 ± 3.7	-28.3 ± 3.5
ΔE slope c	-0.55 ± 0.27	-1.46 ± 0.26

Table 4.3: *Background shape parameters*

Numbers	D^0-$\bar{D}^0$	D^+-$\bar{D}^0$	Combined
ΔE-$M_{\rm bc}$ Plane.	1215	1142	2357
Signal Box	132	62	194
Yield	$102.1^{+10.8}_{-10.3}$	$27.4^{+7.0}_{-6.3}$	$129.5^{+12.9}_{-12.0}$
Purity	(77.3%)	(44.2%)	(66.8%)

Table 4.4: *Event candidates.*

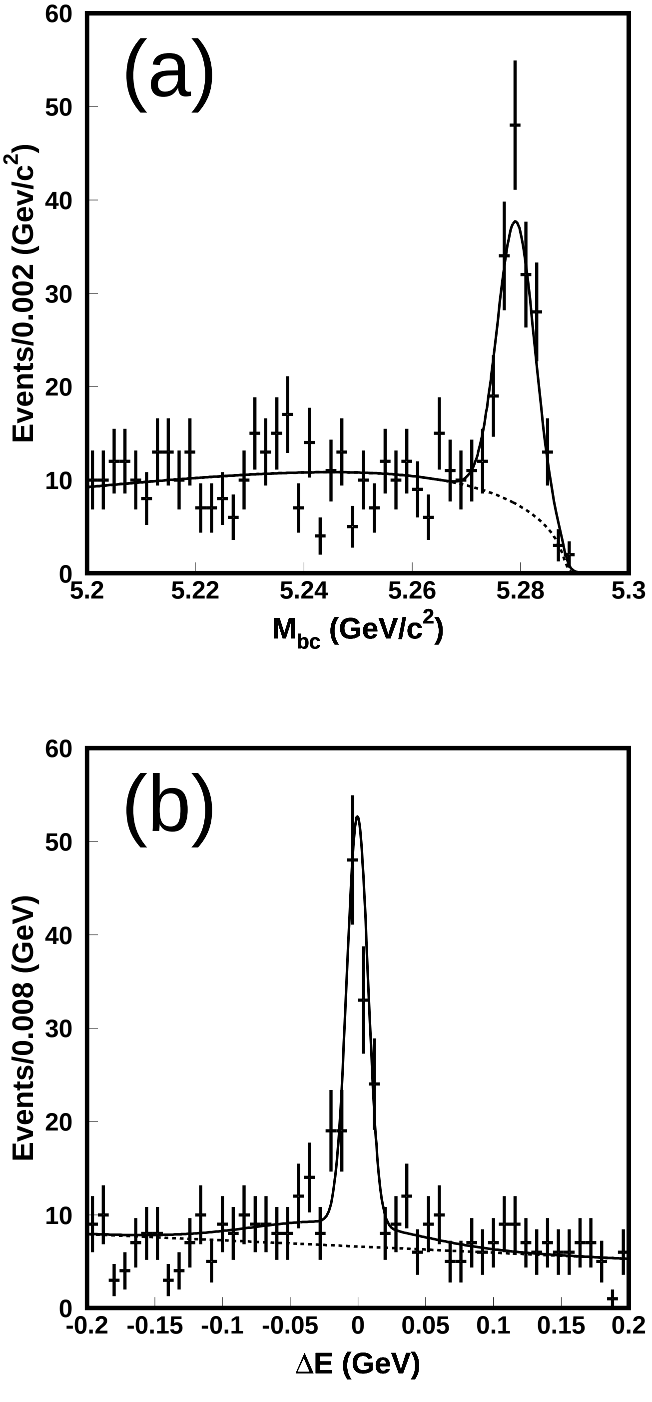

Figure 4.9: *(a) $M_{\rm bc}$ distribution for $B^0 \to D^{*+}D^{*-}$ candidates within the ΔE signal region; (b) ΔE distribution for $B^0 \to D^{*+}D^{*-}$ candidates within the $M_{\rm bc}$ signal region. Solid curves show the fit to signal plus background distributions, and dashed curves show the background.*

Chapter 5

Polarization Measurement

5.1 Probability Density Function for Polarization Measurement

5.1.1 Likelihood for Polarization Measurement

The polarization measurement is performed using the maximum likelihood method, which is explained in Appendix A. The likelihood function is defined as

$$\mathcal{L}(R_\perp, R_0) \equiv \prod \{ f_{\rm sig}(\Delta E, M_{\rm bc}) \mathcal{H}_{\rm sig}(\cos\theta_{tr}, \cos\theta_1) + [1 - f_{\rm sig}(\Delta E, M_{\rm bc})] \mathcal{H}_{\rm bg}(\cos\theta_{tr}, \cos\theta_1) \}, \tag{5.1}$$

where $R_\perp$ and R_0 are polarization parameters defined in Eq. (1.66), the signal fraction $f_{\rm sig}(\Delta E, M_{\rm bc})$ is defined in Eq. (4.12), $\mathcal{H}_{\rm sig}(\cos\theta_{tr}, \cos\theta_1)$ and $\mathcal{H}_{\rm bg}(\cos\theta_{tr}, \cos\theta_1)$ are signal and background probability density functions (PDF's) for the polarization measurement, which are described in the following sections.

5.1.2 Signal PDF

Reconstructed angular distributions are different from generated distributions as shown in Figs. 5.1 and 5.2. The clear discrepancies between generated and reconstructed distributions are mainly due to reconstruction efficiencies and resolutions of slow pions π_s that come from the $D^* \to D\pi_s$ decay. We find that these reconstruction efficiencies and resolutions are functions of momenta of two slow pions, and moreover, correlations between two momenta cannot be ignored. Since it is difficult to prepare functions that well describe such correlations, we use reconstructed MC angular distributions (histograms) for the signal PDF. We call such distributions the MC-PDF's. We generate MC-PDF's with the following procedure:

- Generate MC events with three polarization types (A_0, $A_\parallel$, $A_\perp$) and with two D^{*+} decays (to $D^0\pi_s^+$ or $D^+\pi_s^0$) separately; i.e. we generate six kinds of MC samples.

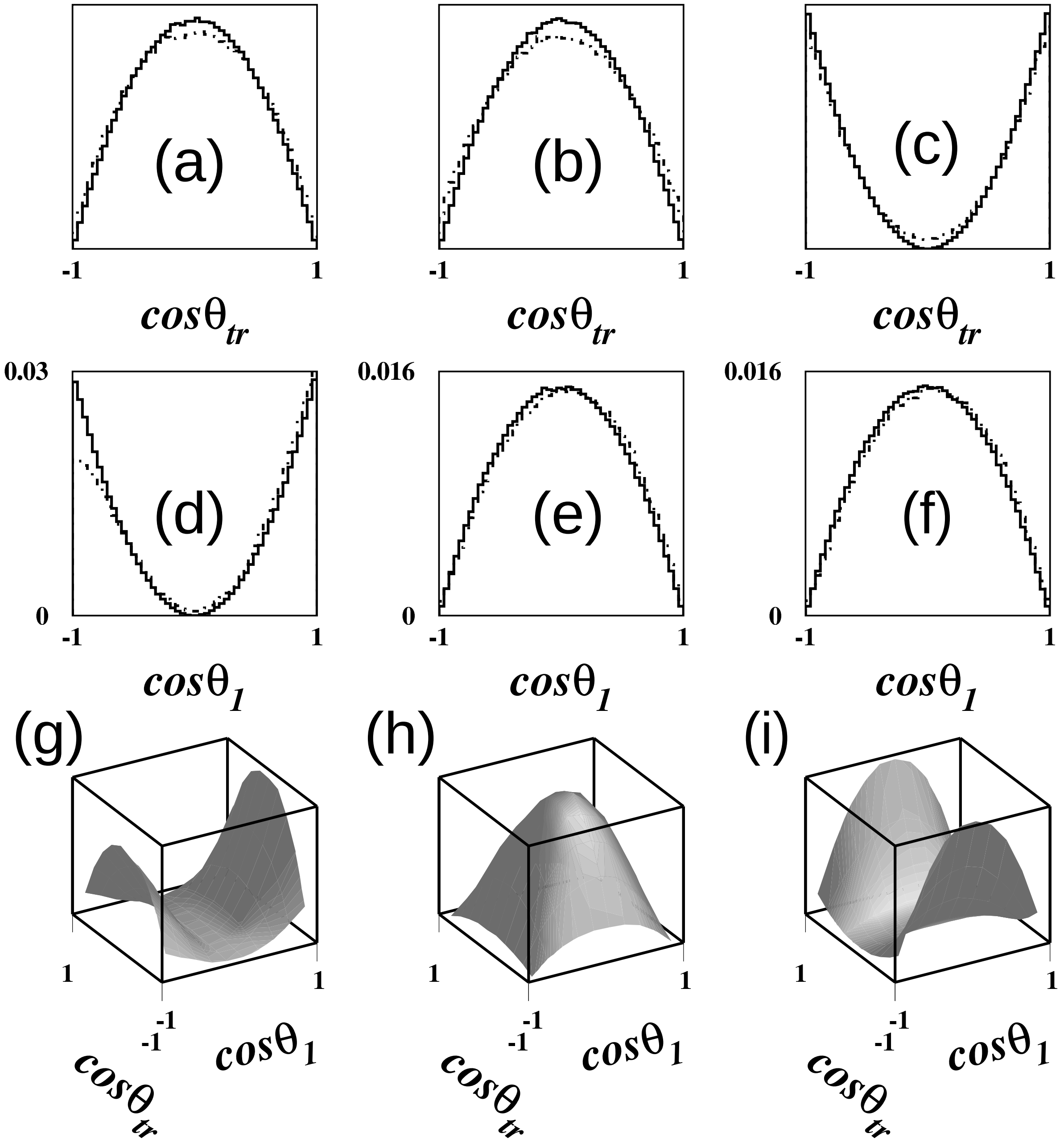

Figure 5.1: *Angular distributions for the decay* $B^0 \to D^{*+}D^{*-}$, $D^{*+} \to D^0\pi_s^+$, $D^{*-} \to \overline{D}^0\pi_s^-$ *(*D^0*-*$\overline{D}^0$ *combination): (a)* $\cos\theta_{tr}$ *distribution for* A_0*; (b)* $\cos\theta_{tr}$ *distribution for* $A_\parallel$*; (c)* $\cos\theta_{tr}$ *distribution for* $A_\perp$*; (d)* $\cos\theta_1$ *distribution for* A_0*; (e)* $\cos\theta_1$ *distribution for* $A_\parallel$*; (f)* $\cos\theta_1$ *distribution for* $A_\perp$*; (g) Two-dimensional* $\cos\theta_{tr}$ *vs.* $\cos\theta_1$ *distribution for* A_0*; (h) Two-dimensional* $\cos\theta_{tr}$ *vs.* $\cos\theta_1$ *distribution for* $A_\parallel$*; (i) Two-dimensional* $\cos\theta_{tr}$ *vs.* $\cos\theta_1$ *distribution for* $A_\perp$*. Solid (dotted) lines show distribution for generated (reconstructed) events.*

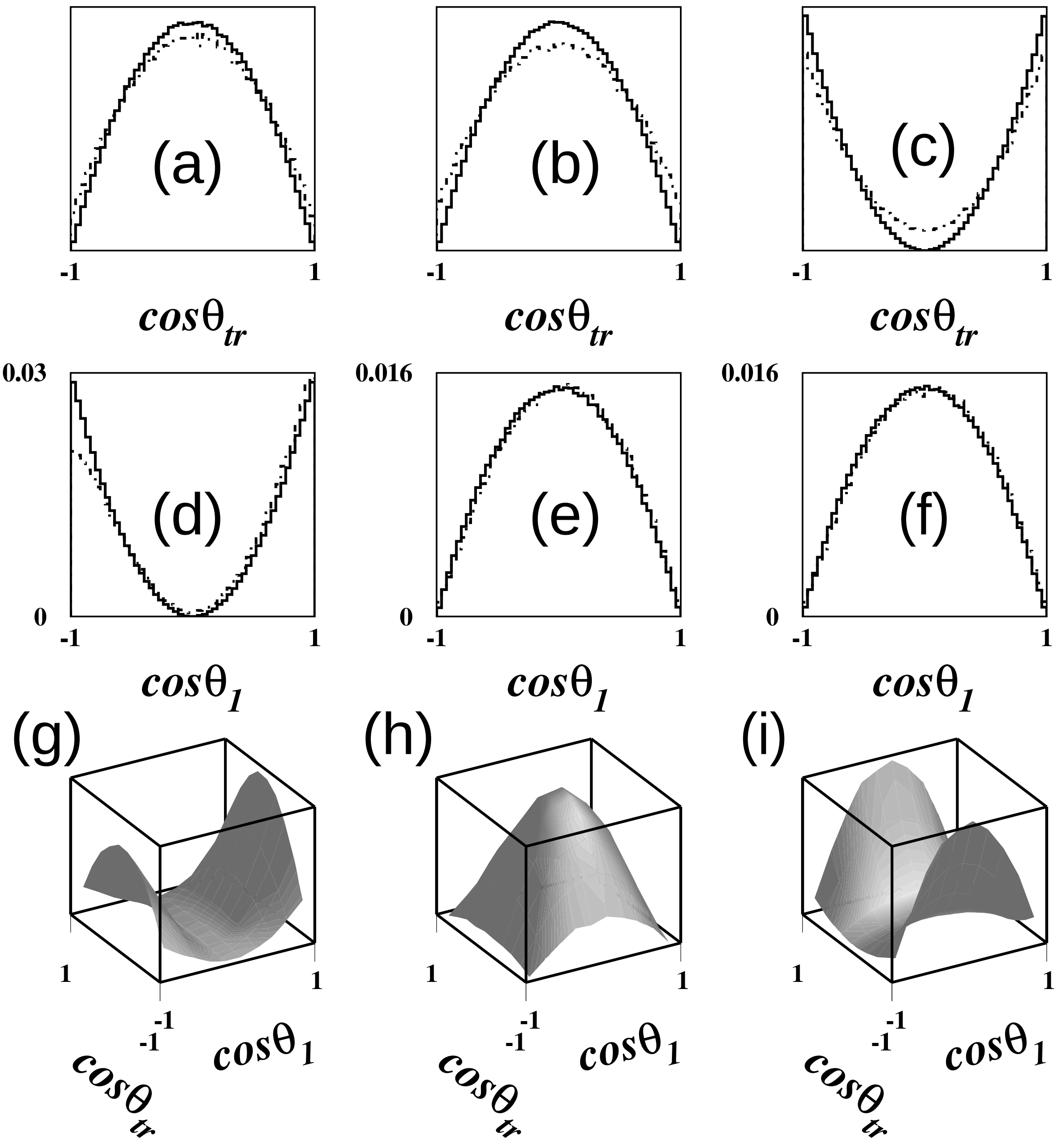

Figure 5.2: *Angular distributions for the decay* $B^0 \to D^{*+}D^{*-}$, $D^{*+} \to D^+\pi^0_s$, $D^{*-} \to \overline{D}^0\pi^-_s$ *(*D^+*-*$\overline{D}^0$ *combination): (a)* $\cos\theta_{tr}$ *distribution for* A_0*; (b)* $\cos\theta_{tr}$ *distribution for* $A_\parallel$*; (c)* $\cos\theta_{tr}$ *distribution for* $A_\perp$*; (d)* $\cos\theta_1$ *distribution for* A_0*; (e)* $\cos\theta_1$ *distribution for* $A_\parallel$*; (f)* $\cos\theta_1$ *distribution for* $A_\perp$*; (g) Two-dimensional* $\cos\theta_{tr}$ *vs.* $\cos\theta_1$ *distribution for* A_0*; (h) Two-dimensional* $\cos\theta_{tr}$ *vs.* $\cos\theta_1$ *distribution for* $A_\parallel$*; (i) Two-dimensional* $\cos\theta_{tr}$ *vs.* $\cos\theta_1$ *distribution for* $A_\perp$*. Solid (dotted) lines show distribution for generated (reconstructed) events.*

- Reconstruct MC events for each of the six sets with the selection criteria we apply to data.
- Make a two-dimensional histogram for $\cos\theta_{tr}$ and $\cos\theta_1$ (50×50 bins) for the selected candidates of each MC set.
- Normalize the histogram with the number of entries.

The resulting six normalized histograms are used as the MC-PDF's. We generated 4 million events for each of six sets. We only use $D^0 \to K^-\pi^+$ and $D^+ \to K^-\pi^+\pi^+$ as subsequent D decay modes. Possible mode dependence is examined by measuring the polarization in the generic signal MC that includes all the D decays modes. No mode dependent polarization bias is seen for both D^0-$\bar{D}^0$ and D^+-$\bar{D}^0$ combinations.

5.1.3 Effective Polarization

Measured polarizations are renormalized, because the reconstruction efficiency of each polarization is different. Such "effective polarizations" are defined by:

$$R_i^{'} = \frac{\epsilon_i R_i}{\epsilon_0 R_0 + \epsilon_{\|} R_{\|} + \epsilon_{\perp} R_{\perp}}, \tag{5.2}$$

where $i = 0, \|$ and $\perp$, R_i is polarization parameters defined in Eq. (1.66), and ϵ_i is the reconstruction efficiency for each MC-PDF. The signal PDF $\mathcal{H}_{sig}$ is obtained by:

$$\mathcal{H}_{sig}(\cos\theta_{tr}, \cos\theta_1) = \sum_i R_i^{'} \mathcal{H}_i(\cos\theta_{tr}, \cos\theta_1), \tag{5.3}$$

where $\mathcal{H}_i(\cos\theta_{tr}, \cos\theta_1)$ is each MC-PDF.

5.1.4 Background PDF

The background PDF is determined from a sideband region defined by $M_{bc} < 5.26\mathrm{GeV/c^2}$ and $|\Delta E| < 0.2\mathrm{GeV}$. We use the following functions that include polarizations in the background:

$$\mathcal{H}_{bg}(\cos\theta_{tr}, \cos\theta_1) \equiv \mathcal{H}_{bg_{\theta_{tr}}}(\cos\theta_{tr}) \mathcal{H}_{bg_{\theta_1}}(\cos\theta_1), \tag{5.4}$$

$$\begin{aligned} \mathcal{H}_{bg_{\theta_{tr}}}(\cos\theta_{tr}) = \quad & N_{bg_{\theta_{tr}}}(a_1 \sin^2\theta_{tr} + a_2 \cos^2\theta_{tr}) \\ = \quad & \alpha + 3(\frac{1}{2} - \alpha)\cos^2\theta_{tr}, \end{aligned} \tag{5.5}$$

$$\begin{aligned} \mathcal{H}_{bg_{\theta_1}}(\cos\theta_1) = \quad & N_{bg_{\theta_1}}(b_{\theta_{1_0}} + b_{\theta_{1_1}}\cos\theta_1 + b_{\theta_{1_2}}\cos^2\theta_1 + b_{\theta_{1_3}}\cos^3\theta_1) \\ = \quad & \frac{1}{2} - \frac{b_{\theta_{1_2}}}{3} + b_{\theta_{1_1}}\cos\theta_1 + b_{\theta_{1_2}}\cos^2\theta_1 + b_{\theta_{1_3}}\cos^3\theta_1, \end{aligned} \tag{5.6}$$

where $N_{bg_{\theta_{tr}}}$ and $N_{bg_{\theta_1}}$ are normalization factors, and α, $b_{\theta_{11}}$, $b_{\theta_{12}}$, $b_{\theta_{13}}$ are fit parameters determined from the events in the sideband. With MC simulation studies, we find that the background $\cos\theta_1$ distribution is asymmetric due to the inefficiency of π_s that has lower momentum ($\cos\theta_1 = -1$ corresponds to lower momentum region, while $\cos\theta_1 = 1$ corresponds to higher momentum region). Therefore, we choose Eq. (5.6) that can include such effects. Figure 5.3 shows the fit results. Table 5.1 shows the background parameter values obtained by the fit.

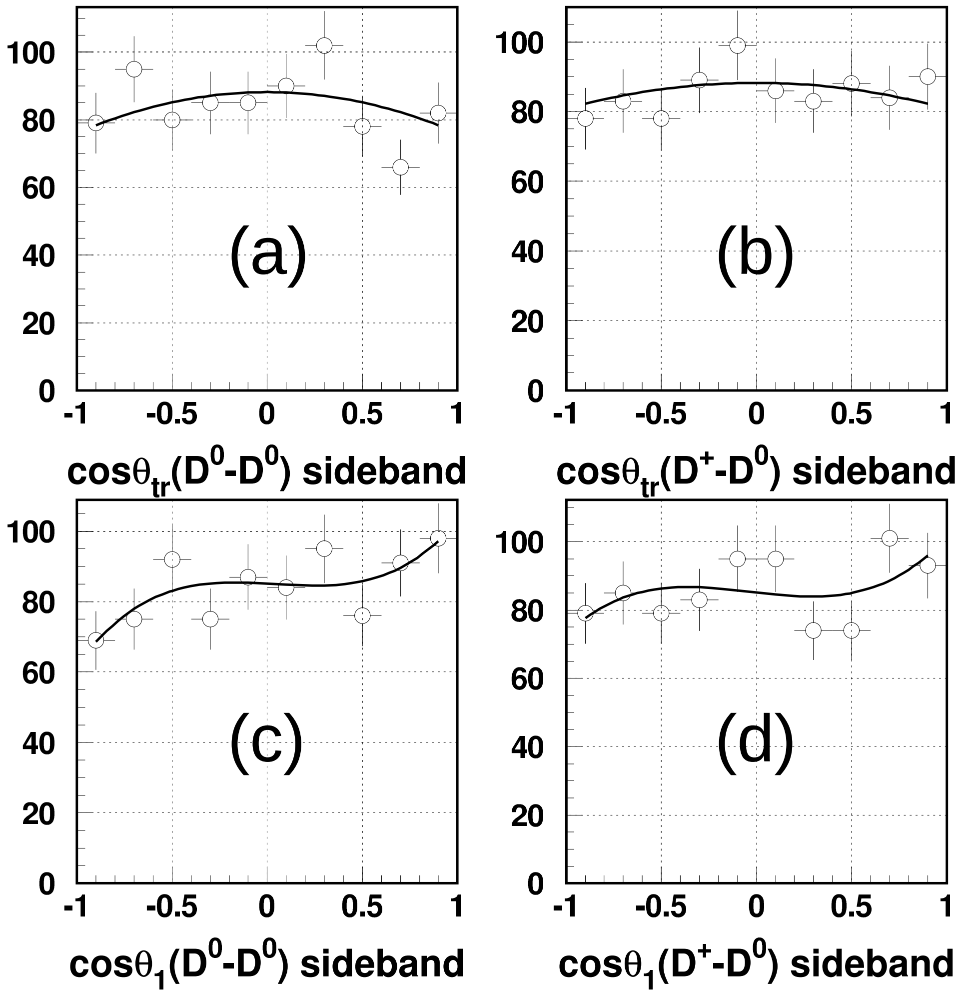

Figure 5.3: *Background angular distributions obtained from the sideband events: (a)* $\cos\theta_{tr}$ *backgrounds for the* D^0-$\bar{D}^0$ *combination; (b)* $\cos\theta_{tr}$ *backgrounds for the* D^+-$\bar{D}^0$ *combination; (c)* $\cos\theta_1$ *backgrounds for the* D^0-$\bar{D}^0$ *combination; (d)* $\cos\theta_1$ *backgrounds for the* D^+-$\bar{D}^0$ *combination.*

Parameter	(D^0-$\bar{D}^0$)	(D^+-$\bar{D}^0$)
α	0.524 ± 0.019	0.514 ± 0.019
$b_{\theta_{11}}$	-0.019 ± 0.078	-0.037 ± 0.079
$b_{\theta_{12}}$	-0.016 ± 0.059	0.012 ± 0.058
$b_{\theta_{13}}$	0.14 ± 0.12	0.12 ± 0.12

Table 5.1: *Background shape parameters for the polarization measurement.*

5.2 Polarization Fit Results

We determine the most probable polarization parameters by minimizing $-2\ln\mathcal{L}$, where the likelihood function, $\mathcal{L}$, is defined in Eq. (5.1):

$$\begin{aligned} R_\perp &= 0.19 \pm 0.08, \\ R_0 &= 0.57 \pm 0.08. \end{aligned} \tag{5.7}$$

Figures 5.4 show $\cos\theta_{tr}$ and $\cos\theta_1$ projections, respectively.

5.3 Systematic Uncertainty

5.3.1 Overview

Sources of systematic errors of the polarization measurement are described in the following sections. As a basic rule, we estimate each systematic uncertainty by varying a parameter by $\pm1\sigma$. If an obtained systematic uncertainty is asymmetric, we take the larger one for both sides. We take only one systematic uncertainty for each source of systematic uncertainty. We add each systematic uncertainty in quadrature.

Systematic errors are summarized in Table 5.2.

Source	R_0	$R_\perp$
Yield	$< 10^{-5}$	$< 10^{-5}$
BG shape parameters	0.0072	0.0056
Fit bias	0.0047	0.0039
Understanding of the angular distributions	0.0062	0.0004
$\pi_s^\pm$ efficiency	0.0022	0.0005
π_s^0 efficiency	0.0006	0.0013
MC-PDF binning	0.0059	0.0050
Misreconstruction	0.0066	0.0062
Sum	0.014	0.011

Table 5.2: *Systematic uncertainties for the $B^0 \to D^{*+}D^{*-}$ polarization parameters.*

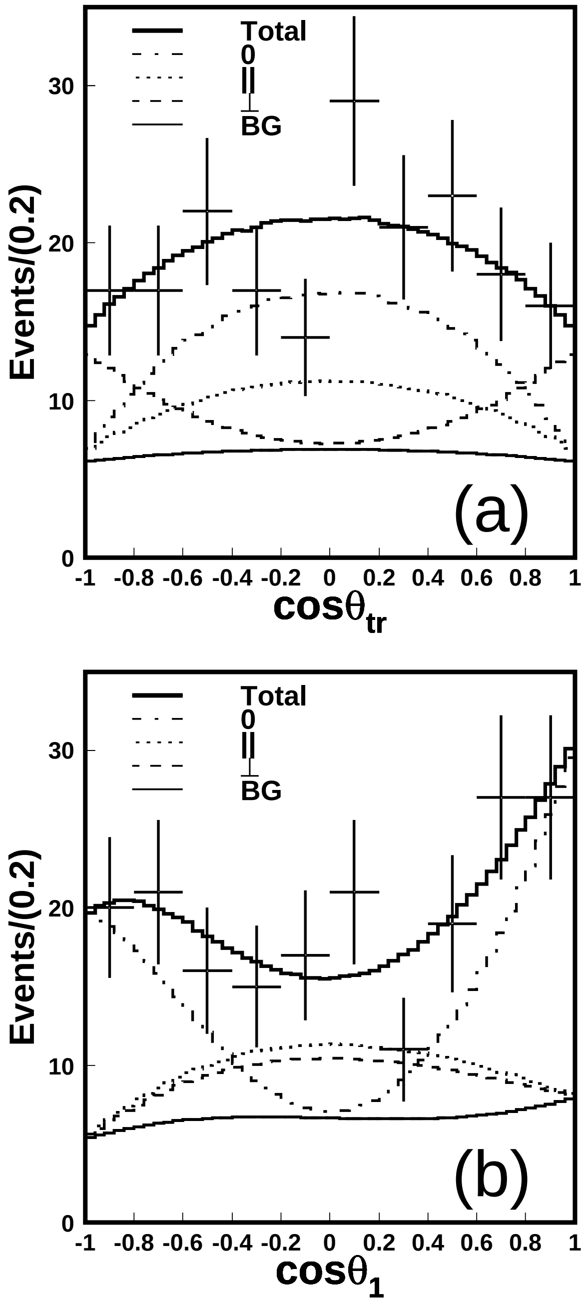

Figure 5.4: *Angular distributions of the $B^0 \to D^{*+}D^{*-}$ candidates in $\cos\theta_{tr}$ (a) and $\cos\theta_1$ (b) projections. In each figure, the dot-dashed, dotted and dashed lines correspond to longitudinal, parallel and transverse polarization components, respectively. The thin solid line is the background, and the thick solid line shows the sum of all contributions.*

5.3.2 Yield Estimation

A systematic uncertainty in the signal fraction measurement is estimated by varying each average signal fraction, $\mathrm{f}_{\mathrm{sig}}^{\mathrm{ave}}$, which is defined in Eq. (4.12), by $\pm 1\sigma$.The σ is the standard deviation of the average signal fraction. We then repeat the fit to obtain the polarization parameters. For each signal fraction, the difference between our nominal fit result and the refitted result is regarded as the systematic uncertainty.

5.3.3 Background Shape Parameters

Each background shape parameter (Table 5.1) is varied by $\pm 1\sigma$ and the polarization parameters fit is repeated. We add each variation from the nominal fit result in quadrature.

5.3.4 Fit Bias

A possible fit bias between generated and reconstructed events is examined with Geant MC events. Results are shown in Figs. 5.5. We estimate the uncertainty of observed polarization by the errors of the fitted line, with taking the correlation between the parameters of the line shape into account.

5.3.5 Understanding of the Angular Distributions

A possible difference in angular distributions between data and MC is examined. We use the $B^0 \to D^{*+} D_s^-$ control sample that has a completely polarized angular distribution. Therefore this helicity angle can be used to extract corrections for $\cos\theta_1$. Figure 5.6 shows angular distribution ratios as a function of $\sin\theta_1$.

To account for the discrepancy, we define an effective additional resolution σ_{add} as:

$$\sigma_{\mathrm{DATA}}^2 = \sigma_{\mathrm{MC}}^2 + \sigma_{\mathrm{add}}^2, \tag{5.8}$$

where σ_{DATA} (σ_{MC}) is the angular resolution for data (MC). Table 5.3 shows the MC angular resolution for each angle as a root-mean-square (RMS). The σ_{add} is estimated with the following procedure:

- obtain a ratio curve between data and MC, and check possible bias,
- smear MC $\cos\theta_1$ with a Gaussian function whose sigma is σ_{add},
- repeat the smearing until the fitted ratio curve becomes flat.

We obtain $\sigma_{\mathrm{add}} = 0.085$. For the MC-PDF, both $\cos\theta_{tr}$ and $\cos\theta_1$ distributions are smeared with this error, where considering differences in error distributions, each σ_{add} is scaled by RMS ratio of MC angular resolutions.

We then obtain polarization parameters using the corrected distributions. Differences from our nominal fit results are used as the systematic errors.

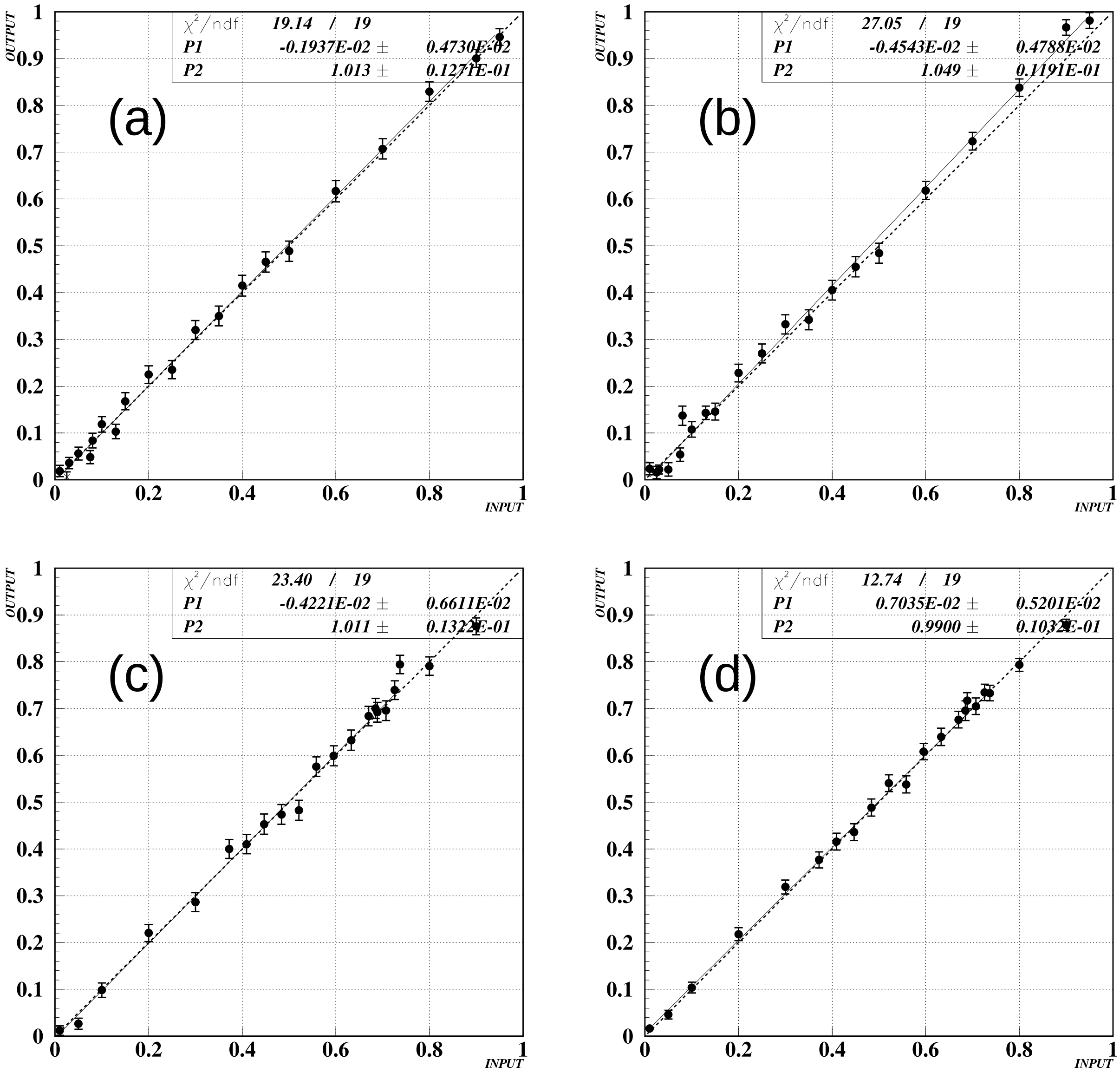

Figure 5.5: *Linearity tests with Geant MC: (a)* $R_\perp$ *for the* $K\pi - K\pi$ *combination; (b)* $R_\perp$ *for the* $K\pi - K\pi\pi$ *combination; (c)* R_0 *for the* $K\pi - K\pi$ *combination; (d)* R_0 *for the* $K\pi - K\pi\pi$ *combination. The filled circle with error shows the fit result at the input polarization. The dashed line is ideal shape (input=output). The solid line is the linear function fitted by output results.*

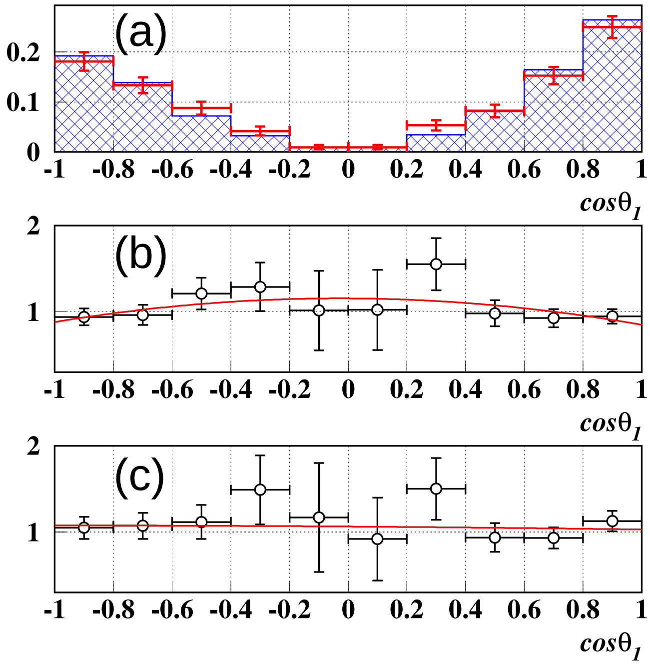

Figure 5.6: *Angular distribution ratio of control sample: (a) The* D^{*+} *helicity distribution in* $B^0 \to D^{*+}D_s^-$*. The hatched histogram is for MC and points with errors are for data; (b) The ratio between data and MC (blank circles with errors) with the fit result (solid curve); (c) The ratio between MC and data with the additional resolution parameter* σ_{add} *(see the text for detail).*

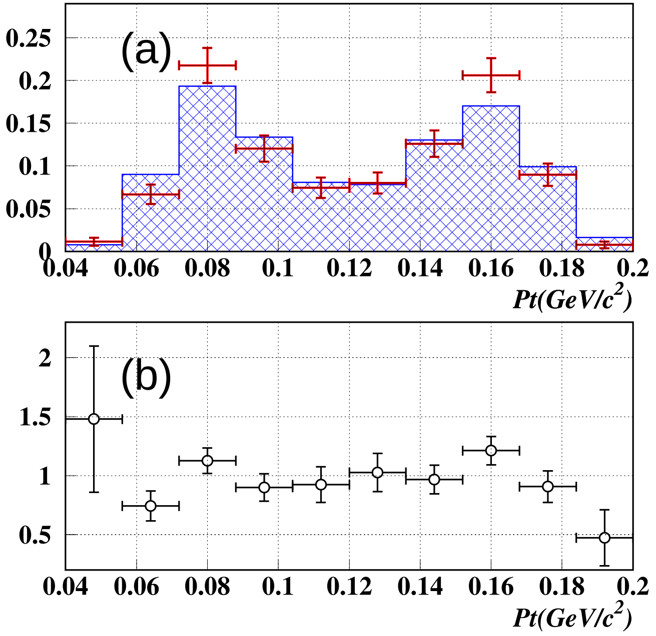

Figure 5.7: *Slow pion ratio of control sample: (a) Transverse momentum of slow pion which comes from* $B^0 \to D^{*+}D_s^-$*. Hatched histogram is for MC and points with errors are for data; (b) The ratio between data and MC (blank circles with errors).*

Angle	Polarization	$(D^0\text{-}\bar{D}^0)$	$(D^+\text{-}\bar{D}^0)$
$\cos\theta_{tr}$	R_0	0.24	0.33
	$R_\parallel$	0.24	0.35
	$R_\perp$	0.27	0.43
$\cos\theta_1$	R_0	0.15	0.14
	$R_\parallel$	0.14	0.13
	$R_\perp$	0.13	0.13

Table 5.3: Angular resolution of each MC-PDF. Each resolution is represented by root-mean-square (RMS) of the residual between the reconstructed angle and the generated angle.

5.3.6 Slow Pion Efficiency

We consider a possible bias caused by the difference of slow pion reconstruction efficiencies between MC and data. To check the possibility of a large bias, we compare slow pion distribution of the $B^0 \to D^{*+}D_s^-$ control sample. Figure 5.7 shows transverse momentum distributions of slow pions in the $B^0 \to D^{*+}D_s^-$ control sample. The distribution for data is in agreement with that for MC within statistical errors. Thus we do not apply any correction to our nominal fit results.

A further check is performed to take minor efficiency corrections into account. The correction factors are obtained from D^* or η candidates in data and MC. We generate signal MC events with adjusting reconstruction efficiencies of slow pions using these correction factors. We refit them and include the difference between efficiency-corrected and uncorrected events as systematic uncertainty.

5.3.7 MC-PDF Binning

The MC-PDF is divided by 50 bins for both $\cos\theta_{tr}$ and $\cos\theta_1$. The binning effect is studied by changing it to 40 and 60 bins.

5.3.8 Misreconstructed Events

When we exchange particles from the $B^0 \to D^{*+}D^{*-}$ decay with those from the accompanying B meson, we still obtain the angular distribution with a worse resolution. In particular, the residual distribution has very long tails. To estimate these effects, we change the likelihood function as follows:

$$\begin{aligned}\mathcal{L} \equiv \prod\Big\{ & f_{\rm corr}(\Delta E, M_{\rm bc})\mathcal{H}_{\rm corr}(\cos\theta_{tr},\cos\theta_1) + f_{\rm miss}(\Delta E, M_{\rm bc})\mathcal{H}_{\rm miss}(\cos\theta_{tr},\cos\theta_1) \\ & + [1 - f_{\rm corr}(\Delta E, M_{\rm bc}) - f_{\rm miss}(\Delta E, M_{\rm bc})]\mathcal{H}_{\rm bg}(\cos\theta_{tr},\cos\theta_1)\Big\},\end{aligned} \tag{5.9}$$

where $f_{\rm corr}(\Delta E, M_{\rm bc})$ is a fraction of correctly-reconstructed signal events and $\mathcal{H}_{\rm corr}(\cos\theta_{tr},\cos\theta_1)$ is its angular distribution, $f_{\rm miss}(\Delta E, M_{\rm bc})$ is a fraction of misreconstructed signal events and $\mathcal{H}_{\mathrm{miss}}(\cos\theta_{tr}, \cos\theta_1)$ is its angular distribution. The shapes of $f_{\mathrm{corr}}(\Delta E, M_{\mathrm{bc}})$ and $f_{\mathrm{miss}}(\Delta E, M_{\mathrm{bc}})$ are decided from ΔE and M_{bc} projections of the signal MC, which are separated to two with the MC information. The shapes of $\mathcal{H}_{\mathrm{corr}}(\cos\theta_{tr}, \cos\theta_1)$ and $\mathcal{H}_{\mathrm{miss}}(\cos\theta_{tr}, \cos\theta_1)$ are similarly decided from the separate MC-PDF's. Average fractions of misreconstruction are $18 \sim 39\%$ of average signal fraction, depending on whether the mode has π^0 in D meson or as slow pion, or not. We repeat the polarization measurement with these separate PDF's. The difference between two methods is considered as the systematic uncertainty.

5.4 Validation Checks for Polarization Measurement

5.4.1 Linearity

We test our fit method with the Geant MC. Figures 5.5 show linearities of $R_\perp$ for the $D^0(K\pi)$-$\overline{D}^0(K\pi)$ combination, $R_\perp$ for $D^0(K\pi)$-$D^-(K\pi\pi)$, R_0 for $D^0(K\pi)$-$\overline{D}^0(K\pi)$ and R_0 for $D^0(K\pi)$-$D^-(K\pi\pi)$, respectively. Since no sizable bias is seen, our nominal fit result is not corrected. We consider the possibility of small bias in Sec. 5.3.4.

5.4.2 Ensemble Test

We generate 1000 pseudo-experiments. The special MC for the ensemble test is generated with the same PDFs that are used to fit data. The merit of this test is that we can detect possible bias owing to the fitting method itself. Figures 5.8 and 5.9 show the distributions of central values, positive errors that corresponds to $+1\sigma$, negative errors that corresponds to -1σ, and pulls, respectively, where the pull is defined as (output-input)/(error of the fit). If the pull follows a Gaussian distribution with $\mu = 0$ and $\sigma = 1$, it indicates that our error estimation is correct. Figure 5.10 is a scatter plot for whole pseudo experiments. Table 5.4 summarizes the results of the ensemble test. We conclude that there is no fit bias and our error sizes for data are in good agreement with the ensemble test expectations.

	$R_\perp$	R_0
Measured	$0.1899^{+0.079}_{-0.076}$	$0.5720^{+0.077}_{-0.079}$
Input	0.1899	0.5720
Output(mean)	0.1927	0.5786
Output(RMS)	0.07241	0.08197
Positive error(mean)	$+0.07263$	$+0.07693$
Negative error(mean)	-0.06715	-0.07879
Pull	0.98 ± 0.02	1.03 ± 0.03

Table 5.4: *Ensemble test results for polarization*

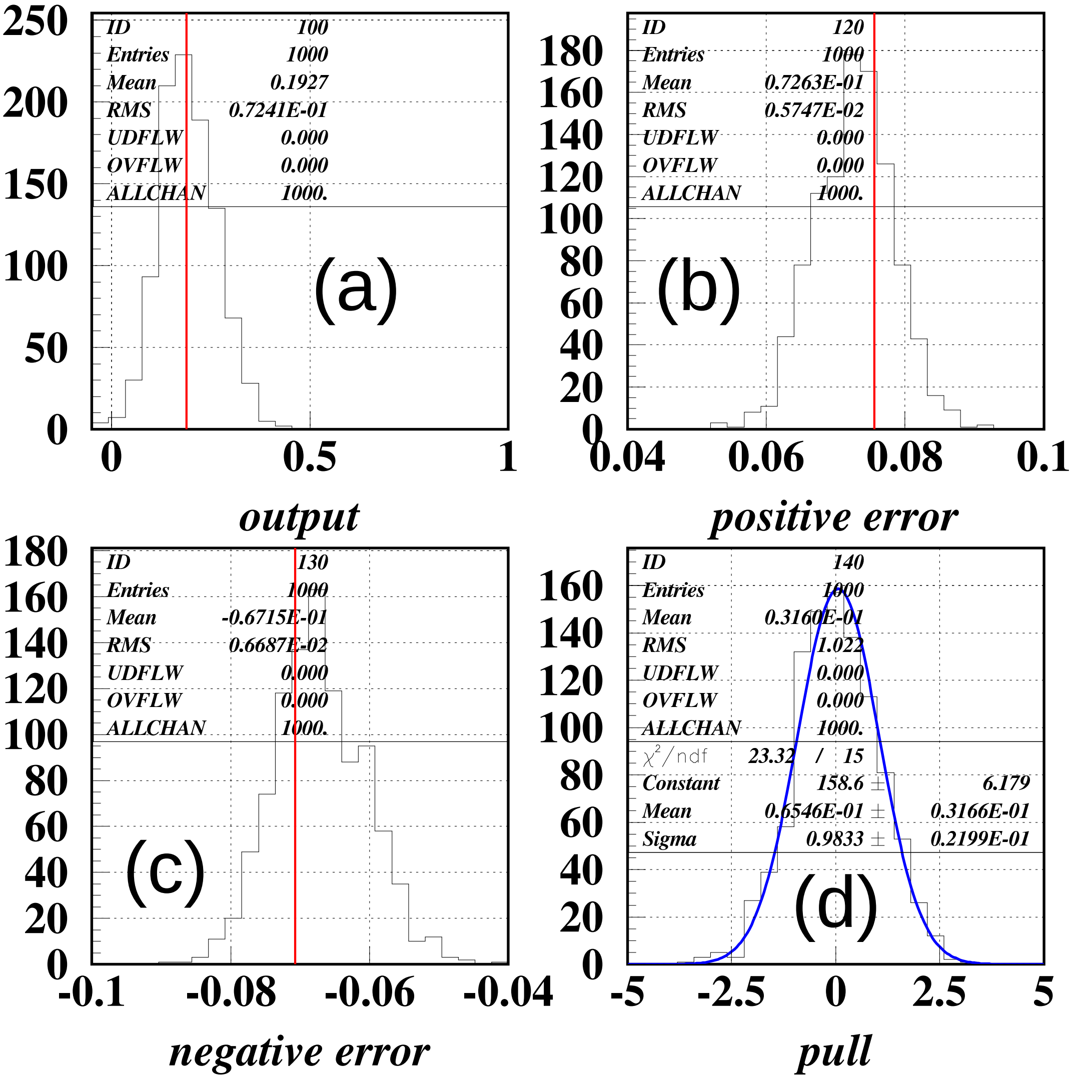

Figure 5.8: *Results of an ensemble test for* $R_\perp$*: (a) The central values; (b) The positive errors; (c) The negative errors; (d) The pulls. Vertical lines show our measurements.*

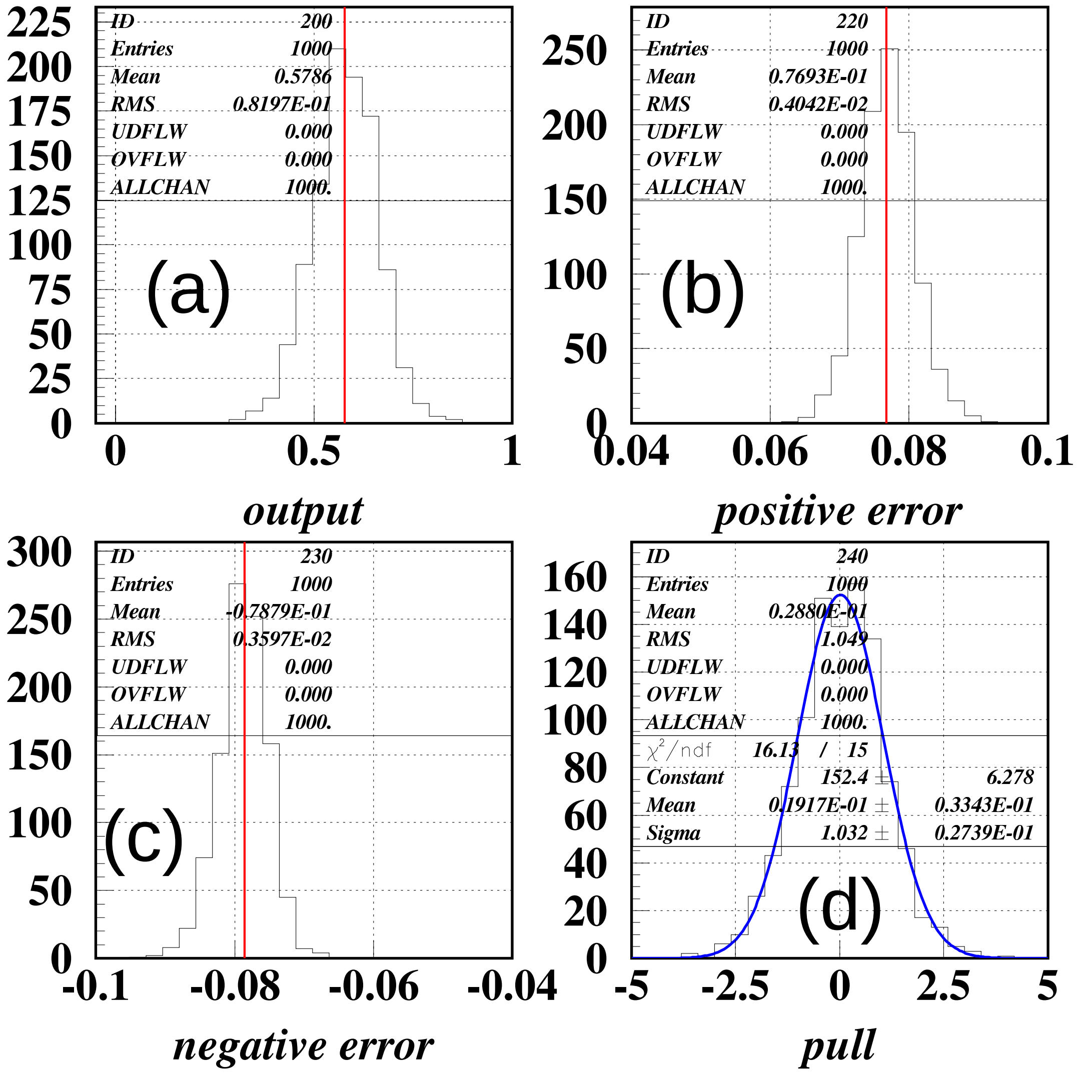

Figure 5.9: *Results of an ensemble test for R_0: (a) The central values; (b) The positive errors; (c) The negative errors; (d) The pulls. Vertical lines show our measurements.*

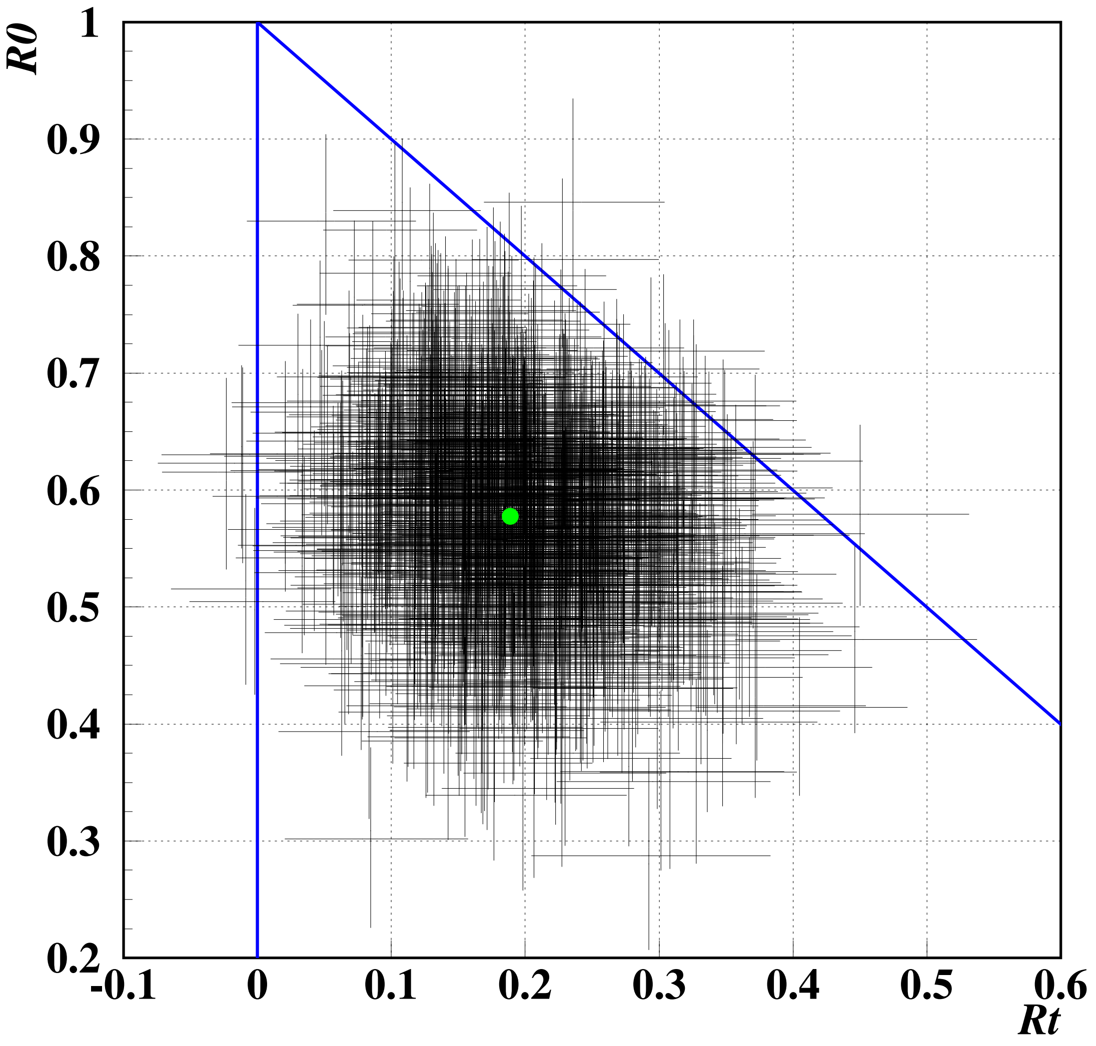

Figure 5.10: *Results of an ensemble test. Each cross corresponds to each experiment and the cross point shows the center values. The length of each cross means the statistical error of each pseudo-experiment. The circle shows our measurement. Solid lines show physical boundaries.*

5.4.3 Likelihood Scanning

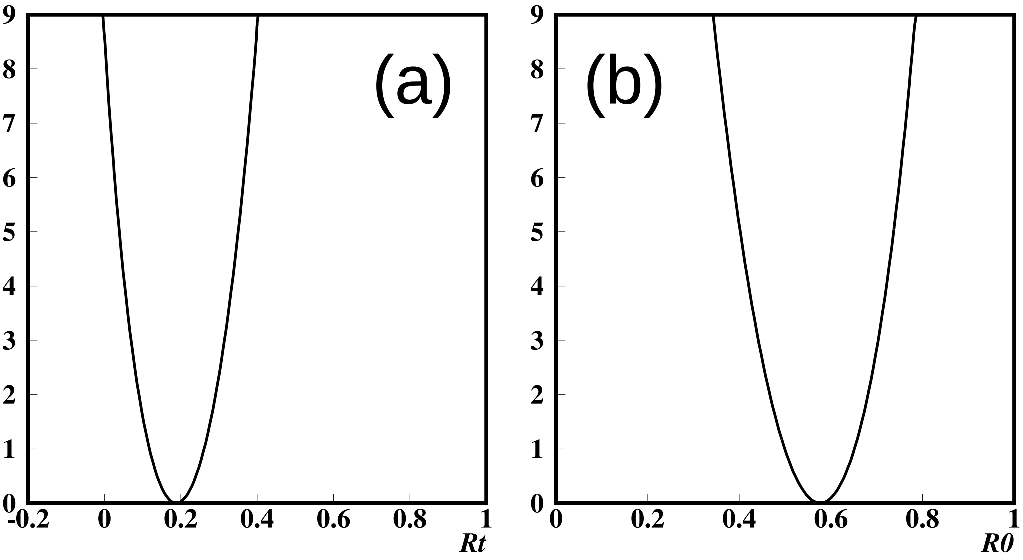

Figure 5.11: $-2\ln(\mathcal{L}/\mathcal{L}_{\max})$ *distribution as function of (a)* $R_\perp$ *(b)* R_0.

We scan the log-likelihood ratio $-2\ln(\mathcal{L}/\mathcal{L}_{\max})$ distribution as a function of $R_\perp$ or R_0. Figures 5.11 show the results of the scan. Both plots show that there is no pathology around $\mathcal{L}_{\max}$.

5.5 Summary of Polarization Measurement

We obtain polarization parameters:

$$R_\perp = 0.19 \pm 0.08(\text{stat}) \pm 0.01(\text{syst}),$$
$$R_0 = 0.57 \pm 0.08(\text{stat}) \pm 0.01(\text{syst}).$$

Chapter 6

Extraction of CP Asymmetry Parameters

6.1 Vertex Reconstruction

In order to extract CP asymmetry parameters, we need to measure the decay time difference, Δt, which is calculated from the distance between the B_{CP} and $B_{\rm tag}$ vertices as

$$\Delta t \sim \frac{\Delta z}{\beta\gamma c} \equiv \frac{Z_{CP} - Z_{\rm tag}}{\beta\gamma c}. \tag{6.1}$$

Here Z_{CP} ($Z_{\rm tag}$) is the z component of the B_{CP} ($B_{\rm tag}$) vertex and $\beta\gamma = 0.425$ is a Lorentz factor. Each B vertex is reconstructed from tracks from the B meson decay and is constrained to the IP profile (called IP constraint fit). A concept of the constraint fit is described in Sec. 4.3.2. The IP profile is calculated for every 10000 events using hadronic events. The typical size of the IP profile is 100 μm in x, 3-5 μm in y and 3-4 mm in z. When we perform the IP constraint fit, we take the effect of the B meson flight from the IP profile in the x-y plane, into account. The effective IP profile is smeared by a Gaussian function with RMS of 21 μm.

6.1.1 Vertex Reconstruction of B_{CP}

We reconstruct $B_{CP} \to D^{*+}D^{*-}$ decays with subsequent decays $D^{*+}D^{*-} \to (D^0\pi^+, \overline{D}{}^0\pi^-)$, $D^{*+}D^{*-} \to (D^0\pi^+, D^-\pi^0)$ or $D^{*+}D^{*-} \to (D^+\pi^0, \overline{D}{}^0\pi^-)$. We do not use daughter slow pions from $D^{*\pm}$ because of their poor resolution. We require that the D meson has at least two daughter tracks that have enough SVD hits,i.e. with both r-ϕ and z hits in at least one layer and with two or more z hits in total. If a D meson does not meet the requirement, we do not use the trajectory for calculating the B vertex. We have two types of reconstructed vertices; the number of used D meson trajectories are two (multi-D) or one (single-D) as illustrated in Fig. 6.2.

We reject poorly reconstructed vertices for the multi-D case. The vertex quality is

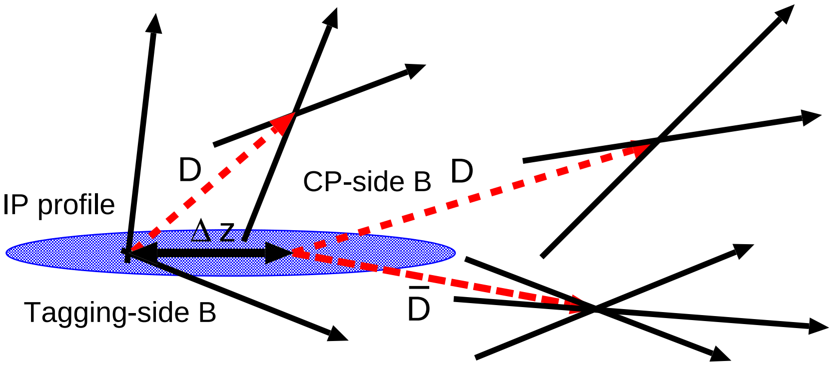

Figure 6.1: *The schematic picture of the vertex reconstruction.*

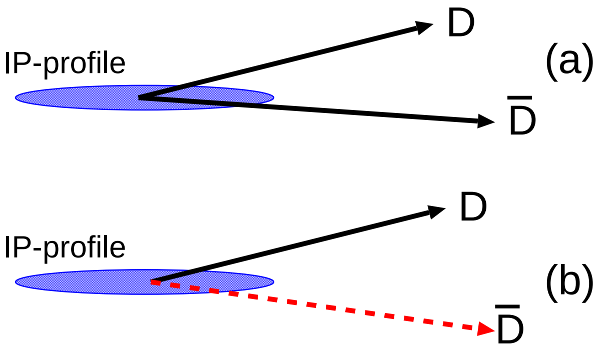

Figure 6.2: *Two types of $D^{*+}D^{*-}$ vertex reconstruction, which depends on the number of D trajectories which are associated with SVD hits: (a) with both D mesons and the IP constraint; (b) with one D meson and the IP constraint.*

represented by a reduced χ^2 projected onto the z axis defined as

$$\xi \equiv \frac{1}{2n} \sum_{i=1}^{n} \left[\frac{z^i_{\text{after}} - z^i_{\text{before}}}{e^i_{\text{before}}} \right]^2 , \tag{6.2}$$

where z^i_{before} and z^i_{after} are the z positions of each track before and after the vertex fit, respectively, and e^i_{before} is the error on z^i_{before}. We do not use the normal χ^2 because it is correlated with the vertex z position due to the IP constraint in the x-y plane. We require $\xi < 100$. The typical z resolution estimated by the signal MC is ~ 140 μm for the multi-D case and ~ 200 μm for the single-D case. The vertex reconstruction efficiency is $\sim 73\%$ and $\sim 82\%$, respectively.

6.1.2 Vertex Reconstruction of B_{tag}

After the exclusive reconstruction of B_{CP}, all the remaining particles should belong to B_{tag}, i.e. the other B meson. The B_{tag} vertex is reconstructed from charged tracks that belong to B_{tag}, although we discard poorly reconstructed tracks; the impact parameter, dr, with respect to the B_{CP} vertex is required to be less than 0.5 mm in the r-ϕ plane. We use a constraint to the IP profile to improve the vertex resolution.

Since the B_{tag} vertex is inclusively reconstructed and we assume all tracks come from the B_{tag} vertex, reconstructed vertex position may be distorted by long-lived particles such as K^0_S, Λ, and charmed hadrons. Therefore, the vertex reconstruction algorithm must be carefully chosen to minimize the effect of secondary particles. We use the same vertex reconstruction algorithm as that used for the $\sin 2\phi_1$ analysis [8, 47]. At first, we remove tracks that form a K^0_S candidate which has an invariant mass within 15 MeV from the nominal K^0_S. The B_{tag} vertex is then reconstructed with remaining tracks and the IP constraint. If the reduced χ^2 of the vertex is less than 20, we accept the vertex. Otherwise we remove the track that gives the largest contribution to the χ^2 and repeat the vertex reconstruction. If the track to be removed is a lepton with $p^* > 1.1$ GeV/c, however, we keep the lepton and remove the track with the second largest χ^2 contribution because high momentum leptons are likely to come from primary semi-leptonic B decays. We repeat this trimming procedure until we obtain a reduced χ^2 less than 20. We accept the vertex if the vertex quality parameter ξ is less than 100. We also apply the selection of $|\Delta t| < 70$ ps to reject poorly reconstructed events.

6.2 Flavor Tagging

It is indispensable to identify the flavor of b-quark of B_{tag}, i.e. to ascertain whether B_{tag} is B^0 or $\overline{B}^0$, for time-dependent CP asymmetry measurement. This technique is called "flavor tagging" [46]. Detail of flavor tagging method is shown in Appendix C. The simplest and most reliable method for flavor tagging uses the charge of high-momentum leptons in semi-leptonic decays, i.e. $B^0 \to Xl^+\nu$ and $\overline{B}^0 \to Xl^-\bar{\nu}$. The charge of final-state kaons can also be used since the decays $B^0 \to K^+X$ ($\bar{\text{b}} \to \bar{c} \to \bar{s}$) and $B^0 \to K^+X$ (with $b \to c \to s$) dominate. In addition to these two leading discriminants, our algorithm

l	r interval	ε_l	w_l	Δw_l	$\varepsilon_{\rm eff}^l$
1	$0.000 - 0.250$	0.398	0.464 ± 0.006	-0.011 ± 0.006	0.002 ± 0.001
2	$0.250 - 0.500$	0.146	0.331 ± 0.008	$+0.004 \pm 0.010$	0.017 ± 0.002
3	$0.500 - 0.625$	0.104	0.231 ± 0.009	-0.011 ± 0.010	0.030 ± 0.002
4	$0.625 - 0.750$	0.122	0.163 ± 0.008	-0.007 ± 0.009	0.055 ± 0.003
5	$0.750 - 0.875$	0.094	0.109 ± 0.007	$+0.016 \pm 0.009$	0.057 ± 0.002
6	$0.875 - 1.000$	0.136	0.020 ± 0.005	$+0.003 \pm 0.006$	0.126 ± 0.003

Table 6.1: *The event fractions ε_l, wrong-tag fractions w_l, wrong-tag fraction differences Δw_l, and average effective tagging efficiencies $\varepsilon_{\rm eff}^l = \varepsilon_l(1-2w_l)^2$ for each r interval. The errors include both statistical and systematic uncertainties. The event fractions are obtained from the $B^0 \to J/\psi K_S^0$ simulation.*

includes other categories of tracks whose charges depend on the b quarks's flavor: lower momentum leptons from $c \to sl^+\nu$; Λ baryons from the cascade decay $b \to c \to s$; high-momentum pions that originate from decays such as $B^0 \to D^{(*)-}(\pi^+, \rho^+, a_1^+, etc.)$; and slow pions from $D^{*-} \to \bar{D}^0\pi^-$.

All these inputs are combined, taking their correlations into account, in a way that maximizes the flavor tagging performance. We use two parameters, q and r, to represent the flavor tagging information. First, q, indicates the determined flavor; $q = +1$ for B^0 and $q = -1$ for $\overline{B}^0$. The parameter r is an event-by-event, MC-determined flavor-tagging dilution factor that ranges from $r = 0$ for no flavor discrimination to $r = 1$ for unambiguous flavor assignment. This assignment is used only to sort data into six r intervals. The average wrong tag probabilities, $w_l \equiv (w_l^+ + w_l^-)/2$ $(l = 1, 6)$ and the difference between B^0 and $\overline{B}^0$ decays, $\Delta w_l \equiv w_l^+ - w_l^-$, where $w_l^{+(-)}$ is the wrong-tag probability for the B^0 ($\overline{B}^0$) decay in each r interval, are directly determined from data. The decision algorithm is optimized to maximize $\varepsilon_{\rm eff}^l \equiv \varepsilon_l(1-2w_l)^2$, which is called effective tagging efficiency, since the asymmetry for a certain statistical significance is proportional to $\varepsilon_{\rm eff}^l$. We use the same values that were used for the $\sin 2\phi_1$ measurement [47]. Table 6.1 lists these values to be used for the flavor-tagging.

6.3 Probability Density Function for CP Asymmetry Measurement

Extraction of CP asymmetry parameters is performed by the unbinned maximum likelihood method, which is described in Appendix A.

The likelihood function for CP asymmetry measurement is

$$\mathcal{L} = \prod (1 - f_{\rm ol})\{f_{\rm sig}P_{\rm sig} + (1 - f_{\rm sig})P_{\rm bg}\} + f_{\rm ol}P_{\rm ol}, \tag{6.3}$$

where the signal fraction $f_{\rm sig}(\Delta E, M_{\rm bc})$ is defined in Eq. (4.12), $P_{\rm sig}$ and $P_{\rm bg}$ are PDF's of signal and background, respectively. The small number of signal and background events that have large Δt are accommodated by the outlier PDF, $P_{\rm ol}$, with fraction $f_{\rm ol}$.

6.3.1 Signal PDF

Theoretical time-dependent Δt distribution of $B^0 \to D^{*+}D^{*-}$, $\mathcal{P}_{D^{*+}D^{*-}}$, was defined in Eq. (2.5). We obtained Eq. (2.8) in Sec. 2.2.3 with considering the wrong flavor tag probability w. Furthermore, we should consider additional smearing effects in our experimental environment. Sources of smearing effects are classified into two types: angular resolutions and Δt resolutions. Angular resolutions were already discussed in Chapter 5. We replace H_i in Eq. (2.8) with normalized MC-PDF $\mathcal{H}_i$, where $i = 0, \|, \perp$. Therefore, the signal probability becomes:

$$\begin{aligned}\mathcal{P}_{D^{*+}D^{*-}} &= \frac{e^{-|\Delta t|/\tau_{B^0}}}{4\tau_{B^0}} \sum_{i=0,\|,\perp} R_i \mathcal{H}_i(cos\theta_{tr}, cos\theta_1) \\ &\qquad \left\{1 - q\Delta w + q(1-2w)(\mathcal{A}_{D^{*+}D^{*-}} \cos \Delta m \Delta t + \eta_i \mathcal{S}_{D^{*+}D^{*-}} \sin \Delta m \Delta t)\right\}.\end{aligned} \tag{6.4}$$

To account for finite Δt resolutions, $\mathcal{P}_{D^{*+}D^{*-}}$ is convoluted with a resolution function $R_{\rm sig}$:

$$P_{\rm sig}(\Delta t) = \int \mathcal{P}_{D^{*+}D^{*-}}(\Delta t') R_{\rm sig}(\Delta t - \Delta t') d(\Delta t'), \tag{6.5}$$

where the $R_{\rm sig}$ consists of three resolution functions:

$$R_{\rm sig} = R_{\rm det} \otimes R_{\rm np} \otimes R_{\rm k}. \tag{6.6}$$

Here $R_{\rm det}$ represents the detector resolution, $R_{\rm np}$ the smearing and bias from non-primary tracks to the $B_{\rm tag}$ vertex, and $R_{\rm k}$ the smearing due to the kinematic approximation that we neglect the transverse momentum of B mesons in the center of mass system in the Δt calculation [Eq. (2.7)]. For multi-D case, $R_{\rm det}$ is described as the sum of two Gaussian functions, whose resolutions are the function of error of the vertex-constraint fit. The error of the vertex depends on ξ. We assume the dependence as a first order of polynomial of ξ and the difference from the assumption is taken as systematic uncertainty into account.

6.3.2 Background PDF

A background PDF is defined in the similar way to $P_{\rm sig}$:

$$P_{\rm bg}(\Delta t) = \int \mathcal{P}_{\rm bg}(\Delta t') R_{\rm bg}(\Delta t - \Delta t') d(\Delta t'), \tag{6.7}$$

where $\mathcal{P}_{\rm bg}$ is the background Δt distribution and $R_{\rm sig}$ is the background resolution function. The background Δt distribution consists of lifetime, and prompt-components:

$$\mathcal{P}_{\rm bg} = (1 - f_\delta) \frac{e^{-|\Delta t|/\tau_{\rm BG}}}{2\tau_{\rm BG}} + f_\delta \cdot \delta(\Delta t), \tag{6.8}$$

where $\tau_{\rm BG}$ is an effective lifetime and f_δ is a fraction of prompt component.

Background resolution function is treated as a sum of two Gaussian functions:

$$R_{\rm bg} = (1 - f_{\rm tail})G(\Delta t, \mu_{\rm mean}, S_{\rm main}\sigma) + f_{\rm tail}G(\Delta t, \mu_{\rm mean}, S_{\rm tail}\sigma), \tag{6.9}$$

where $f_{\rm tail}$ is a fraction of the second Gaussian function, $\mu_{\rm mean}$ is a mean shift and S_i is a global scaling factor for an event-by-event vertexing error, which is obtained from the vertex reconstruction. We use different parameters depending on whether both vertices are reconstructed with multiple tracks or not. Each parameter is determined from a sideband region defined by $M_{bc} < 5.25{\rm GeV}/{\rm c}^2$ and $|\Delta E| < 0.2{\rm GeV}$. To reduce statistical error of background parameters, we also use $B \to D^{(*)}D_s^{(*)}$ control samples that have similar decay topology. We confirm that there is no difference between obtained parameters from $B^0 \to D^{*+}D^{*-}$ and obtained parameters from $B \to D^{(*)}D_s^{(*)}$, with MC simulation. The fit results are summarized in Table 6.2.

Parameter	Fit value	
	$\delta_{\rm mean}$	-0.058 ± 0.017
	$\tau_{\rm BG}$	$2.38^{+0.12}_{-0.10}$
	$\mu_{\rm mean}$	-0.148 ± 0.069
Single track	f_δ	0.594 ± 0.035
	$f_{\rm tail}$	0.43 ± 0.12
	$S_{\rm main}$	$1.020^{+0.079}_{-0.104}$
	$S_{\rm tail}$	$1.95^{+0.20}_{-0.17}$
Multi tracks	f_δ	$0.739^{+0.031}_{-0.033}$
	$f_{\rm tail}$	$0.472^{+0.050}_{-0.049}$
	$S_{\rm main}$	$1.130^{+0.060}_{-0.062}$
	$S_{\rm tail}$	$2.61^{+0.17}_{-0.16}$

Table 6.2: Δt background shape parameters

6.3.3 Outlier PDF

To account for a small number of events that give large Δt in both signal and background, we introduce the PDF of the outlier component, $P_{\rm ol}$ and its fraction $f_{\rm ol}$. The source of outlier component is considered as misreconstructed tracks. The outlier PDF is given by a Gaussian with zero mean and a large width ($\sim$ 40 ps):

$$P_{\rm ol}(\Delta t) = G(\Delta t; 0, \sigma_{\rm ol}). \tag{6.10}$$

The fraction of the outlier $f_{\rm ol}$ and the width $\sigma_{\rm ol}$ in data are determined from the lifetime analysis. We use different $f_{\rm ol}$ values depending on whether both vertices are reconstructed with multiple tracks or not. Their values are shown in Table 6.3.

Parameter		Fit value
	$\sigma_{\rm ol}$	$38.8^{+1.6}_{-1.5}$
Single track	$f_{\rm ol}$	$(2.1^{+0.6}_{-0.5}) \times 10^{-4}$
Multi tracks	$f_{\rm ol}$	$(3.1 \pm 0.1) \times 10^{-2}$

Table 6.3: *Parameters for the outlier PDF.*

6.4 Fitting Result

The number of events used for the fit is summarized in Table 4.4. we find 194 (132+62) candidates in the signal box, where the first (second) number in the parenthesis is the number of D^0-$\overline{D}^0$ (D^+-$\overline{D}^0$) sub-decay mode. After quality cuts for the vertex and flavor tagging are required, there are 164 (111+53) events in the signal box. The number of multi-D candidates is 129 (97+32).

The PDF is obtained with using results of previous sections:

$$\begin{aligned} P(q, w_l, \Delta t; \mathcal{S}_{D^{*+}D^{*-}}, \mathcal{A}_{D^{*+}D^{*-}}) = (1 - f_{\rm ol})[f_{\rm sig} P_{\rm sig}(q, \Delta t, w_l; \mathcal{S}_{D^{*+}D^{*-}}, \mathcal{A}_{D^{*+}D^{*-}}) \\ + \frac{1}{2}(1 - f_{\rm sig}) P_{\rm bg}(\Delta t)] + f_{\rm ol} P_{\rm ol}(\Delta t). \end{aligned} \tag{6.11}$$

Then the likelihood function becomes:

$$\mathcal{L}(\mathcal{S}_{D^{*+}D^{*-}}, \mathcal{A}_{D^{*+}D^{*-}}) = \prod_i P(q_i, \Delta t_i; \mathcal{S}_{D^{*+}D^{*-}}, \mathcal{A}_{D^{*+}D^{*-}}), \tag{6.12}$$

where q_i and Δt_i are for i-th event and the product runs over all events. We determine the most probable CP asymmetry parameters by minimizing $-2 \ln \mathcal{L}$. We obtain

$$\begin{aligned} \mathcal{S}_{D^{*+}D^{*-}} &= -0.75 \pm 0.56, \\ \mathcal{A}_{D^{*+}D^{*-}} &= -0.26 \pm 0.26. \end{aligned} \tag{6.13}$$

These are consistent with the SM prediction with neglecting penguin contribution; $\mathcal{S}_{D^{*+}D^{*-}} \sim -0.731$ and $\mathcal{A}_{D^{*+}D^{*-}} \sim 0$.

Figures 6.3 show Δt distributions for $q = +1$ and $q = -1$, and time-dependent CP asymmetries.

6.5 Systematic Uncertainty

6.5.1 Overview

Sources of systematic errors of the CP asymmetry measurement are described in the following sections. As a basic rule, we estimate each systematic uncertainty by varying a parameter that is obtained from data by $\pm 1\sigma$, and varying a parameter that is obtained from MC by $\pm 2\sigma$. If an obtained systematic uncertainty is asymmetric, we take the larger one for both sides. Systematic errors are summarized in Table 6.4.

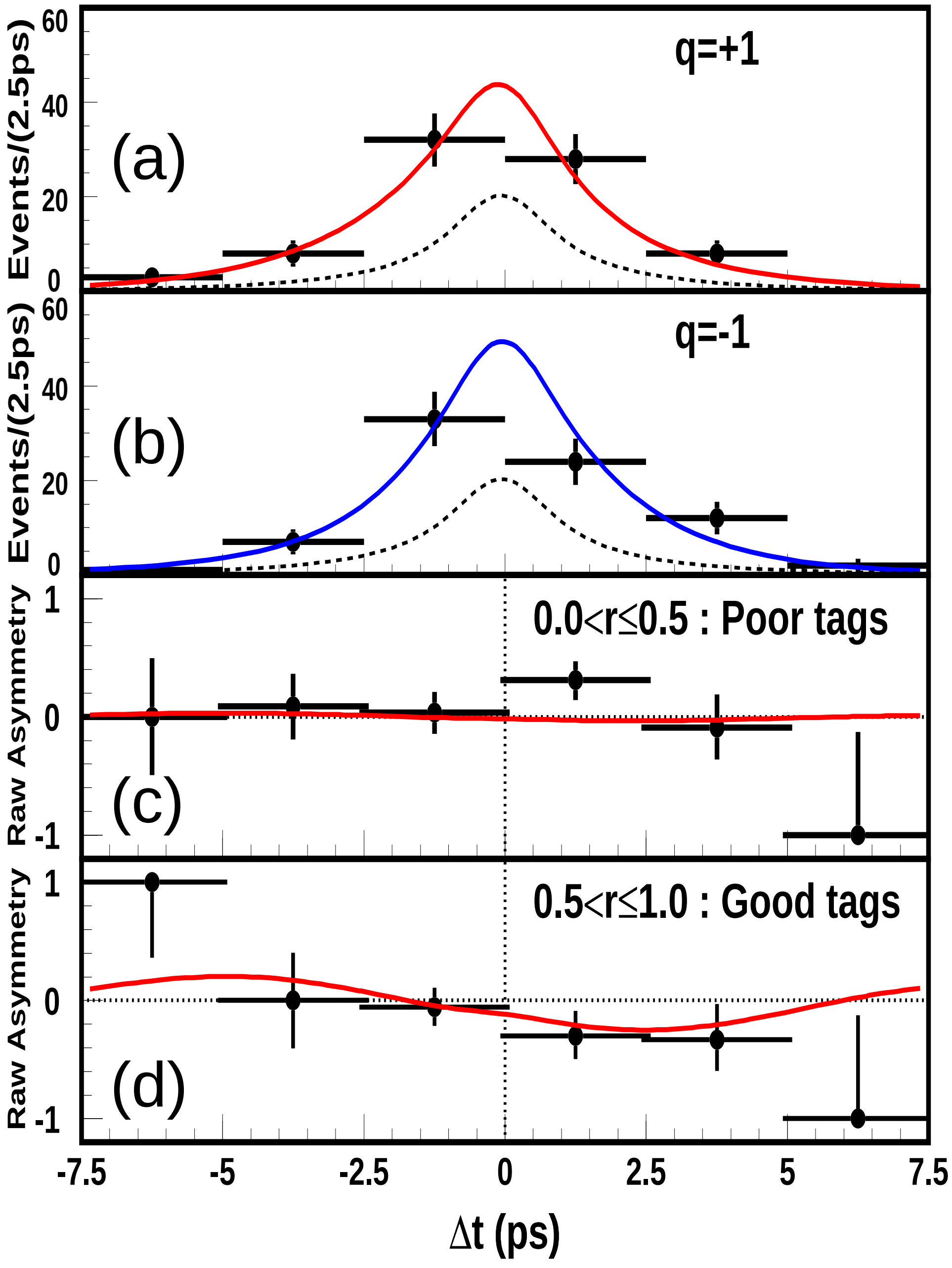

Figure 6.3: *The* Δt *distributions with a 140 fb*$^{-1}$ *data sample: (a)* $q = +1$ *tagged candidates; (b)* $q = -1$ *tagged candidates; (c) time dependent* CP *asymmetry for* $0 < r \leq 0.5$ *candidates; (d) time dependent* CP *asymmetry for* $0.5 < r \leq 1.0$ *candidates. Filled circles with error bars show data, the solid lines show the fit results and dashed lines show the background.*

Source	$\mathcal{S}_{D^{*+}D^{*-}}$	$\mathcal{A}_{D^{*+}D^{*-}}$
Vertex Reconstruction	0.054	0.027
Flavor Tagging	0.036	0.022
Resolution Function	0.047	0.010
Fit Bias	0.039	0.0017
Background	0.043	0.022
Physics Parameters	0.022	0.00021
Polarization	0.055	0.014
Tag-Side Interference	0.0074	0.034
Sum	0.12	0.06

Table 6.4: *Systematic uncertainties of* $B^0 \to D^{*+}D^{*-}$ *CP asymmetries*

6.5.2 Vertex Reconstruction

Δt Selection Dependence

We used events which satisfied $|\Delta t| < 70$ ps. In order to evaluate this selection dependence, we changed the limit to 10 ps and infinity.

Vertex Selection Dependence

We required $\xi < 100$ for CP and tagging side vertices. We changed the limit to 50 and 150.

Track Selection for Tagging Side Vertex

The track selection criteria for the tagging side vertex were $|dr| < 500$ μm and the error on $z < 500$ μm. The systematic error due to the track selection criteria for the tagging side vertexing is estimated by varying the requirement for $|dr|$ and the error of z by ±10%.

Δz Bias

Possible differences between measured Δz distribution and true Δz distribution are taken into account. The Δz bias depends on charge, momentum and angle of each track. The source of Δz bias is considered as misalignment between the SVD and the CDC. The correction parameters are obtained from the large amount of events. They were then applied to whole tracks in the event candidates, to estimate the uncertainty in Δz.

Scaling Error Dependence

For each charged track, errors on tracking parameters are corrected by global scaling parameters obtained from cosmic ray events. We compare fit results with and without these global scaling parameters, and take the difference as a source of systematic errors.

Flight Length of B Meson

When the IP constraint is used, we take into account the finite flight length of B meson in the x-y plane. It is modeled by a Gaussian function with $\sigma = 21\ \mu$m, although it actually has an exponential component. We estimated the systematic error by varying the σ of the Gaussian function by $\pm 10\ \mu$m.

6.5.3 Flavor Tagging

Wrong Tagging Fraction

The systematic errors associated with w_l and Δw_l are estimated by following the "basic rule". We divide w_l and Δw_l into six r regions, and add them in quadrature.

Decay-mode dependence in wrong-tag fractions

We used w_l and Δw_l that are determined from flavor-specific decay modes, such as $D^{(*)}l\nu$, $D^{(*)}\pi$, etc., from data. For the $B^0 \to D^{*+}D^{*-}$ decay, these w_l and Δw_l parameters may have some difference owing to flavor-non-specific decays, the difference in the track multiplicity and so on. Using w_l and Δw_l obtained from 171×10^6 MC samples for each $B^0 \to D^{*+}D^{*-}$ and $\overline{B}^0 \to D^{*+}D^{*-}$, we repeat the CP fit to evaluate the systematic uncertainties.

6.5.4 Resolution Function

The estimation of the systematic uncertainty that comes from the resolution function follows the "basic rule". In our nominal fit, we assume that the scaling parameter for R_{det} has a linear ξ dependence for multi-D case. This assumption overestimates the scaling parameter in a region for large ξ, although the number of events in the region is small. We estimate the possible systematic uncertainty due to this assumption, with comparing the linear function model and a more complex function model.

6.5.5 Fit Bias

We test a linearity of CP asymmetry measurements using MC events. Figures 6.4 show the results from Geant MC, and Figures 6.5 show the results from an ensemble test. Detail for each figure is described in Sec. 6.6.2.

We find that the linearity of the ensemble test shows a slight deviation from an ideal line. We take the deviation for the measured value as the systematic error.

6.5.6 Background

Background Fraction

Background fractions are determined on an event-by-event basis from the the ΔE and M_{bc} values. The parameters to model the ΔE and M_{bc} shapes are varied according to

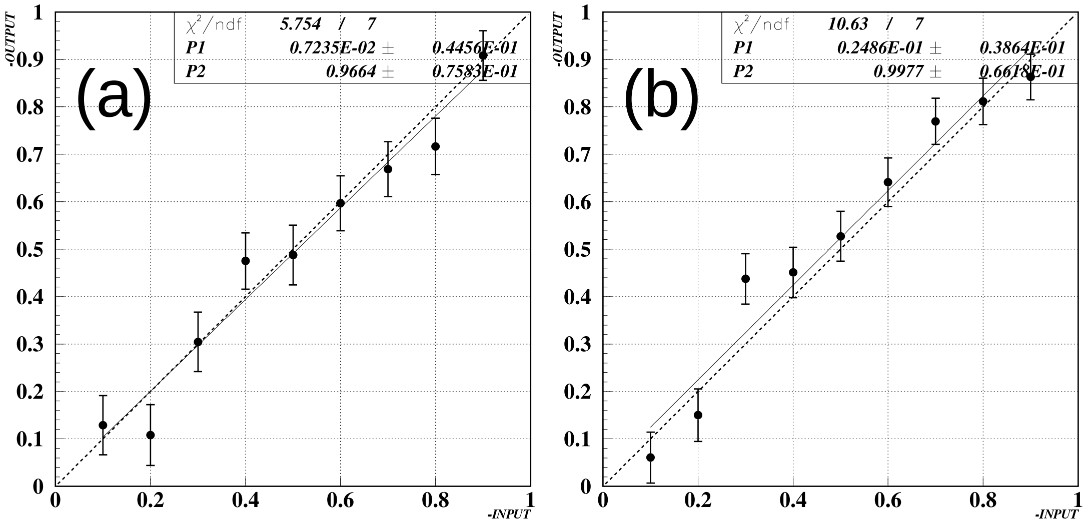

Figure 6.4: *Linearity tests with Geant MC: (a)* $\mathcal{S}_{D^{*+}D^{*-}}$ *for the* D^0-$\overline{D}^0$ *combination; (b)* $\mathcal{S}_{D^{*+}D^{*-}}$ *for the* D^+-$\overline{D}^0$ *combination. Filled circle with error is mean of output results. The dashed line is ideal shape (input=output). The solid line is the linear function fitted by output results.*

the “basic rule” to estimate the systematic uncertainty.

Background Δt Shape

The systematic error coming from parameters describing Δt shape is also estimated by the “basic rule”.

Background CP Contents

From a study of the background sources in generic decay MC samples, we estimate that the fraction of B decay background events that may have CP asymmetries is at most 10%. In the nominal fit, we thus assume that background does not have a CP asymmetry.

In order to evaluate a possible systematic effect due to this approximation, we assume that 10% of the background has CP asymmetry $S_{\rm bg} = \pm \sin 2\phi_1$. The resulting deviation from the nominal fit result is taken as the systematic error.

Misreconstructed Events

Similar to the case of polarization measurement, which is described in Sec. 5.3.8, the effect of misreconstructed events is studied. We change the likelihood function as follows:

$$\mathcal{L} = \prod (1 - f_{\rm ol})\{f_{\rm corr}P_{\rm corr} + f_{\rm miss}P_{\rm miss} + (1 - f_{\rm corr} - f_{\rm miss})P_{\rm bg}\} + f_{\rm ol}P_{\rm ol}, \qquad (6.14)$$

where $f_{\rm corr}$ is a fraction of correctly-reconstructed signal events and $P_{\rm corr}$ is its signal PDF. $f_{\rm miss}$ is a fraction of misreconstructed signal events and $P_{\rm miss}$ is its signal PDF. We

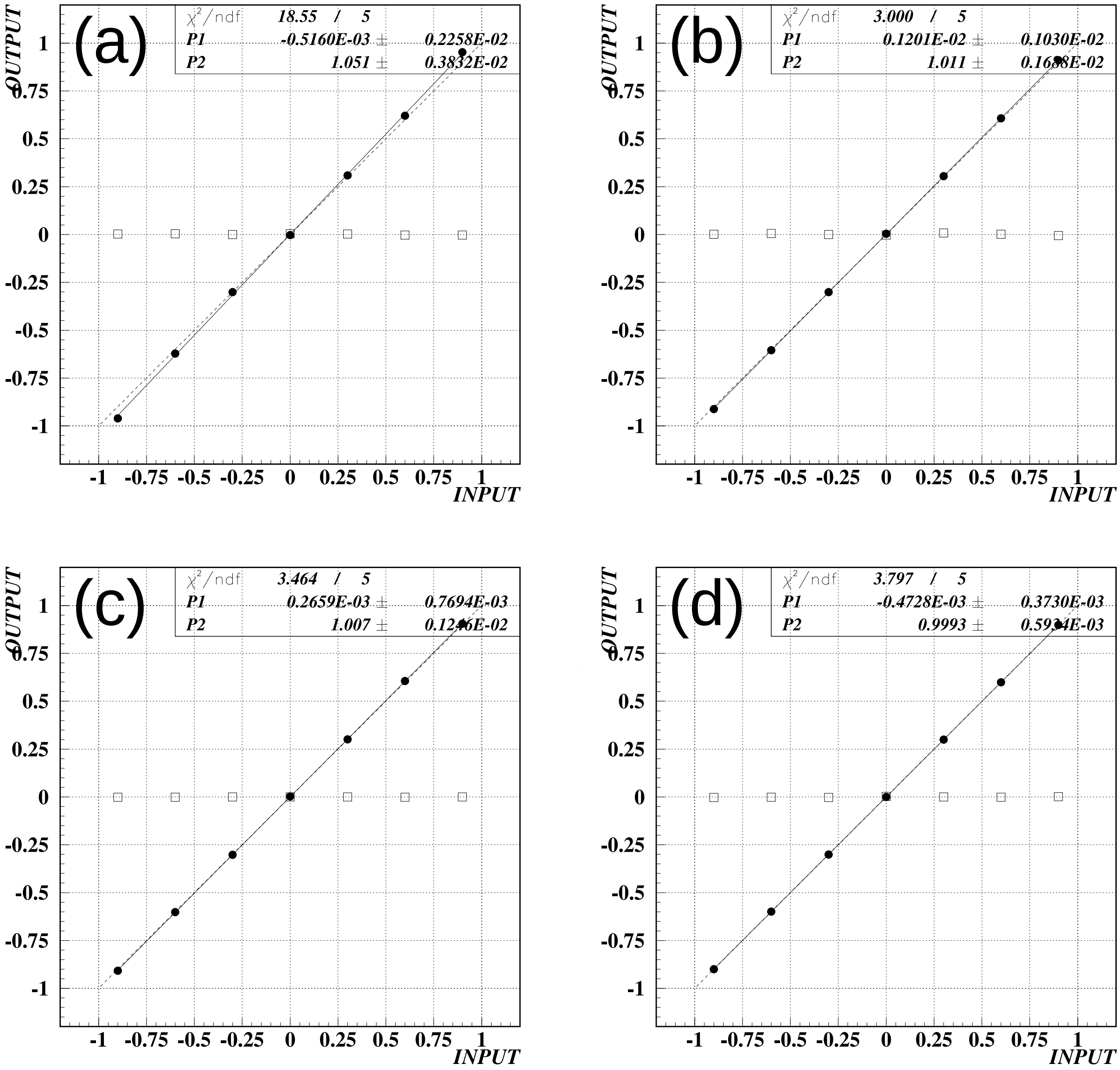

Figure 6.5: *Results of an ensemble test for* $\mathcal{S}_{D^{*+}D^{*-}}$ *and* $\mathcal{A}_{D^{*+}D^{*-}}$*: (a)* $\mathcal{S}_{D^{*+}D^{*-}}$ *ensemble test at* 140 fb^{-1}*; (b)* $\mathcal{A}_{D^{*+}D^{*-}}$ *ensemble test at* 140 fb^{-1}*; (c)* $\mathcal{S}_{D^{*+}D^{*-}}$ *ensemble test at* 1 ab^{-1}*; (d)* $\mathcal{A}_{D^{*+}D^{*-}}$ *ensemble test at* 1 ab^{-1}*. Filled circle is mean of fitted output results. Open square shows* $\mathcal{S}_{D^{*+}D^{*-}}$ *(input=0) fit results for* $\mathcal{A}_{D^{*+}D^{*-}}$ *test, and* $\mathcal{A}_{D^{*+}D^{*-}}$ *(input=0) fit results for* $\mathcal{S}_{D^{*+}D^{*-}}$ *test. The dashed line is ideal shape (input=output). The solid line is the linear function fitted by output results.*

repeat the measurement of CP asymmetry parameters with these separate PDF's. The difference between two methods is considered as the systematic uncertainty.

6.5.7 Physics Parameters

We used B^0 lifetime, τ_{B^0}, and the mass difference between B mass eigenstates, Δm_d, obtained from the semi-leptonic and hadronic B^0 decays [13]. Uncertainties due to these measurements are estimated by the "basic rule".

6.5.8 Polarization

Uncertainties from $R_\perp$ and R_0 which are obtained in the angular analysis are also estimated with the "basic rule".

6.5.9 Tag-Side Interference

We investigate the effects of interference between CKM-favored and CKM-suppressed $B \to D$ transitions in the final state of the accompanying B meson [48]. A small correction to the PDF for the signal distribution arises from the interference. We estimate the amount of correction using the $B^0 \to D^{(*)} l\nu$ sample. We then generate MC pseudo-experiments and make an ensemble test to obtain systematic biases in $\mathcal{S}_{D^{*+}D^{*-}}$ and $\mathcal{A}_{D^{*+}D^{*-}}$. We take the dilution effect due to CP-odd component of $B^0 \to D^{*+}D^{*-}$ ($R_\perp = 0.19$) into account.

6.6 Validation Checks for CP Asymmetry Measurement

6.6.1 Ensemble Test

We perform an ensemble test in a similar way to the polarization measurement described in Sec. 5.4.1. The MC experiments for the ensemble test are generated with the same PDF's and resolution parameters used in the fit to data including measured polarization and CP asymmetries. Figures 6.6 and 6.7 show the distributions of central values, positive errors that corresponds to $+1\sigma$, negative errors that corresponds to -1σ, and pulls that are defined as (output-input)/(error of the fit), respectively. Figure 6.8 shows a plot for whole pseudo-experiments. Results are summarized in Table 6.5. The result of the ensemble test tells us that there is no fit bias and our error sizes in data are consistent with expectations.

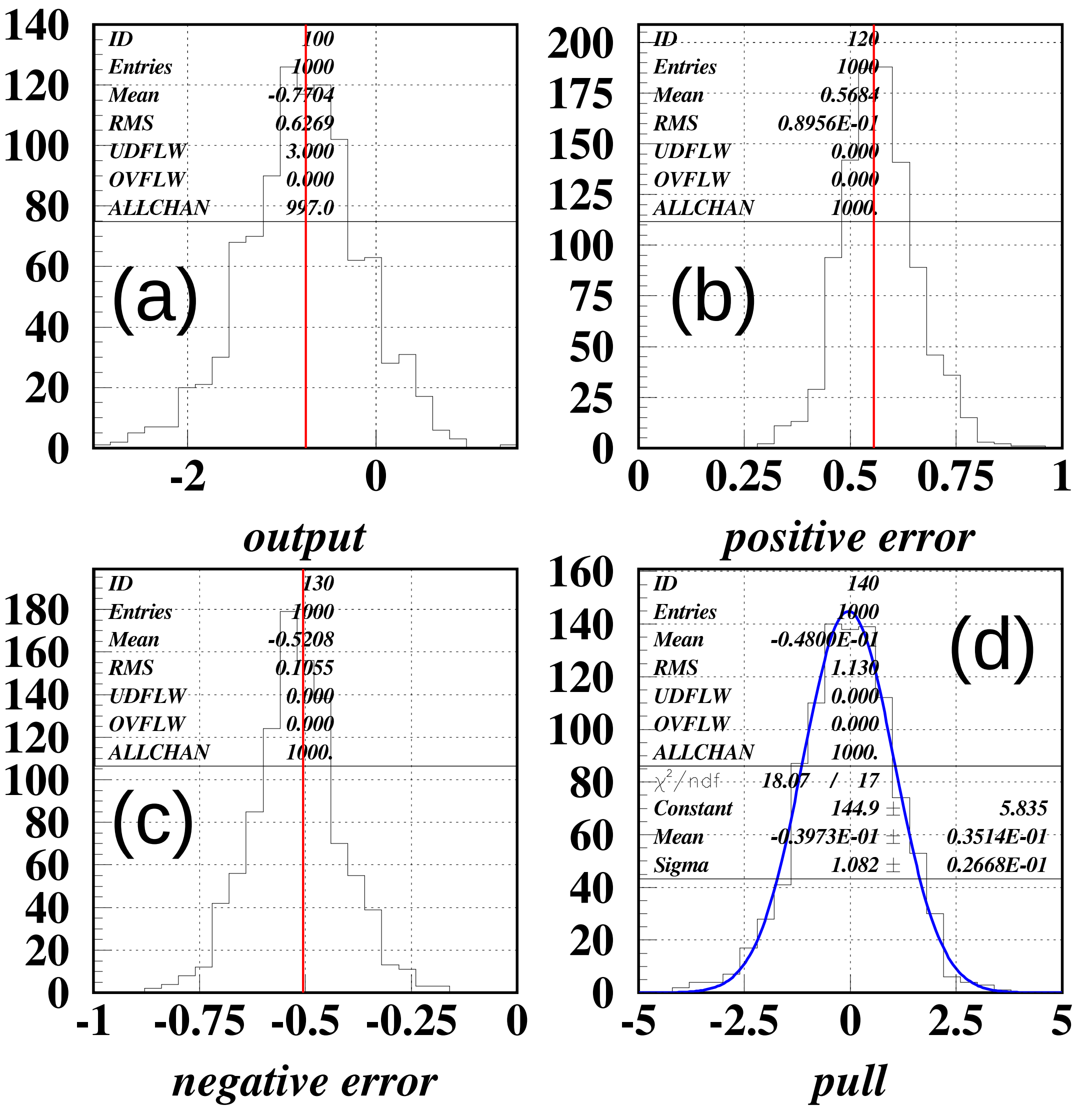

Figure 6.6: *Results of an ensemble test for* $\mathcal{S}_{D^{*+}D^{*-}}$*: (a) The central values; (b) The positive errors; (c) The negative errors; (d) The pulls. Vertical lines show our measurements.*

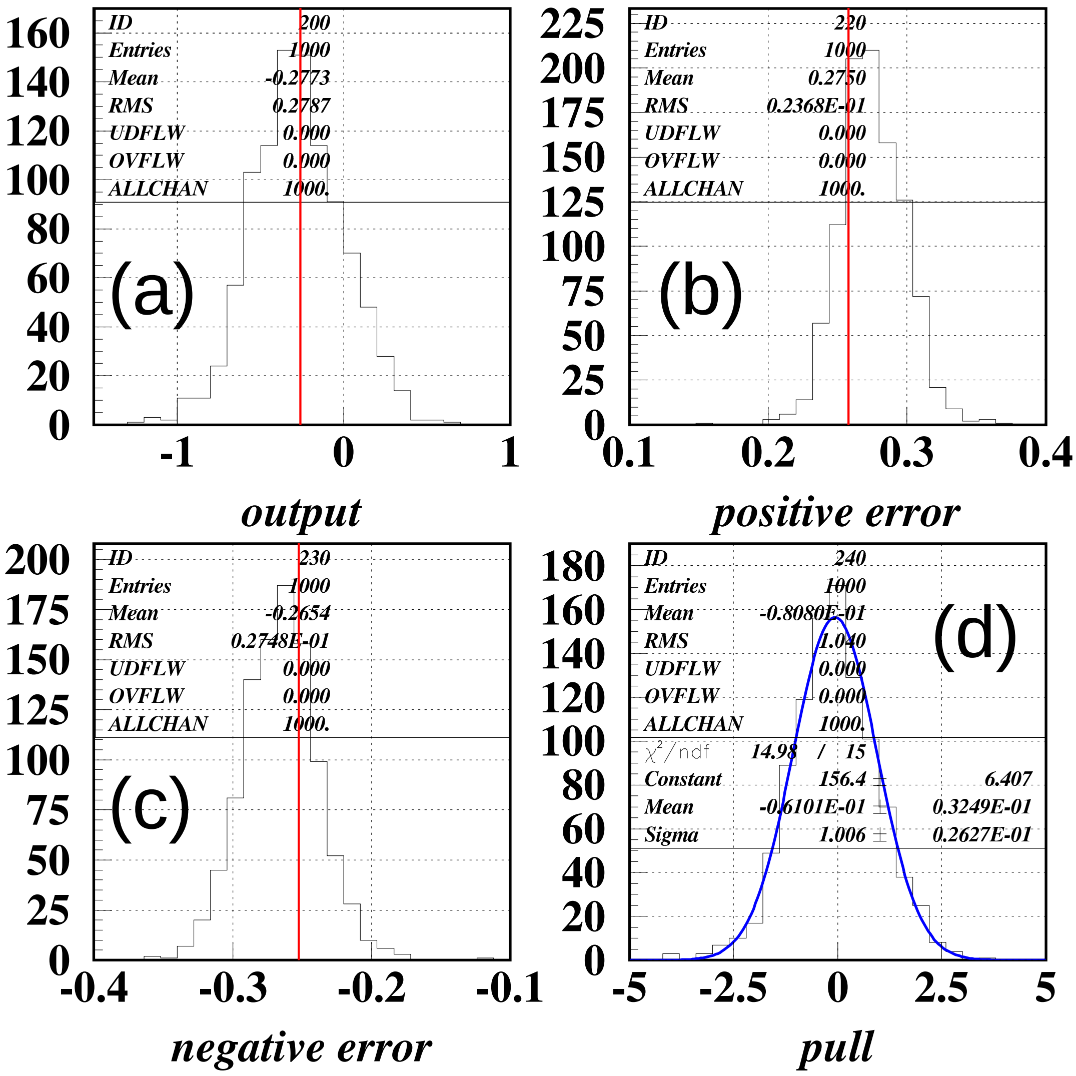

Figure 6.7: *Results of an ensemble test for* $\mathcal{A}_{D^{*+}D^{*-}}$*: (a) The central values; (b) The positive errors; (c) The negative errors; (d) The pulls. Vertical lines show our measurements.*

	$\mathcal{S}_{D^{*+}D^{*-}}$	$\mathcal{A}_{D^{*+}D^{*-}}$
Measured	$-0.7476^{+0.5559}_{-0.5049}$	$-0.2612^{+0.2578}_{-0.2525}$
Input	-0.7476	-0.2612
Output(mean)	-0.7704	-0.2773
Output(RMS)	0.6269	0.2787
Positive error(mean)	0.5684	0.2750
Negative error(mean)	-0.5208	-0.2654
Pull	1.08 ± 0.03	1.01 ± 0.03

Table 6.5: Ensemble test results for the CP asymmetries measurement

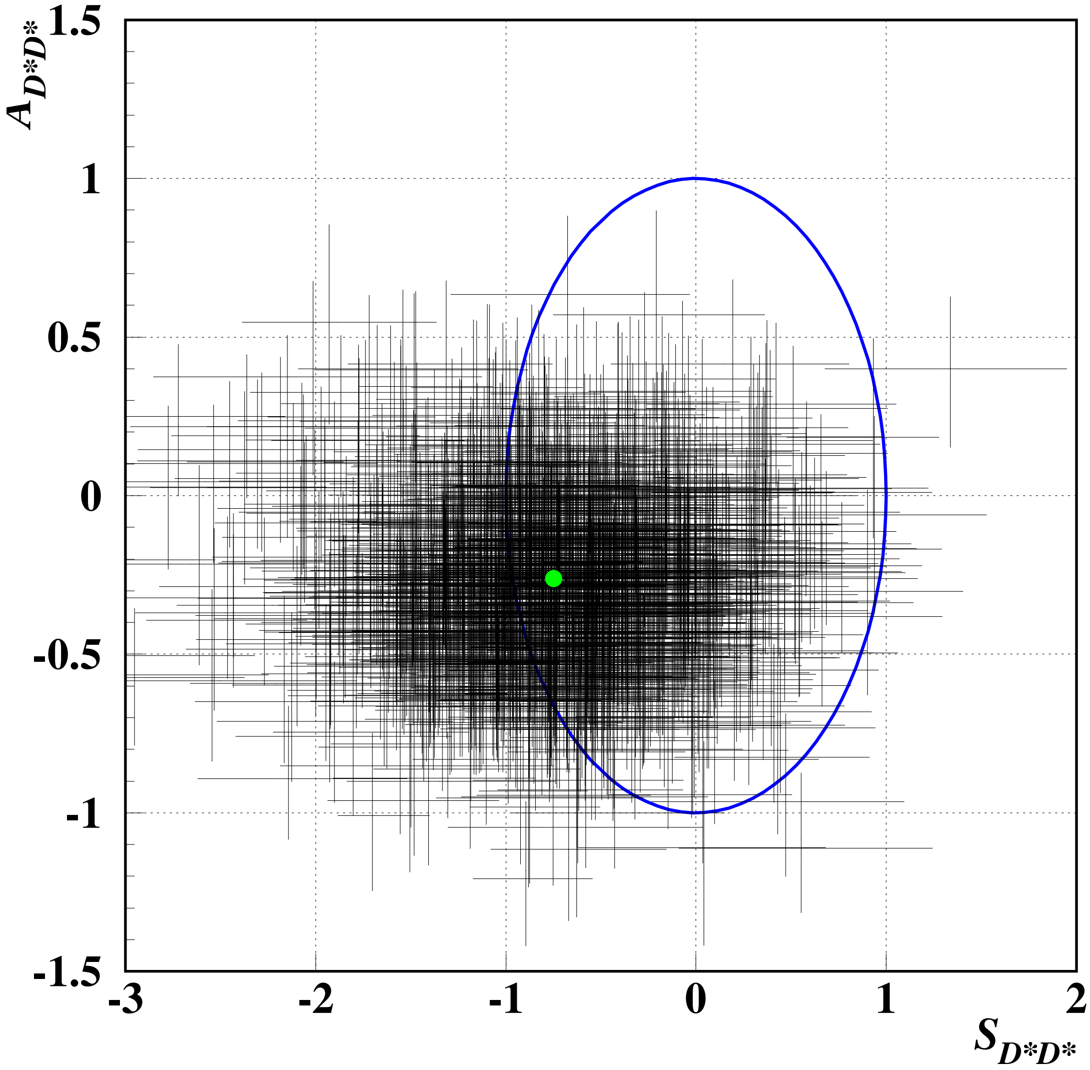

Figure 6.8: *Results of an ensemble test. Each cross corresponds to each pseudo-experiment and the cross point shows the center values. The length of each cross shows the statistical error of each pseudo-experiment. The small circle shows our measurement. The ellipse show physical boundaries.*

6.6.2 Linearity Test

Linearity Test with Geant MC

Linearity check with Geant MC is performed. Only $\mathcal{S}_{D^{*+}D^{*-}}$ is varied and $\mathcal{A}_{D^{*+}D^{*-}}$ is fixed at 0. To check mode dependence, we prepare separate samples for D^0-$\overline{D}^0$ and D^+-$\overline{D}^0$ combinations. Figures 6.4 show the results of ensemble tests. Fit results show that there is no bias.

Linearity Test with Ensemble Test

Linearity check with MC pseudo-experiments is also performed. We generate 10000 pseudo-experiments, each of which contains same statistics as data, for each input parameters. Figure 6.5 (a) shows a small mean shift that depends on $\mathcal{S}_{D^{*+}D^{*-}}$. It is not seen in $\mathcal{A}_{D^{*+}D^{*-}}$ which is plotted in Fig. 6.5 (b). The small bias is seen when fit results are outside physical boundary. We also test the case that corresponds to 1000 fb^{-1} [Figs. 6.5 (c) and (d)]. We do not see any bias in both plots. We thus conclude that the small bias is due to limited statistics. We include this shift in the systematic uncertainty. To confirm our fit method, we repeat the same check with $J/\psi K^0_S$ pseudo experiments which corresponds to 140 fb^{-1}. Figures 6.9 show fit results. Both $\mathcal{S}_{J/\psi K^0_S}$ and $\mathcal{A}_{J/\psi K^0_S}$ terms show good linearity.

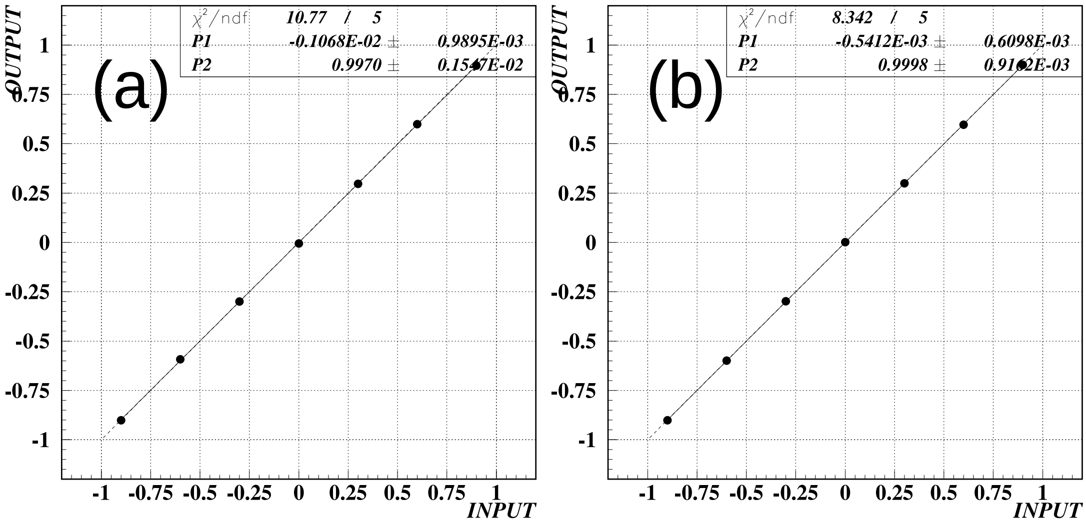

Figure 6.9: *Results of an ensemble test for* $\mathcal{S}_{J/\psi K^0_S}$ *and* $\mathcal{A}_{J/\psi K^0_S}$*: (a)* $\mathcal{S}_{J/\psi K^0_S}$ *ensemble test at* 140 fb^{-1}*; (b)* $\mathcal{A}_{J/\psi K^0_S}$ *ensemble test at* 140 fb^{-1}*; Filled circle is mean of fitted output results. The dashed line is ideal shape (input=output). The solid line is the linear function fitted by output results.*

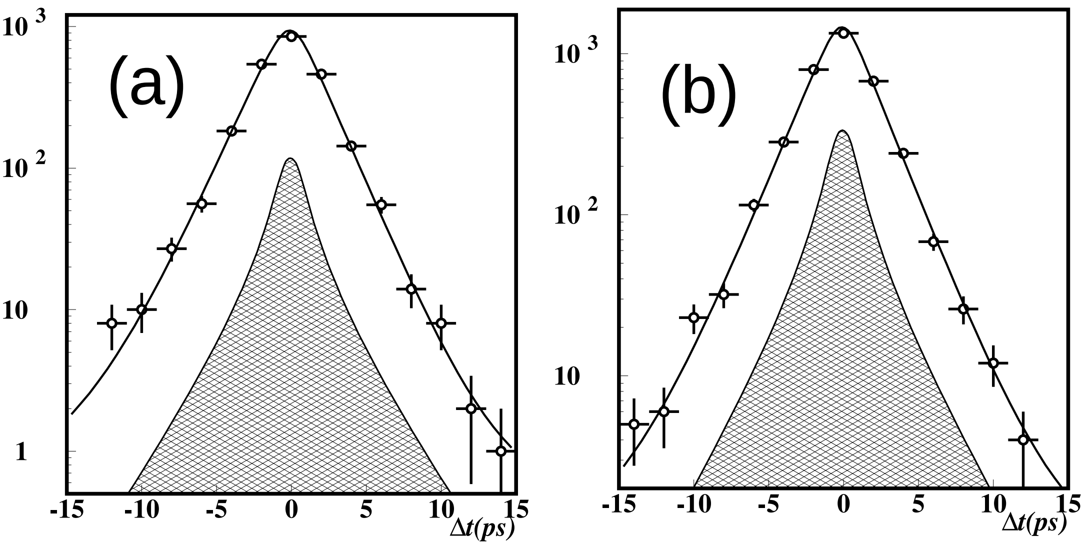

Figure 6.10: *The* Δt *distribution for (a)* $B^0 \rightarrow D^{(*)}D_s^{(*)}$ *(b)* $B^+ \rightarrow D^{(*)}D_s^{(*)}$. *The solid curve represents the fit and the hatched curve represents the background.*

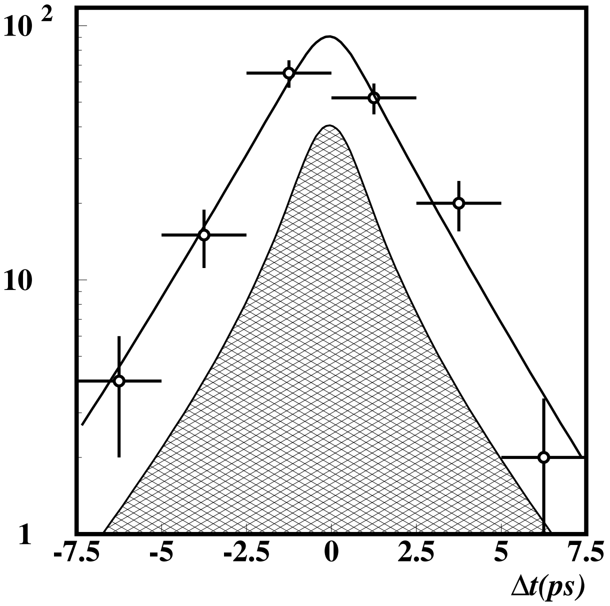

Figure 6.11: *The* Δt *distribution for the* $B^0 \rightarrow D^{*+}D^{*-}$. *The solid curve represents the fit and the hatched curve represents the background.*

6.6.3 B Lifetime measurement

The B^0 lifetime is measured with the same data set. To check consistency and to obtain resolution parameters from data, B^0 and B^+ lifetimes are also measured with the $D^{(*)}D_s^{(*)}$ control samples. From the control sample, fit results are as follows:

$$\begin{aligned} \tau_{B^+} =& \quad 1.68 \pm 0.04 \text{ (ps) [PDG2003 [13] : } 1.671 \pm 0.018 \text{ (ps)]}, \\ \tau_{B^0} =& \quad 1.60^{+0.05}_{-0.04} \text{ (ps) [PDG2003 [13] : } 1.537 \pm 0.015 \text{ (ps)]}, \end{aligned} \tag{6.15}$$

where our errors are only statistical, while PDG values include both statistical and systematic uncertainties. From the $D^{*+}D^{*-}$ data,

$$\tau_{B^0} = 1.7 \pm 0.2 \text{ (ps)}. \tag{6.16}$$

Figs. 6.10 and Fig. 6.11 show the Δt distributions for the lifetime measurements for $B^0 \to D^{(*)}D_s^{(*)}$, $B^+ \to D^{(*)}D_s^{(*)}$ and $B^0 \to D^{*+}D^{*-}$ decays. These results are consistent with the world average values [13].

6.6.4 Null Asymmetry Test

To check reconstruction bias, we perform CP asymmetry measurement with control samples which should have no CP asymmetry. We use the same procedure as the $B^0 \to D^{*+}D^{*-}$ measurement. Only a CP-even term is assumed in the PDF used for the fit. The fit yields:

$$\begin{aligned} \mathcal{S}_{B^0 \to D^{(*)}D_s^{(*)}} =& \quad -0.12 \pm 0.08, \\ \mathcal{A}_{B^0 \to D^{(*)}D_s^{(*)}} =& \quad +0.02 \pm 0.05, \\ \mathcal{S}_{B^+ \to D^{(*)}D_s^{(*)}} =& \quad -0.10 \pm 0.07, \\ \mathcal{A}_{B^+ \to D^{(*)}D_s^{(*)}} =& \quad -0.001 \pm 0.050. \end{aligned} \tag{6.17}$$

Time-dependent CP asymmetry plots are shown in Figs. 6.12. These results show that there is no asymmetry.

6.6.5 Polarization Blind Fit

We perform a fit assuming no polarization. In other words, we ignore the dilution from the CP-odd component. The fit yields:

$$\begin{aligned} \mathcal{S}_{D^{*+}D^{*-}} &= -0.57 \pm 0.45, \\ \mathcal{A}_{D^{*+}D^{*-}} &= -0.29 \pm 0.26. \end{aligned} \tag{6.18}$$

This result suggests that the CP-odd component is small, supporting our polarization measurement in Chapter 5.

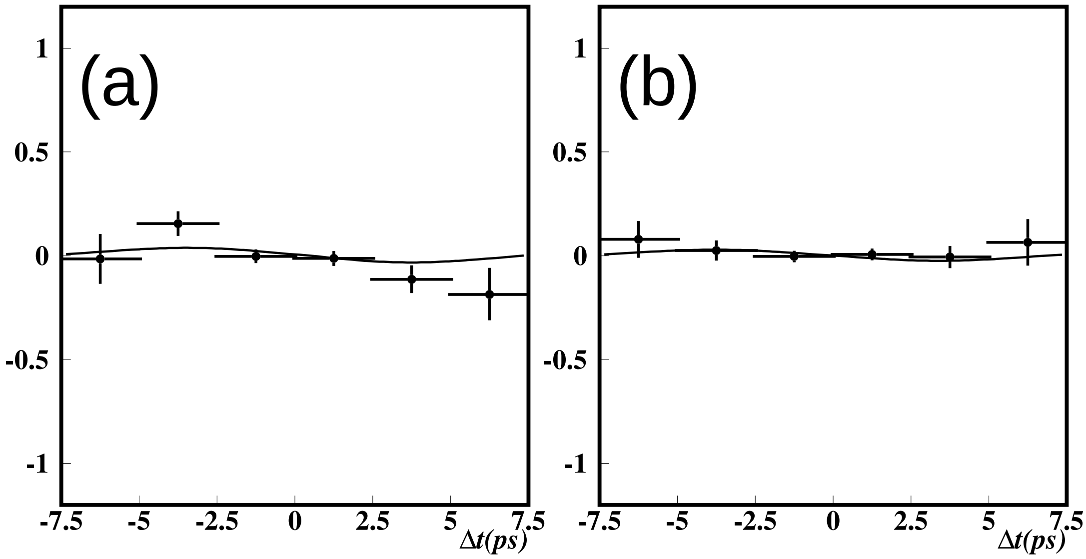

Figure 6.12: *Null asymmetry test for (a)* $B^0 \to D^{(*)}D_s^{(*)}$ *(b)* $B^+ \to D^{(*)}D_s^{(*)}$*. The solid curve represents the fit.*

6.6.6 Special Event Scanning

A further check is made to know whether we have special events that are sensitive to the central values or errors. We repeat the fit with removing each event from whole data sample. The results are plotted in Fig. 6.13. We do not find any event that largely shift the result.

6.6.7 Likelihood Scanning

We scan log-likelihood ratio $-2\ln(\mathcal{L}/\mathcal{L}_{\rm max})$ distribution as function of $\mathcal{S}_{D^{*+}D^{*-}}$ or $\mathcal{A}_{D^{*+}D^{*-}}$. Figures 6.14 show results. Both plots are consistent with parabolic behavior around $\mathcal{L}_{\rm max}$.

6.7 Summary of Time-Dependent CP Asymmetry Measurement

We obtain the following CP asymmetry parameters for the $B^0 \to D^{*+}D^{*-}$ decay with 140 fb^{-1} data sample.

$$\begin{aligned}\mathcal{S}_{D^{*+}D^{*-}} &= -0.75 \pm 0.56(\text{stat}) \pm 0.12(\text{syst}),\\ \mathcal{A}_{D^{*+}D^{*-}} &= -0.26 \pm 0.26(\text{stat}) \pm 0.06(\text{syst}).\end{aligned}$$

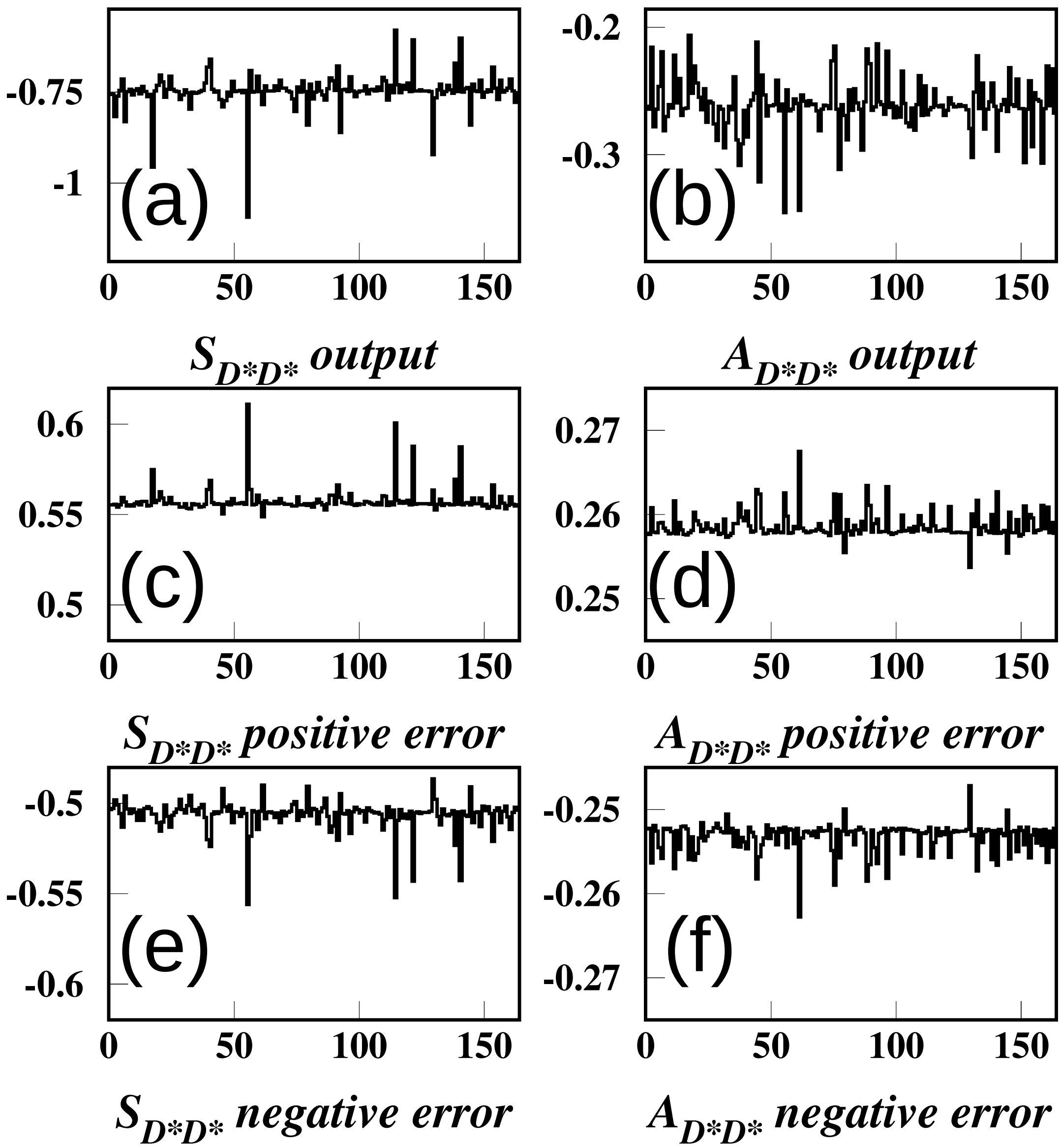

Figure 6.13: *Special event scanning during CP asymmetries measurement for (a) $\mathcal{S}_{D^{*+}D^{*-}}$ output; (b) $\mathcal{A}_{D^{*+}D^{*-}}$ output; (c) $\mathcal{S}_{D^{*+}D^{*-}}$ positive error; (d) $\mathcal{A}_{D^{*+}D^{*-}}$ positive error; (e) $\mathcal{S}_{D^{*+}D^{*-}}$ negative error; (f) $\mathcal{A}_{D^{*+}D^{*-}}$ negative error. The horizontal axis shows the id of the removed event.*

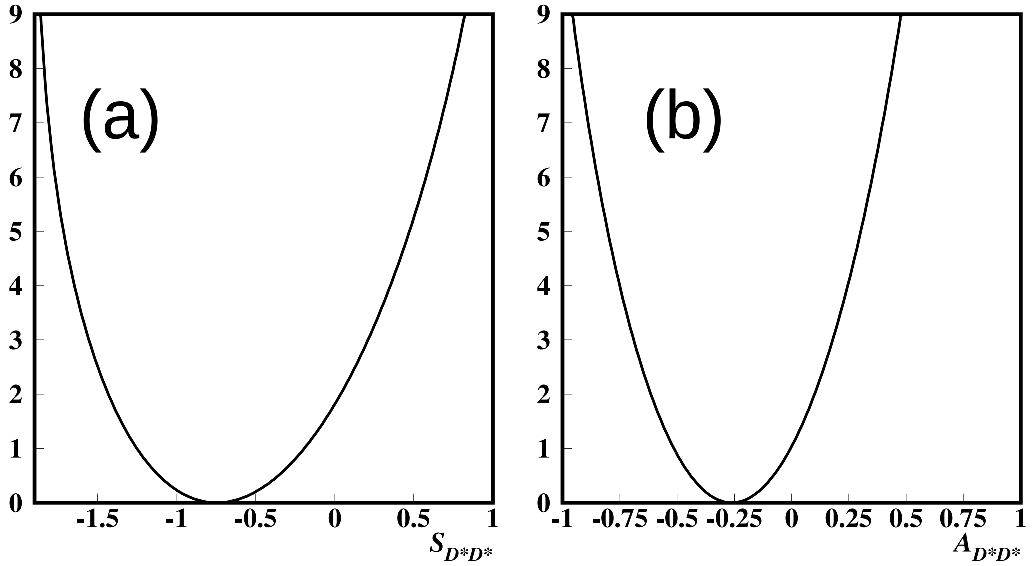

Figure 6.14: $-2\ln(\mathcal{L}/\mathcal{L}_{\max})$ *distribution as function of* (a) $\mathcal{S}_{D^{*+}D^{*-}}$ (b) $\mathcal{A}_{D^{*+}D^{*-}}$.

Chapter 7

Discussion

7.1 Comparison with Other Measurements

7.1.1 Comparison between $b \to c\bar{c}d$ and $b \to c\bar{c}s$ Modes

Figures 7.1 summarize measurements of CP asymmetry parameters $\mathcal{S}_f$ and $\mathcal{A}_f$, where f denotes each decay mode. Our result is consistent with the world average value for the $b \to c\bar{c}s$ transitions (i.e. $\sin 2\phi_1$) and there is no $b \to c\bar{c}d$ mode which shows a significant inconsistency with the $b \to c\bar{c}s$ measurements.

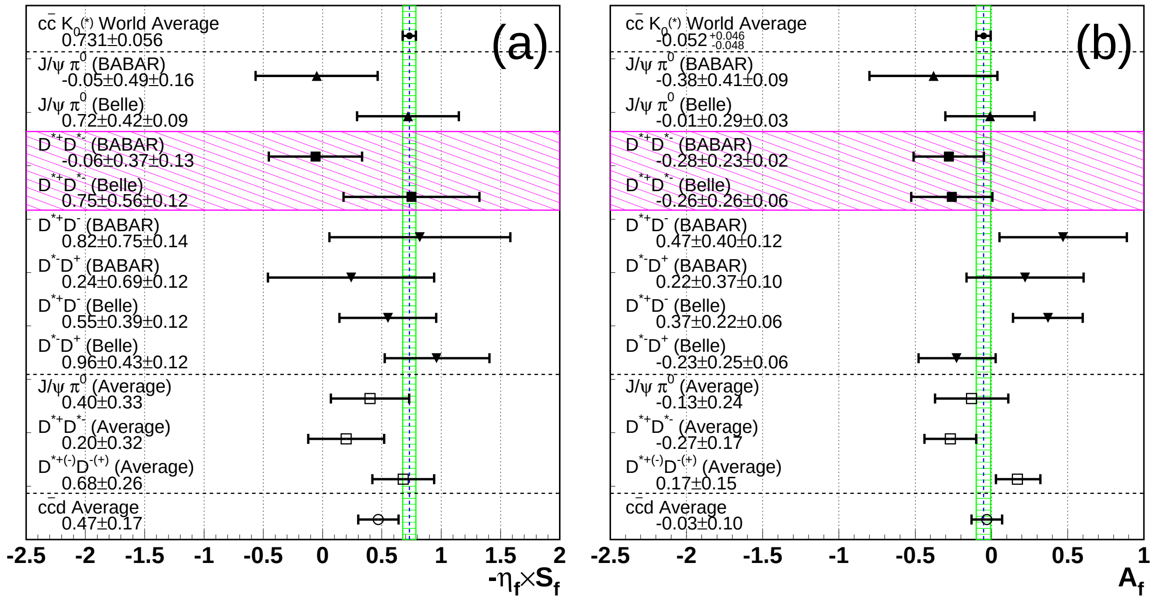

Figure 7.1: *Comparison of the results for time-dependent CP asymmetry measurements of $b \to c\bar{c}s$ and $b \to c\bar{c}d$ modes. (a) Comparison of $-\eta_f \times S_f$, where η_f means internal CP sign; (b) Comparison of A_f. $b \to c\bar{c}s$ is obtained from PDG2003 [13] and other values are obtained from HFAG [49]. Averages of $b \to c\bar{c}d$ modes are computed from Belle and BaBar's results. Bar means total error including statistical and systematics error.*

7.1.2 Comparison with BaBar Experiment

The BaBar collaboration measured CP asymmetry parameters and obtained [27],

$$\begin{aligned} \Im\lambda_+ &= \ 0.05 \pm 0.29 \pm 0.10, \\ |\lambda_+| &= \ 0.75 \pm 0.19 \pm 0.02. \end{aligned} \tag{7.1}$$

These results correspond to

$$\begin{aligned} \mathcal{S}_{D^{*+}D^{*-}+} &= +0.06 \pm 0.37 \pm 0.13, \\ \mathcal{A}_{D^{*+}D^{*-}+} &= -0.28 \pm 0.23 \pm 0.02, \end{aligned} \tag{7.2}$$

where subscripts + indicate that they only measured CP asymmetry parameters for the CP-even component while the CP-odd term is fixed at their $\sin 2\phi_1$ measurement value. In our analysis, on the contrary, we assume that both components have the same absolute value.

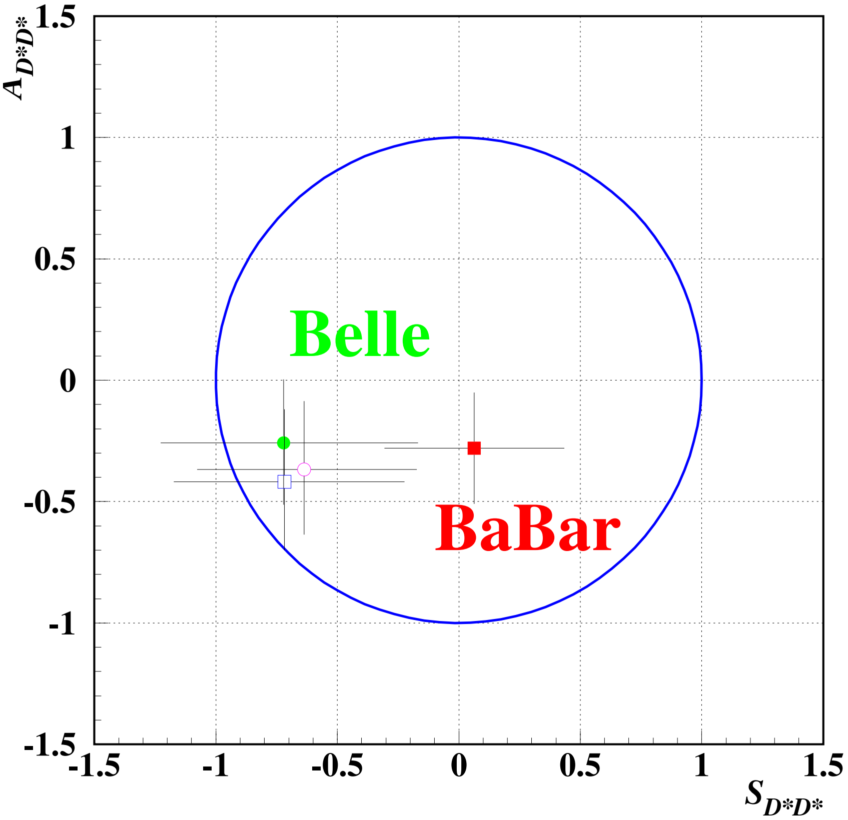

Figure 7.2: *Two-dimensional scatter plot of* CP *asymmetry measurements with different methods. The filled circle shows our nominal fit, the filled square shows BaBar's measurement [27], the open square is the result with fixing* $\mathcal{S}_{D^{*+}D^{*-}\perp}$ *at the world average value of* $\sin 2\phi_1$ *and* $\mathcal{A}_{D^{*+}D^{*-}\perp}$ *at 0. The open circle is the result with using* $R_\perp = 0.063$*. The ellipse shows the physical boundary.*

Following their method, i.e. fixing $\mathcal{S}_{D^{*+}D^{*-}}$ of CP-odd component, $\mathcal{S}_{D^{*+}D^{*-}\perp}$, at the world average value of $\sin 2\phi_1$ and $\mathcal{A}_{D^{*+}D^{*-}}$ of CP-odd component, $\mathcal{A}_{D^{*+}D^{*-}\perp}$ at 0, we obtain

$$\begin{aligned} \mathcal{S}_{D^{*+}D^{*-}+} &= -0.72 \pm 0.50, \\ \mathcal{A}_{D^{*+}D^{*-}+} &= -0.42 \pm 0.30, \end{aligned} \tag{7.3}$$

where only statistical errors are shown. Note that the statistical error of $\mathcal{S}_{D^{*+}D^{*-}}$ depends on the measured value of $R_\perp$, since the fraction of the CP-odd term is considered as a dilution factor to CP asymmetries. To demonstrate the effect of the dilution, we fix $R_\perp$ at the value obtained by the BaBar collaboration (0.063). We obtain

$$\begin{aligned} \mathcal{S}_{D^{*+}D^{*-}+} &= -0.64 \pm 0.46, \\ \mathcal{A}_{D^{*+}D^{*-}+} &= -0.37 \pm 0.28. \end{aligned} \tag{7.4}$$

The statistical errors are much reduced. Figure 7.2 shows a scatter plot of BaBar's result and ours. In spite of applying different methods, our result is always stable around the nominal fit value.

7.2 Significance of the CP Asymmetry Parameters

We evaluate the significance of our obtained CP asymmetry parameters with following the idea proposed by the Feldman and Cousins [50]. To calculate the confidence level, we assume that the two-dimensional distribution of $\mathcal{S}_{D^{*+}D^{*-}}$ and $\mathcal{A}_{D^{*+}D^{*-}}$ is the sum of two Gaussian functions whose standard deviations correspond to measurement errors of $\mathcal{S}_{D^{*+}D^{*-}}$ and $\mathcal{A}_{D^{*+}D^{*-}}$, and use the distribution as the likelihood function. We add statistical and systematic errors in quadrature. Figure 7.3 shows the confidence regions. Our CP asymmetry parameters are consistent with the SM prediction neglecting the penguin contribution; the deviation from the SM point is at a level of 0.54σ. Our fit result is also consistent with the BaBar measurement at a level of 0.91σ. A 2σ confidence region (C.L.=95.45%) covers 47% of the physically allowed region. In other words, 53% of the physically allowed region is ruled out at a 2σ level.

7.3 Assumption of Different λs

As explained in Chap. 1, the $B^0 \to D^{*+}D^{*-}$ decay has in general three kinds of λs corresponding to three polarization amplitudes. While their absolute values should be the same assuming the tree diagram dominance, some difference may exist due to different contributions of penguin diagrams.

We generate pseudo-experiments to investigate such cases. Results are shown in Fig. 7.4. We see a tendency that measured asymmetries mainly depend on input asymmetry values of the CP-even component. The observed differences, which are much smaller than the statistical errors we obtained, indicate that our statistics are not large enough to be sensitive to different penguin contributions. Thus we conclude that our fit method is sufficient for the present data.

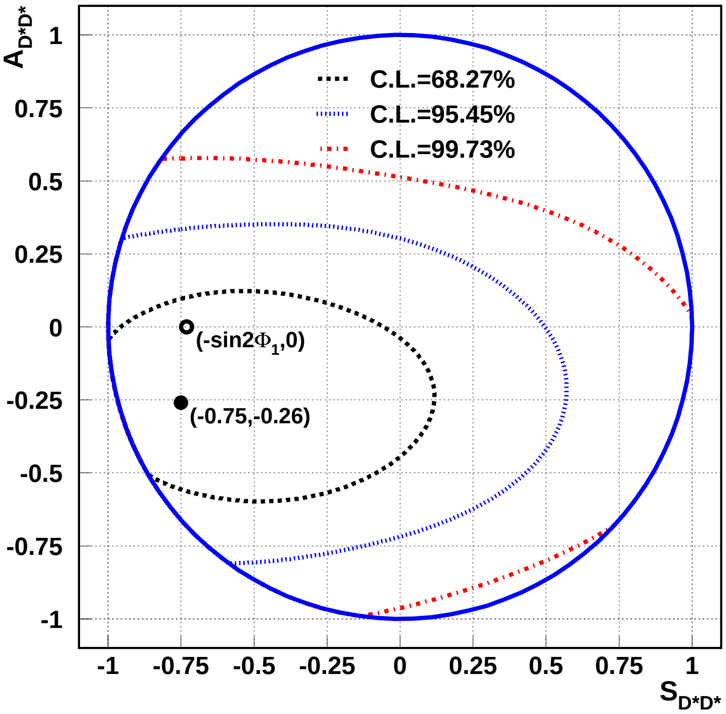

Figure 7.3: *Two-dimensional confidence regions for CP asymmetry measurements. Dashed, dotted, dashed-dotted curves correspond to the confidence level of* 68.27%, 95.45%, 99.73%, *respectively. Filled circle shows our fit result. Open circle shows the world average* ($\mathcal{S}_f = -\sin 2\phi_1, \mathcal{A}_f = 0$) *for the* $b \to c\bar{c}s$ *transitions. The ellipse shows the physical boundary.*

7.4 Constraint on the Physics Parameters

7.4.1 Constraint on the New Physics Parameters

With our obtained CP asymmetry parameters, we evaluate the constraint on the generic new physics parameters, $\phi_{\rm NP}$, $\delta_{\rm N}$ and $|\mathcal{N}|$, which are introduced in Sec. 1.5.3. We compute three-dimensional allowed region for these three parameters, by using Eq. (1.41). Figures 7.5 (a)-(d) show the several slices of the confidence regions. For an illustration, we neglect the contribution from the SM penguin, i.e. $|R| = 0$ is assumed. Although our statistics are limited, some parameter regions are excluded with the confidence level of 99.73%.

7.4.2 Effect of the SM Penguin Parameters

To evaluate the contribution from the SM penguin process, we compute the three-dimensional allowed region for new physics parameters, with assuming $|R| = 0.06$ and $\delta = 12^\circ$. Figure 7.5 (e) shows the slice of the confidence region at $\delta_{\rm N} = 3\pi/4$. Although the shapes of the confidence regions are slightly affected, they are totally unchanged. This tendency supports that $|R| = 0$ assumption is sufficient for the current condition. The correct

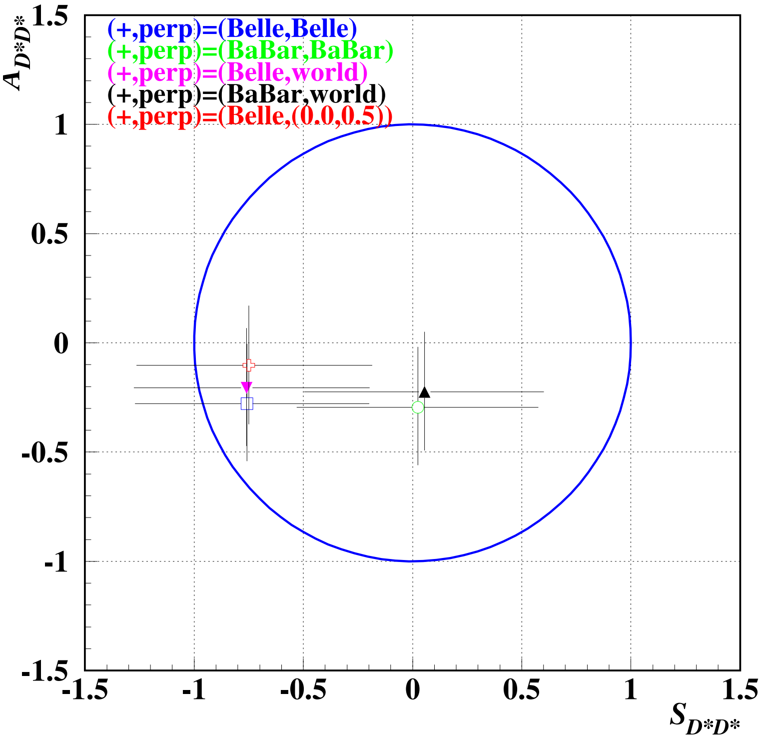

Figure 7.4: *Results of an ensemble test with assuming different CP asymmetries between CP-even and CP-odd components of $B^0 \to D^{*+}D^{*-}$ decays. The inputs for CP-even and CP-odd term are chosen from our result, BaBar's result and the world average ($\mathcal{S}_f = -\sin 2\phi_1, \mathcal{A}_f = 0$). The expression (x, y) denotes that x (y) is an input for the CP-even (CP-odd) term. The open square is the result for the case (Belle,Belle). The inverted triangle is the result using (Belle,world-average). The open circle is the result using (BaBar,BaBar). The triangle is the result using (BaBar,world-average). The cross is the result for an extreme case (Belle, $(\mathcal{S}_{D^{*+}D^{*-}\perp}, \mathcal{A}_{D^{*+}D^{*-}\perp}) = (0, 0.5)$), which demonstrates the stability of our assumption in this analysis. The ellipse shows physical boundary.*

knowledge about $|R|$, however, may help us determine the new physics parameters precisely.

We also demonstrate the constraint on the SM penguin parameters δ and $|R|$, with assuming that there is no new physics ($|\mathcal{N}| = 0$). Figure 7.5 (f) shows the confidence region. From the contour plot, we find the constraint on the SM penguin parameters is not sufficient for theoretically expected region ($|R| \sim$ a few %).

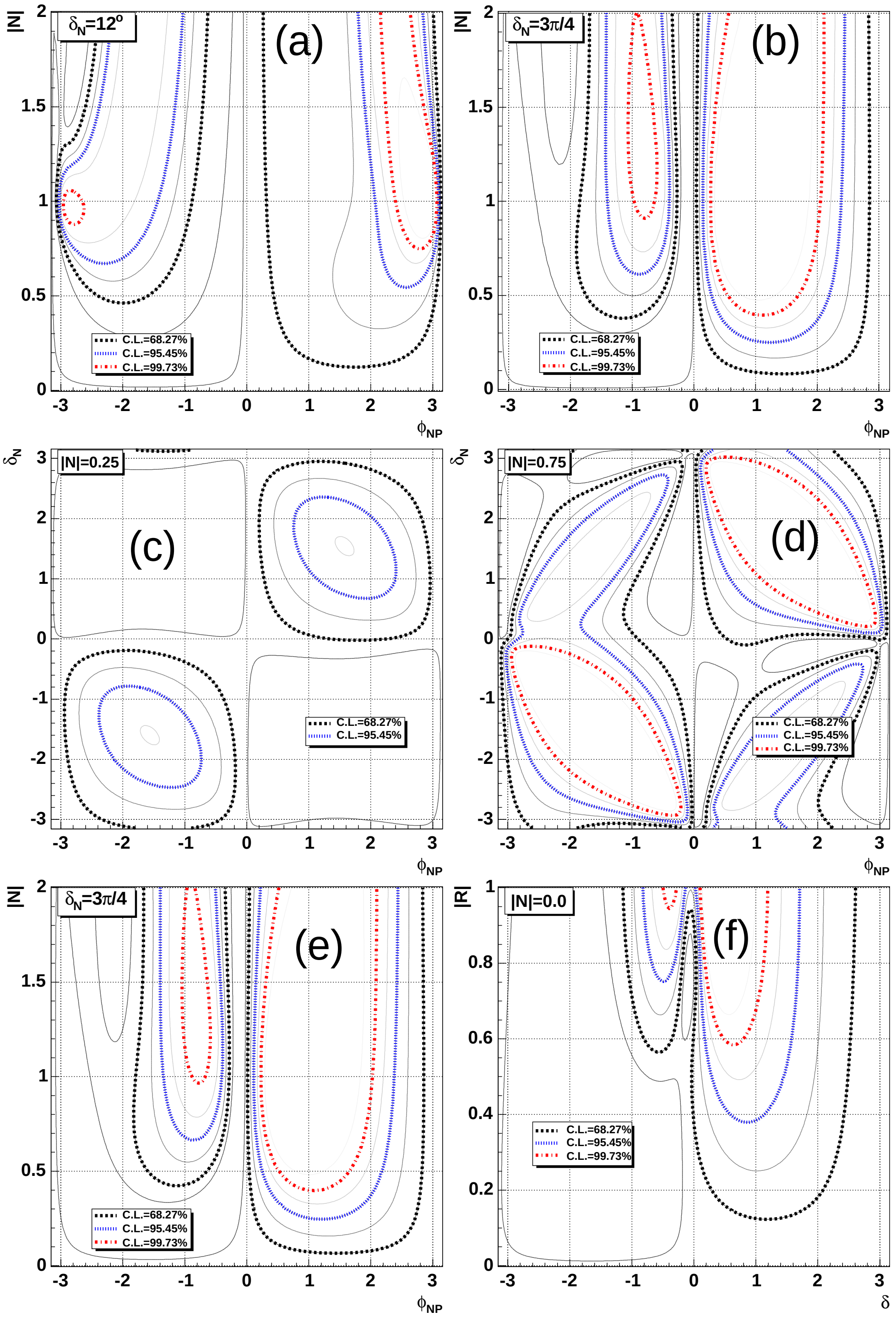

Figure 7.5: *The confidence regions for the SM and new physics parameters; (a)* $|\mathcal{N}|$-$\phi_{\rm NP}$ *plane for* $\delta_{\rm N} = 12°$*; (b)* $|\mathcal{N}|$-$\phi_{\rm NP}$ *plane for* $\delta_{\rm N} = 3\pi/4$*; (c)* $\delta_{\rm N}$-$\phi_{\rm NP}$ *plane for* $|\mathcal{N}| = 0.25$*; (d)* $\delta_{\rm N}$-$\phi_{\rm NP}$ *plane for* $|\mathcal{N}| = 0.75$*; (e)* $|\mathcal{N}|$-$\phi_{\rm NP}$ *plane for* $\delta_{\rm N} = 3\pi/4$ *and* $|R|$*=0.06; (f)* $|R|$-δ *plane for* $|\mathcal{N}| = 0$*. Dashed, dotted, dashed-dotted curves correspond to the confidence level of* 68.27%, 95.45%, *and* 99.73%, *respectively.*

7.5 Future Prospect

As described in previous sections, the uncertainties of our measurement are dominated by statistical errors. This means that we can improve the precision of our measurement by accumulating more data. Within a few years, we expect that the integrated luminosity at Belle will reach 1000 fb^{-1}, which is approximately 7 times larger than the statistics used in this analysis. Furthermore the SuperKEKB upgrade is being planned to accumulate 50000 fb^{-1} of data [51]. As the integrated luminosity increases, some sources of systematic errors, which are limited by the statistics of control samples, will decrease. Examples include errors due to uncertainties of polarization parameters or wrong tag fractions. On the other hand, there are other sources of systematic errors, such as the one due to the Δt cut dependence, which will not decrease. Therefore we divide the sources of systematic errors into two; "reducible" and "irreducible" sources. For $\mathcal{S}_{D^{*+}D^{*-}}$ ($\mathcal{A}_{D^{*+}D^{*-}}$), the total reducible error is 0.10 (0.04) and the irreducible error is 0.06 (0.04) in our measurement. The dominant sources of the irreducible systematic error come from vertex reconstruction.

Figure 7.6 shows future prospects of CP asymmetry measurements for the $B^0 \to D^{*+}D^{*-}$ decay extrapolated from our measurements. The experimental errors will be at the level of 0.06. Figure 7.7 shows the combined confidence regions of 99.73% for the integrated luminosity of 140 fb^{-1}, 1 ab^{-1} and 50 ab^{-1}. We will rule out 97% of physical allowed region with 99.73% confidence level at the integrated luminosity of 50 ab^{-1}. Figures 7.8 and 7.9 demonstrate the sensitive regions for the SM and new physics parameters at the integrated luminosity of 1 ab^{-1}, 50 ab^{-1}, respectively.

Large statistics will also allow us to perform full angular analyses, which use all transversity angles θ_{tr}, θ_1 and ϕ_{tr}, to reduce systematic uncertainties from the polarization measurement. Furthermore, a measurement of ϕ_3, another angle of the unitarity triangle [52], may become possible with large statistics of $B^0 \to D^{*+}D^{*-}$ decays.

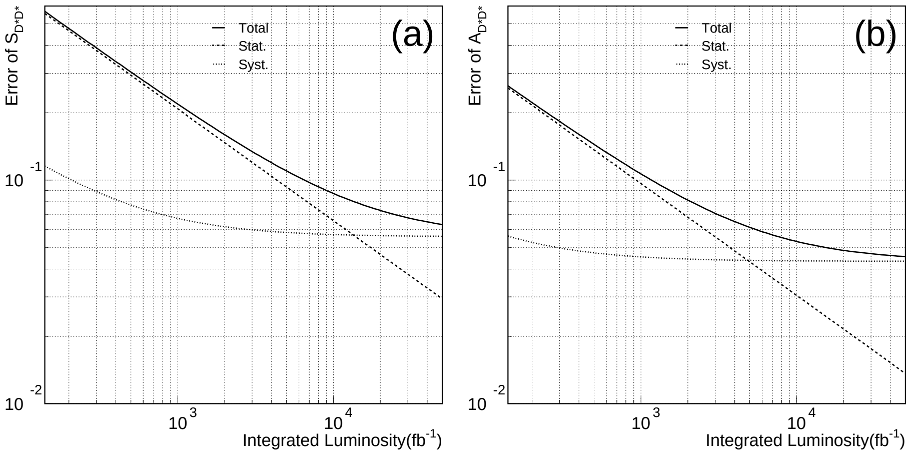

Figure 7.6: *Expected errors of* CP *asymmetry parameters of* $B^0 \to D^{*+}D^{*-}$ *decays as a function of the integrated luminosity. The solid line shows the quadratic sum of statistical and systematic errors. Dashed and dotted lines are statistical and systematic errors, respectively.*

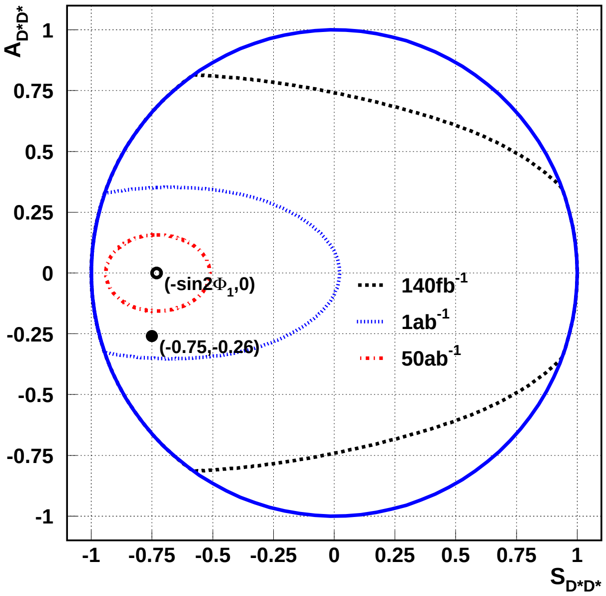

Figure 7.7: *Two-dimensional confidence regions for* CP *asymmetry measurements for future experiments. Dashed, dotted, dashed-dotted curves correspond to the confidence level of* 99.73% *for* 140 fb^{-1}, 1 ab^{-1}, 50 ab^{-1}, *respectively. To illustrate the size of allowed region, we assumed that* $(\mathcal{S}_{D^{*+}D^{*-}} = -\sin 2\phi_1, \mathcal{A}_{D^{*+}D^{*-}} = 0)$. *Filled circle shows our fit result from data. Open circle shows the world average* $(\mathcal{S}_f = -\sin 2\phi_1, \mathcal{A}_f = 0)$ *for the* $b \to c\bar{c}s$ *transitions. The ellipse shows the physical boundary.*

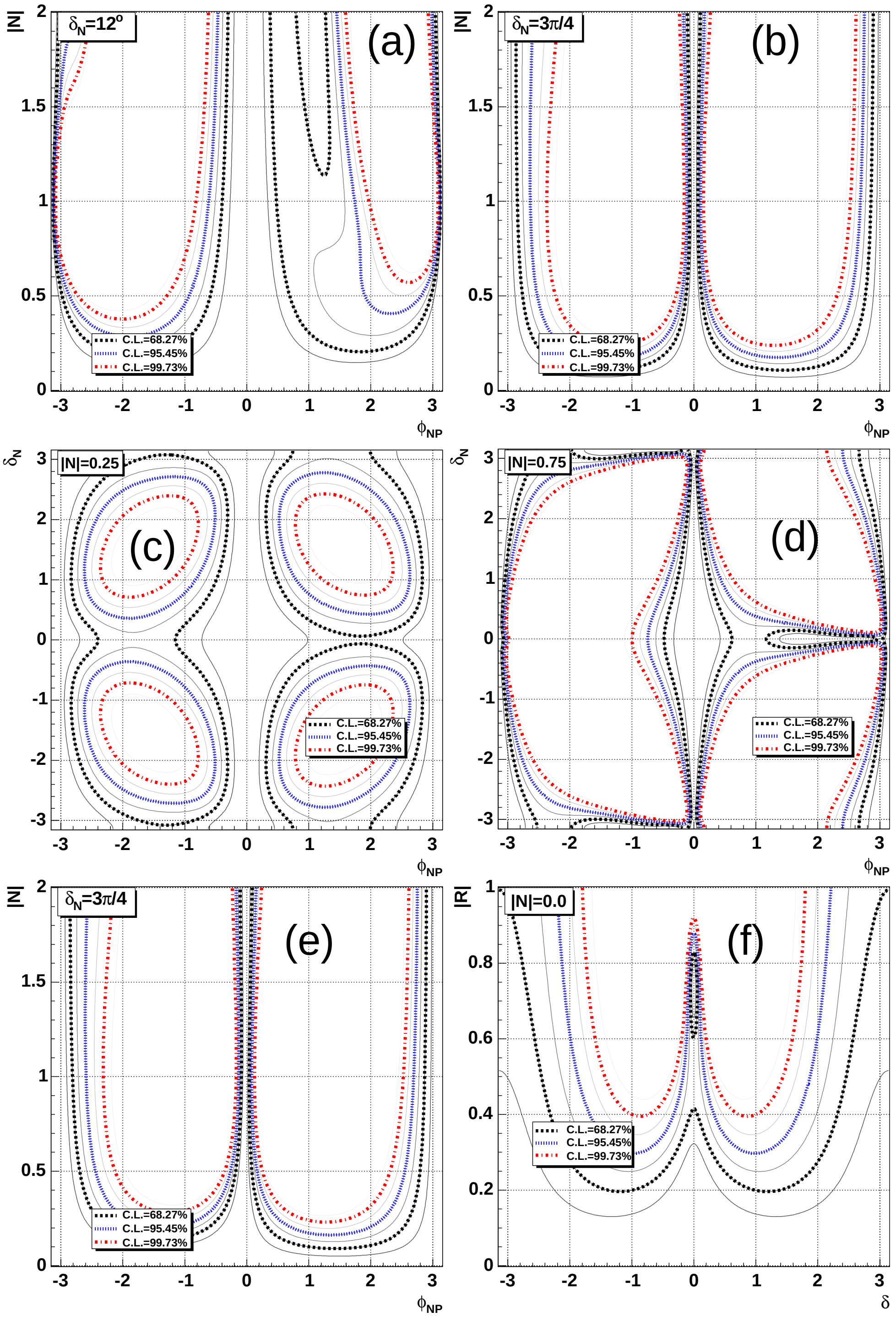

Figure 7.8: *The* 1 ab^{-1} *expected confidence regions for the SM and new physics parameters; (a)* $|\mathcal{N}|$*-*$\phi_{\rm NP}$ *plane for* $\delta_{\rm N} = 12°$*; (b)* $|\mathcal{N}|$*-*$\phi_{\rm NP}$ *plane for* $\delta_{\rm N} = 3\pi/4$*; (c)* $\delta_{\rm N}$*-*$\phi_{\rm NP}$ *plane for* $|\mathcal{N}| = 0.25$*; (d)* $\delta_{\rm N}$*-*$\phi_{\rm NP}$ *plane for* $|\mathcal{N}| = 0.75$*; (e)* $|\mathcal{N}|$*-*$\phi_{\rm NP}$ *plane for* $\delta_{\rm N} = 3\pi/4$ *and* $|R|$*=0.06; (f)* $|R|$*-*δ *plane for* $|\mathcal{N}| = 0$*. For illustration, (*$\mathcal{S}_{D^{*+}D^{*-}} = -\sin 2\phi_1, \mathcal{A}_{D^{*+}D^{*-}} = 0$*) is assumed. Dashed, dotted, dashed-dotted curves correspond to the confidence level of* 68.27%, 95.45%, 99.73%, *respectively.*

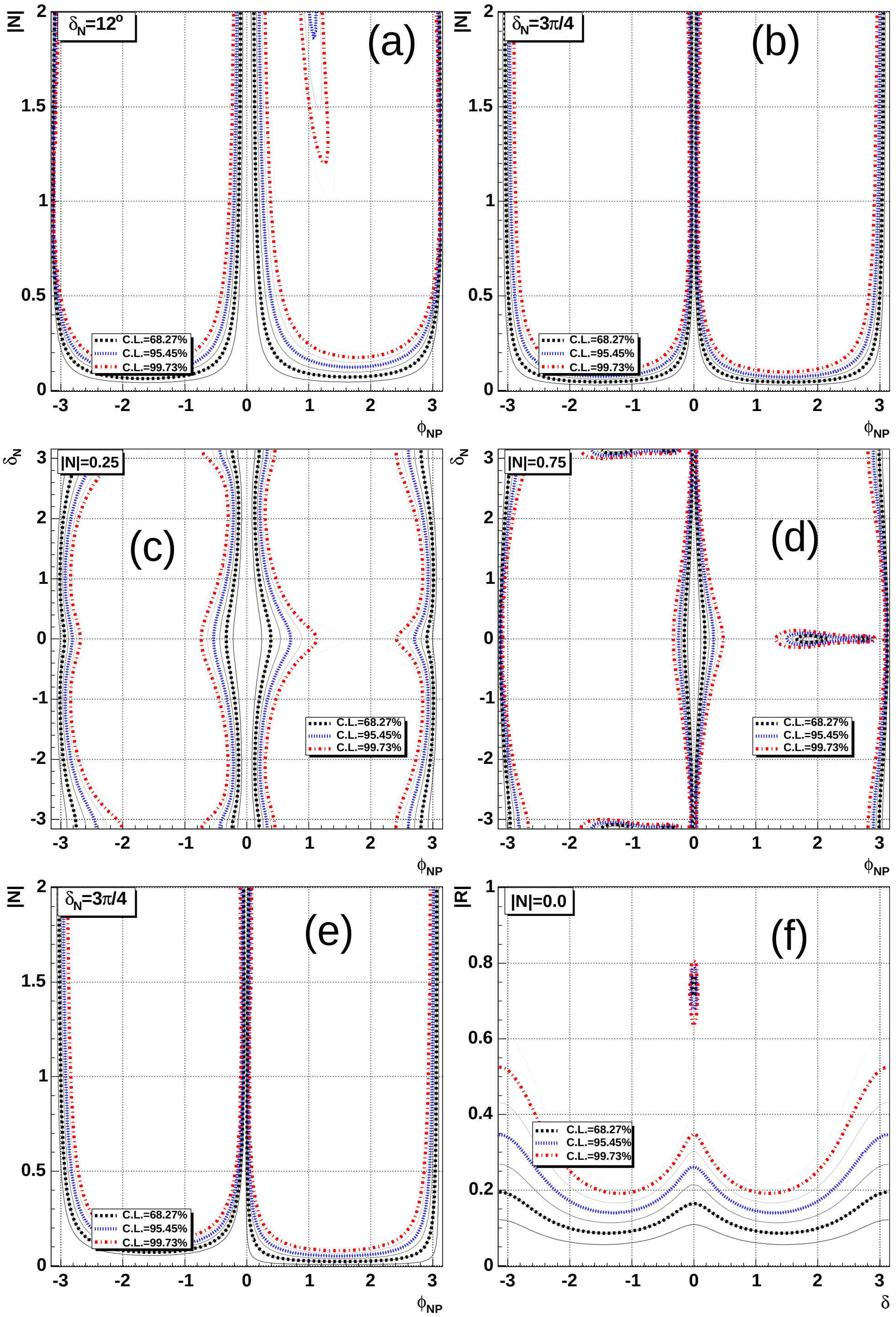

Figure 7.9: *The* 50 ab^{-1} *expected confidence regions for the SM and new physics parameters; (a)* $|\mathcal{N}|$-$\phi_{\rm NP}$ *plane for* $\delta_{\rm N} = 12°$*; (b)* $|\mathcal{N}|$-$\phi_{\rm NP}$ *plane for* $\delta_{\rm N} = 3\pi/4$*; (c)* $\delta_{\rm N}$-$\phi_{\rm NP}$ *plane for* $|\mathcal{N}| = 0.25$*; (d)* $\delta_{\rm N}$-$\phi_{\rm NP}$ *plane for* $|\mathcal{N}| = 0.75$*; (e)* $|\mathcal{N}|$-$\phi_{\rm NP}$ *plane for* $\delta_{\rm N} = 3\pi/4$ *and* $|R|$*=0.06; (f)* $|R|$-δ *plane for* $|\mathcal{N}| = 0$*. For illustration,* $(\mathcal{S}_{D^{*+}D^{*-}} = -\sin 2\phi_1, \mathcal{A}_{D^{*+}D^{*-}} = 0)$ *is assumed. Dashed, dotted, dashed-dotted curves correspond to the confidence level of* 68.27%, 95.45%, 99.73%, *respectively.*

Chapter 8

Conclusion

We have measured time-dependent CP asymmetry parameters in $B^0 \to D^{*+}D^{*-}$ decays, using the Belle detector at the KEKB energy-asymmetric e^+e^- collider. The $B^0 \to D^{*+}D^{*-}$ decay is dominated by the $b \to c\bar{c}d$ transition that is sensitive to new physics process via the penguin diagram. The CP violation in the tree diagram of this mode should yield the $\sin 2\phi_1$, which is the CP asymmetry parameter of the Cabibbo-Kobayashi-Maskawa matrix. The $\sin 2\phi_1$ has already been measured with the $B^0 \to J/\psi K^0_S$ and other $c\bar{c}K^{(*)0}$ decays. Since the correction from the penguin diagram is expected to be small as a few % in the Standard Model, measurements of CP violation in $B^0 \to D^{*+}D^{*-}$ decays should yield the $\sin 2\phi_1$ value to a good approximation within the Standard Model. Thus a significant deviation from what is observed in $b \to c\bar{c}s$ decays would be evidence for a new CP-violating phase.

The analysis is based on a sample of $152 \times 10^6 B\bar{B}$ pairs, which correspond to an integrated luminosity of 140 fb^{-1} on the $\Upsilon(4S)$ resonance accumulated from January 2000 to June 2003. The number of fully-reconstructed $B^0 \to D^{*+}D^{*-}$ signals is 130.

Although the $B^0 \to D^{*+}D^{*-}$ decay is a mixture of CP-odd and CP-even components as the $D^{*+}D^{*-}$ system is a superposition of S-, P-, and D-waves, we can extract correct CP-asymmetry parameters by knowing their fractions with the angular information of $B^0 \to D^{*+}D^{*-}$ decay products. An unbinned maximum likelihood fit to the angular distributions of the $D^{*+}D^{*-}$ decay products yields

$$\begin{aligned} R_\perp &= 0.19 \pm 0.08(\mathrm{stat}) \pm 0.01(\mathrm{syst}), \\ R_0 &= 0.57 \pm 0.08(\mathrm{stat}) \pm 0.01(\mathrm{syst}). \end{aligned}$$

The result is consistent with the Standard Model expectation that CP-even component is dominant. Using these fractions of polarization components, we obtain CP asymmetry parameters $\mathcal{S}_{D^{*+}D^{*-}}$ and $\mathcal{A}_{D^{*+}D^{*-}}$:

$$\begin{aligned} \mathcal{S}_{D^{*+}D^{*-}} &= -0.75 \pm 0.56(\mathrm{stat}) \pm 0.12(\mathrm{syst}), \\ \mathcal{A}_{D^{*+}D^{*-}} &= -0.26 \pm 0.26(\mathrm{stat}) \pm 0.06(\mathrm{syst}). \end{aligned}$$

The result is consistent with $(\mathcal{S}_{D^{*+}D^{*-}}, \mathcal{A}_{D^{*+}D^{*-}}) = (-\sin 2\phi_1, 0)$, which is the Standard Model expectation for small penguin contributions. The BaBar collaboration claims that CP asymmetries of $B^0 \to D^{*+}D^{*-}$ have a 2.5σ discrepancy from the Standard Model expectation above, while the corresponding deviation is only 0.5σ in our case.

This is the first measurement at the Belle experiment, and establishes the analysis method for more precise measurements in the future.

Since the Belle experiment is expected to accumulate data with an integrated luminosity of 1 ab^{-1} within a few years, the statistical error will be about 40 percent of this analysis. Furthermore, a major upgrade plan of the KEK B-factory is proposed recently; its goal is to accumulate an integrated luminosity of 50 ab^{-1}. The experimental errors will be at the level of 0.06 in this case. Such measurements will allow us to test the Standard Model very precisely in the $b \to c\bar{c}d$ transition.

Appendix A

Maximum Likelihood Method

In this paper, we frequently use a maximum likelihood method to yield most probable values from obtained data. Suppose we obtain a set of N independently measured quantities x_i $(i = 1, N)$, where x_i follows a probability density function (PDF) $P(x; \vec{\alpha})$, and $\vec{\alpha} = (\alpha_1, ..., \alpha_n)$ is a set of n parameters whose values are unknown. The idea of the maximum likelihood method is to find the set of the most probable values for $\vec{\alpha}$, which maximizes the joint PDF for all the data, which is given by

$$\mathcal{L}(\alpha) = \prod_{i}^{N} P(x_i, \vec{\alpha}), \tag{A.1}$$

where $\mathcal{L}$ is called the likelihood.

It is usually easier to work with $\ln \mathcal{L}$, since $\mathcal{L}$ can be too small to be computed. Because both $\mathcal{L}$ and $\ln \mathcal{L}$ are maximized for the same set of $\vec{\alpha}$, both methods find the same maximum likelihood estimator $\vec{\alpha}$ that satisfies

$$\frac{\partial \ln \mathcal{L}}{\partial \alpha_n} = 0. \tag{A.2}$$

Furthermore, we usually use $-2 \ln \mathcal{L}$, which behaves like a χ^2, where $\mathcal{L}$ behaves like a Gaussian function. We define $\mathcal{L}_{\max}$ as the maximum likelihood obtained from Eq. (A.2). For a given $\vec{\alpha}$, if the difference between $-2 \ln \mathcal{L}(\vec{\alpha})$ and $-2 \ln \mathcal{L}_{\max}$ is unity, it corresponds to one standard deviation of the estimate. More generally, a contour for n standard deviations is given by the difference of n^2. By examining the likelihood contours, therefore, one can obtain a confidence interval of the measurement at any confidence level.

Appendix B

Angular Distribution in the $B \to VV$ System

B.1 Rotation of an Angular Momentum State

In general, a rotation operator around rotation axis i is denoted by

$$R_i(\theta) = e^{-i\mathcal{J}_i\theta}, \tag{B.1}$$

where θ is the rotation angle and $\mathcal{J}_i$ is the angular momentum operator.

Now we prepare an angular momentum state $|J, M\rangle$, where J is the angular momentum eigenvalue and $M = J_i$ is the projection of j to the rotation axis. The rotation of $|J, M\rangle$ is described by super-positioned (itself and others) angular momentum states $|J, M'\rangle$:

$$R(\alpha, \beta, \gamma)|J, M\rangle = \sum_{M'=-J}^{J} |J, M'\rangle D^J_{M'M}(\alpha, \beta, \gamma), \tag{B.2}$$

where $D^J_{M'M}$ is so-called rotation function:

$$D^J_{M'M}(\alpha, \beta, \gamma) \equiv e^{-i\alpha M'} d^J_{M'M}(\beta) e^{-i\gamma M}, \tag{B.3}$$

where Wigner's rotation matrix (hereafter we call it d-matrix) is

$$d^J_{M'M}(\theta) \equiv \langle J, M| e^{-ij_i\theta} |J, M'\rangle. \tag{B.4}$$

Explicit formula of d-matrix is found elsewhere [13, 53] and especially

$$d^J_{M0}(\theta, \phi) = \sqrt{\frac{4\pi}{2J+1}} Y^J_M(\theta, \phi) e^{-iM\phi}. \tag{B.5}$$

There are some important characters in the d-matrix:

$$\textstyle\int_{-1}^{1} dcos\theta d^j_{M'M} d^{J'}_{M'M} = \frac{2}{2J+1}\delta_{JJ'}, \tag{B.6}$$

$$d^J_{MM'} = (-1)^{M-M'} d^J_{M'M} = d^J_{-M'-M}, \tag{B.7}$$

$$\textstyle\int_0^{2\pi} d\alpha \int_0^{2\pi} d\gamma \int_0^{\pi} \sin\beta d\beta D^J_{MN}(\alpha, \beta, \gamma) D^{J'}_{M'N'}(\alpha, \beta, \gamma) = \frac{8\pi^2}{2J+1}\delta_{MM'}\delta_{NN'}\delta_{JJ'}. \tag{B.8}$$

B.2 Partial Wave Expansion of Two Body Decay

Now we consider $B \to V_1 V_2$ decay in the rest frame of B meson. The daughter particle V_1 has a momentum $\vec{p} = (p, \theta, \phi)$ and helicity λ_1. The other daughter V_2 has a momentum $-\vec{p}$ and helicity λ_2. Then this event is specified by the plane wave state: $|p\theta\phi;\lambda_1\lambda_2\rangle$. This basis should be equivalent to the partial wave basis, $|JM;\lambda_1\lambda_2\rangle$:

$$|p\theta\phi;\lambda_1\lambda_2\rangle = \sum_{JM} C_{JM}|JM;\lambda_1\lambda_2\rangle. \tag{B.9}$$

We aim to find these coefficients C_{JM}. Following Jacob-Wick notation, we introduce a rotation operator

$$R(\theta,\phi) \equiv R(\phi,\theta,-\phi) = e^{-iJ_z\phi}e^{-iJ_y\theta}e^{iJ_z\phi}. \tag{B.10}$$

Then partial wave which turns to the parent momentum direction is described as

$$|p\theta\phi;\lambda_1\lambda_2\rangle = R(\theta,\phi)|p00;\lambda_1\lambda_2\rangle. \tag{B.11}$$

The plane wave state is described by super-positioned partial waves:

$$\begin{aligned}|p\theta\phi;\lambda_1\lambda_2\rangle =& \sum_{JM\lambda_1'\lambda_2'} \langle JM;\lambda_1'\lambda_2'|p\theta\phi;\lambda_1\lambda_2\rangle|JM;\lambda_1'\lambda_2'\rangle\\ =&\sum_{JM}\langle JM;\lambda_1\lambda_2|p\theta\phi;\lambda_1\lambda_2\rangle|JM;\lambda_1\lambda_2\rangle,\end{aligned} \tag{B.12}$$

where we used invariance of helicity against rotation.

From Eq. (B.2) and (B.11),

$$\begin{aligned}\langle JM;\lambda_1\lambda_2|p\theta\phi;\lambda_1\lambda_2\rangle =&\langle JM;\lambda_1\lambda_2|R(\theta,\phi)R^{-1}(\theta,\phi)|p\theta\phi;\lambda_1\lambda_2\rangle\\ =&\sum_{M'} D^J_{MM'}(\phi,\theta,-\phi)\langle JM';\lambda_1\lambda_2|p00;\lambda_1\lambda_2\rangle\\ =&D^J_{M\lambda}(\phi,\theta,-\phi)\langle J\lambda;\lambda_1\lambda_2|p00;\lambda_1\lambda_2\rangle,\end{aligned} \tag{B.13}$$

where $\lambda \equiv \lambda_1 - \lambda_2$ and we used $M' = \lambda$, since there is no orbital angular momentum projection along with z-axis for $|p00;\lambda_1\lambda_2\rangle$ state ($\vec{L}\cdot\vec{P} = 0$).

Furthermore, we utilize

$$\begin{aligned}1 =&\langle JM;\lambda_1\lambda_2|JM;\lambda_1\lambda_2\rangle\\ =&\sum_{\mu\nu}\int d\phi d\cos\theta\langle JM;\lambda_1\lambda_2|p\theta\phi;\mu\nu\rangle\langle p\theta\phi;\mu\nu|JM;\lambda_1\lambda_2\rangle\\ =&\int d\phi d\cos\theta\langle JM;\lambda_1\lambda_2|p\theta\phi;\lambda_1\lambda_2\rangle\langle p\theta\phi;\lambda_1\lambda_2|JM;\lambda_1\lambda_2\rangle\\ =&\int d\phi d\cos\theta D^J_{M\lambda}(\phi,\theta,-\phi)\langle J\lambda;\lambda_1\lambda_2|p00;\lambda_1\lambda_2\rangle\langle p00;\lambda_1\lambda_2|J\lambda;\lambda_1\lambda_2\rangle D^{J*}_{M\lambda}(\phi,\theta,-\phi)\\ =&\int d\phi d\cos\theta d^J_{M\lambda}(\theta)d^J_{M\lambda}(\theta)|\langle J\lambda;\lambda_1\lambda_2|p00;\lambda_1\lambda_2\rangle|^2\\ =&\frac{2\pi\cdot 2}{2J+1}|\langle J\lambda;\lambda_1\lambda_2|p00;\lambda_1\lambda_2\rangle|^2.\end{aligned}$$

(B.14)

If we choose $C_{JM} = \langle J\lambda;\lambda_1\lambda_2|p00;\lambda_1\lambda_2\rangle = \sqrt{(2J+1)/4\pi}$, we obtain

$$|p\theta\phi;\lambda_1\lambda_2\rangle = \sum_{JM} D^J_{M\lambda}(\phi,\theta,-\phi)\sqrt{\frac{2J+1}{4\pi}}|JM;\lambda_1\lambda_2\rangle. \tag{B.15}$$

B.3 Helicity Basis

B.3.1 Decay Amplitude of $B \to V_1V_2$ Decay

We define an angle-dependent decay amplitude:

$$A^J_M(\theta,\phi;\lambda_1,\lambda_2) \equiv \langle p\theta\phi\lambda_1\lambda_2|\mathcal{H}_{\text{eff}}|JM;\lambda_1\lambda_2\rangle, \tag{B.16}$$

where $\mathcal{H}_{\text{eff}}$ is an effective Hamiltonian. From Eq. (B.15),

$$\begin{aligned} A^J_M(\theta,\phi;\lambda_1,\lambda_2) =& \sum_{J'M'}\sqrt{\frac{2J'+1}{4\pi}}D^{J'*}_{M'\lambda_1-\lambda_2}(\phi,\theta,-\phi)\langle J'M'|\mathcal{H}_{\text{eff}}|JM\rangle \\ =&\sqrt{\frac{2J+1}{4\pi}}D^{J*}_{M\lambda_1-\lambda_2}(\phi,\theta,-\phi)A(\lambda_1,\lambda_2), \end{aligned} \tag{B.17}$$

where $A(\lambda_1,\lambda_2) \equiv \langle JM;\lambda_1\lambda_2|\mathcal{H}_{\text{eff}}|JM;\lambda_1\lambda_2\rangle$ is the amplitude of specific helicity state.

Since we treat $B \to V_1V_2$ decay, $J = M = 0$ is held from conservation law. Therefore allowed helicity states are

$$(\lambda_1,\lambda_2) = (+1,+1),(0,0),(-1,-1). \tag{B.18}$$

We define a helicity amplitude

$$A(\lambda,\lambda) \equiv \langle f_\lambda|\mathcal{H}_{\text{eff}}|f_\lambda\rangle, \tag{B.19}$$

where

$$|f_\lambda\rangle = |JM;\lambda\lambda\rangle(\lambda = +1,0,-1). \tag{B.20}$$

B.3.2 Decay Amplitude with Subsequential Decay

When a subsequent decay occurs in a particle system, we should consider angular distributions of daughter particles. As the helicity state is invariant under rotation and boost, we can choose individual coordinate systems for each subsequent decay. Following definition of helicity, we choose z-axis of local frame to the momentum direction in the B rest frame. Therefore, spin component $m = \lambda$ owing to no orbital angular momentum.

We consider $B \to D^{*+}D^{*-}$ decay followed by subsequential decay $D^{*\pm} \to D^{\pi}$. Decay amplitude become:

$$\begin{aligned}
&A^J_M(\theta,\phi,\theta_1,\phi_1,\theta_2,\phi_2;\lambda,\lambda',\lambda'') = \sqrt{\frac{2J+1}{4\pi}}\sqrt{\frac{2J_1+1}{4\pi}}\sqrt{\frac{2J_2+1}{4\pi}}\cdot \\
&\sum_{\lambda',\lambda''} D^{J*}_{M\lambda}(\phi,\theta,-\phi)A(\lambda,\lambda)D^{J_1*}_{\lambda\lambda'}(\phi_1,\theta_1,-\phi_1)B(\lambda',\lambda')D^{J_2*}_{\lambda\lambda''}(\phi_2,\theta_2,-\phi_2)C(\lambda'',\lambda''),
\end{aligned} \tag{B.21}$$

where $B(\lambda',\lambda')$ and $C(\lambda'',\lambda'')$ is helicity amplitude of subsequential decay. Decay angles are measured by π from each $D^{*\pm}$ in the each $D^{*\pm}$ rest frame. θ_i is angle between the π and $D^{*\pm}$ momentum vector. ϕ_i, which is angle around $D^{*\pm}$ momentum vector, can not be uniquely decided, since decay plane is not anchored to any fixed coordinate system. We take $i=1$ ($i=2$) for D^{*-} (D^{*+}).

Since $D^{*\pm}$ is spin-1 particle and also D and π are spin-0,

$$J_1 = 1, J_2 = 1, \lambda' = 0, \lambda'' = 0. \tag{B.22}$$

With applying them to the decay amplitude in Eq. (B.21):

$$\begin{aligned}
&A^0_0(\theta,\phi,\theta_1,\phi_1,\theta_2,\phi_2;\lambda,0,0) = \frac{3}{(4\pi)^{3/2}}\cdot \\
&D^{0*}_{0\lambda}(\phi,\theta,-\phi)A(\lambda,\lambda)D^{1*}_{\lambda 0}(\phi_1,\theta_1,-\phi_1)B(\lambda',\lambda')D^{1*}_{\lambda 0}(\phi_2,\theta_2,-\phi_2)C(\lambda'',\lambda'') \\
=&e^{i\chi\lambda}d^1_{\lambda 0}(\theta_1)d^1_{\lambda 0}(\theta_2)A_\lambda,
\end{aligned} \tag{B.23}$$

where $A_\lambda \equiv 3(4\pi)^{-3/2}A(\lambda,\lambda)B(\lambda',\lambda')C(\lambda'',\lambda'')$ and $\chi \equiv \phi_1 + \phi_2$.

Total decay amplitude A_{hel} is derived from calculation of d-matrix with utilizing Eq. (B.5) and (B.7):

$$\begin{aligned}
A_{\mathrm{hel}} =& \sum_\lambda A^0_0(\theta,\phi,\theta_1,\phi_1,\theta_2,\phi_2;\lambda,0,0) \\
=&A_+g_+ + A_0g_0 + A_-g_-,
\end{aligned} \tag{B.24}$$

where

$$\begin{aligned}
g_0 =& \cos\theta_1\cos\theta_2, \\
g_+ =& \frac{1}{2}e^{i\chi}\sin\theta_1\sin\theta_2, \\
g_- =& \frac{1}{2}e^{-i\chi}\sin\theta_1\sin\theta_2.
\end{aligned} \tag{B.25}$$

Decay width is also calculated:

$$\begin{aligned}
\Gamma_{\mathrm{hel}}(\chi,\theta_1,\theta_2) \equiv& N_{\mathrm{hel}}|A_{\mathrm{hel}}|^2 = \frac{9}{32\pi}\Big[(|A_+|^2+|A_-|^2)\sin^2\theta_1\sin^2\theta_2 + 4|A_0|^2\cos^2\theta_1\cos^2\theta_2 \\
&+2\{\Re(A_+A_-^*)\cos 2\chi - \Im(A_+A_-^*)\sin 2\chi\}\sin^2\theta_1\sin^2\theta_2 \\
&+\{\Re(A_+ + A_-)A_0^*\cos\chi - \Im(A_+ - A_-)A_0^*\sin\chi\}\sin^2 2\theta_1\sin^2 2\theta_2\Big],
\end{aligned} \tag{B.26}$$

where the normalization factor N_{hel} is decided from

$$N_{\mathrm{hel}} \iiint d\chi d\cos\theta_1 d\cos\theta_2 \Gamma_{\mathrm{hel}}(\chi, \theta_1, \theta_2) = |A_+|^2 + |A_0|^2 + |A_-|^2. \tag{B.27}$$

This is called helicity basis angular distribution. Figure B.1 (left) shows schematic view of helicity basis frame.

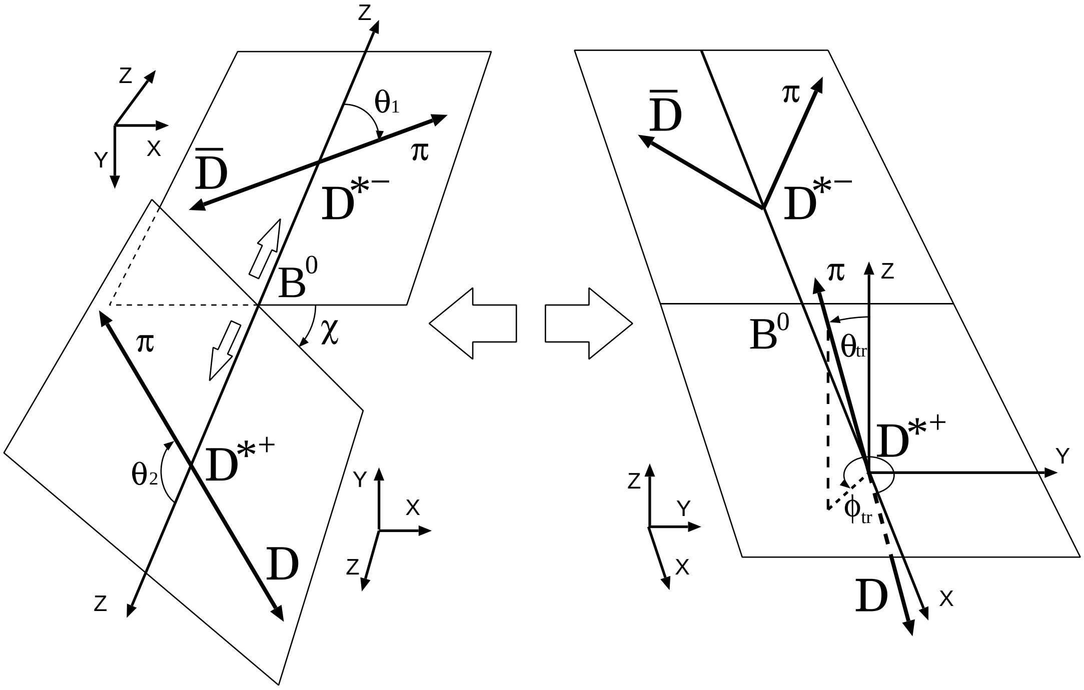

Figure B.1: *Left (Right):Schematic View of Helicity (Transversity) basis of* $B^0 \to D^{*+}D^{*-}$.

B.3.3 Introduction of Parity Eigenstates

We consider parity transformity of helicity states. Firstly we introduce "reflection", which is not parity transformation but ordinal mirror:

$$R_P \equiv Pe^{-i\pi J_y}, \tag{B.28}$$

where J_y is angular momentum projection to normal of the x-z plane. Since spin s is invariant against P transformation but changes its sign against rotation,

$$R_P|p; s\rangle = \eta|p; -s\rangle, \tag{B.29}$$

where $|p; s\rangle$ is plane wave state along with z-axis and η is intrinsic parity.

Here we go to $p = 0$. We wee

$$P|0; \lambda\rangle = \eta|0, \lambda\rangle. \tag{B.30}$$

With utilizing expansion of plane wave state and orthogonality:

$$\begin{aligned} e^{-i\pi J_y}|0,\lambda\rangle &= \sum_{\lambda'} d^s_{\lambda'\lambda}(\pi)|0,\lambda'\rangle \\ &= (-1)^{s-\lambda}|0,-\lambda\rangle, \end{aligned} \tag{B.31}$$

where we used

$$d^s_{\lambda'\lambda}(\pi) = (-1)^{s-\lambda}\delta_{\lambda',-\lambda}. \tag{B.32}$$

Parity transformation of the state $|JM;\lambda_1\lambda_2\rangle$ is given by [54]:

$$P|JM;\lambda_1\lambda_2\rangle = \eta_1\eta_2(-1)^{J-S_1-S_2}|JM;-\lambda_1-\lambda_2\rangle, \tag{B.33}$$

where $\eta_i(i=1,2)$ is intrinsic parity and $S_j(j=1,2)$ is spin of each daughter.

Then we derive Parity transformation of each helicity state $|f_\lambda\rangle$:

$$P|f_{+1}\rangle = |f_{-1}\rangle, \quad P|f_0\rangle = |f_0\rangle, \quad P|f_{-1}\rangle = |f_{+1}\rangle. \tag{B.34}$$

Therefore, $|f_{\pm 1}\rangle$ are not parity (and also CP) eigenstates.

We can construct parity eigenstates from states above:

$$\begin{aligned} &|f_0\rangle && (P:+1), \\ &|f_\parallel\rangle \equiv \frac{|f_{+1}\rangle + |f_{-1}\rangle}{\sqrt{2}} && (P:+1), \\ &|f_\perp\rangle \equiv \frac{|f_{+1}\rangle - |f_{-1}\rangle}{\sqrt{2}} && (P:-1). \end{aligned} \tag{B.35}$$

Thus decay amplitudes are:

$$\begin{aligned} &A_0, \\ &A_\parallel \equiv \frac{A_{+1}+A_{-1}}{\sqrt{2}}, \\ &A_\perp \equiv \frac{A_{+1}-A_{-1}}{\sqrt{2}}. \end{aligned} \tag{B.36}$$

Corresponding angular distributions are also derived from Eq. (B.25):

$$\begin{aligned} g_0 &= \cos\theta_1\cos\theta_2, \\ g_\parallel &= \frac{1}{\sqrt{2}}\cos\chi\sin\theta_1\sin\theta_2, \\ g_\perp &= \frac{i}{\sqrt{2}}\sin\chi\sin\theta_1\sin\theta_2. \end{aligned} \tag{B.37}$$

Clearly, this new amplitudes are useful for CP analysis. In order to grasp the character of these amplitudes, it is convenient to introduce new coordinates which is sensitive to CP transformation. This is called transversity basis. Detail of transversity basis is described later.

B.4 Transversity Basis

From Eq. (B.25), we know that D^{*-} polarization (θ_2 term) is the standard of this system, and χ term separates both two transverse polarizations and θ_1 also separates them and the other polarization, A_0. In short, polarization of the system is measured by D^{*+} which is anchored by D^{*-} decay plane. To clearfy their relations, we choose new coordinate system, which pays attention to transversely polarized states from decay plane:

$$\begin{aligned} x' &= \sin\theta_{tr}\cos\phi_{tr} &&= \cos\theta_2 &&= z, \\ y' &= \sin\theta_{tr}\cos\phi_{tr} &&= \sin\theta_2\cos\chi &&= x, \\ z' &= \cos\theta_{tr} &&= \sin\theta_2\sin\chi &&= y. \end{aligned} \tag{B.38}$$

Then Eq. (B.37) become:

$$\begin{aligned} g_0 &= \cos\theta_1\sin\theta_{tr}\cos\phi_{tr}, \\ g_{\parallel} &= \frac{1}{\sqrt{2}}\sin\theta_1\sin\theta_{tr}\sin\phi_{tr}, \\ g_{\perp} &= \frac{i}{\sqrt{2}}\sin\theta_1\cos\theta_{tr}. \end{aligned} \tag{B.39}$$

Angular dependent decay rate is obtained from Eq. (B.26) with applying Eq. (B.36) and (B.39):

$$\begin{aligned} \Gamma_{\mathrm{tr}}(\theta_1, \theta_{tr}, \phi_{tr}) = & \frac{9}{32\pi}\Big[4|A_0|^2\cos^2\theta_1\sin^2\theta_{tr}\cos^2\phi_{tr} + 2|A_{\parallel}|^2\sin^2\theta_1\sin^2\theta_{tr}\sin^2\phi_{tr} \\ & + 2|A_{\perp}|^2\sin^2\theta_1\cos^2\theta_{tr} + \sqrt{2}\Re(A_{\parallel}^{*}A_0)\sin 2\theta_1\sin^2\theta_{tr}\sin 2\phi_{tr} \\ & - \sqrt{2}\Im(A_0^{*}A_{\perp})\sin 2\theta_1\sin 2\theta_{tr}\cos\phi_{tr} - 2\Im(A_{\parallel}^{*}A_{\perp})\sin^2\theta_1\sin 2\theta_{tr}\sin\phi_{tr}\Big]. \end{aligned} \tag{B.40}$$

From Eq. (B.40), we can see a merit of this coordinate system that CP-even terms (A_0, $A_{\parallel}$) are distinguished from CP-odd term ($A_{\perp}$) with single angular term (θ_{tr}).

Appendix C

Flavor Tagging Method

C.1 Principle of Flavor Tagging

We use the same flavor tagging method and values as those used in the $\sin 2\phi_1$ measurement [47]. The details of the flavor tagging technique are found in the reference [46]. Here, we describe the flavor tagging method briefly.

The flavor of $B_{\rm tag}$ is determined by the information of the final state particles that belong to $B_{\rm tag}$. $B_{\rm tag}$ is reconstructed from remaining particles in the event after reconstructing a B_{CP} candidate. The flavor of $B_{\rm tag}$ can be determined from the charge (flavor) of

- high-momentum leptons from $B^0 \to X\ell^+\nu$,
- kaons from the $\bar{b} \to \bar{c} \to \bar{s}$ cascade decay,
- intermediate momentum leptons coming from $\bar{b} \to \bar{c} \to \bar{s}\ell^-\bar{\nu}$,
- high momentum pions from $B^0 \to D^{(*)}\pi^+X$ decay,
- slow pions from $B^0 \to D^{*-}X, D^{*-} \to \bar{D}^0\pi^-$ decay, and
- Λ baryons from the cascade decay $\bar{b} \to \bar{c} \to \bar{s}$.

The flavor tagging efficiency ε is not always perfect owing to several reasons, such as inefficiencies of particle detection, wrong particle identification, or rare physical processes that give opposite charge information to the dominant process.

The effective tagging efficiency $\varepsilon_{\rm eff} = \varepsilon(1-2w)^2$ (w is a wrong tag fraction) is introduced to optimize statistical significance of time-dependent CP asymmetry, since the statistical significance is proportional to $(1-2w)\sqrt{\varepsilon}$. In order to maximize $\varepsilon_{\rm eff}$, maximizing ε and minimizing w is required. As described in detail in the following sections, a larger $\varepsilon_{\rm eff}$ is obtained by treating events with large w's and small w's separately. For this purpose, we use an expected event-by-event dilution factor r. The r value is determined using MC and is related to w as $r = 1-2w$ if the MC represents data perfectly. For each r region, we assign w, which is measured using the control data sample. We use

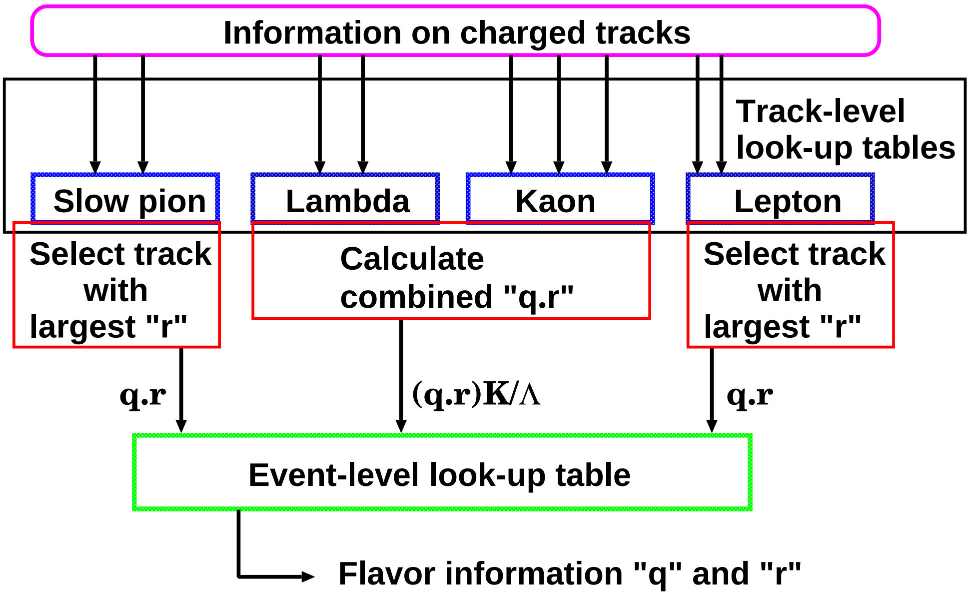

Figure C.1: *A schematic diagram of the two-stage flavor tagging.*

either of two event generators, QQ [40] or EvtGen [41] to simulate the tag-side B-meson decays. We used QQ-generated MC for early measurements of $\sin 2\phi_1$. EvtGen-generated MC was used for recent $\sin 2\phi_1$ measurements [8, 47], as well as for the CP asymmetry parameter measurement in $B^0 \to D^{*+}D^{*-}$ decays.

The correlations and variables representing the particle properties are expressed by look-up tables. We assign q and r to each cell of look-up tables.

The q can be either a 1 or -1 and indicates that the flavor is B^0 ($q = 1$) or $\bar{B}^0$ ($q = -1$). The r ranges from 0 for no flavor discrimination to $r = 1$ for unambiguous flavor assignment. The q and r are calculated by

$$q \cdot r \equiv \frac{N(B^0) - N(\bar{B}^0)}{N(B^0) + N(\bar{B}^0)}, \tag{C.1}$$

where $N(B^0)$ and $N(\bar{B}^0)$ are the numbers of B^0 and $\bar{B}^0$ in the cell determined by the MC sample.

Since the number of particles in an event is not limited, it is practically difficult to consider all the correlations at once. The flavor tagging procedure is, therefore, divided in two stages: the track stage and the event stage. Figure C.1 shows the schematic diagram of the flavor tagging. At first, each charged track is classified into four categories depending on the particle species: lepton class; kaons class; Λ baryon and slow pions, and we assign $q \cdot r$ to each track using a look-up table of specific variables in each category. An event-level look-up table is made of outputs of each track class to determine the final flavor information. In the following, we explain each stage.

C.2 Track-Level Flavor Tagging

C.2.1 Classification of Charged Tracks

We use charged tracks that do not belong to B_{CP} for track-level flavor tagging. These charged tracks should also be well-reconstructed tracks satisfying $|dr| < 2$ cm and $|dz| < 10$ cm, where dr and dz are distances from the nominal interaction point in the r-ϕ plane and the z direction, respectively. K_S^0 and Λ tracks are founded by a secondary vertex reconstruction algorithm. The charged tracks from their vertices are not used, but the number of K_S^0's in the event is used as a discriminant for kaon-like and Λ-like particle categories. The Λ candidates themselves are assigned into the Λ category.

C.2.2 Lepton Track Class

This category includes electron-like tracks and muon-like tracks. The electron-like track should satisfy that the momentum in the center of mass system (cms), p^*, of a track is larger than 0.4 GeV/c and the ratio of its electron and kaon likelihoods is larger than 0.8. The muon-like track should satisfy that p^* is larger than 0.8 GeV/c and the ratio of its muon and kaon likelihoods is larger than 0.95. The likelihoods are calculated by combining the ACC, TOF, dE/dx in CDC, and ECL or KLM information. Within the lepton track class, leptons from semi-leptonic B decays yield the highest effective efficiency. Leptons from semi-leptonic decays of D mesons which originate from $B \rightarrow D$ cascade decays and high momentum pions from $B^0 \rightarrow D^{(*)-}\pi^+ X$ also make a small contribution to this class. A look-up table of following six variables are prepared to determine $q \cdot r$ for each track; (1) magnitude of the momentum in cms, p^*; (2) recoil mass, M_{recoil}, which is an invariant mass of the tagging side tracks except for the lepton track; (3) magnitude of the missing momentum in cms, p^*_{miss}; (4) polar angle in the laboratory frame, θ_{lab}; (5) lepton identification likelihood value, L_{lep}; (6) charge of the lepton track. The p^*, M_{recoil} and p^*_{miss} are used to discriminate between the leptons from primary B decays and from secondary D decays. The p^*, θ_{lab} and L_{lep} are used to take into account the momentum and the angular dependence of lepton identification performance. Figure C.2 shows the p^*, M_{recoil} and p^*_{miss} distributions for the MC and the data of control samples:$B^0 \rightarrow D^{*-}\ell^+\nu$, $D^{*-}\pi^+$, $D^-\pi^+$ and $D^{*-}\rho^+$ decays and their charge conjugates.

Although some disagreement is visible, the experimental bias due to this disagreement is found to be negligible since we evaluate wrong tagging probability from the control samples. These discriminant variables are divided into bins: 11 for p^*; 10 for M_{recoil}; 6 for p^*_{miss}; 6 for θ_{lab}; 4 for L_{lep} and 2 for track charge, and form a look-up table of 31680 bins in total.

Among lepton tracks, one lepton track with the highest r is selected, and the $q \cdot r$ value of the track is passed to the event-level flavor tagging.

C.2.3 Slow Pion Track Class

A charged track assigned to the slow-pion track class should satisfy that p^* of a track is less than 0.25 GeV/c and it is not identified as a kaon.

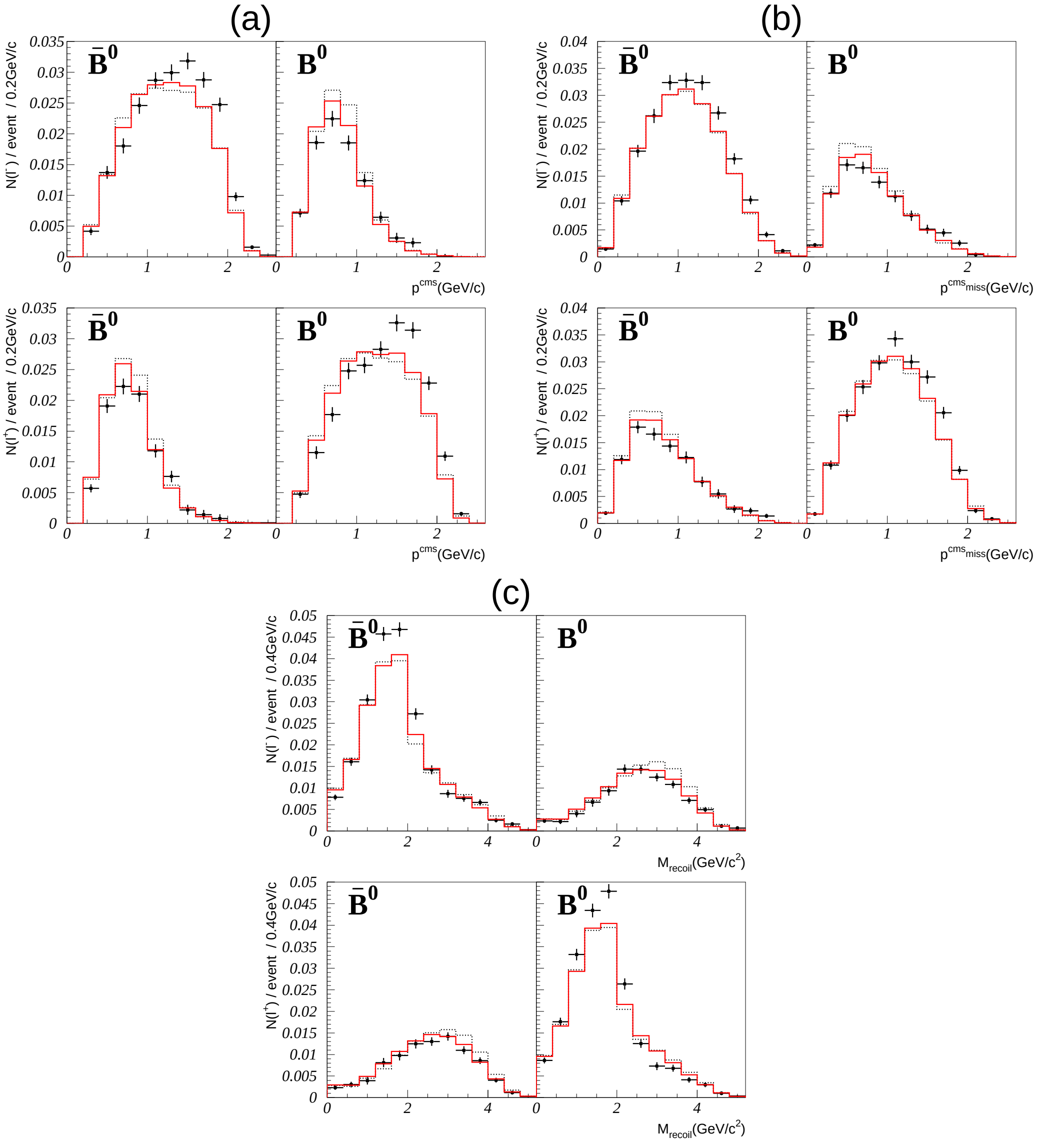

Figure C.2: *Distributions of (a)* p^**, (b)* p^*_{miss} and *(c)* M_{recoil} *for* $\overline{B}^0$ *and* B^0*. The points are for the data of control samples:* $B^0 \rightarrow D^{*-}\ell^+\nu$*,* $D^{*-}\pi^+$*,* $D^-\pi^+$ *and* $D^{*-}\rho^+$ *decays and their charge conjugates. Histograms with solid lines and dotted lines are for the EvtGen-MC and QQ-MC, respectively. All distributions are made with a requirement on lepton ID to exclude the dominating pion component. Upper two figures and lower two figures in each of (a), (b) or (c) are for* ℓ^-*-like tracks and for* ℓ^+*-like tracks, respectively. Upper left and lower right figures in each (a), (b) or (c) contain primary leptons from B decays, while upper right and lower left figures in each (a), (b) or (c) contain secondary leptons from D decays.*

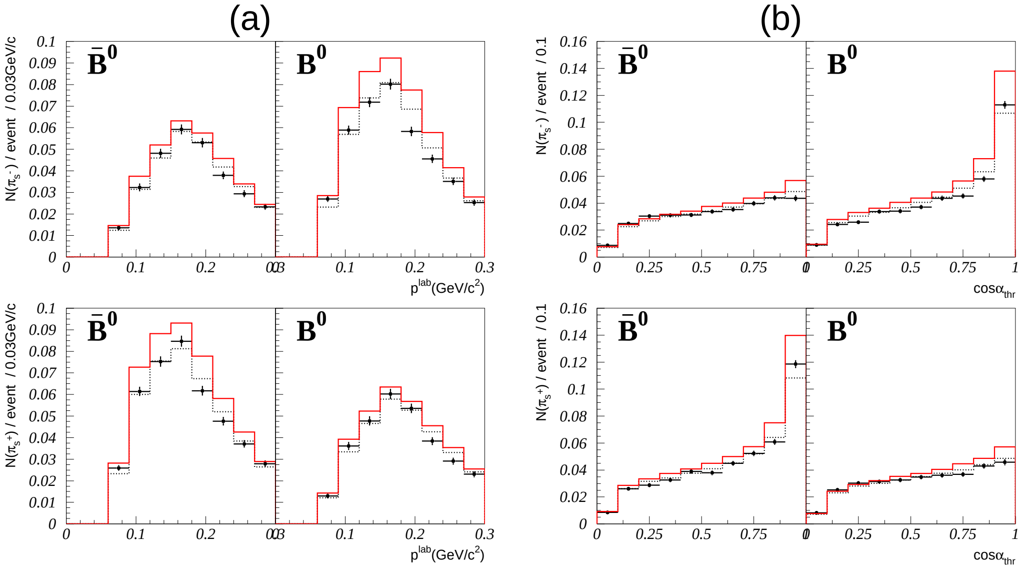

Figure C.3: *Distributions of (a) the lab. momentum and (b)* $\cos\alpha_{thr}$ *of slow pions for* $\overline{B}^0$ *and* B^0*. The points are for the data of control samples, while the histograms with solid lines and dotted lines are for the EvtGen-MC and QQ-MC, respectively. All distributions are made with a requirement on* π/e *ID to exclude the soft electrons originating from photon conversions and* π^0 *Dalitz decays. Upper two figures and lower two figures in each (a) or (b) are for* π_s^-*-like tracks and for* π_s^+*-like tracks, respectively. Upper right and lower left figures in each (a) or (b) contain slow pions from* $D^{*\pm}$ *decays.*

This class is intended to utilize the charge of low momentum pions from $D^{*\pm}$. Due to the low momentum which is 39 MeV/c in the $D^{*\pm}$ rest frame, the direction of the slow pions follows the direction of $D^{*\pm}$. The direction of $D^{*\pm}$ is approximated by the thrust axis of tagging side tracks, and the angle between the pion and the thrust axis can be used to discriminate the slow pion. The main background in this class comes from low momentum pions from other decays and electrons from photon conversions or π^0 Dalitz decays. The electrons can be separated by dE/dx measured with CDC. The discriminant variables in this class are summarized as: (1) magnitude of the momentum in the laboratory frame, p_{lab}; (2) polar angle in the laboratory frame, θ_{lab}; (3) cosine of the angle between the slow pion candidate and the thrust axis of the tagging side particles in cms, $\cos\alpha_{thr}$; (4) pion likelihood value by dE/dx ($L_{dE/dx}$); (5) charge of the track, where p_{lab} is used instead of p^* because e/π separation of dE/dx strongly depends on the momentum in the laboratory frame. The p^* is then determined uniquely by θ_{lab} and p_{lab}. Figure C.3 shows the distribution of $\cos\alpha_{thr}$ and the momenta of the slow pion candidates in the laboratory frame. The number of bins for each variable in the look-up table is 10 for p_{lab}, 10 for θ_{lab}, 7 for $\cos\alpha_{thr}$, 5 for $L_{dE/dx}$ and 2 for charge of the track (7000 bins in total).

Among tracks of this class, one pion track with the highest r is selected, and the $q \cdot r$

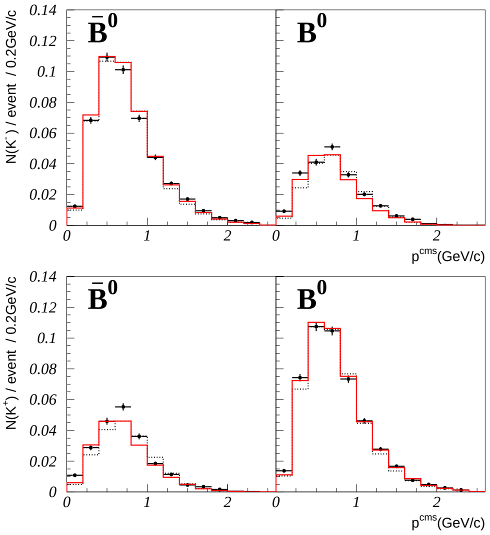

Figure C.4: *The cms momentum distributions of kaon candidates for* $\overline{B}^0$ *and* B^0. *The points are for the data of control samples, while the histograms with solid line and dotted line are for the EvtGen-MC and QQ-MC, respectively. The distribution of kaon cms momentum is made with a requirement on* K/π *ID to exclude the dominating pion component. Upper two figures and lower two figures are for* K^-*-like tracks and for* K^+*-like tracks, respectively. Upper right and lower left figures contain kaons from cascade* $b \to c \to s$ *transition.*

value of the track is passed to the event-level flavor tagging.

C.2.4 Kaon and Λ Track Class

This track class is intended to utilize the information of strangeness from $b \to c \to s$ cascade decays.

If a track is not categorized into any of lepton and slow pion class and is not identified as a proton, it is classified as a kaon. Discriminant variables are: (1) kaon likelihood value, L_K; (2) momentum in cms (p^*); (3) polar angle in the laboratory frame, θ_{lab}; (4) existence of K_S^0 candidates; (5) charge of the track. The L_K is used to discriminate kaons from pions and determined by combined information of ACC, TOF and dE/dx measured with CDC. The p^* and θ_{lab} are used to take into account the momentum and polar angle dependence of the kaon identification performance. If there are K_S^0 candidates, correlation of the kaon charge and the flavor of B is diluted. Figure C.4 shows cms momentum distribution of kaon-like track candidates compared to those in MC. The number of bins for each variable in the look-up table is 13 for L_K, 21 for p^*, 18 for θ_{lab}, 2 for K_S^0 existence (with or without) and 2 for charge of the track (19656 bins in total).

If a track is identified as a proton and forms a Λ candidate with a pion track, the Λ candidate is assigned to Λ track class. The discriminant variables are: (1) flavor of

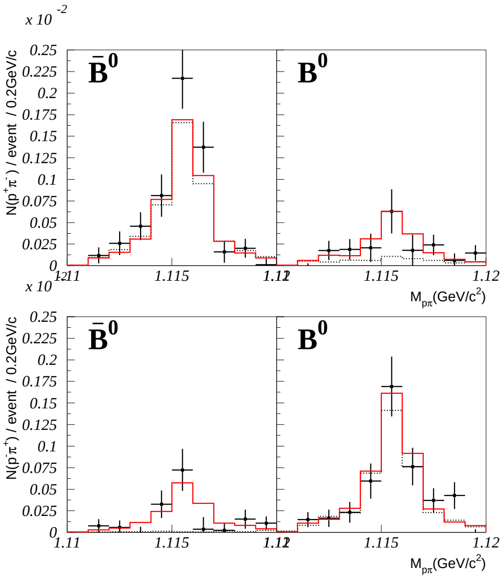

Figure C.5: *$M_{p\pi}$ distributions of Λ candidates for $\overline{B}^0$ and B^0. The points are for the data of control samples. Histograms with solid line and dotted line are for the EvtGen-MC and QQ-MC, respectively. Upper two figures and lower two figures are for Λ candidates and for $\overline{\Lambda}$ candidates, respectively. Upper left figure and lower right figure contain Λ particle from cascade $b \to c \to s$ transition.*

the Λ candidate, Λ or $\bar{\Lambda}$; (2) existence of K^0_S candidates; (3) invariant mass $M_{P\pi}$ of the Λ candidate; (4) angle difference between the Λ momentum vector and the direction of the Λ vertex from IP; (5) a distance in z direction between two tracks at the Λ vertex. Figure C.5 shows $M_{P\pi}$ distributions for the data and the MC. Each discriminant variables are divided into two bins, and a look-up table of 32 total bins are made.

The output of the kaon and Λ track class is given by the product of $q \cdot r$ for all kaon/Λ tracks assigned to this class:

$$(q \cdot r)_{K/\Lambda} \equiv \frac{\prod_i (1 + (q \cdot r)_i) - \prod_i (1 - (q \cdot r)_i)}{\prod_i (1 + (q \cdot r)_i) + \prod_i (1 - (q \cdot r)_i)}. \tag{C.2}$$

C.3 Event-Level Flavor Tagging

The event-level stage combines the track-level tagging results using $q \cdot r$ of three track classes as inputs. Figure C.6 shows the distribution of the track level $q \cdot r$. The $q \cdot r$ variables are divided into 25 for lepton class, 19 for slow pion class and 35 for kaon/Λ class and form a look-up table of 16625 total bins. The final $q \cdot r$ output of the event-level flavor tagging of the data and MC is shown in Fig. C.7. In the figure, separation between $\bar{B}^0$ and B^0 sample is clearly seen and distributions of the data and the MC show good agreement.

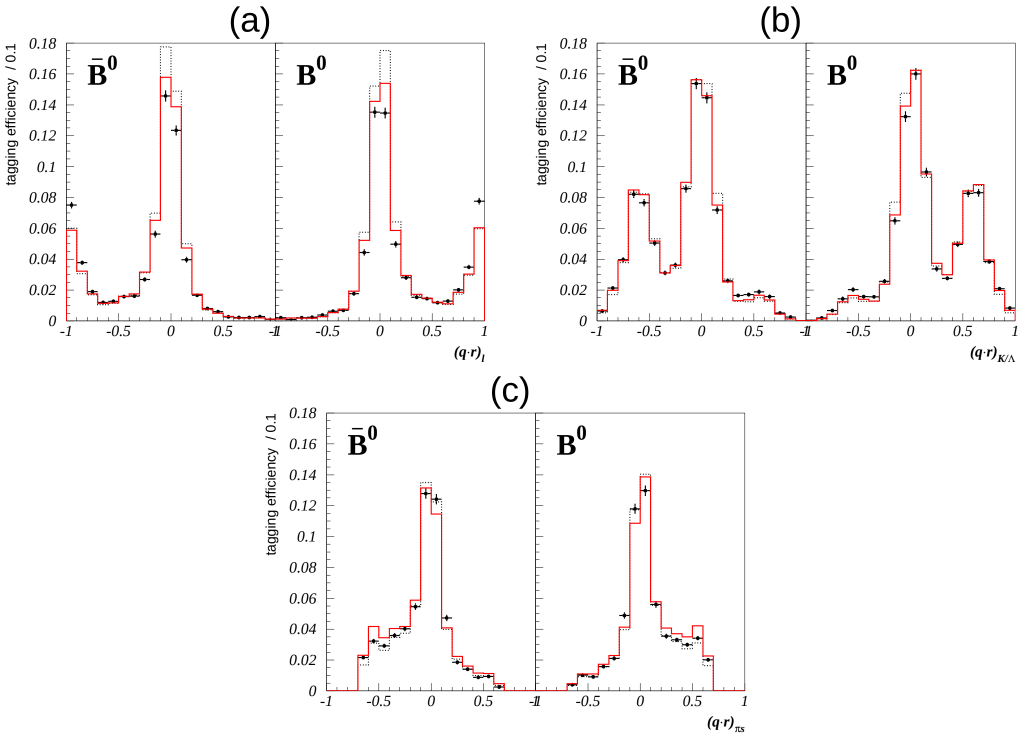

Figure C.6: *Distributions of input variables of event layer (a)* $(q \cdot r)_l$*, (b)* $(q \cdot r)_{K/\Lambda}$ *and (c)* $(q \cdot r)_{\pi_s}$ *for* $\overline{B}^0$ *and* B^0*. The points are for the data of control samples. The histograms with solid line and dotted line are for the EvtGen-MC and QQ-MC, respectively. For these distribution, the* $(q \cdot r)$ *values of corresponding track-layer outputs are obtained with EvtGen-MC look-up table. Events which have* $r = 0$ *due to no input tracks are excluded from each plots. The fractions of* $r = 0$ *are 36% for lepton category, 10% for Kaon/*Λ *category and 41% for slow pion category.*

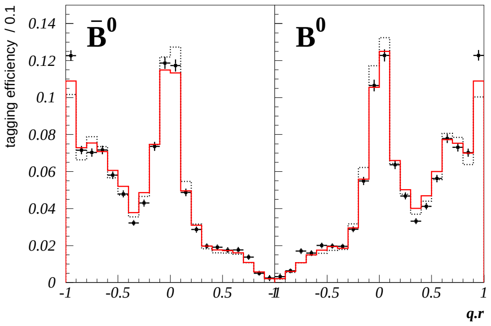

Figure C.7: *The* $q \cdot r$ *distribution for* $\overline{B}^0$ *and* B^0*. The points are for the data of control samples, while the histograms with solid line and dotted line are for the EvtGen-MC and the QQ-MC, respectively.*

C.4 Performance

We utilized the flavor quality value r to categorize the candidate events into six groups: $0.0 < r \leq 0.25$, $0.25 < r \leq 0.5$, $0.5 < r \leq 0.625$, $0.625 < r \leq 0.75$, $0.75 < r \leq 0.875$ and $0.875 < r$. The wrong tagging probabilities of these six tagging categories are measured with the self-tagged B^0 decays to $D^{*-}\ell^+\nu$, $D^-\pi^+$, $D^{*-}\pi^+$, $D^{*-}\rho^+$ and $J/\psi K^{*0}(K^{*0} \to K^+\pi^-)$. We determine directly from data the average wrong tag probabilities, $w_l \equiv (w_l^+ + w_l^-)/2(l = 1, 6)$, and differences between B^0 and $\overline{B}^0$ decays, $\Delta w_l \equiv w_l^+ - w_l^-$, where $w_l^{+(-)}$ is the wrong-tag probability for the $B^0(\overline{B}^0)$ decay in each r interval. Table C.1 summarizes these quantities used for the CP asymmetry measurement for the $B^0 \to D^{*+}D^{*-}$ decay. The overall tagging efficiency is found to be 99.8%. The total effective tagging efficiency is 28.7%.

l	r interval	ε_l	w_l	Δw_l	$\varepsilon_{\text{eff}}^l$
1	$0.000 - 0.250$	0.398	0.464 ± 0.006	-0.011 ± 0.006	0.002 ± 0.001
2	$0.250 - 0.500$	0.146	0.331 ± 0.008	$+0.004 \pm 0.010$	0.017 ± 0.002
3	$0.500 - 0.625$	0.104	0.231 ± 0.009	-0.011 ± 0.010	0.030 ± 0.002
4	$0.625 - 0.750$	0.122	0.163 ± 0.008	-0.007 ± 0.009	0.055 ± 0.003
5	$0.750 - 0.875$	0.094	0.109 ± 0.007	$+0.016 \pm 0.009$	0.057 ± 0.002
6	$0.875 - 1.000$	0.136	0.020 ± 0.005	$+0.003 \pm 0.006$	0.126 ± 0.003

Table C.1: *The event fractions* ε_l, *wrong-tag fractions* w_l, *wrong-tag fraction differences* Δw_l, *and average effective tagging efficiencies* $\varepsilon_{\text{eff}}^l = \varepsilon_l(1 - 2w_l)^2$ *for each* r *interval. The errors include both statistical and systematic uncertainties. The event fractions are obtained from the* $B^0 \to J/\psi K_S^0$ *simulation.*

Appendix D

Δt Resolution Function

D.1 Overview

We use almost same Δt resolution function as that used in the $\sin 2\phi_1$ measurement [47]. The details of the resolution function are found in the reference [55]. Here, we describe the resolution function briefly.

The Δt measurement requires a fully reconstructed B meson, B_{rec} and an associated B mesons, B_{asc}. We measure both vertices of B meson, z_{ful} and z_{rec}. The resolution function of the signal event, R_{sig}, is constructed as a convolution of four different contributions: (1) the detector resolution of B_{ful}, R_{ful}; (2) the detector resolution of B_{asc}, R_{asc}; (3) an additional smearing on z_{asc} due to the inclusion of tracks which do not originate from the B_{asc} vertex, R_{np}, which are mostly due to charm and K_S^0 decays; (4) the kinematic approximation that the B mesons are at rest in the center of mass system (cms), R_{k}. The overall resolution function, $R_{\mathrm{sig}}(\Delta t)$, is expressed as

$$\begin{aligned} R_{\mathrm{sig}}(\Delta t) = \iiint_{-\infty}^{\infty} & d(\Delta t')d(\Delta t'')d(\Delta t''')R_{\mathrm{ful}}(\Delta t - \Delta t')R_{\mathrm{asc}}(\Delta t' - \Delta t'') \\ & \times R_{\mathrm{np}}(\Delta t'' - \Delta t''')R_{\mathrm{k}}(\Delta t'''). \end{aligned} \tag{D.1}$$

D.2 Detector Resolution

D.2.1 Multiple-track vertex

The detector resolutions (R_{ful} and R_{asc}) describe primary tracks which are directly produced by B mesons. There are two types of vertices, multiple-tracks and single-track vertices. Because the resolution for multiple-track vertices is better than that for the single-track vertices, we treat them separately.

For multiple-track vertices, the detector resolution is represented as a sum of two Gaussian functions, which are parameterized by vertex-by-vertex determined errors. The error is obtained from the z-coordinate error of the fitted vertex and correction factors depending on the quality of the vertex. The vertex quality is represented by a reduced

χ^2 projected onto the z axis defined as

$$\xi \equiv \frac{1}{2n}\sum_{i=1}^{n}\left[\frac{z^i_{\mathrm{after}} - z^i_{\mathrm{before}}}{e^i_{\mathrm{before}}}\right], \tag{D.2}$$

where z^i_{before} and z^i_{after} are the z positions of each track before and after the vertex fit, respectively, and e^i_{before} is the error of z^i_{before}. We do not use the normal χ^2 because it is correlated with the vertex z position due to the IP constraint in the x-y plane. We require $\xi < 100$ to eliminate poorly reconstructed vertices.

The detector resolution function for multiple-track vertices are given by

$$R^{\mathrm{multiple}}_{\mathrm{q}}(\delta z_{\mathrm{q}}) = G(\delta z_{\mathrm{q}}; s_{\mathrm{q}}\sigma_{\mathrm{q}}), \tag{D.3}$$

where $q = (\mathrm{rec}, \mathrm{asc})$, δz is defined as a difference between a reconstructed z and the true z, $\delta z \equiv z - z_{\mathrm{true}}$, σ_{q} is a vertex error calculated from track errors for B_{q} vertex, s_{q} is the correction factor which is expressed as a first order polynomial of ξ:

$$\begin{aligned} s_{\mathrm{ful}} &\equiv (s^0_{\mathrm{ful}} + s^1_{\mathrm{ful}}\xi), \\ s_{\mathrm{asc}} &\equiv (s^0_{\mathrm{asc}} + s^1_{\mathrm{asc}}\xi), \end{aligned} \tag{D.4}$$

and G is a Gaussian function,

$$G(x;\sigma) \equiv \frac{1}{\sqrt{2\pi}\sigma}\exp\left(-\frac{x^2}{2\sigma^2}\right). \tag{D.5}$$

D.2.2 Single-track vertex

For the single-track vertex, the vertex quality can not be defined. Therefore, we use global correction factors. The detector resolution function for the single-track vertex is given by

$$R^{\mathrm{single}}_{\mathrm{q}}(\delta z_{\mathrm{q}}) = (1 - f_{\mathrm{tail}})G(\delta z_{\mathrm{q}}; s_{\mathrm{main}}\sigma) + f_{\mathrm{tail}}G(\delta z_{\mathrm{q}}; s_{\mathrm{tail}}\sigma), \tag{D.6}$$

where s_{main} and s_{tail} are global correction factors which are common to all the single track vertices, where one for the main part of the detector resolution and the other for the tail part that represents effects of poorly-reconstructed tracks.

D.2.3 Determination of Correction Factors

For B_{asc}, used parameters for correction factors are the same as those for the $\sin 2\phi_1$ measurement, since decay mode for B_{asc} is same. For B_{ful}, we obtained correction factors from control samples which have similar decay topology such as $B^0 \to D^{(*)+}D_S^{(*)-}$. Possible bias is found as negligible with comparison of $B^0 \to D^{*+}D^{*-}$ and control samples MC.

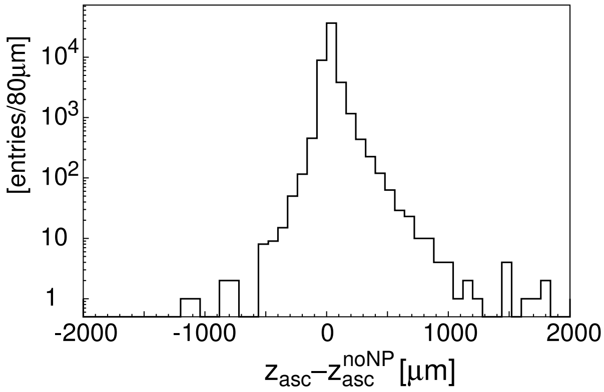

Figure D.1: *Distribution of* $z_{\mathrm{asc}} - z_{\mathrm{asc}}^{\mathrm{noNP}}$ *for vertices reconstructed with two or more tracks. In making this plot the events in which* $z_{\mathrm{asc}} = z_{\mathrm{asc}}^{\mathrm{noNP}}$ *are removed.*

D.3 Smearing due to Non-Primary Tracks

The vertex resolution of B_{asc} is smeared by contamination of non-primary tracks, which are charm decays and K_S^0. The resolution function R_{np} describes the effect with a prompt component expressed by Dirac's δ function which represents vertices without the contamination, and with components which account for the smearing due to the contamination. The R_{np} shape is studied by comparing two MC samples. One is normal $B\bar{B}$ MC sample. In another special MC sample, all secondary short-lived ($\tau < 10^{-9}$ s) particles are forced to decay with zero lifetime at the B meson decay point. We reconstruct B_{asc} in two MC samples and compare differences of reconstructed z positions between two samples. Figure D.1 shows distribution of $z_{\mathrm{asc}} - z_{\mathrm{asc}}^{\mathrm{noNP}}$, where z_{asc} is the z position of the associated side vertex in normal MC and $z_{\mathrm{asc}}^{\mathrm{noNP}}$ is the z vertex position in the special MC.

The resolution function R_{np} is determined as

$$R_{\mathrm{np}}(\delta z_{\mathrm{asc}}) \equiv f_\delta \delta(\delta z_{\mathrm{asc}}) + (1-f_\delta)[f_{\mathrm{p}} E_{\mathrm{p}}(\delta z_{\mathrm{asc}}; \tau_{\mathrm{np}}^{\mathrm{p}}) + (1-f_{\mathrm{p}}) E_{\mathrm{n}}(\delta z_{\mathrm{asc}}; \tau_{\mathrm{np}}^{\mathrm{n}})], \tag{D.7}$$

where f_δ is the prompt-component fraction, f_{p} is a fraction of the $\delta z_{\mathrm{asc}} > 0$ component and E_{p} and E_{n} are lifetime components of secondary vertices:

$$\begin{aligned} E_{\mathrm{p}}(x;\tau) &\equiv \frac{1}{\tau}\exp\left(-\frac{x}{\tau}\right) \text{ for } x > 0, \text{ otherwise } 0, \\ E_{\mathrm{n}}(x;\tau) &\equiv \frac{1}{\tau}\exp\left(-\frac{x}{\tau}\right) \text{ for } x \le 0, \text{ otherwise } 0. \end{aligned} \tag{D.8}$$

The τ_{np}^{p} and τ_{np}^{n} depend on the vertex quality, since non-primary particles from longer lived particles are farther from the primary vertex and deteriorate the vertex quality and the error. Based on a similar idea as that applied for the detector resolution part, the τ_{np}^{p} and τ_{np}^{n} are categorized by the number of track belonging to the vertex.

For vertices reconstructed with two or more tracks, τ_{np}^{p} and τ_{np}^{n} are parametrized as:

$$\begin{aligned} \tau_{\mathrm{np}}^{p} &= \tau_{\mathrm{p}}^{0} + \tau_{\mathrm{p}}^{1}(s_{\mathrm{asc}}^{0} + s_{\mathrm{asc}}^{1}\xi) \times \sigma_{\mathrm{asc}}/c(\beta\gamma)_\Upsilon, \\ \tau_{\mathrm{np}}^{n} &= \tau_{\mathrm{n}}^{0} + \tau_{\mathrm{n}}^{1}(s_{\mathrm{asc}}^{0} + s_{\mathrm{asc}}^{1}\xi) \times \sigma_{\mathrm{asc}}/c(\beta\gamma)_\Upsilon. \end{aligned} \tag{D.9}$$

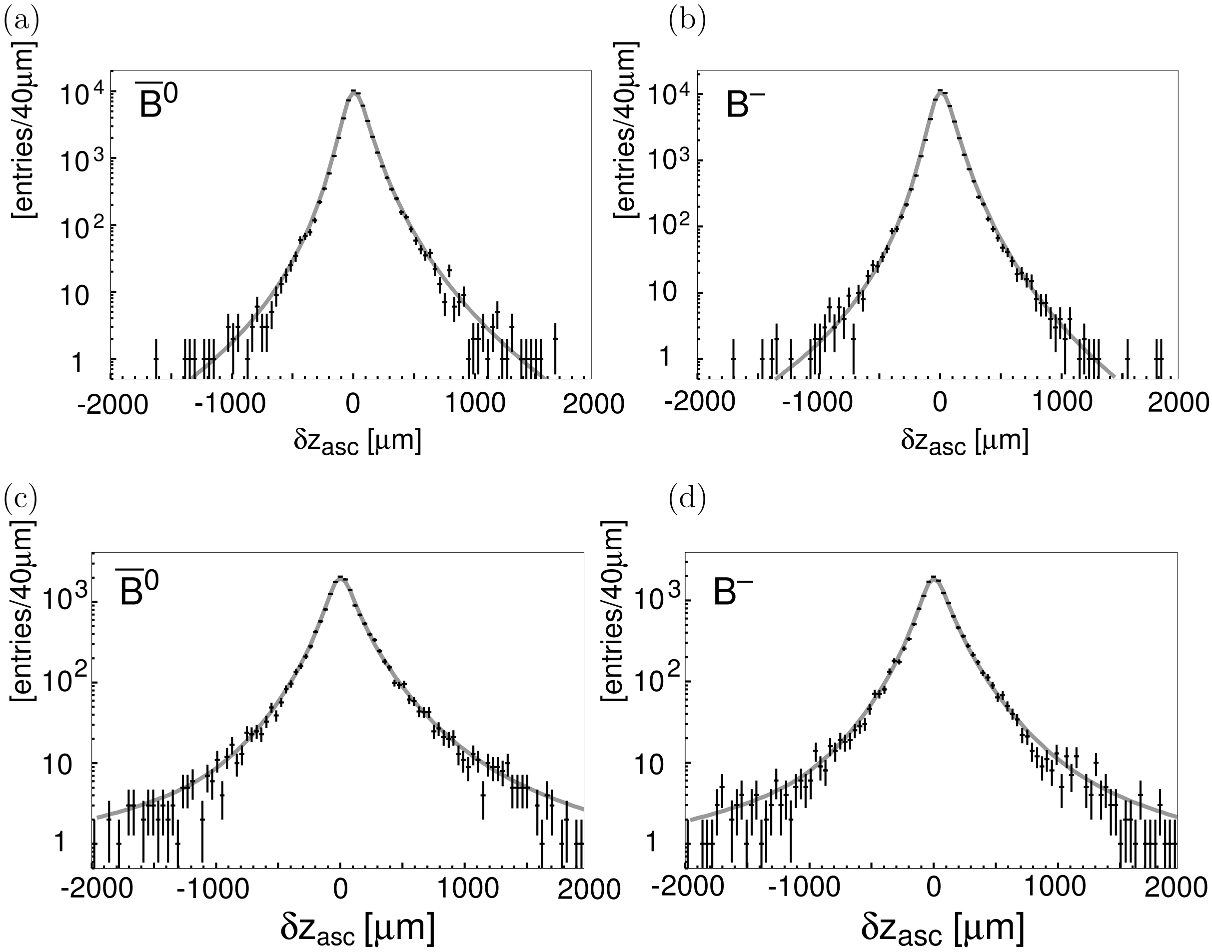

Figure D.2: *The $\delta z_{\rm asc}$ distributions of (a) multiple-track vertices for neutral B, (b) multiple-track vertices for charged B, (c) single-track vertices for neutral B (d) single-track vertices for charged B. The full reconstructed side B mesons decay into $J/\psi K^0_{\rm S}$ or $J/\psi K^-$.*

For vertices reconstructed with single tracks, they are given by:

$$\begin{cases} (\tau^p_{\rm np}) = \tau^0_{\rm p} + \tau^1_{\rm p} \times s_{\rm single} \times \sigma_{\rm asc} \\ (\tau^n_{\rm np}) = \tau^0_{\rm n} + \tau^1_{\rm p} \times s_{\rm single} \times \sigma_{\rm asc} \end{cases} \tag{D.10}$$

The parameters of $R_{\rm np}$ are determined with a MC study. Since the distribution shown in Fig. D.1 includes detector resolution effect of additional tracks as well, we do not use it to determine the parameters but fit the $\delta z_{\rm asc}$ distribution with the convolution of $R_{\rm asc}$ and $R_{\rm np}$. Because of the difference between neutral D lifetime (0.412 ps) and charged D lifetime (1.051 ps), the parameters are determined separately for neutral and charged B mesons. Figure D.2 shows the $\delta z_{\rm asc}$ distributions with fitted curves. The $R_{\rm asc}$ and $R_{\rm np}$ reproduce the distribution well. Table D.1 shows the determined parameters.

	neutral B		charged B	
	multiple	single	multiple	single
$f_{\rm p}$	0.929 ± 0.003	0.791 ± 0.009	0.935 ± 0.003	0.804 ± 0.011
$\tau_{\rm p}^0$ (ps)	0.056 ± 0.006	0.453 ± 0.005	0.052 ± 0.006	0.301 ± 0.004
$\tau_{\rm p}^1$	0.725 ± 0.015	$1.320^{+0.064}_{-0.063}$	0.630 ± 0.013	$1.130^{+0.061}_{-0.060}$
$\tau_{\rm n}^0$ (ps)	0.025 ± 0.032	$0.295^{+0.086}_{-0.085}$	-0.069 ± 0.029	$-0.148^{+0.193}_{-0.189}$
$\tau_{\rm n}^1$	$1.280^{+0.064}_{-0.061}$	$1.476^{+0.141}_{-0.134}$	$1.349^{+0.065}_{-0.062}$	$1.759^{+0.152}_{-0.144}$

Table D.1: *List of $R_{\rm np}$ parameters determined with the MC simulation.*

D.4 Kinematic Approximation

We calculate Δt as $\Delta z/\beta\gamma c$ with neglecting motion of B mesons in cms. The smearing due to this kinematic approximation is calculated analytically. ¿From the kinematics of the $\Upsilon(4S)$ two body decay, the difference between measured Δt and the $\delta t_{\rm true} = t_{\rm ful} - t_{\rm asc}$ is calculated to be:

$$\begin{aligned} x \equiv \Delta t - \Delta t_{\rm true} &= (z_{\rm ful} - z_{\rm asc})/c(\beta\gamma)_\Upsilon - (t_{\rm ful} - t_{\rm asc}) \\ &= [t_{\rm ful}c(\beta\gamma)_{\rm ful} - t_{\rm asc}c(\beta\gamma)_{\rm asc}]/c(\beta\gamma)_\Upsilon - (t_{\rm ful} - t_{\rm asc}) \\ &= [(\beta\gamma)_{\rm ful}/(\beta_\gamma)_\Upsilon - 1]t_{\rm ful} - [(\beta\gamma)_{\rm asc}/(\beta_\gamma)_\Upsilon - 1]t_{\rm asc}, \end{aligned} \tag{D.11}$$

where $(\beta\gamma)_{\rm ful}$ and $(\beta\gamma)_{\rm asc}$ are Lorentz boost factors of $B_{\rm ful}$ and $B_{\rm asc}$, respectively. Their ratios to $(\beta\gamma)_\Upsilon$ are given by:

$$\begin{aligned} (\beta\gamma)_{\rm ful}/(\beta\gamma)_\Upsilon &= \frac{E_B^{\rm cms}}{m_B} + \frac{p_B^{\rm cms}\cos\theta_B^{\rm cms}}{\beta_\Upsilon m_B}, \\ (\beta\gamma)_{\rm asc}/(\beta\gamma)_\Upsilon &= \frac{E_B^{\rm cms}}{m_B} - \frac{p_B^{\rm cms}\cos\theta_B^{\rm cms}}{\beta_\Upsilon m_B}, \end{aligned} \tag{D.12}$$

where $E_B^{\rm cms}$ is the energy of B meson which corresponds to the beam energy ~ 5.29GeV, m_B is the B meson mass, $p_B^{\rm cms} \sim 0.34$ GeV/c is the B momentum in the cms and $\theta_B^{\rm cms}$ is the polar angle of the fully reconstructed B in the cms.

Since $t_{\rm ful}$ and $t_{\rm asc}$ distributions follow $E_{\rm p}(t_{\rm ful};\tau_B) = 1/\tau_B \exp(-t_{\rm ful}\tau_B)$ and $E_{\rm p}(t_{\rm asc};\tau_B) = 1/\tau_B \exp(-t_{\rm asc}\tau_B)$, respectively, the probability density of obtaining x and $\Delta t_{\rm true}$ simultaneously is given by

$$\begin{aligned} F(x, \Delta t) = \int_0^\infty \int_0^\infty & dt_{\rm ful} dt_{\rm asc} E_{\rm p}(t_{\rm ful};\tau_B) E_{\rm p}(t_{\rm asc};\tau_B) \delta(\Delta t_{\rm true} - (t_{\rm ful} - t_{\rm asc})) \\ & \times \delta(x - \{[(\beta\gamma)_{\rm ful}/(\beta\gamma)_\Upsilon - 1]t_{\rm ful} - [(\beta\gamma)_{\rm asc}/(\beta\gamma)_\Upsilon - 1]t_{\rm asc}\}), \end{aligned} \tag{D.13}$$

and the probability density of obtaining $\Delta t_{\rm true}$ is given by

$$F(\Delta t) = \int_0^\infty \int_0^\infty dt_{\rm ful} dt_{\rm asc} E_{\rm p}(t_{\rm ful};\tau_B) E_{\rm p}(t_{\rm asc};\tau_B) \delta(\Delta t_{\rm true} - (t_{\rm ful} - t_{\rm asc})). \tag{D.14}$$

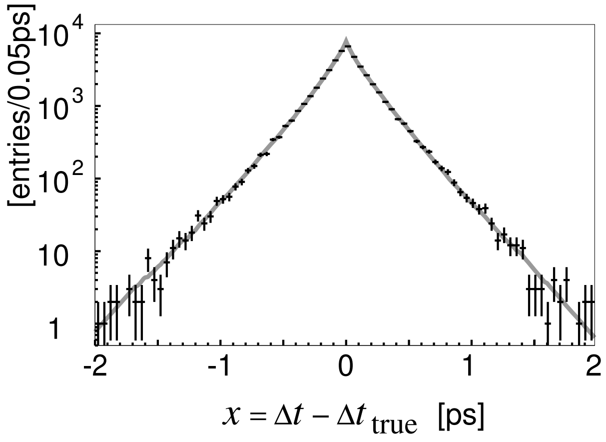

Figure D.3: *The* $x = \Delta t - \Delta t_{\mathrm{true}}$ *distribution for neutral* B *meson MC sample together with the function* $R_{\mathrm{k}}(x)$.

The $R_{\mathrm{k}}(x)$ is then defined as the conditional probability density of obtaining x for a given Δt_{true}. It is expressed as $R_{\mathrm{k}}(x) = F(x, \Delta t_{\mathrm{true}})/F(\Delta t_{\mathrm{true}})$ which gives:

$$R_{\mathrm{k}}(x) = \begin{cases} E_{\mathrm{p}}\left(x - \left[(\frac{E_B^{cms}}{m_B} - 1)\Delta t_{\mathrm{true}} + \frac{p_B^{\mathrm{cms}}\cos\theta_B^{\mathrm{cms}}}{\beta_\Upsilon m_B}|\Delta t_t rue|\right]; |\frac{p_B^{\mathrm{cms}}\cos\theta_B^{\mathrm{cms}}}{\beta_\Upsilon m_B}|\tau_B\right) & (\cos\theta_B^{\mathrm{cms}} > 0) \\ \delta\left(x - (\frac{E_B^{\mathrm{cms}}}{m_B} - 1)\Delta t_{\mathrm{true}}\right) & (\cos\theta_B^{\mathrm{cms}} = 0) \\ E_{\mathrm{n}}\left(x - \left[(\frac{E_B^{\mathrm{cms}}}{m_B} - 1)\Delta t_{\mathrm{true}} + \frac{p_B^{\mathrm{cms}}\cos\theta_B^{\mathrm{cms}}}{\beta_\Upsilon m_B}|\Delta t_t rue|\right]; |\frac{p_B^{\mathrm{cms}}\cos\theta_B^{\mathrm{cms}}}{\beta_\Upsilon m_B}|\tau_B\right) & (\cos\theta_B^{\mathrm{cms}} < 0) \end{cases} \tag{D.15}$$

Figure D.3 shows the x distribution for B^0 MC sample with the function $R_{\mathrm{k}}(x)$. The $R_{\mathrm{k}}(x)$ function represents the distribution correctly.

D.5 Outlier

We find that there still exists a small component with a very long tail, which is order of several tens ps, that cannot be described by the resolution functions above. The outlier term is introduced to describe this long tail and represented by a Gaussian with zero mean and event-independent width,

$$P_{\mathrm{ol}}(\Delta t) = G(\Delta t, \sigma_{\mathrm{ol}}). \tag{D.16}$$

The fraction of outlier f_{ol} is typically less than 10^{-3} for multiple-track vertices and $\sim 10^{-2}$ for single-track vertices.

Appendix E

Measurement of Branching Fraction of $B^0 \to D^{*+}D^{*-}$

E.1 Yield Extraction

In this chapter, we calculate the branching fraction of the $B^0 \to D^{*+}D^{*-}$ decay. To obtain the branching fraction, we use the reconstruction efficiency and the known branching fraction for each sub-decay mode.

Event selection and yield extraction were already described in Chapter 4. The fit yields 129.5 ± 12.9 signal events, where 20% include $D^{*+} \to D^+\pi^0$ decays.

E.2 Reconstruction Efficiencies

We estimate reconstruction efficiencies and expected yields for $Br = 10^{-3}$ at 140 fb^{-1} with signal MC events generated with EvtGen [41]. No polarization is assumed. The total expected yield is 202.1 ± 2.7. Small corrections are applied to the reconstruction efficiencies for charged tracks, π^0's and K_S^0's to account for differences between data and MC. After the efficiency correction is applied, the total signal yield becomes 160.1 ± 2.1. The reconstruction efficiency and expected yield for each decay mode is summarized in Table E.1-E.3.

E.3 Calculation of Branching Fraction

The branching fraction $\mathcal{B}(B^0 \to D^{*+}D^{*-})$ is calculated by the following equation:

$$N(B\bar{B}) \cdot \mathcal{B}(B^0 \to D^{*+}D^{*-}) \cdot (\sum_i \epsilon_i \mathcal{B}'_i) \quad = \quad Y_{Data}, \tag{E.1}$$

where $N(B\bar{B})$ is the number of $B\bar{B}$ pairs in data, ϵ_i and $\mathcal{B}'_i$ are a reconstruction efficiency and the total sub-decay branching fraction for each final state i, respectively (Table E.1-E.3). Y_{Data} is the total signal yield. We obtain

$$\mathcal{B}(B^0 \to D^{*+}D^{*-}) = [0.81 \pm 0.08(\mathrm{stat}) \pm 0.11(\mathrm{syst})] \times 10^{-3}. \tag{E.2}$$

Table E.1: Efficiencies and expected signal yields for $B^0 \to D^{*+}D^{*-}$. The yield is calculated assuming $Br(B^0 \to D^{*+}D^{*-}) = 10^{-3}$.

$B^0 \to D^{*+}D^{*-}$			
$D^{*+} \to D^0\pi_s^+$	$D^{*-} \to \overline{D}^0\pi_s^-$	Efficiency	Yield for $Br = 10^{-3}$
$D^0 \to K^-\pi^+$	$\overline{D}^0 \to K^+\pi^-$	0.128 ± 0.003	12.7 ± 0.3
	$\overline{D}^0 \to K^+\pi^-\pi^0$	0.047 ± 0.002	16.1 ± 0.7
	$\overline{D}^0 \to K^+\pi^-\pi^+\pi^-$	0.053 ± 0.002	10.4 ± 0.4
	$\overline{D}^0 \to K_S^0\pi^+\pi^-$	0.048 ± 0.002	2.5 ± 0.1
	$\overline{D}^0 \to K_S^0\pi^+\pi^-\pi^0$	0.018 ± 0.001	1.8 ± 0.1
	$\overline{D}^0 \to K^+K^-$	0.118 ± 0.003	1.27 ± 0.03
$D^0 \to K^-\pi^+\pi^0$	$\overline{D}^0 \to K^+\pi^-$	0.052 ± 0.002	17.7 ± 0.8
	$\overline{D}^0 \to K^+\pi^-\pi^0$	0.019 ± 0.001	22.7 ± 1.6
	$\overline{D}^0 \to K^+\pi^-\pi^+\pi^-$	0.024 ± 0.002	15.9 ± 1.0
	$\overline{D}^0 \to K_S^0\pi^+\pi^-$	0.019 ± 0.001	3.4 ± 0.2
	$\overline{D}^0 \to K_S^0\pi^+\pi^-\pi^0$	0.007 ± 0.001	2.3 ± 0.3
	$\overline{D}^0 \to K^+K^-$	0.045 ± 0.002	1.68 ± 0.08
$D^0 \to K^-\pi^+\pi^-\pi^+$	$\overline{D}^0 \to K^+\pi^-$	0.057 ± 0.002	11.1 ± 0.5
	$\overline{D}^0 \to K^+\pi^-\pi^0$	0.022 ± 0.001	14.5 ± 1.0
	$\overline{D}^0 \to K^+\pi^-\pi^+\pi^-$	0.022 ± 0.001	8.6 ± 0.6
	$\overline{D}^0 \to K_S^0\pi^+\pi^-$	0.019 ± 0.001	2.0 ± 0.1
	$\overline{D}^0 \to K_S^0\pi^+\pi^-\pi^0$	0.006 ± 0.001	1.2 ± 0.1
	$\overline{D}^0 \to K^+K^-$	0.049 ± 0.002	1.04 ± 0.05
$D^0 \to K_S^0\pi^+\pi^-$	$\overline{D}^0 \to K^+\pi^-$	0.049 ± 0.002	2.6 ± 0.1
	$\overline{D}^0 \to K^+\pi^-\pi^0$	0.018 ± 0.001	3.2 ± 0.2
	$\overline{D}^0 \to K^+\pi^-\pi^+\pi^-$	0.016 ± 0.001	1.6 ± 0.1
	$\overline{D}^0 \to K^+K^-$	0.042 ± 0.002	0.24 ± 0.01
$D^0 \to K_S^0\pi^+\pi^-\pi^0$	$\overline{D}^0 \to K^+\pi^-$	0.019 ± 0.001	1.8 ± 0.1
	$\overline{D}^0 \to K^+\pi^-\pi^0$	0.006 ± 0.001	2.0 ± 0.3
	$\overline{D}^0 \to K^+\pi^-\pi^+\pi^-$	0.007 ± 0.001	1.2 ± 0.2
	$\overline{D}^0 \to K^+K^-$	0.016 ± 0.001	0.17 ± 0.01
$\overline{D}^0 \to K^-K^+$	$\overline{D}^0 \to K^+\pi^-$	0.117 ± 0.003	1.26 ± 0.03
	$\overline{D}^0 \to K^+\pi^-\pi^0$	0.046 ± 0.002	1.71 ± 0.08
	$\overline{D}^0 \to K^+\pi^-\pi^+\pi^-$	0.044 ± 0.002	0.93 ± 0.04
	$\overline{D}^0 \to K_S^0\pi^+\pi^-$	0.042 ± 0.002	0.23 ± 0.01
	$\overline{D}^0 \to K_S^0\pi^+\pi^-\pi^0$	0.012 ± 0.001	0.12 ± 0.01
	$\overline{D}^0 \to K^+K^-$	0.106 ± 0.003	0.125 ± 0.004
Total expected yield for $Br = 10^{-3}$			164.1 ± 2.6
Total corrected yield for $Br = 10^{-3}$			134.4 ± 2.1

Table E.2: Efficiencies and expected signal yields for $B^0 \to D^{*+}D^{*-}$. The yield is calculated assuming $Br(B^0 \to D^{*+}D^{*-}) = 10^{-3}$.

$B^0 \to D^{*+}D^{*-}$			
$D^{*+} \to D^0\pi_s^+$	$D^{*-} \to D^-\pi_s^0$	Efficiency	Yield for $Br = 10^{-3}$
$D^0 \to K^-\pi^+$	$D^- \to K^+\pi^-\pi^-$	0.057 ± 0.002	6.0 ± 0.2
	$D^- \to K^0_S\pi^-$	0.057 ± 0.002	0.61 ± 0.02
	$D^- \to K^0_S\pi^-\pi^0$	0.019 ± 0.001	0.74 ± 0.05
	$D^- \to K^+K^-\pi^-$	0.048 ± 0.002	0.50 ± 0.02
	$D^- \to K^0_S K^-$	0.050 ± 0.002	0.114 ± 0.005
$D^0 \to K^-\pi^+\pi^0$	$D^- \to K^+\pi^-\pi^-$	0.021 ± 0.001	7.6 ± 0.5
	$D^- \to K^0_S\pi^-$	0.020 ± 0.001	0.75 ± 0.05
	$D^- \to K^0_S\pi^-\pi^0$	0.010 ± 0.001	1.3 ± 0.1
	$D^- \to K^+K^-\pi^-$	0.017 ± 0.001	0.61 ± 0.05
	$D^- \to K^0_S K^-$	0.023 ± 0.001	0.18 ± 0.01
$D^0 \to K^-\pi^+\pi^-\pi^+$	$D^- \to K^+\pi^-\pi^-$	0.024 ± 0.002	5.0 ± 0.3
	$D^- \to K^0_S\pi^-$	0.024 ± 0.002	0.51 ± 0.03
	$D^- \to K^0_S\pi^-\pi^0$	0.009 ± 0.001	0.73 ± 0.07
	$D^- \to K^+K^-\pi^-$	0.022 ± 0.001	0.44 ± 0.03
	$D^- \to K^0_S K^-$	0.023 ± 0.001	0.101 ± 0.007
$D^0 \to K^0_S\pi^+\pi^-$	$D^- \to K^+\pi^-\pi^-$	0.019 ± 0.001	1.03 ± 0.07
	$D^- \to K^+K^-\pi^-$	0.015 ± 0.001	0.082 ± 0.007
$D^0 \to K^0_S\pi^+\pi^-\pi^0$	$D^- \to K^+\pi^-\pi^-$	0.009 ± 0.001	0.85 ± 0.09
	$D^- \to K^+K^-\pi^-$	0.005 ± 0.001	0.054 ± 0.007
$\overline{D}^0 \to K^-K^+$	$D^- \to K^+\pi^-\pi^-$	0.017 ± 0.001	0.19 ± 0.01
	$D^- \to K^0_S\pi^-$	0.050 ± 0.002	0.058 ± 0.003
	$D^- \to K^0_S\pi^-\pi^0$	0.017 ± 0.001	0.070 ± 0.005
	$D^- \to K^+K^-\pi^-$	0.016 ± 0.001	0.018 ± 0.001
	$D^- \to K^0_S K^-$	0.046 ± 0.002	0.011 ± 0.0005
Total expected yield for $Br = 10^{-3}$			27.5 ± 0.7
Total corrected yield for $Br = 10^{-3}$			22.4 ± 0.6

Table E.3: Efficiencies and expected signal yields for $B^0 \to D^{*+}D^{*-}$. The yield is calculated assuming $Br(B^0 \to D^{*+}D^{*-}) = 10^{-3}$.

$B^0 \to D^{*+}D^{*-}$			
$D^{*+} \to D^+\pi^0_s$	$D^{*-} \to \overline{D}^0\pi^-_s$	Efficiency	Yield for $Br = 10^{-3}$
$D^+ \to K^-\pi^+\pi^+$	$\overline{D}^0 \to K^+\pi^-$	0.063 ± 0.002	6.6 ± 0.3
	$\overline{D}^0 \to K^+\pi^-\pi^0$	0.025 ± 0.002	8.9 ± 0.6
	$\overline{D}^0 \to K^+\pi^-\pi^+\pi^-$	0.029 ± 0.002	6.0 ± 0.3
	$\overline{D}^0 \to K^0_S\pi^+\pi^-$	0.022 ± 0.001	1.19 ± 0.08
	$\overline{D}^0 \to K^0_S\pi^+\pi^-\pi^0$	0.009 ± 0.001	0.85 ± 0.09
	$\overline{D}^0 \to K^+K^-$	0.058 ± 0.002	0.65 ± 0.03
$D^+ \to K^0_S\pi^+$	$\overline{D}^0 \to K^+\pi^-$	0.055 ± 0.002	0.59 ± 0.02
	$\overline{D}^0 \to K^+\pi^-\pi^0$	0.024 ± 0.002	0.88 ± 0.06
	$\overline{D}^0 \to K^+\pi^-\pi^+\pi^-$	0.026 ± 0.002	0.56 ± 0.03
	$\overline{D}^0 \to K^+K^-$	0.047 ± 0.002	0.055 ± 0.002
$D^+ \to K^0_S\pi^+\pi^0$	$\overline{D}^0 \to K^+\pi^-$	0.022 ± 0.001	0.86 ± 0.06
	$\overline{D}^0 \to K^+\pi^-\pi^0$	0.009 ± 0.001	1.2 ± 0.1
	$\overline{D}^0 \to K^+\pi^-\pi^+\pi^-$	0.009 ± 0.001	0.68 ± 0.07
	$\overline{D}^0 \to K^+K^-$	0.020 ± 0.001	0.085 ± 0.006
$D^+ \to K^-K^+\pi^+$	$\overline{D}^0 \to K^+\pi^-$	0.041 ± 0.002	0.42 ± 0.02
	$\overline{D}^0 \to K^+\pi^-\pi^0$	0.017 ± 0.001	0.59 ± 0.05
	$\overline{D}^0 \to K^+\pi^-\pi^+\pi^-$	0.019 ± 0.001	0.39 ± 0.03
	$\overline{D}^0 \to K^0_S\pi^+\pi^-$	0.018 ± 0.001	0.097 ± 0.007
	$\overline{D}^0 \to K^0_S\pi^+\pi^-\pi^0$	0.005 ± 0.001	0.052 ± 0.007
	$\overline{D}^0 \to K^+K^-$	0.043 ± 0.002	0.048 ± 0.002
$D^+ \to K^0_SK^+$	$\overline{D}^0 \to K^+\pi^-$	0.052 ± 0.002	0.118 ± 0.005
	$\overline{D}^0 \to K^+\pi^-\pi^0$	0.018 ± 0.001	0.14 ± 0.01
	$\overline{D}^0 \to K^+\pi^-\pi^+\pi^-$	0.022 ± 0.001	0.099 ± 0.007
	$\overline{D}^0 \to K^+K^-$	0.043 ± 0.002	0.010 ± 0.0005
Total expected yield for $Br = 10^{-3}$			31.0 ± 0.7
Total corrected yield for $Br = 10^{-3}$			25.2 ± 0.6

The result is consistent with the present world-average values [13]. The systematic error is described in the following section.

E.4 Systematic Uncertainty

E.4.1 Calculation of Systematic Uncertainty

We consider the following sources of systematic uncertainties. A summary is given in Table E.4.

Source	$B^0 \to D^{*+}D^{*-}$(%)
Tracking efficiency	10.5
π^0 reconstruction	1.7
K_S^0 reconstruction	0.8
Particle ID (K and π)	3.3
Fit parameters and methods	0.8
Daughter branching fractions	7.3
MC Statistics	1.3
Number of $B\bar{B}$	0.5
Polarization	1.8
Sum	13.6

Table E.4: *Systematic uncertainty of $D^{*+}D^{*-}$ branching fraction*

E.4.2 Reconstruction Efficiency

Uncertainties that arise from efficiency corrections for charged tracks, π^0's and K_S^0's are taken into account. Tracking efficiency for charged tracks are obtained from comparison of data and MC samples. For example, efficiency ratio of data/MC between $\eta \to \pi^+\pi^-\pi^0$ and $\eta \to \gamma\gamma$ and efficiency ratio of $D^{*+} \to D^0\pi^+$ decays are used.

E.4.3 Particle Identification

Uncertainties of particle identification are estimated.

E.4.4 Fit Parameters and Methods

Uncertainties of fit parameters are obtained by varying each signal and background shape parameter. We also varied the signal box by 10 (3.5) MeV for ΔE (M_{bc}), each of which approximately corresponds to one standard deviation of the narrow Gaussian.

E.4.5 Daughter Branching Fractions

An expected yield for each final state of the $B^0 \to D^{*+}D^{*-}$ decay is proportional to the product branching fractions of D^* and D decays, which are taken from [13]. Systematic uncertainties of daughter branching fractions are estimated with varying them by $\pm 1\sigma$. This estimation is done by taking correlations among daughter branching fractions into account.

E.4.6 MC Statistics

The reconstruction efficiencies are estimated from signal MC. Their statistical errors are taken as systematic uncertainties.

E.4.7 Number of $B\bar{B}$

The number of $B\bar{B}$ and its error are take into account.

E.4.8 Polarization

If the polarization parameters assumed in MC are different from those in data, the total reconstruction efficiency is affected. This effect is estimated by the following efficiency ratio ($r_{MC/Data}$):

$$\begin{aligned} r_{MC/Data} &= \frac{\epsilon_{MC}}{\epsilon_{Data}} \\ &= \frac{\epsilon_0 R_{0MC} + \epsilon_{||} R_{\|MC} + \epsilon_{\perp} R_{\perp MC}}{\epsilon_0 R_{0Data} + \epsilon_{||} R_{\|Data} + \epsilon_{\perp} R_{\perp Data}}, \end{aligned} \tag{E.3}$$

where ϵ_i is MC reconstruction efficiency for each polarization, R_{iData} is the polarization parameters obtained from data, which will be described in the next chapter. Because signal MC is generated with assuming no polarization,

$$R_{0MC} = R_{\|MC} = R_{\perp MC} = 1/3. \tag{E.4}$$

Appendix F

Control Sample Selection

F.1 Event Selection

For the $B^0 \to D^{*+}D^{*-}$ analysis, $D^{(*)}D_s^{(*)}$ decay modes are good control sample, because their decay topology is quite similar to $D^{*+}D^{*-}$ and their yields are much larger as they are Cabibbo-allowed decays.

We reconstruct the following decay modes:

- $\overline{B}^0 \to D^- D_s^+$
- $\overline{B}^0 \to D^- D_s^{*+}$
- $\overline{B}^0 \to D^{*-} D_s^+$
- $\overline{B}^0 \to D^{*-} D_s^{*+}$
- $B^- \to D^0 D_s^-$
- $B^- \to D^0 D_s^{*-}$
- $B^- \to D^{*0} D_s^-$
- $B^- \to D^{*0} D_s^{*-}$

Event selection criteria are almost the same as those for the $D^{*+}D^{*-}$ selection. Additionally we reconstruct $D^{*0} \to D^0\pi^0$ and $D_s^{*+} \to D_s^+\gamma$. D_s^+ decays into $\phi(K^+K^-)\pi^+$, $K^{*0}(K^+\pi^-)K^+$ and $K_S^0K^+$. Each reconstructed mass is required to be within 3 sigmas from the nominal mass, except for $|\Delta M(\phi)| < 0.012$ GeV and $|\Delta M(K^{*0})| < 0.1$ GeV.

F.2 Yield Extraction

Yield extraction is performed with M_{bc} projection. To avoid feed across from other decay modes, we applied ΔE signal box ($|\Delta E| < 0.04$ GeV). Signal shape is decided from each signal MC and background shape is simultaneously fitted with yield. Figures F.1 show whole event candidates in M_{bc}-ΔE plane. Figures F.2 show M_{bc} projection in ΔE signal region and fit results. Extracted yields are summarized in Table F.1.

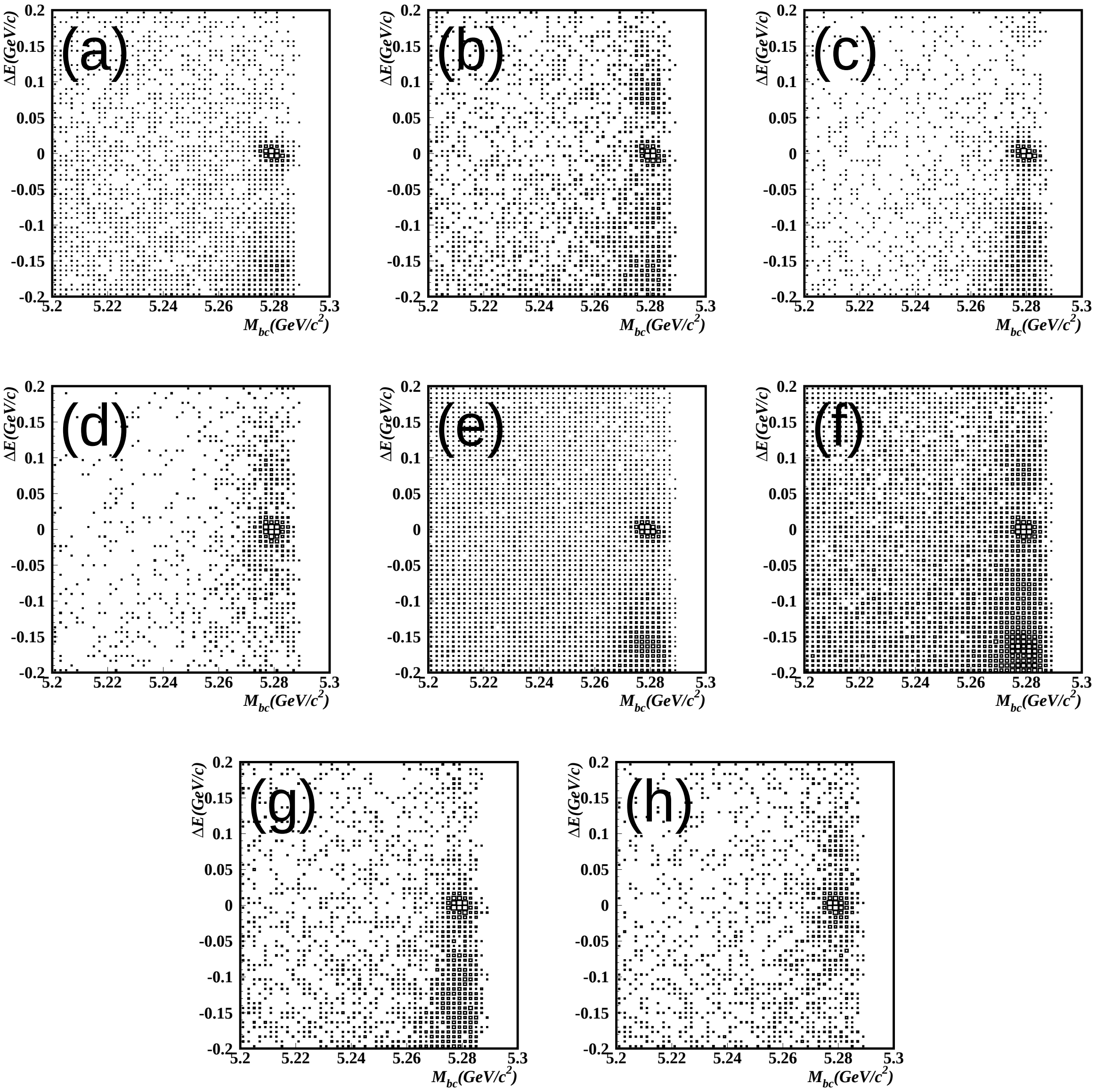

Figure F.1: *Two-dimensional distribution for control samples in the* ΔE-$M_{\rm bc}$ *plane; (a)* $\overline{B}^0 \to D^- D_s^+$*; (b)* $\overline{B}^0 \to D^- D_s^{*+}$*; (c)* $\overline{B}^0 \to D^{*-} D_s^+$*; (d)* $\overline{B}^0 \to D^{*-} D_s^{*+}$*; (e)* $B^- \to D^0 D_s^-$*; (f)* $B^- \to D^0 D_s^{*-}$*; (g)* $B^- \to D^{*0} D_s^-$*; (h)* $B^- \to D^{*0} D_s^{*-}$*.*

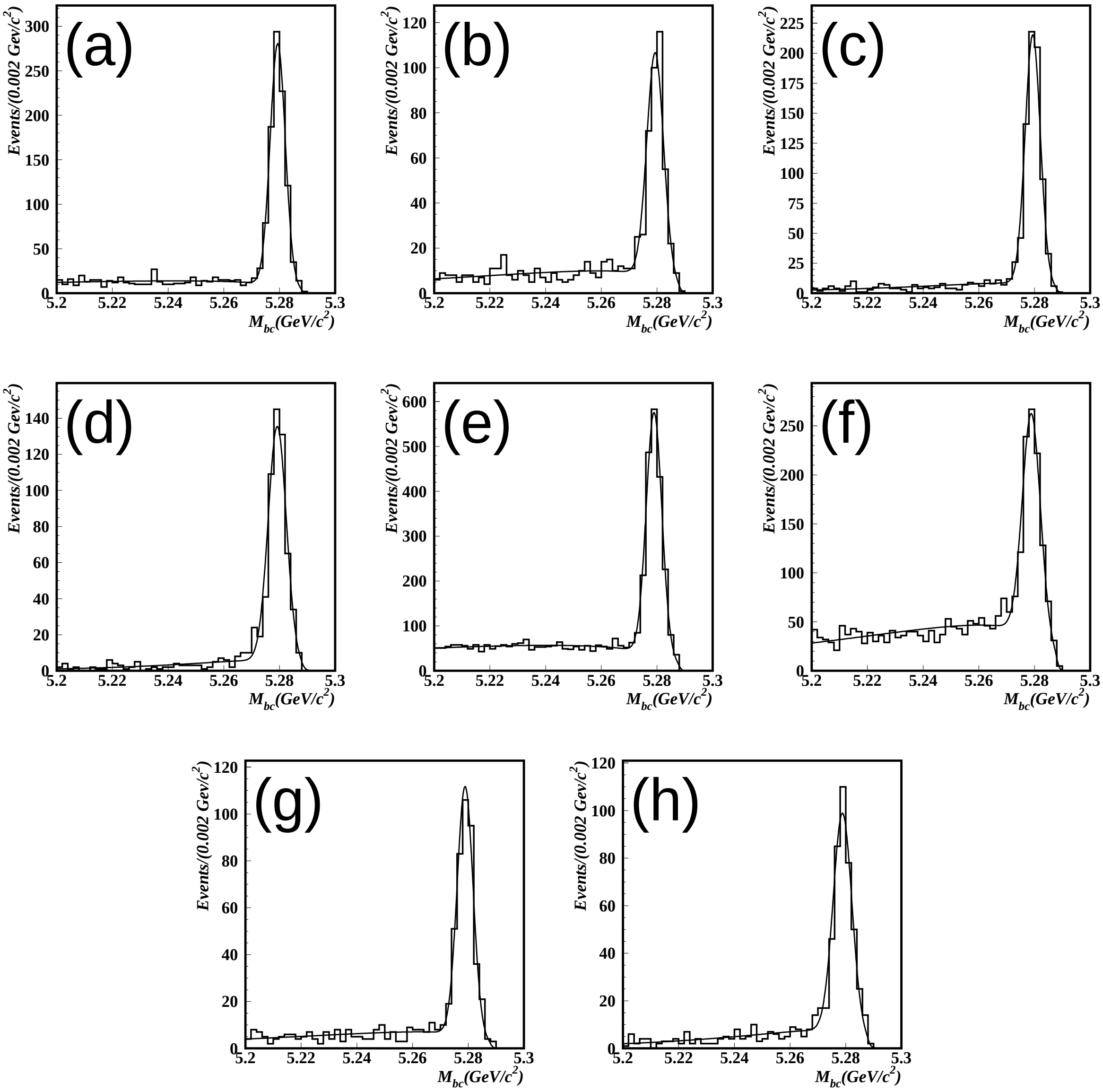

Figure F.2: $M_{\rm bc}$ *distribution for control samples within the* ΔE *signal region; (a)* $\overline{B}^0 \to D^- D_s^+$*; (b)* $\overline{B}^0 \to D^- D_s^{*+}$*; (c)* $\overline{B}^0 \to D^{*-} D_s^+$*; (d)* $\overline{B}^0 \to D^{*-} D_s^{*+}$*; (e)* $B^- \to D^0 D_s^-$*; (f)* $B^- \to D^0 D_s^{*-}$*; (g)* $B^- \to D^{*0} D_s^-$*; (h)* $B^- \to D^{*0} D_s^{*-}$*.*

Mode	No in signal box	Yield(Purity)
$\overline{B}^0 \rightarrow D^- D_s^+$	998	$921 \pm 21(92\%)$
$\overline{B}^0 \rightarrow D^- D_s^{*+}$	433	$371 \pm 17(86\%)$
$\overline{B}^0 \rightarrow D^{*-} D_s^+$	777	$709 \pm 70(91\%)$
$\overline{B}^0 \rightarrow D^{*-} D_s^{*+}$	571	$528^{+15}_{-16}(92\%)$
$\overline{B}^0$ all	2779	$2529^{+77}_{-78}(91\%)$
$B^- \rightarrow D^0 D_s^-$	2178	$1886^{+37}_{-38}(87\%)$
$B^- \rightarrow D^0 D_s^{*-}$	1202	$905 \pm 32(76\%)$
$B^- \rightarrow D^{*0} D_s^-$	425	$376 \pm 15(90\%)$
$B^- \rightarrow D^{*0} D_s^{*-}$	437	$382^{+16}_{17}(94\%)$
B^- all	4242	$3549^{+54}_{-55}(84\%)$
Sum	7021	$6078^{+94}_{-95}(87\%)$

Table F.1: *Extracted yields of* $D^{(*)} D_s^{(*)}$

Bibliography

[1] J. H. Christensen, J. W. Cronin, V. L. Fitch and R. Turlay, Phys. Rev. Lett. **13**, 138 (1964).

[2] M. Kobayashi and T. Maskawa, Prog. Theor. Phys. **49**, 652 (1973).

[3] S. L. Glashow, Nucl. Phys. **22**, 579 (1961); S. Weinberg, Phys. Rev. Lett. **19**, 1264 (1967); G. t'Hooft, Nucl. Phys., **33** 173 (1971); **35** 167 (1971);

[4] G. Arnison *et al.* (UA1 Collaboration), Phys. Lett. **B122** 103(1983); **B126** 398 (1983);

[5] J. J. Aubert *et al.*, Phys. Rev. Lett. **33** 1404 (1974); J. E. Augustin *et al.* Phys. Rev. Lett. **33** 1406 (1974);

[6] L. K. Gibbons *et al.* (E731 Collaboration), Phys. Rev. Lett. **70**, 1203 (1993); G. D. Barr *et al.* (NA31 Collaboration), Phys. Lett. **B317**, 233 (1993).

[7] A. Carter and A. I. Sanda, Phys. Rev. Lett. **45**, 952 (1980); Phys. Rev. **D23**, 1567 (1981); I. I. Bigi and A. I. Sanda, Nucl. Phys. **193**, 851 (1981).

[8] K. Abe *et al.* (Belle Collaboration), Phys. Rev. Lett. **87**, 091802 (2001); K. Abe *et al.* (Belle Collaboration), Phys. Rev. **D66**, 032007 (2002).

[9] B. Aubert *et al.* (BaBar Collaboration), Phys. Rev. Lett. **87**, 091801 (2001); B. Aubert *et al.* (BaBar Collaboration) Phys. Rev. **D66** 032003 (2002).

[10] A. D. Sakharov, JETP Lett. 5, 24 (1967).

[11] Stephen M. Barr, Gino Segre and H. Arthur Weldon, Phys. Rev. **D20**, 2494 (1979).

[12] John R. Ellis, M. K. Gaillard, D. V. Nanopoulos and S. Rudaz, Nucl. Phys. **B131**, 285 (1977).

[13] Particle Data Group, K. Hagiwara *et al.*, Particle Listings in the 2003 Review of Particle Physics, `http://www-pdg.lbl.gov/2003/contents_listings.html`.

[14] M. Gronau, Phys. Rev. Lett. **63**,1451 (1989).

[15] Yuval Grossman and Mihir P. Worah, Phys. Lett. **B395**, 241 (1997).

[16] X. Y. Pham and Z. Z. Xing, Phys. Lett. **B458**, 375 (1999).

[17] I. Dunietz, H. Quinn, W. Toki, and H. Lipkin, Phys. Rev. **D43**, 2193 (1991).

[18] Z. Z. Xing, Phys. Rev. **D61**, 014010 (2000).

[19] L. Wolfenstein, Phys. Rev. Lett. **51**, 1945 (1983).

[20] N. Cabibbo, Phys. Rev. Lett. **8**, 214 (1964).

[21] T. Inami and C.S. Lim, Prog. Theor. Phys., **65**, 297 (1981); F. Gilman and M. Wise, Phys. Rev. **D27**, 1128 (1983); A. J. Buras, M. Jamin and P. H. Weisz, Nucl. Phys. **B347**, 491 (1990); J. S. Hagelin, Nucl. Phys. **B193**, 123 (1981).

[22] N. G. Deshpande, Xiao-Gang He and Sechul Oh, hep-ph/9511462, Z.Phys.C **74**, 359 (1997).

[23] M. Artuso *et al.* (CLEO Collabolarion), Phys. Rev. **D82**, 3020 (1999).

[24] E. Lipeles *et al.* (CLEO Collaboration), Phys. Rev. **D62**, 032005 (2000).

[25] K. Abe *et al.* (Belle Collaboration), BELLE-CONF-0104 (2001).

[26] B. Aubert *et al.* (BaBar Collaboration), Phys. Rev. Lett. **89**, 061802 (2002).

[27] B. Aubert *et al.* (BaBar Collaboration), Phys. Rev. Lett. **91**, 131801 (2003).

[28] P. F. Harrison *et al.* (BaBar Collaboration), The BaBar physics book: Physics at an asymmetric B factory (1998).

[29] A. M. Dighe *et al.* (CLEO Collaboration), Phys. Lett. **B369**, 144 (1996).

[30] E. Kikutani ed., KEK Preprint 2001-157 (2001), to appear in Nucl. Instr. and Meth. A.

[31] A. Abashian *et al.* (Belle Collaboration), Nucl. Instr. and Meth. **A479**, 117 (2002).

[32] V. Chabaud *et al.*, Nucl. Instr. and Meth. **A368**, 314 (1996).

[33] E. Nygård *et al.*, Nucl. Instr. and Meth. **A301**, 506 (1991).

[34] O. Toker *et al.*, Nucl. Instr. and Meth. **A340**, 572 (1994).

[35] G. Alimonti *et al.* (Belle Collaboration), Nucl. Instr. and Meth. **A453**, 71 (2000).

[36] K. Hanagaki *et al.* (Belle Collaboration), Nucl. Instr. and Meth. **A485**, 490 (2002).

[37] R. E. Kalman, Trans. ASME, J. Bas. Eng. **82D**, 35 (1960); R. E. Kalman and R. S. Bucy, Trans. ASME, J. Bas. Eng. **82D**, 95 (1961).

[38] A. Abashian *et al.* (Belle Collaboration), Nucl. Instr. and Meth. **A491**, 69 (2002).

[39] “HBOOK, CERN Program Library Long Writeup Y250 (1993)”

[40] “QQ event generator”: `http://www.lns.cornell.edu/public/CLEO/soft/QQ/`

[41] “The EvtGen package home page”: `http://hep.ucsb.edu/people/lange/EvtGen/`

[42] D. J. Lange, Nucl. Instr. and Meth. **A462**, 152 (2001).

[43] R. Itoh, “QQ quick reference for Belle”: `http://belle.kek.jp/~software/qq/html/belle_qq.html`, (1996).

[44] “GEANT detector Description and Simulation Tool”, CERN Program Library Long Writeup W5013 (1993).

[45] ARGUS Collaboration, H. Albrecht *et al.*, Phys. Lett. B **241**, 278 (1990).

[46] H. Kakuno *et al.* (Belle Collaboration), Nucl. Instr. and Meth. **A533**, 516 (2004).

[47] K. Abe *et al.* (Belle Collaboration), hep-ex/0408111.

[48] O. Long, M. Baak, R. N. Cahn and D. Kirkby, Phys. Rev. D **68**, 034010 (2003).

[49] “Heavy Flavor Avereging Group, Results Summer (2004)” : `http://www.slac.stanford.edu/xorg/hfag/triangle/ichep2004/index.shtml`

[50] G. J. Feldman and R. D. Cousins, Phys. Rev. **D57**, 3873 (1998).

[51] A. G. Akeroyd *et al.* (SuperKEKB Physics Working Group), hep-ex/0406071.

[52] A. Datta and D. London, Phys. Lett. **B584**, 81 (2004).

[53] D. A. Varshalouich, A. N. Moskalev and V. K. Khersonskii, Quantum theory of angulr-momentum (World Scientific, Singapore), 76 (1988).

[54] M. Jacob and G. C. Wick, Ann. of Phys. **7**, 404 (1959).

[55] H. Tajima *et al.*, Nucl. Instrum. Meth. **A533**, 370 (2004).

[56] G. C. Fox and S. Wolfram, Nucl. Phys. **B149**, 413 (1979).